University of Southampton

Faculty of Engineering and Physical Sciences

School of Chemistry

Kinetic studies of Metal Hexacyanoferrate electrode using Energy Dispersive EXAFS

by

Thomas Simon Andrew Wakelin

Doctor of Philosophy

Supervisors

Prof Andrea E. Russell

Dr Monica Amboage

January 2025

University of Southampton

Faculty of Engineering and Physical Sciences

School of Chemistry

Doctor of Philosophy

Kinetic studies of Metal Hexacyanoferrate electrode using Energy Dispersive EXAFS

by

Thomas Simon Andrew Wakelin

Abstract

Metal hexacyanoferrate (MHCF) compounds are candidate electrode materials for aqueous sodium and potassium ion batteries and supercapacitors. This is due to their large open structure, long cycling stability and high current density. In this work we have investigated the electron transfer kinetics during the (de)intercalation of cations into/from the MHCF lattice using energy dispersive EXAFS for the cases where M = Fe, Cu, Ni, Co, and Mn. Energy dispersive EXAFS enables the oxidation state (XANES, edge position) to be determined in real time during cycling or following a potential step applied electrochemically. By comparison of the EDE and electrochemical data we were able to explore the differences in the rates of ion and electron transfer in some cases. These differences were most apparent when the oxidation/reduction of the metal ions resulted in a change in the conductivity of the MHCF. For FeHCF we observed that the change from insulator to conductor when the high-spin, carbon bound Fe atom, is reduced, the rate of the process was limited by the electron transfer reaction, whilst the reoxidation (conductor to insulator) was limited by the rate of diffusion of the cations in the FeHCF lattice. In the case of CuHCF and NiHCF, only the low spin, nitrogen bound Fe, atom is electrochemically active and, as there was little change in the conductivity of the material upon oxidation from Fe^{2+} to Fe^{3+}, we were unable to separate the rates of the ion and electron transfer. For CoHCF and MnHCF, both the Co or Mn and Fe atoms are electrochemically active and by using EDE we were able to monitor the rates of change of the oxidation states of both species in a truly simultaneous manner by collecting the data over an energy range that covered both absorption edges. As in the case of FeHCF, the rate determining process (ion or electron transfer) was found to be dependent on the oxidation state of the carbon bound metal atom, but not on the oxidation state of the nitrogen bound metal atom.

Table of Contents

Table of Tables

Table of Figures

Table of Figures

Table of Figures

Table of Figures

Table of Figures

Table of Figures

Research Thesis: Declaration of Authorship

Print name: Thomas Simon Andrew Wakelin

Title of thesis: Kinetic studies of Metal Hexacyanoferrate electrode using Energy Dispersive EXAFS

I declare that this thesis and the work presented in it are my own and has been generated by me as the result of my own original research.

I confirm that:

1. This work was done wholly or mainly while in candidature for a research degree at this University.
2. Where any part of this thesis has previously been submitted for a degree or any other qualification at this University or any other institution, this has been clearly stated.
3. Where I have consulted the published work of others, this is always clearly attributed.
4. Where I have quoted from the work of others, the source is always given. With the exception of such quotations, this thesis is entirely my own work.
5. I have acknowledged all main sources of help.
6. Where the thesis is based on work done by myself jointly with others, I have made clear exactly what was done by others and what I have contributed myself.

#Delete as appropriate#None of this work has been published before submission #or# Parts of this work have been published as:- #please list references below#

Signature: ..... Date:.....

Acknowledgements

I would like to dedicate this thesis to my grandfather, James Pidgeon, he would be just as confused and amazed that I am doing a PhD in Chemistry as I am.

I would first like to thank Dr Gabriella Kissling, it's her fault I got in this mess. Then I would like to thank Prof Andrea Russell for her support, guidance and mentoring during my PhD. We have certainly had our ups and downs, but I guess I did my homework, and we came out the other side. Your patience, determination and insight have been infinitely valuable throughout my PhD, and also a good dose of angry supervisor. Most importantly, even though we both tried our best it seems we did not kill each other - who'd have thought it. I look forward to my future electrochemical career drawing on the many lessons you have taught me, most importantly Russell's first law: "Don't forget the units".

I would also like to thank Dr Monica Amboage for her support and for teaching me how to drive (albeit drive EDE) during my PhD. The time that you gave me on and off the beam line has always been of great value and enrichment to myself as a scientist and to my PhD.

To my dear friends in the Russell and Spectroscopy groups at Diamond Light Source, and in no particular order, Amber Watson, Connor Sherwin, Abbey Telfer, Armando Ibraliu, Alex Wallace, Nikolay Zhelev and Oliver Blackman, I thank you all for your support and friendship. For the many hours spent arguing the finer points of science with some (Connor and Alex) to the human form of Xanax (Amber and Abby), I cannot thank you all enough, and I doubt I will ever fully comprehend how helpful you have all been/how vital your support has been. I can only hope that someday I will get to return the favour. Also, a special thanks to Dr Robert Laverick, once again your friendship has been of crucial support during my PhD. I would also like to thank all the other wonderful scientists I have worked with during this PhD from both Southampton and Diamond, of whom there are too many to mention; but special thanks to Prof Phil Bartlett, Dr Sofia Diaz-Moreno, Prof John Owen, Prof Andrew Hector, and the guys in the mechanical workshops, who built my *in situ* cell.

To my Mum and Dad - your part in this PhD has by no means been small, your constant support has ensured my ability to complete this work. In short, without you both this would not have been possible. I would like to thank my Nan for her continual support and guidance throughout my whole life, you truly have been a most valuable asset., and a source of excellent wisdom and guidance during my entire University career. I would also like to thank my sister, Hannah, and Faye my aunt for their continued support.

I would also like to thank Bruce Walton and Slavena Koneva and my other wonderful companions at the Gordon Arms pub for their support during my PhD. Always there to provide a mental break from the Chemistry.

Again, I would like to thank you all - each one of you proves that no one gets through chemistry alone, and least of all a Chemistry PhD. It takes a village, and I am so grateful to you all for being part of that village.

Chapter 1 Introduction

1.1 Project outline.

Electrical energy storage needs to grow and adapt to meet ever increasing demands because of government initiatives designed to tackle climate change.[1] This will also involve developing energy sources to become more sustainable and finding better ways to store this energy. Currently lithium-ion technologies provide a viable solution, especially for transportation applications, and the storage of electrical energy[2]. However, Li-ion batteries (LIB) have drawbacks especially when applied to larger scale battery needs[3].These drawbacks include the use of toxic electrolytes and expensive metals that are in low abundance. Batteries that rely on more abundant ions like sodium and potassium are of interest as well as extension to the use of aqueous electrolytes in so-called aqueous ion batteries (AIB). It is important, therefore, to evaluate a wider range of materials for AIB application, especially as they have a high potential for stationary (grid scale) energy storage (see section 1.2.3) By using such electrolytes and battery technology in combination with renewable generated electrical energy, a future where fossil fuels are redundant is entirely possible.

This Introduction introduces the electrochemical theory and applications used during this thesis and will set the research into the wider scientific environment. The chapter then concludes with an outline of the thesis.

Prussian blue (PB) is a type of metal hexacyanoferrate (MHCFS) with e analogs (PBA) derived from changing the metals within the MHCFS structure. They are promising candidates as electrode materials for AIBs.[4–6] The voltage and charge capacity of MHCFS materials as a battery electrode directly results from the metals which make up the material. Whilst the stability and capacity are related to number of CN vacancies in the lattice as well as the water content of the material.

Further research into three areas is required to advance the understanding of such electrode materials.

1. A better understanding of the rates of electron transport during the charge and discharge cycle.
2. The better measure of the rate of oxidation state changes of the metal ions within MHCFS electrodes.
3. A clearer understanding of the factors that limit the transport of the stored ion through the lattice.

1.2 Metal hexacyanoferrate as a battery material

1.2.1 Metal hexacyanoferrates

Metal hexacyanoferrate (MHCF) compounds are not only interesting due to the structural and electronic properties, but also possess features useful for electro catalysis, ion-exchange, electrochromic and photo magnetic applications.[7,8] MHCFs can be written in the two forms, oxidised AM' [Fe(III)$(CN)_6$] or reduced A_2 M' [Fe(II)$(CN)_6$]. Where M' is a transition metal, in the case of Prussian blue both are Fe, and A is an alkali metal cation. Most importantly, they contain 2 metal centres. Prussian blue (PB), Iron (III) hexacyanoferrate (II) (FeHCF), is a type of MHCF with a deep blue colour.[9] PB was first discovered by accident in the early 18th century.[10] The pigment was named after the location of its discovery. PB is a mixed-valence transition metal complex, with maximum absorption of 700 nm.[11]

Synthesis of PB occurs through a precipitation reaction, between hexacyanoferrate complexes and iron salts.[9] During the synthesis vacancies, missing -CN- bridging ligands, within the PB structure can occur. These vacancies are associated with the ion transportation properties of PB. Most of these vacancies within the cubic structure will be occupied with water or interstitial coordinated alkali cations. Much work on PB has focused on removing the coordinated water or the inactive coordinated cations to allow for more efficient ion storage.[12]

As mentioned above, the cage structure of PB makes it such a useful electrode material for battery applications. Keggin and Miles defined the first structure for PB.[13] This structure was determined from x-ray powder patterns and established that PB has interstitial metal ions within the cubic face-centred unit cell. Further analysis of the metal hexacyanoferrate shows they have a perovskite-type structure and a characteristic lattice parameter of 10.2 Å and a face-centred cubic lattice with Pm3m symmetry.[14] The crystal structure and unit cell of PB are shown in the figure below.

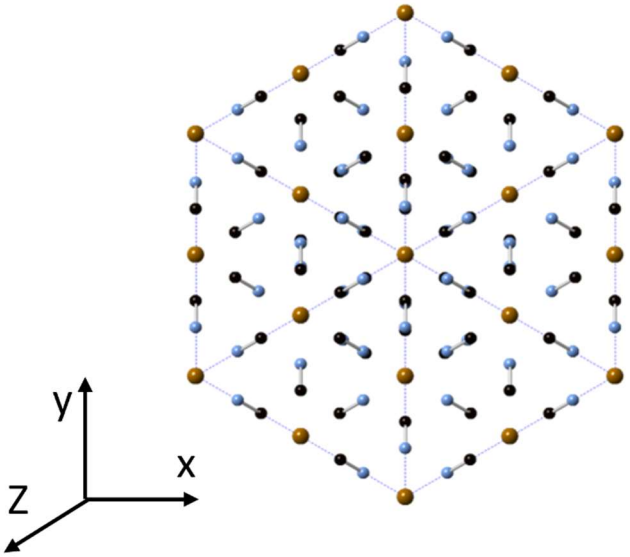

Figure 1 Structure of PB, shows the crystal structure of Iron (II) hexacyanoferrate (III). Where brown is Fe^{3+} (bound to nitrogen) and Fe^{2+} (bound to carbon), blue is nitrogen and black is carbon.

Figure 1 shows the high spin Fe^{3+} is octahedrally surrounded by 6 nitrogen atoms and the low spin Fe^{2+} ligated by 6 carbon atoms. The high spin Fe^{3+} and the low spin Fe^{2+} are joined by a linear $C\equiv N^-$ bridging ligand. This results in the cage like network. In the perfect structure the interstitial positions in the PB are occupied by cations for charge compensation. PB can be both in a reduced form, known as Prussian white (PW), $A_2Fe^{II}[Fe^{II}(CN)6]$, or oxidised as Prussian green (PG), $Fe^{III}[Fe^{III}(CN)6]$[21]. These forms are named because of the colour change of the PB from either white to green.

1.2.2 Metal hexacyanoferrates as a battery material.

FeHCF is a promising material for ion storage. Firstly, this is due to a high specific capacity for inserting ions. This is done via two reversible one-electron reaction. Secondly, the cubic geometry with wide channels and an open framework allows for rapid ionic conduction. Thirdly it undergoes a minimal change in this geometry during this insertion, this leads to a long cycle life. There are however some drawbacks to FeHCF in that it has a low crystal density of around 1.96 g cm^{-3} for a defect free sodium iron hexacyanoferrate. [15] This is less than half the density compared to high performing lithium ion cathodes.[16] As a result of this combination of advantages and disadvantages FeHCF is only realistically a candidate for stationary grid-scale energy storage. In this case a high energy density is not a major requirement but the low cost, long cycling life and fast rate are of great advantage.

Nickel hexacyanoferrate (NiHCF) is a prime example of the adaptivity of MHCFs for battery materials NiHCF has the same structure as FeHCF with the substitution of Ni^{II} in the M' position.[17] A capacity of 71 mA h g^{-1} with a 100 % retention and current density as high as 500 mA h g^{-1} has been reported for NiHCF cathode in Na^+ ion aqueous batteries.[18]

Copper hexacyanoferrate (CuHCF) is another example of a MHCF that has demonstrated excellent cycling retention and a specific capacity of 46 mA h g^{-1} at a current density of 20 mA g^{-1}.[19] The same open cubic structure is still present for CuHCF as in FeHCF but now the M' site is occupied by a Cu^{II}. The common connection between NiHCF an CuHCF unlike FeHCF is that they only have a single redox active couple.[20]

Other examples of MHCFs include CoHCF and MnHCF.[21] In these the Fe-N is replaced by a Co or Mn respectively. Once again, they excellent cycling stability for Na^+ ions have been reported and is attributed to the large open frame work.[22–26]

The MHCFs mentioned above will be used for the focus of this thesis. However, there are many other possible forms that MHF can take, including ones where the Fe-C centre is replaced with another metal.[27,28]

1.2.3 Aqueous ion batteries.

Aqueous ion batteries (AIBs) offer a safer alternative to non-aqueous lithium-ion batteries. The aqueous electrolyte offers a great alternative in terms of its low cost, low risk and high abundance, the production of aqueous electrolytes does not require any removal of oxygen or drying so the manufacturing costs are much lower. They have low environmental impact due to the nonvolatile, nontoxic, and nonflammable nature of water. AIBs are capable of rapid charging due to the high ionic conductivity and are very tolerant to mechanical or electrical fault.

The main two issues facing the use of AIB for large scale application are their limited energy density and their low cycling stability. The limited energy density is a result of the narrow thermodynamic potential window of water, around 1.23 V.[29] This results from inherent thermodynamic oxygen reduction potential. Aqueous electrolytes with varying pH ranges have been adopted to overcome this issue. These, however, cause water-based side reactions which restricts the lifespan of the AIB.

Due to their low cost, minimal environmental impact, and enhanced safety AIB can become the leading candidates as the solution for the energy storage problem. However, there are still obstacles to overcome. The design and application of electrode materials to be used in AIBs are crucial to achieving high performance and high output energy. Depending on the nature of the

migrating ion, AIB batteries come under two categories: metal-ion AIBs and non-metal-ion AIBS. Currently many metal-ion AIBS, including Li^+, Na^+, K^+, Zn^{2+}, Mg^{2+}, Ca^{2+} and Al^{3+} have been explored based on metal-ion intercalation chemistry.[30] Due to the issues arising from the conventional non-aqueous Li ion battery the Li-AIBs has been extensively developed. This has much greater benefits in terms of cost, safety, and power capability compared to non-aqueous ion batteries. Nevertheless, due to their higher natural abundance, Na^+ and K^+ based AIBs represent more attractive AIBs. However, when comparing the radii of Na^+ and K^+ ions, 0.9 Å and 1.33 Å respectively, they are much larger than that of Li^+, 0.60 Å. This means the selection criteria of compounds that allow for K^+ and Na^+ intercalation is limited.

Non-metal-ion charge carriers consist of anions, including halides, F^- and Cl^-, or hydroxyl, OH^- and cations such as protons, H^+ ammonium, NH_4^+.[31] Compared with metal-ion carries, non-metal ion carrier are made up of lighter molar masses and exhibit lower hydrated ionic. This results in faster diffusion in aqueous electrolytes. In contrast to the highly corrosive and very polluting nature of the strong alkaline electrolytes, the halides used in AIBs use a salt-based electrolyte such as NaCl. Although, NH_4^+ is much less corrosive and less prone to hydrogen evolution reaction (HER), which can result in a superior cycling performance.

MHCFSs have in recent years had a renewal in their interest for AIB materials due to their unique properties and variability. Primarily they have a high capacity for alkali and non-metal alkali ion insertion via two electron transfer reactions. They have a cubic structure with wide channels which allows rapid ionic conduction for high-rate capacity. This intercalation and deintercalation also does not usually result in significant geometric change to the MHCFSs structure leading to much longer cycling stability. Additionally, MHCFSs are easily prepared in a simple precipitation reaction between two inexpensive aqueous precursors.

1.2.4 MHCFSs as cathodes for Sodium aqueous ion batteries.

Much investigation has been conducted into MHCFSs as a cathode material for sodium ion batteries (SIBs). The major difficulty facing the development of SIB is identifying appropriate cathode and anode materials. A paper by Goodenough *et al.*[32] report that the open framework of MHCFSs gives the perfect structure for SIBs, allowing for facile (de)intercalation of cation without causing major structural changes.[33] A paper by Lu *et al.*[34] identifies that the linear $(C\equiv N)^-$ allows for a M(II)-N≡C-Fe(III) bond length that is ideal for Na ion intercalation with high reversibility. Furthermore, the C≡N bond provides a strong π–bond which can enhance the crystal field splitting of the 3d manifolds of the transition metal cations, especially for the carbon bound Fe. This in turn favours the stabilisation of the low-spin Fe(III) $3d^5$ configuration of the octahedrally

coordinated Fe atom. The Fe(II) $3d^6$ atom is coordinated to N atoms in a high-spin state. One paper reports synthesis of PB in a high Na rich environment with a capacity retention of 90 % after 200 cycles.[35] For FeHCF (PB), both Fe atoms are electrochemically accessible with the water window, maximising the storage capacity of the materials. In contrast, for many PBAs, only one of the metal centres will be electrochemically accessible, limiting the theoretical specific capacity. Thus, the more promising analogues are those with a two-electron reaction. In particular, the analogues of Mn and Co show a much higher capacity. Unfortunately, some of the analogues show poor cycling stability possibly because of the Jahn-Teller effect.[36]

Another issue facing MHCFs in their application for both types of AIB is interstitial water.[37] If water molecules occupy the coordination sites within the MHCFs framework this inhibits cation intercalation. This leads to an overall decrease in the Columbic efficiency and cycling stability.[38] Furthermore an increase in the number of CN vacancies will reduce the electronic conductivity of the material and lead to the collapse of the open 3D network. If prepared with a highly crystalline PB crystals and low crystal water content and few vacancies a theoretical capacity of 170 mA h g^{-1} can be achieved with almost no capacity loss for 150 cycles.[39,40]

From the summary above, in the case of using PBAs or MHCFs as a material for either potassium ion batteries (KIB) or SIB four elements are required to achieve a high specific capacity. Firstly, both metal centres in the PBA or MHCF must be electrochemically accessible. If this is not the case the material is limited to a very low specific capacity and is not competitive with current standards. Secondly, the PBA or MHCF should be synthesised/prepared in a cation rich environment appropriate to the electrolyte of the battery to maximise the initial occupancy of the ion storage sites, which will assist in the cycling stability and reversibility. Thirdly the minimisation of interstitial water, which blocks coordination sites that would be available to intercalating cations, and finally ensuring the smallest amount of (CN) vacancies to allow for excellent cycling stability.[32,41,42]

1.3 Coupled ion-electron transfer kinetics

Charge transfer reactions underly many energy storage and conversion reactions. Using well established models, such as the Butler-Volmer (BV) and Marcus kinetics, the rate of charge transfer redox reactions can be described.[43,44] At a basic level intercalation is comprised of two steps, electron transfer (ET) and ion transfer (IT). ET occurs between the current collector and the redox active material resulting in the oxidation/reduction of the transition metal(s) in the material.[45] IT is the movement of the ions into and out of the metal crystal lattice structure of the

redox active material and/or the electrode structure from or to the electrolyte.[46] For ion insertion materials both processes are important, and the combination is termed coupled ion-electron transfer (CIET). Either of the two processes can be rate determining. In the case of insertion materials (with ion intercalation) much work is still needed to improve the models to analyse the rate of the charge transfer beyond standard BV kinetics. The rate of IT is best measured using BV kinetics in standard outer sphere models. This builds on previous work carried out by Tafel and using Eyring transition-state (TS) theory leading to the BV equation (Equation 1).

$$i = i_0 \left\{ e^{\left[\frac{a_f n\mathrm{F}(E-E_0)}{\mathrm{RT}}\right]} - e^{\left[\frac{-a_r n\mathrm{F}(E-E_0)}{\mathrm{RT}}\right]} \right\}$$

Equation 1

Where i is current, A, i_0 , is the exchange current density also in A cm^{-2}, α the transfer coefficient for the forward, f, and reverse, r, reactions, n the number of electrons, R the ideal gas constant, F Faraday constant, T temperature in K and $E - E_0$the overpotential in V.

This BV type analysis has also been used in a more general sense for reactions with non-ideal thermodynamics (to allow consistent comparison), for example reactions with phase transformations that are driven by charge transfer.[47] Marcus theory was the first theory that recognised that classical treatment of TS theory cannot be applied to ET. Marcus theory proposes that ET occurs iso-electronically as a response to changes in the local environment of the redox species. In the case of outer-sphere ET reaction Marcus correlates the ET activation energy barrier to the reorganisation energy of the solvent, λ. Therefore, these reactions are dominated by dielectric polarization of the medium. After this Hush derived a similar rate expression for adiabatic inner sphere ET reactions, leading to Marcus -Hush theory,[48] in which the ET occurs in direct response to molecular vibrations, therefore, λ is dominated by the phonons of the molecular complex.[49] This leads to a reduced version of the BV equation for overpotentials that are much smaller than the λ value. This is to say that ET transfer reaction depends on interactions of the electrons that are participating with the reaction with the environment of the partial redox active site, meaning that when fluctuation is large enough to make the reduced and oxidised state iso-energetic, ET transfer can occur via tunnelling. It is the goal of this thesis to further attempt the separation of ET kinetics from the CIET kinetics response given for standard electrochemical reactions.

Figure 2 gives a graphical representation of the difference between and IT and ET reaction. In Figure 2 a) for the ion transfer, the reaction coordinate ξ is the distance the distance of the ion

from the reduced state, under an applied overpotential, η. For example, a cation is attracted towards the surface of the electrode, where at a distance (red point) near the electrode the species is reduced by an electron (dashed green arrow) This distance is described by the charge transfer coefficient, α. For Figure 2 b) the electron transfers along the reaction coordinate, x corresponds to the environment of the polarization coordinate. To enable an ET to occur both states of the reactant and product need to be at the same energy. This allows the electron to tunnel between the two. This leads to the reorganisation step (discussed in a later section) shown by the blue shade in the diagram.[43,50–53]

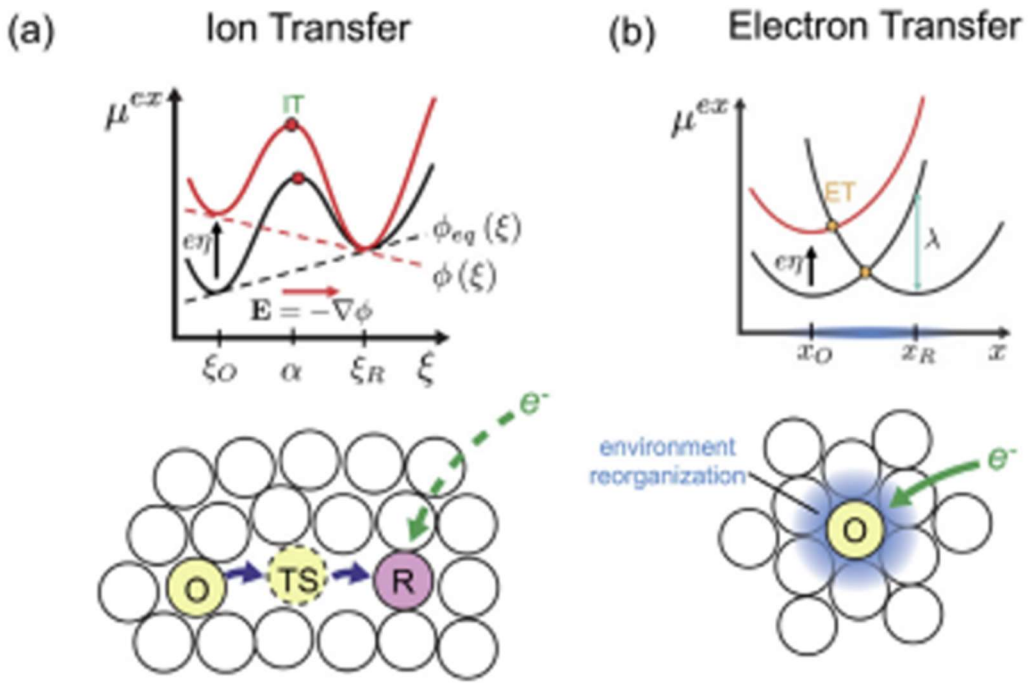

Figure 2 A physical picture of a) ion and b) electron transfer, as a function of excess electrochemical potential, μ_{ex}. For both images O, Ts and R correspond to the oxidised, transition and reduced state respectively. Image taken from "Theory of coupled ion-electron transfer kinetics" by Fraggedakis *et al.* [43]

Figure 3 is a graphical representation of a CIET reaction. Shown in Figure 3 (a) is a schematic of an amorphous medium made up of neutral particles, with a reduced and oxidised species. At first the transferring ion moves towards to the site where it will be reduced (blue shaded region) during this stage the reorganisation occurs because of thermal fluctuations. Then when the reactant and product states have similar energies and the ion is in a transition state an electron, from either the metal or the dopant, will tunnel and reduce the site. Figure 3 (b) and (c) show the energy landscape of the ion-polaron pair formed, drawn as a contour plot with a three-dimensional landscape in terms of the ionic ξ and polarization coordinates, x.[54–56] In Figure 3 (b) and (c) there

are four minima, two of these correspond to the redox states, which can only be accessed via a single point (yellow diamond) with the lowest energy barrier allowing the transfer of both ions and electrons to the product state. The red dashed line shows the minimum energy path on the contour plot Figure 3 b) whilst in the three-dimensional plot the minimum energy path is shown by the solid and thin dashed red line. The solid and thin dashed green line show the intersection of the energy landscape with x-normal plane, where $x = x_O$ and $x = x_R$. Lastly the dashed red line on Figure 3 (c) is the projection of the minimum energy path.

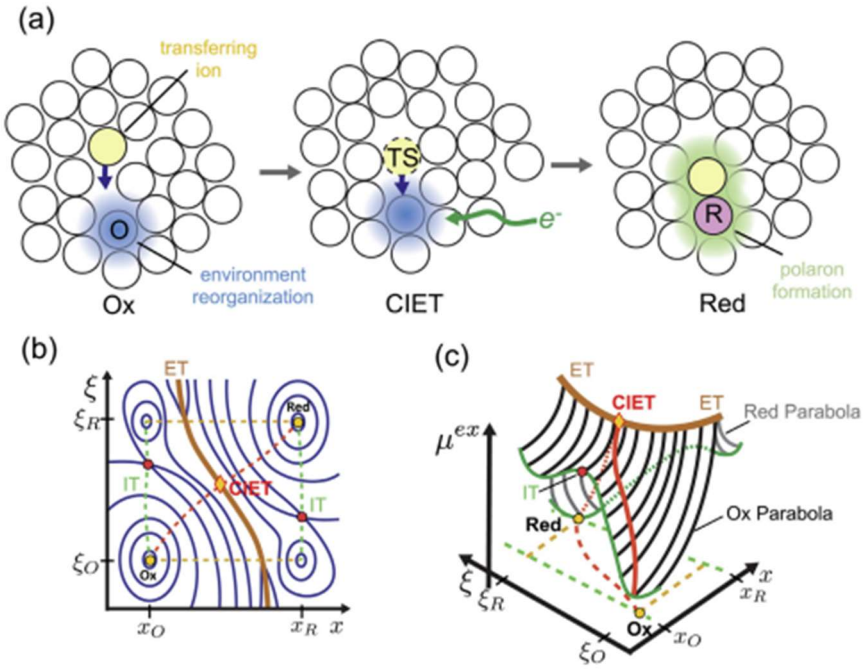

Figure 3 Physical and energy picture of coupled ion-electron transfer. Image taken from "Theory of coupled ion-electron transfer kinetics" by Fraggedakis *et al.* [43]

The origins of inner and outer sphere redox systems are well known and discussed at length when applying IT or ET mechanisms to redox systems.[57] An outer sphere electron transfer (OSET) mechanism involves transition metal complexes in a solution taking part in an ET reaction undergoing a ligand exchange reaction that is much slower than the ET process. As a result of this the ligand coordination spheres are unchanged during the electron donation and acceptance. In contrast to this, inner sphere electron transfer (ISET) involves the exchange of a ligand as well as the ET process. Both inner and outer sphere models have been used when discussing the kinetics of electrode materials when MHCFs are used as a redox probe.[58–65] Interestingly in most cases outer sphere kinetics are used when the solution has not been de-oxygenated. However, when reviewing the literature, it is apparent that the in most cases the Fe-N redox reaction generally is attributed to a ISET mechanism. However, this debate in the literature leads to ambiguity, enhanced when using a carbon-based electrode, such as those which will be used in this thesis, and suggests in the context of MHCFs that the inner/outer sphere designation should be

discontinued as a wide variety of factors influence the ET, such as supporting electrolyte cation, the presence of surface oxides, electrode surface energy effects, double layer potential effects (Frumkin correction) and solvent reorgansiation.[66]

A better description for the electron transfer in FeHCF redox system is that it occurs on in a quasi-reversible manner in the Inner Helmholtz Plane of the electrode diffusion layer (EDL). This is contrast to the well-known $Ru(NH_3)_6^{2+/3+}$ redox couple that is considered to be a surface-sensitive ET, which is reversible ET in the Outer Helmholtz Plane of the EDL. In this case the EDL is depicted with the OSET represented by a transition metal complex oriented such that electron transfer occurs through a solvent molecule on the electrode surface.

An important factor in Marcus' theory is the reorganisation energy, λ. This parameter relates to the energy required for the reconstruction of the precursor complex. The value of λ is not the activation energy but is a the parameter that determines the activation energy. More specifically the reorganisation value is generally used to describe the energy needed to reorganise reactant bonds and surrounding solvents to match those of the product and it related to the Gibbs free energy of the system. The reorganisation parameter is made up of both components of the inner and outer sphere λ_i and λ_o respectively:

$$\lambda = \lambda_i + \lambda_o$$

Equation 2

Where the value of λ_i is related to the precursor state; reactants, products, or electrode and the λ_o related to the environment of the reaction, like solvents.

From semi-log plots of rate *vs.* magnitude of applied potential, we can use the following equation to find a value for the reorganisation energy based on the work done by Todd P. Silverstein.[53]

$$\lambda = \frac{\Delta E_{mid}}{\left[1 - \left(\frac{2\mathrm{RT}}{\mathrm{F}}\right) x\ gradient\right]}$$

Equation 3

Where ΔE_{mid} is the midpoint of the range of potentials investigated, R is the ideal gas constant, T = 298 K and the $gradient$ is taken from the fitted semi log plot of ln(k) *vs.* ΔE (see section 3.2.4.3).

However, we must first look to the methods used to analyse the IT kinetics, which takes the form of an effective diffusion coefficient. As mentioned previously standard IT models have been used to measure the rate of insertion kinetics, operating under the assumption that IT is the limiting factor even though in a CIET model either IT or ET can be limiting. This has been shown in the

context of Li-ion batteries.[67] In this work they used exported charge-transfer rates from chronoamperometric measurements on carbon-coated $LiFePO_4$ porous electrode. The Tafel plots obtained contradicted the BV model, but when the MHC model was applied a more appropriate fit was found. This leads to the conclusion that the kinetics are limited by electron transfer in the solid-state rather than ion transfer at the liquid solid interface.

There is a large volume of literature dedicated to the study of IT in MHCF materials. It is well documented that MHCF materials exhibit non-linear diffusion behaviour (NLD).[68,69] NLD is a diffusion profile that does not follow Fick's laws of diffusion, this is to say that the rate of diffusion is not proportional to the inverse square of time. The published works generally focus on quantifying the IT in FeHCF using a combination of cyclic voltammetry, chronoamperometry, and potential intermittent titration. They report that the thermodynamic properties of FeHCF have been wildly studied showing that the reduced form of PB can be viewed as a solid solution of PB and PW. However, the kinetics of the process are not as well understood. There are two major models used to define the differences in diffusivity among these materials. Firstly, a standard Fick's law model which leads to an effective diffusion coefficient[70] and a second that defines the electronic diffusivity as a ratio of the electronic conductivity to the redox capacity. [71,72] .The models which rely on Fick's laws they do not consider the NLD behaviour of the MHCFs materials.

One study which clearly explains the study of the IT in a solid-state material, is the work conducted by Baltruschat *et al.* on the insertion of magnesium into antimony layers on gold electrodes for the application of Mg based secondary batteries. Here they investigated the kinetics of the insertion/extraction mechanism of cations.[73] In this work a combination of cyclic voltametric and chronocoulometric measurements were analysed using standard BV kinetics and the integrated Cottrell equation was used to explore the IT kinetics of the system. To determine the diffusion coefficient large potential step experiments were conducted using both chronoamperometric and potential intermittent titration experiments. From these measurements they were able to calculate the solid-state diffusion coefficient of Mg into the Sb layers and found a value in the range of 10^{-14} cm^2 s^{-1}. The methods outlined in this paper will be further discussed and used during the analysis of diffusion coefficient in this thesis (section 3.2.2).

As mentioned above, standard Cottrell analysis of NLD systems is not effective, as the current is rarely proportion to the $t^{-1/2}$ as defined by Fick's law. In most cases when solid-state diffusion is a limiting factor the analysis for an effective diffusion coefficient needs include contributions from the thickness of the electrode.[74] In this work, by Eftekhari, they use chronoamperometric studies on $LiFe_{0.5}Mn_{1.5}O_4$ to determine a time dependent diffusion coefficient based on the thickness of their electrode. These results allowed them to define effective diffusion coefficients for longer

periods, which then show the variation of diffusion coefficient with potential (or insertion level). This method of thickness dependent effective diffusion coefficient outlined in this paper is applied in 3.2.2.2.

Much less previous work exploring the electronic conductivity of each MHCFs and its fully intercalated or deintercalated forms is available in the literature. The electronic conductivity of each of the MHCFs compounds will have a direct effect on the rate of ET and as mentioned above, may determine the rate limiting step. In the work of Pasta and co-workers [75] density functional theory (DFT) was used to model the structure of Fe/Co/Mn HCF and by determine the band gaps for each MCHF (found to be in a range of 1.90 eV to 4.94 eV) they found that the carbon bound metal atom, and its oxidation state contributed significantly to the electronic conductivity. This paper is one of few that attempt to compare the spin state dependent inorganic conductivities of the MHCF compounds and their effects on ET. This builds on work carried out where i-V cures are used to attempt to calculate the ohmic threshold for Prussian Blue ($Fe^{2+}[Fe^{3+}(CN)_6]$), PG ($Fe^{2+}[Fe^{2+}(CN)_6]$) and PW ($Fe^{3+}[Fe^{3+}(CN)_6]$).[76] In these i-V studies they report that, whilst PB is a poor conductor due do the "conduction electrons in narrow bands that are fully occupied," but provided no explanation as to why they found that PG and PY are better conductors. The insulating nature of PB and the conductive nature of PG and PY is also discussed in other sources.[77,78.] However, in each case little rational is given for the findings and this suggests limitations of DFT when looking at MHCF compounds. Further to this, in these papers a small-polaron hoping mechanism was proposed to interpret the electronic conductivity of each material, however much more work to develop this model and the understanding of polarons in MHCF is required.

The electronic conductivity of Mn/Fe/Co HCF were also modelled using DFT in a study by Volonakis *et al.*[79] They found that these materials can act as semiconductors or insulators with band gaps ranging from 1.90 eV to 4.94 eV. Once again hinting to the small-polaron hopping mechanism for the electron transport. The importance of the carbon coordinated iron in the electronic conductivity is also highlighted, even though the experimental focus is on doping the nitrogen coordinated site, again suggesting that doping at this site will lead to higher charging densities.

Wittstock *et al.*[80] Carried out thin-film electrical conductivity measurements on various CuHCF samples. They found that the conductivity of their samples depended heavily on the method of synthesis and the way in which the material was processed. Once again highlighting the effect of removal of water from the MHCF structure has on reducing the conductivity.

1.4 Operando studies of MHCFS materials

A wide range of *in situ* techniques have been employed to further understand the processes of IT and ET in MHCF materials. Work by Kwak *et al.* [81] has attempted to use an electrochemical quartz crystal microbalance (eQCM) to measure the rate of ion transport in electrochemically prepared PB samples. Their results support the proposed theory that structural reorganization occurs upon intercalation and the transition from PB to PW. Furthermore, they report that a large amount of water is removed from the FeHCF structure during the initial reduction, leading to ion transport being the dominant during the redox process. Further work carried out on FeHCF using an eQCM has been conducted by Augustyn *et al.*[82] Where they demonstrate that the cycling stability of FeHCF depends heavily on the intercalating cation, being worse for larger hydrated ions such as Li^+ and better for smaller once such as K^+. They also show using *in situ* atomic force microscopy that on insertion and removal of cation there is an expansion and contraction of the FeHCF lattice for K^+ ions. Although they make no comment on the rate of the reaction based on the identity of the inserting cation.

Work by Nordstrand *et al.* [83] applied a quantum chemical approach, self-consistent mean field theory and a finite -element modeling to investigate the IT in MHCF materials. They identified a cyanide-mediated ladder mechanism as the main process of IT. This is heavy impacted by any defects present in the electrode material. This model allowed them to accurately predict diffusion coefficients for their system when applied to a range of MHCFs.

Work done by Liqiang *et al.* [84] used a combination of *in situ* X-ray diffraction and Raman on highly crystalline FeHCF to investigate the electron transport in PB and showed that this uniform structure with a low amount of defects effects allowed for improved electron transport when compared to other synthesized FeHCF electrodes. Other studies conducted by Wang *et al.*[85] also employed operando X-ray diffraction and Raman to study the cation intercalation mechanism. There work focused on PG during the (de)intercalation of Na^+ and K^+ cations. Where they conclude that the intercalation of Na^+ follows a solid solution mechanism giving a higher capacity compared with the intercalation of K^+ ions which followed a two-phase transition mechanism. They conclude that an electrolyte containing a combination of both Na^+ and K^+ would lead to a higher energy density.

There are several studies using X-ray absorbance spectroscopy (XAS) to better understand the structural parameters of MHCFs.[85,86] One example of using operando XAS studies for MHCF materials is given in a paper Giorgetti *et al.,*[87] where they studied the electronic and structural evolution of CuHCF during galvanostatic cycling in a Li^+ ion electrolyte. Both the Fe and Cu edges were studied together using a monochromatic beam, scanning across the Fe and Cu K-edges. An

in-depth analysis of their XANES data confirmed the reversibility of the redox active Cu and Fe sites in CuHCF. The X-ray absorption near edge (XANES) response is strongly influenced by the oxidation state and the electron spin configuration of the CuHCF sample. From there results on the changes in the XANES during charge and discharge they were able to draw conclusions that the system relies on an electronic and structural stability, to maintain cycling stability. The paper further stresses the importance of a deeper understanding of the electronic conductivity of MHCFS materials when discussing the rate of ET.

Another study of the operando XANES of MHCF materials is shown in a paper by Abruna *et al.,*[88] in which the XANES were monitored during the charge and discharge of the material accompanied by the (de)intercalation of Na^+ ions. The paper focusses on both FeHCF and NiHCF, concluding that Fe is active in both compounds, but the Ni remains electrochemically inactive in NiHCF. They further conclude that by the substitution of Ni a larger lattice space is provided that facilitates faster diffusion of Na^+ ions. This larger spacing results in improved cycling stability and a better rate capacity for the NiHCF.

The effect of high spin and low spin on the capacity retention of FeHCF cathode materials is investigated in a paper by Wang *et al.*[89] they attempt to deepen the understanding of the relevance and effect that the high spin and low spin iron centers have on the reaction process for FeHCF. They used highly crystalized monoclinic FeHCF that demonstrated an excellent electrochemical performance and good cycling stability when cycling in a Na^+ ion electrolyte. Using operando Mossbaur spectroscopy along with ex situ Mossbaur and X-ray absorbance spectroscopy, they found that the high-spin Fe-N reaction contributed more to the capacity of the material compared to the low-spin Fe-C. They conclude that enhancing the activity of the low-spin Fe-C could lead to better cycling performance and help to achieve higher working capacities for these materials.

A study by Margadonna *et al.*[90] focused on using operando XRD and XAS to investigate the Na^+ ion insertion into MHCFs cathode materials. They carried out quasi-simultaneous XRD and XAS studies on monoclinic and cubic MnHCF, where they observed a reversible structural phase transition during the (de)intercalation of Na^+. Once again, they were able to link the structural and electronic difference of the monoclinic and cubic MnHCF structures to the charge response. They also observed the formation of $NaMnCl_3$ during cycling which contributed to the poor cycling stability.

Li^+ ion and Na^+ ion intercalation into MHCFs was studied by Yutake Moritomo *et al.*[91] They again investigated the structural and electronic response of the MHCFS framework during intercalation of the cations. They confirm, using a combination of XRD and XAS data, the robust structure of

MHCFS is excellent for stable cycling and attribute the flat region in the discharge curve to a phase separation within the material but provide little insight into the conductive effect on the electron transfer mechanism.

1.5 Aims and outline of thesis.

The objective of this project is to use novel time resolved X-ray spectroscopic techniques to follow the charge and discharge of alkali cations in real time and to attempt to separate the contributions from the ion and electron transport kinetics. The aim is to provide a detailed on how the electron transport kinetics vary from the coupled ion-electron kinetics and what affect the material has on these.

The aims of this project will be to.

- Synthesis high quality MHCFS materials.
- Prepare inks from the MHCFS materials to make electrode with fast and stable electrochemical kinetics.
- Design and assess an electrochemical cell to enable *in situ* X-ray absorbance spectroscopic studies (XAS) for studies of those MHCF electrodes.
- To collect time-resolved X-ray absorption spectroscopy data using the operando cell.

Accomplishing the XAS aims will require interfacing the electrochemical control system and with the beamline hardware and software to achieve accurate time resolution. The resulting data will uniquely contribute to understanding of the relative rates of the oxidation state changes of each of the metal ions in the PBA materials. With the XAS data, we will attempt to shed light on the electron transfer (ET) kinetics and separate these from the electrochemical results where both the ET and ion transfer (IT) processes more commonly known as couple ion-electron (CIET) charge transfer contribute.

This thesis will focus on the electrochemistry of Fe/Ni/Cu/Co and MnHCF in aqueous media containing Na^+ or K^+ ions.

Chapter 1 will outline the aims and objective of the thesis and report a literature review setting the work in the wider context of MHCFS electrochemical research.

Chapter 2 will outline the methods used both experimentally and for the analysis of each experiment. Furthermore chapter 2 will report the results of the material characterisation and electrode preparation.

Chapter 3 will focus on FeHCF in both Na^+ ion and K^+ ion electrolytes. Demonstrating the electrochemical experiments conducted and the analysis to find an effective diffusion coefficient. This leads to a comparison of the spectroscopic results (ET) and the electrochemical results (CIET).

Chapter 4 will then focus on comparing NiHCF and CuHCF using the same methods of analysis demonstrated in chapter 3.

Chapter 5 will focus on CoHCF and MnHCF, but this time using EDE set up so that spectra are collected across both relevant edges in a dual edge configuration, enabling true simultaneous measurement of the oxidation states of both metals in real time.

Finally, **Chapter 6** will conclude the findings of this thesis and discuss future experimentation and analysis that this work could lead to.

Chapter 2 Experimental and material characterisation

This chapter will cover the experimental details of the methods used during this work, along with the methodologies followed to obtain the data, and the methods of analysis used and the results of the materials characterisation.

2.1 Chemicals and materials

All chemicals and materials used in this work are summarized in **Table 1**.

Table 1 Details of the chemicals and materials used in this work and their suppliers

Chemical	Purity	Supplier
Sodium ferrocyanide $Na_4Fe(CN)_6$	98%	Alfa Aesar
Perfluorinated resin solution containing Nafion™ 1100W	5 wt.% in lower aliphatic alcohols and water, contains 15-20% water	Sigma-Aldrich
Polyvinylpyrrolidone (PVP)	Average mol wt 40000	Sigma-Aldrich
Hydrochloric acid (HCl)	37%	Sigma-Aldrich
Potassium hydroxide	99% extra pure	Sigma-Aldrich
Sodium Chloride (NaCl)	99% extra pure	Sigma-Aldrich
Cobalt nitrate ($Co(NO_3)\cdot 6H_2O$)	98% pure	Sigma-Aldrich
Nickel nitrate ($Ni(NO_3)\cdot 6H_2O$)	98% pure	Sigma-Aldrich
Copper nitrate ($Cu(NO_3)$)	98% pure	Sigma-Aldrich
Manganese nitrate ($Mn(NO_3)$)	98% pure	Sigma-Aldrich
Trisodium citrate dihydrate	98% pure	Sigma-Aldrich
Potassium ferrocyanide $K_4Fe(CN)_6$	98% pure	Alfa Aesar
Potassium nitrate (KNO_3)	99% extra pure	ACROS Organics
Sodium nitrate ($NaNO_3$)	99% extra pure	ACROS Organics
Polytetrafluoroethylene (PTFE)	60 wt. % dispersion in H_2O	Aldrich
KetjenEC300J carbon	Lab grade	Johnson Matthey
Propanol	laboratory reagent grade	Fisher
Toray carbon paper		Alfa-Aesar

2.2 Synthesis of materials

2.2.1 Synthesis of iron(II) hexacyanoferrate

The synthesis for FeHCF follows the following process. Firstly, the addition of concentrated HCl too a solution of $K_3[Fe(CN)_6]$, released the $[Fe(CN)_6]^{3-}$ ions and reduces them to form $[Fe(CN)_6]^{4-}$ ions. Secondly, the presence of the acid also forms the ferric ions, Fe^{3+}. The blue precipitate (Prussian blue) then forms when the Fe^{3+} ions react with the $[Fe(CN)_6]^{4-}$ ions. This reaction is summarised in Equation 4.

The reaction for FeHCF follows three steps in solution.

$$4Fe^{3+} \;\; 3[Fe(CN)_6]^{4-} \rightarrow \; Fe_4[Fe(CN)_6]_3$$

Equation 4

The reaction is conducted in an NaCl solution Na^+ ions will be intercalated into the FeHCF structure to complete the charge neutrality.

The synthesis of Prussian blue followed a 'one-pot' method.[92,93] Equimolar amounts of $Na_4Fe(CN)_6.10H_2O$ (0.5954g) and PVP (0.9912 g), which acts as a kinetic inhibitor, are added to 100 ml of saturated NaCl solution. The solution is then heated to 80°.Once this temperature is reached 2 ml of concentrated HCl is added drop wise to the solution, which is 3.6 times the concentration of the $Na_4Fe(CN)_6.10H_2O$. This forms a translucent white suspension, Prussian white, $Na_2Fe[Fe(CN)_6]$. The solution is then left to stir overnight maintaining a temperature of 80°. The translucent suspension turns to a deep blue over time, corresponding to the Prussian blue $NaFe[Fe(CN)_6]$. The solution is then left to cool whilst still stirring. Once cooled the sample is then centrifuged at 8000 rpm for 20 minutes. This leaves a blue precipitate and a clear solution which is discarded. The precipitate is then washed three times with ultra-pure water and centrifuged each time at 8000 rpm for 20 minutes. Each time the precipitate is kept, and the solution discarded. After the three washes with ultra-pure water the remaining precipitate is then washed with ethanol and centrifuged once more at 8000 rpm. This final precipitate is then dried in an oven over night at 120° and yields the PB.

2.2.2 Synthesis of Prussian blue Analogue

The PBA were also synthesised using a 'one-pot' method. Two solutions, corresponding to the Fe and analogue M source, being added dropwise using a peristatic pump into 100 ml of saturated NaCl. **Table 2** outlines the specifics for each PBA. The general method is as follows. Two equimolar solutions of A and B (25 mM in 100 ml of ultra-pure water) are added dropwise to 50 ml of

saturated NaCl solution, at room temperature. The saturated NaCl solution was constantly being stirred whilst solutions A and B are added. This produced a coloured suspension. Once both A and B have been fully added the new solution is left to stir overnight. The solution is then centrifuged at 8000 rpm for 20 minutes. This leaves a coloured precipitate and a clear solution. The precipitate is then washed three times with ultra-pure distilled water and centrifuged each time at 8000 rpm for 20 minutes. Each time the precipitate is kept, and the solution discarded. After the three washes with ultra-pure water the remaining precipitate is then washed with ethanol and centrifuged once more at 8000 rpm. This final precipitate is then dried in an oven at a minimum of 120°overnight and yields the PBA.

The reaction for the PBA follows a simple reductio reaction shown in

$$Fe^{2+}(CN)_6 + M^{3+}(NO)_3 \rightarrow M^{2+}(Fe^{2+}(CN)_6)$$

Equation 5

Where M is the transition metal being dopped at the M-N site.

Table 2 Outlining the specifics for synthesis of the different metal hexacyanoferrate compounds

PBA	Solution A (5mM)	Solution B (5mM of each)	Temperature	Colour of suspension	Colour of Powder
NiHCF	$Na_4Fe(CN)_6{\cdot}10H_2O$	$Ni(NO_3).6H_2O$ + trisodium citrate dihydrate	Room temperature (around 22 °C – 25 °C).	Light blue	Green
CoHCF	$Na_4Fe(CN)_6{\cdot}10H_2O$	$Co(NO_3).6H_2O$ + trisodium citrate dihydrate	Room temperature (around 22 °C – 25 °C).	Green	Green
CuHCF	$Na_4Fe(CN)_6{\cdot}10H_2O$	$Cu(NO_3).6H_2O$ + trisodium citrate dihydrate	Room temperature (around 22 °C – 25 °C).	Brown	Light brown
MnHCF	$Na_4Fe(CN)_6{\cdot}10H_2O$	$Mn(NO_3).6H_2O$ + trisodium citrate dihydrate	Room temperature (around 22 °C – 25 °C).	White	White

2.2.3 Materials characterisation

2.2.3.1 XRD

X-ray diffraction (XRD) patterns were collected using a D8 Advance Bruker diffractometer. with a Cu anode and an X-ray wavelength of 1.5406 Å. The 2 theta angle started at 10.0° up to 60.0°, scanning in increments of 0.005°. The samples were held in a support made in house. The analysis of the XRD data was performed using GSAS-II to complete the Rietveld refinement.[94]

2.2.3.2 SEM

All SEM images and EDX maps shown in this report were obtained using a Zeiss Sigma 500 VP Scanning Electron microscope fitted with an Oxford Instruments X-max 170 mm^2 detector. EDX maps done using Aztec analysis software. The assistance of Amber Watson and Nikolay Zhelev in the collection of the Sem/EDX data is greatly acknowledged.

2.2.3.3 Elemental analysis

Elemental analysis was carried out at MEDAC ltd, analysing metal, carbon, and nitrogen percentages.

2.2.4 Making MHCFS inks and electrodes

2.2.4.1 Neutralised Nafion binder inks

All electrodes used during the *in situ* experiments were made using a mixture of the MHCFS, carbon black and neutralised nafion. In a ratio of 70/20/10 by mass. To neutralize the Nafion equal volumes of Nafion and 1 M NaOH are mixed. To prepare the inks, appropriate amounts of the MHCFS and carbon black are ground together in a pestle and mortar until they form a fine powder. To this powder the appropriate amount of the neutralised Nafion is added. This mixture is then further dispersed in a solution of IPA and ultra-pure water 70/30 by volume.

The electrodes are made by painting Toray carbon paper with the ink mixture using a spray gun. Due to the risk of spraying a fine mist of the inks containing carbon and metals this procedure is carried out in a fume hood and a dust mask should be worn. Each electrode has a diameter of 2.2 cm (area of 3.8 cm^2) with a loading on each electrode at 8 mg cm^{-2}. The loading of 8 mg cm^{-2} was selected to allow for an edge jump, change in absorbance at the Fe K-edge for FeHCF, of 1 during the *in situ* experiments. After each layer of painting the electrode is dried on a hot plate. Once the desired mass is reached the electrodes are pressed using a 3 kg steel brick at 119 C for approximately 15 minutes. This process of hot pressing is to ensure the binding agent is well mixed through the electrode material on the Toray paper. To enable good contact with the electrode and proper adhesion to the carbon paper.

2.2.5 Results of materials characterization and electrodes

2.2.5.1.1 Characterization of the synthesized FeHCF powder

Figure 4 shows the powder diffraction pattern for FeHCF synthesized according to the method outlined in section 2.2.1.

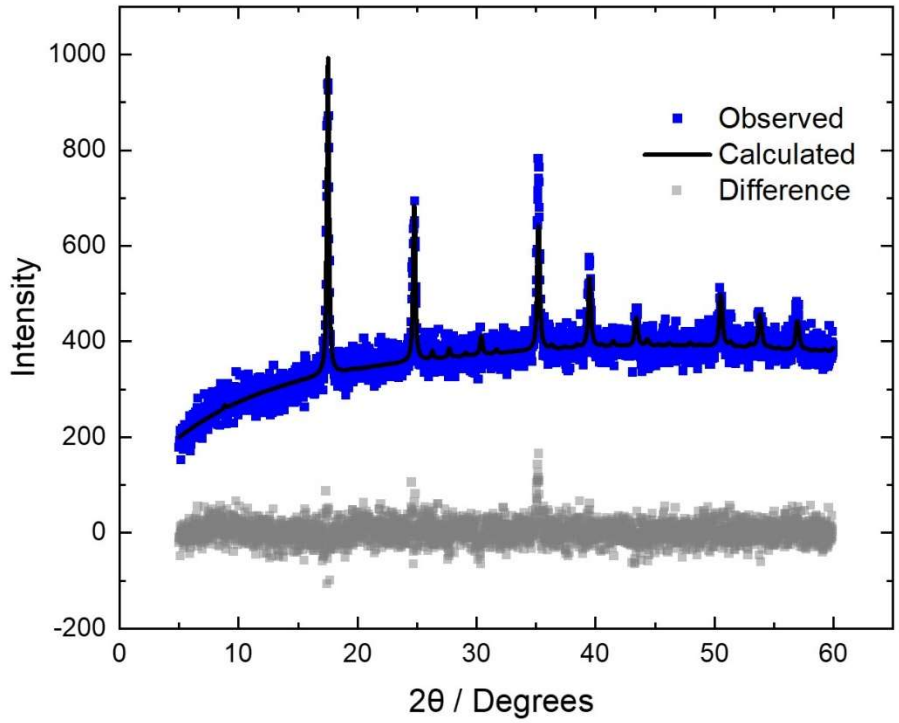

Figure 4 Diffraction pattern for FeHCF synthesised using the method mentioned in section 2.2. Showing the observed diffraction pattern (blue) and the calculated diffraction pattern (black line) along with the difference between the two (grey). Experimental procedure for XRD outlined in section 2.2.3.1.

Rietveld analysis of the diffraction pattern gave a space group of Pm3m corresponding to the primitive cubic lattice, with a unit cell length of 10.251 Å. These values are all in good agreement with literature.[95] From this data we can expect to produce electrodes with good cycling stability for the (de)intercalation of cations.[96]

Figure 5 shows the SEM image of the FeHCF powder. The image has a magnification of 1980 X.

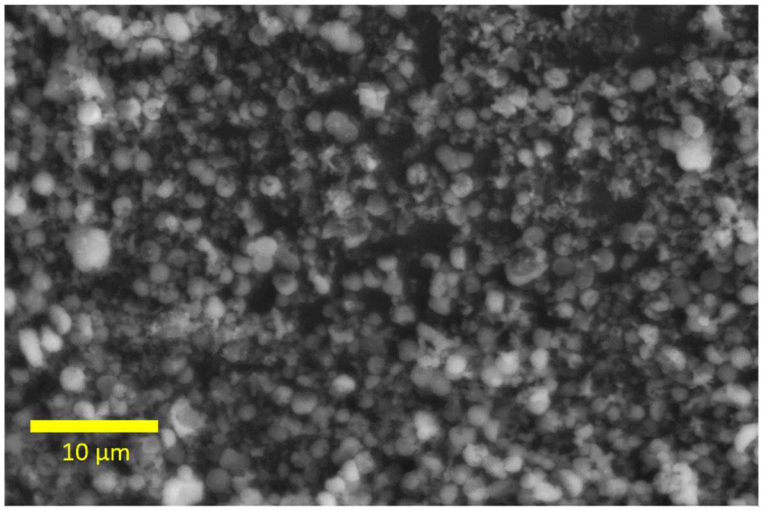

Figure 5 SEM image of FeHCF powder, magnification 1980 X, Image taken using method outlined in section 2.2.3.2.

From the SEM image the particle sizes found are on the order of 1 – 2 µm. This particle size is important as it will help produce a more homogeneous electrode. **Table 3** shows the results of EDX mapping of the SEM samples.

Table 3 Atomic % from EDX of FeHCF powder SEM

Element	**Atomic %**
Fe	14.99
N	50.47
Na	10.15

The ratio of Fe:N should be 1:3 for $NaFe[Fe(CN)_6]$. From the data in **Table 3** our sample has a ratio of 1:3.4, which implies we have a low fraction of CN vacancies present. Secondly, the ratio of Fe:Na should be either 1:0.5 or 1:2 depending on the extent of oxidation of the Fe atom. A ratio of 1:0.7 is calculated from the data in **Table 3**. This would result in a FeHCF sample that is a mix of the two with water also in the structure, $Na_{0.7}Fe_{0.3}[Fe(CN)_6]$.

Table 4 shows the results of the elemental analysis for the FeHCF powder, showing the weight percentage of each element. The results show a slightly low amount of Fe but a good agreement for the C:N ratio of 1:1 within error of the measurement. The low percentage of Fe appears to be

a systematic error as the percentage of Fe for the analogues is also off by a similar amount and we note that MEDAC conducted the metal and HCN quantification using two different methods.

Table 4 Elemental analysis results for FeHCF from MEDAC LTD

Element	**H**	**C**	**N**	**Fe**
wt%	2.20	23.05	23.56	24.82
Theoretical wt%	N/A	24.7	28.89	38.4
Ratio of $\frac{Wt\,\%}{Theoretical\,Wt\%}$	N/A	0.93	0.82	0.64

Combining the results from these characterisation techniques the results show that FeHCF has been successfully synthesised, following the “one-pot” method. The results show a low CN vacancy cubic structure for the FeHCF.

2.2.5.1.2 Characterisation of FeHCF electrode

The distribution of material on the Toray carbon paper for the FeHCF is shown in the SEM images in Figure 6.

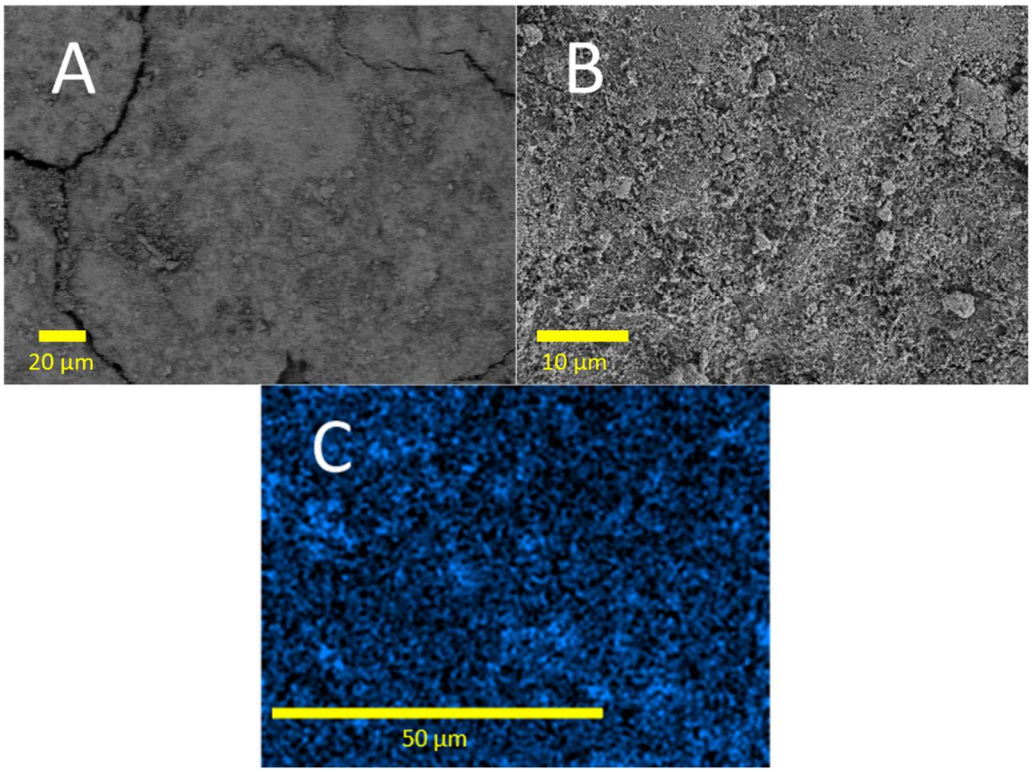

Figure 6 A and B) SEM of a FeHCF electrode at a magnification of 500 X and 2000 X respectively. C) showing the EDX map of B the iron composition. Image taken using method outlined in section 2.2.3.2.

In Figure 6 A we have an image of the electrode at a scale of 2000 X magnification. From this image we can see large cracks present in the layer of material. These cracks may cause artificial diffusion channels for cations and can influence the resulting diffusion coefficient. However, the SEM images are collected for dried out electrodes at approximately in the vacuum of the SEM and, therefore the channels may be an artifact. In Figure 6 B an image for the FeHCF electrode is zoomed to a magnification of 2000 X is shown. In this image we can see the roughness of the electrode surface.

In Figure 6 C we can see an EDX map of the image in Figure 6 B. In this image we can see that the distribution of Fe across the electrode is good, in that there is Fe present throughout the image. However, the contrast between each point is not uniform.

2.2.5.2 Nickel Hexacyanoferrate

2.2.5.2.1 Characterization of the synthesized NiHCF powder

Figure 7 shows the powder diffraction pattern for NiHCF synthesized according to the method outlined in section 2.2.2.

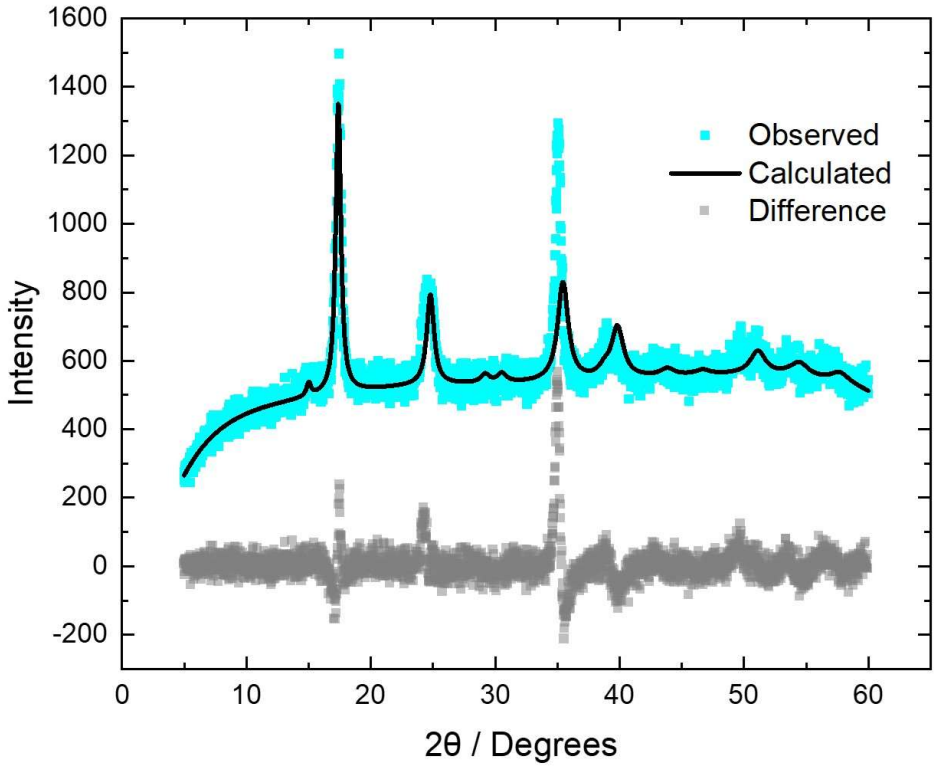

Figure 7 Diffraction pattern for NiHCF synthesised using the method mentioned in section 2.2.2. Showing the observed diffraction pattern (light blue) and the calculated diffraction pattern (black line) along with the difference between the two (grey). Experimental procedure for XRD outlined in section 2.2.3.1.

Analysis of the diffraction pattern gave a space group of Fm-3m, face centred cubic lattice, with a unit cell length of 10.3 Å. These values are all in good agreement with literature values.[97–99]

In Figure 8 we see the SEM image of the NiHCF powder magnified to 2000 X.

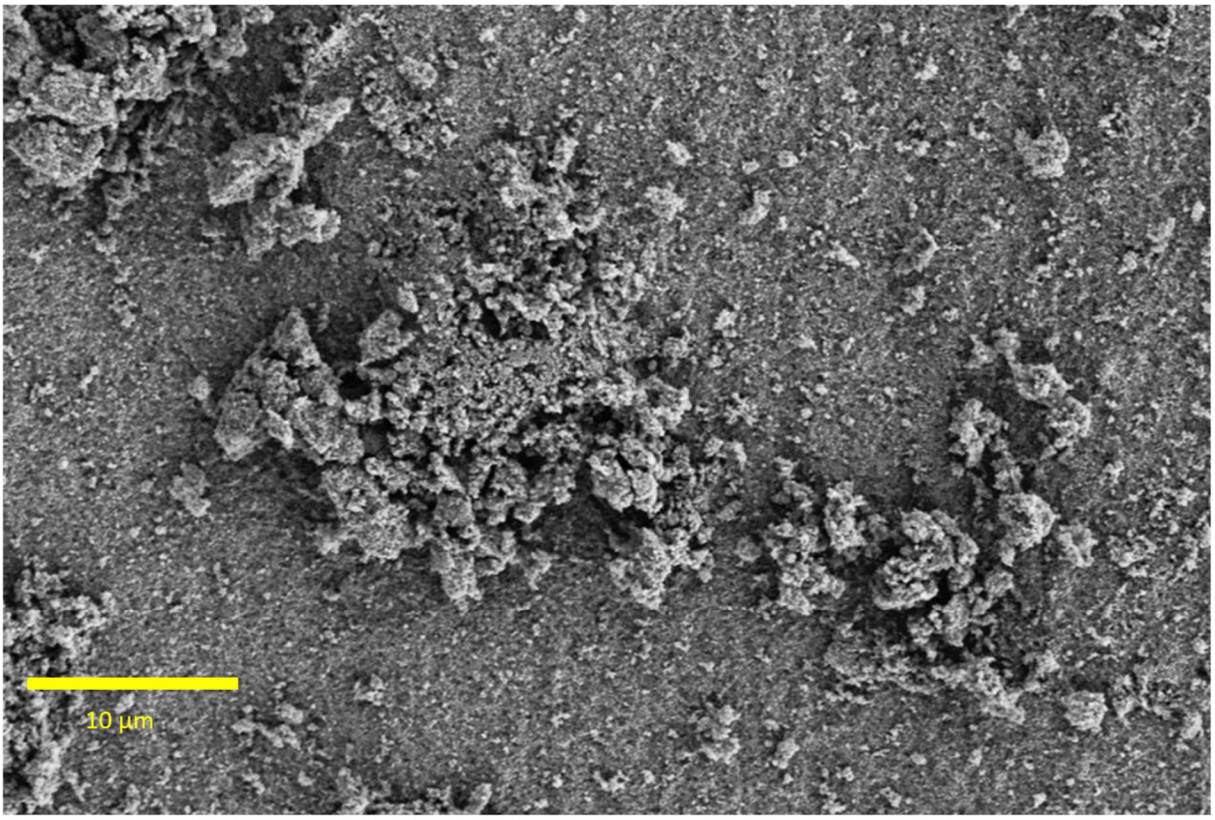

Figure 8 SEM of NiHCF powder, magnification 2000 X. Image taken using method outlined in section 2.2.3.2.

The SEM image gives a range of particle sizes for NiHCF from 4 – 7 µm. Below in **Table 5** the results of the atomic % calculated from the EDX mapping are presented.

Table 5 Atomic % from EDX of NiHCF powder SEM

Element	Atomic %
Fe	4.04
Ni	4.63
Na	9.83
N	35.35

For each of the Prussian blue analogue (PBA) a ratio of 1:1 is expected for Fe:M. From the data in **Table 5** a ratio of 1:1.15 is calculated for Fe:Ni. The Fe:N ratio, for each PBA the ratio should be 1:6. For NiHCF a ratio of 1:8.75 is calculated. This suggests an excess of N in the sample. This may come from the metal nitrate that is used as a starting product and all of the nitrates may have not been removed fully during the workup of the sample. Finally, the Fe:Na ratio for PBA should be 1:1 or 1:2 depending on the oxidation state. In most cases we would expect to synthesise the most reduced form of PBA. Therefore, expecting a ratio of Fe:Na to be 1:2. From the data in **Table 5** a ratio of 1:2.4 for Fe:Na shows that we have synthesised a low vacancy NiHCF full of Na. This gives a formula of $Na_2Ni[Fe(CN)_6]$. Furthermore, any excess Na is most likely from the NaCl used during the synthesis.

Table 6 shows the results of the elemental analysis of the NiHCF powder. The ratio of C to N is approximately 1:1. Again we see the effects of the systematic error in underreporting the amount of Fe as the Fe:Ni ratio is not 1:1.

Table 6 Elemental analysis results for NiHCF from MEDAC LTD

Element	H	C	N	Fe	Ni
Wt %	2.27	17.86	19.37	10.49	14.57
Theoretical Wt%	N/A	22.75	26.54	17.65	18.54
Ratio of $\frac{Wt\,\%}{Theoretical\,Wt\%}$	N/A	0.79	0.73	0.59	0.79

2.2.5.2.2 Characterisation of NiHCF electrode

Figure 9 shows the SEM mapping and EDX mapping of the NiHCF electrode. Figure 9 A shows the SEM image at a magnification of 500 X. In this image large areas of the electrode material are observed with large cracks in the sheet. As with the FeHCF electrode in Figure 6 these cracks may have been caused by drying in the SEM environment or if present in the electrode they may produce additional diffusion channels.

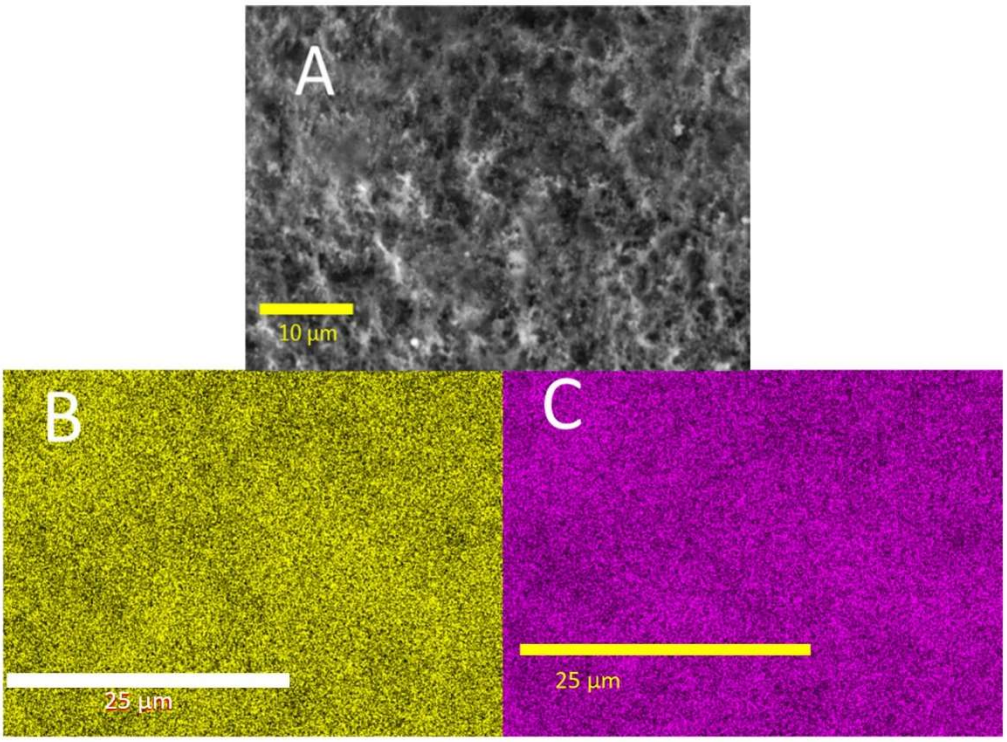

Figure 9 SEM of NiHCF electrode A) The SEM image with 500 X magnification B) EDX mapping showing Ni distribution across A and C) EDX mapping of Fe distribution across A. Image taken using method outlined in section 2.2.3.2.

Figure 9 B shows the distribution of Ni across the electrode surface. The image shows a uniform distribution of the metal. Combined with Figure 9 C where we see the distribution of Fe across the electrode, we see a homogeneous distribution of the active material.

2.2.5.3 Cobalt Hexacyanoferrate

2.2.5.3.1 Characterization of the synthesized CoHCF powder

Figure 10 shows the powder diffraction pattern for CoHCF synthesized according to the method outlined in section 2.2.2.

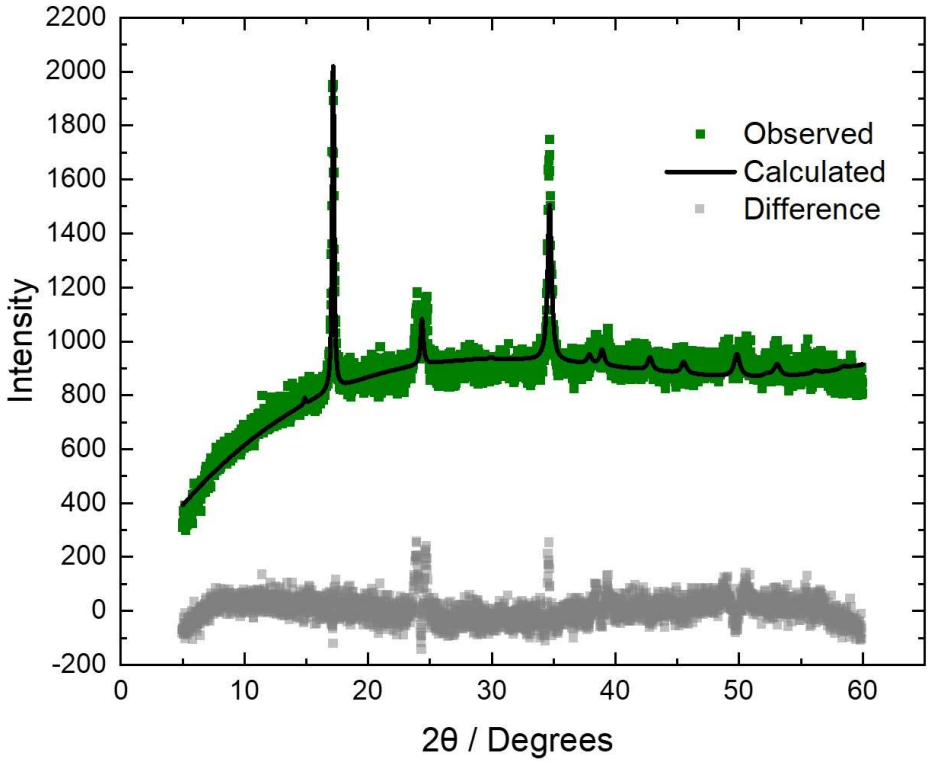

Figure 10 Diffraction pattern for CoHCF synthesised using the method mentioned in section 2.2.2. Showing the observed diffraction pattern (dark green) and the calculated diffraction pattern (black line) along with the difference between the two (grey). Experimental procedure for XRD outlined in section 2.2.3.1.

Analysis of the diffraction pattern gave a space group of Fm3m, face centred cubic lattice. With a unit cell length of 10.07 Å. These values are all in good agreement with literature values.[21,23,100]

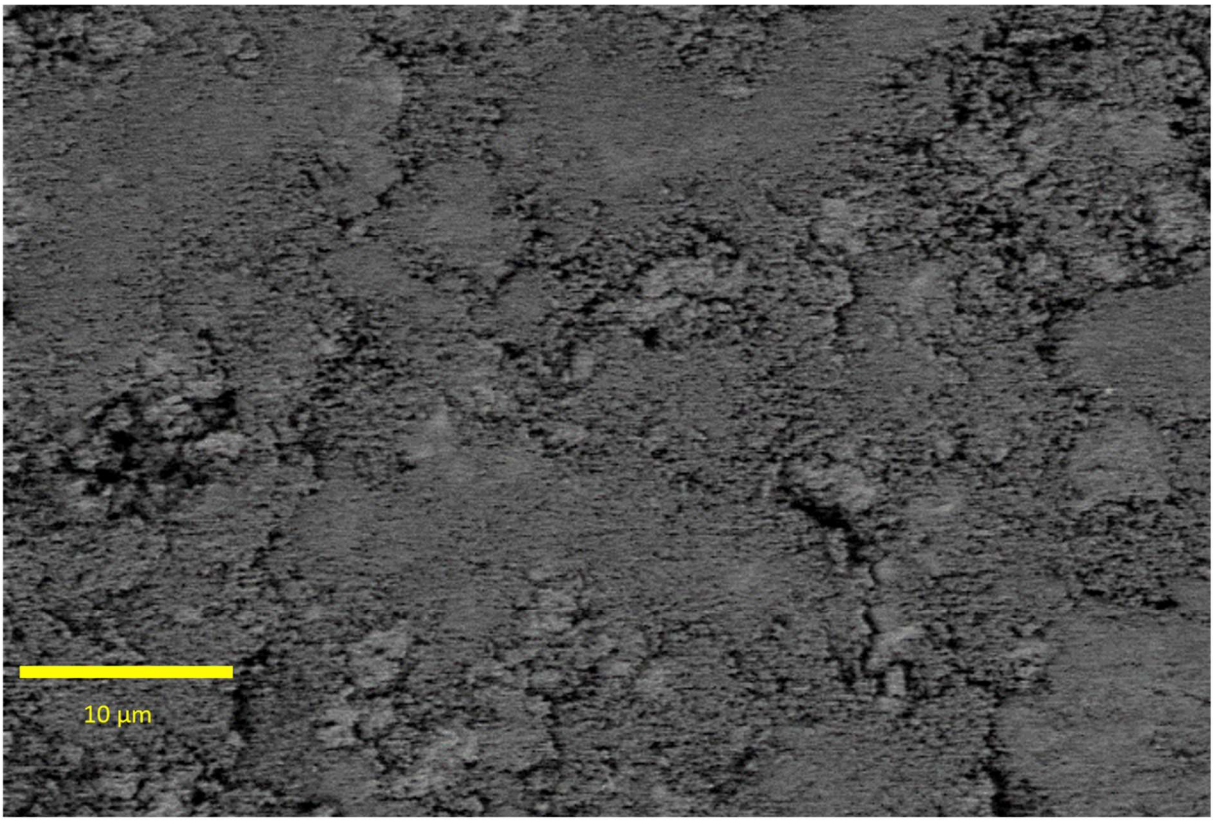

Figure 11 SEM CoHCF powder, magnification 2000 X. Image taken using method outlined in section 2.2.3.2.

Figure 11 shows the SEM image of the synthesised CoHCF powder magnified to 2000 X. From this image we can again see a uniform powder with very small ≤ nm particle sizes. In **Table 7** the results of the atomic ratios from the EDX of the image in Figure 11 are reported.

Table 7 Atomic % from EDX of CoHCF powder SEM

Element	**Atomic %**
Fe	5.29
Co	5.78
Na	9.82
N	34.16

From the values in **Table 7** a ratio of 1:1.09 is calcualted for Fe:Co as expected for these sample. A ratio of 1:6.46 is found for Fe:N which is also as expected. Finally the ratio of Fe:Na is 1:1.86. This

suggests that some of the vaccancies in the CoHCF structure may contain water and not Na^+ ions. This leads to a possible formula of $Na_{1.86}Co[Fe(CN)_6]$ as a ratio of 1:2 would be expected.

Table 8 reports the results of the elemental analysis for CoHCF. This again shows the amount of Fe is low with respect to the Co. However this is not corroberrated by the EDX and again is a result of the systmeatic error in the elemental analysis data as described above.

Table 8 Elemental analysis results for CoHCF from MEDAC LTD

Element	**H**	**C**	**N**	**Fe**	**Co**
wt %	1.98	18.69	20.81	11.78	16.05
Theoretical wt%	N/A	22.73	26.52	17.63	18.60
Ratio of $\frac{Wt\,\%}{Theoretical\,Wt\%}$	N/A	0.82	0.78	0.67	0.86

The data in **Table 8** does give a good agreement for the ratio of C:N which again suggests we have no or a very low level of CN vaccanices.

2.2.5.3.2 Characterisation of CoHCF electrode

Below in Figure 12, we see the results of the SEM images and EDX mapping for the CoHCF electrodes. Again, in this image we see large sheet of the electrode material but with cracks in the surface. From the EDX map in Figure 12 B we see that the distribution for Co is much the same as that for Ni. The Co is well distributed around the surface of the electrode. Figure 12 C shows the distribution of Fe throughout the electrode, which is just as uniform as the Co distribution.

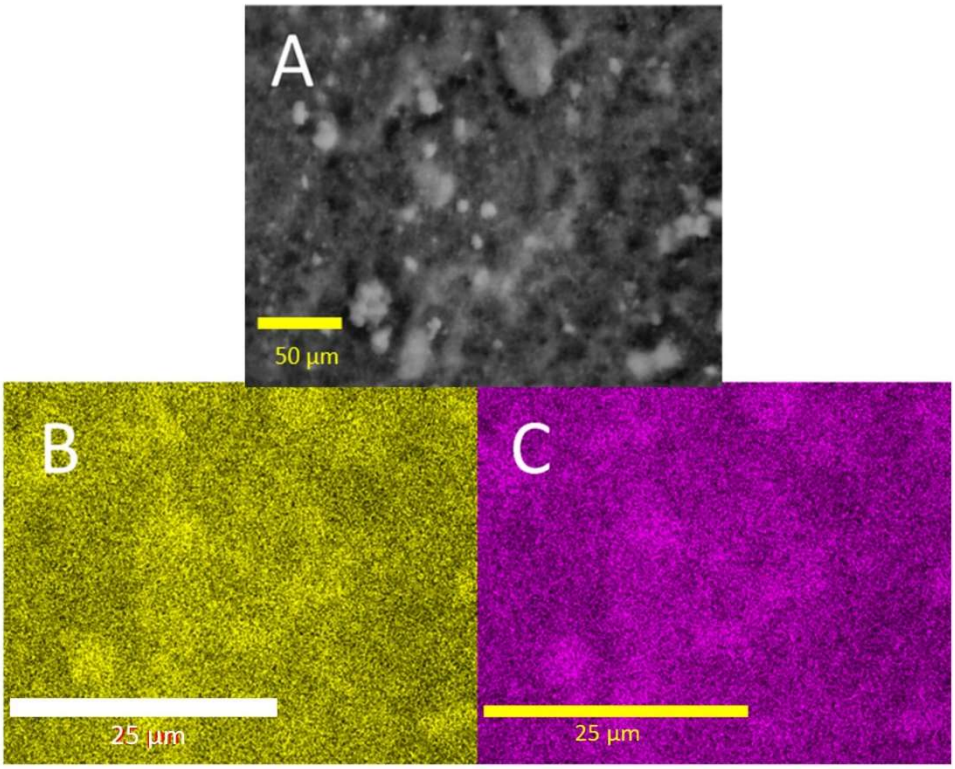

Figure 12 SEM of CoHCF electrode A) The SEM image of the CoHCF electrode B) EDX mapping showing Co distribution across A and C) EDX mapping of Fe distribution across A. Image taken using method outlined in section 2.2.3.2.

2.2.5.4 Manganese Hexacyanoferrate

2.2.5.4.1 Characterization of the synthesized MnHCF powder

Figure 13 shows the powder diffraction pattern for MnHCF synthesized according to the method outlined in section 2.2.2.

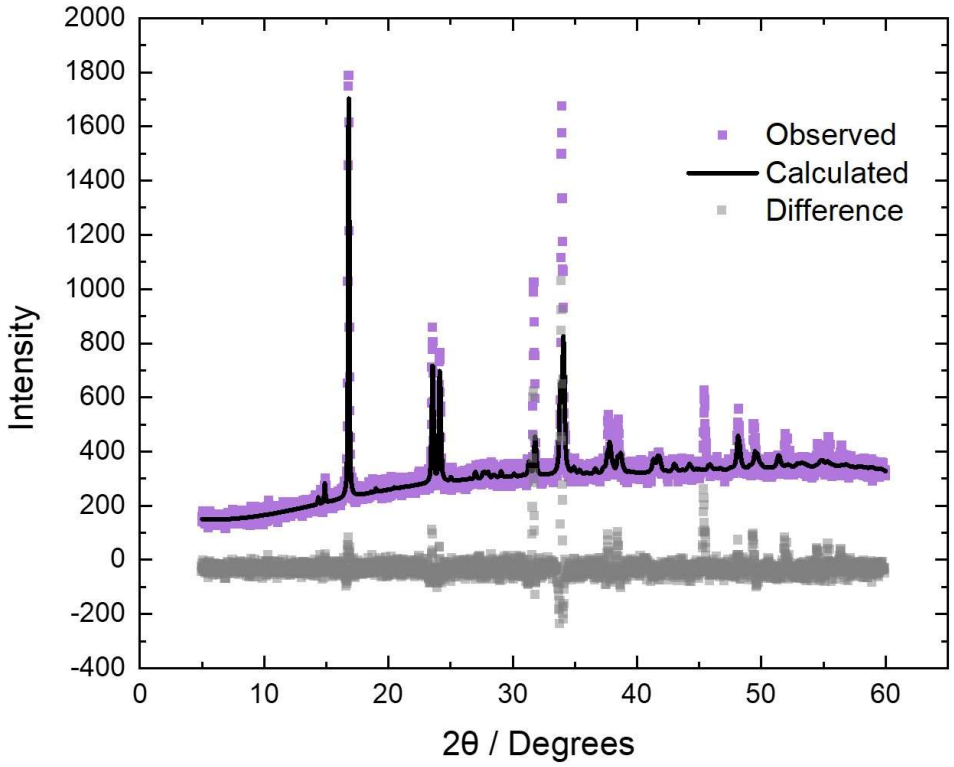

Figure 13 Diffraction pattern for MnHCF synthesised using the method mentioned in section 2.2.2. Showing the observed diffraction pattern (purple) and the calculated diffraction pattern (black line) along with the difference between the two (grey). Experimental procedure for XRD outlined in section 2.2.3.1.

Analysis of the diffraction pattern gave a space group of P 21/n corresponding to the monoclinic structure, with a unit cell length of a = 10.573 Å, B = 7.542 Å and c = 7.326 Å. These values are all in good agreement with literature sources. [21,101]

Below in Figure 14 we see the SEM image of the MnHCF powder, magnified 2010 X. showing particle size of around 1 – 2 µm.

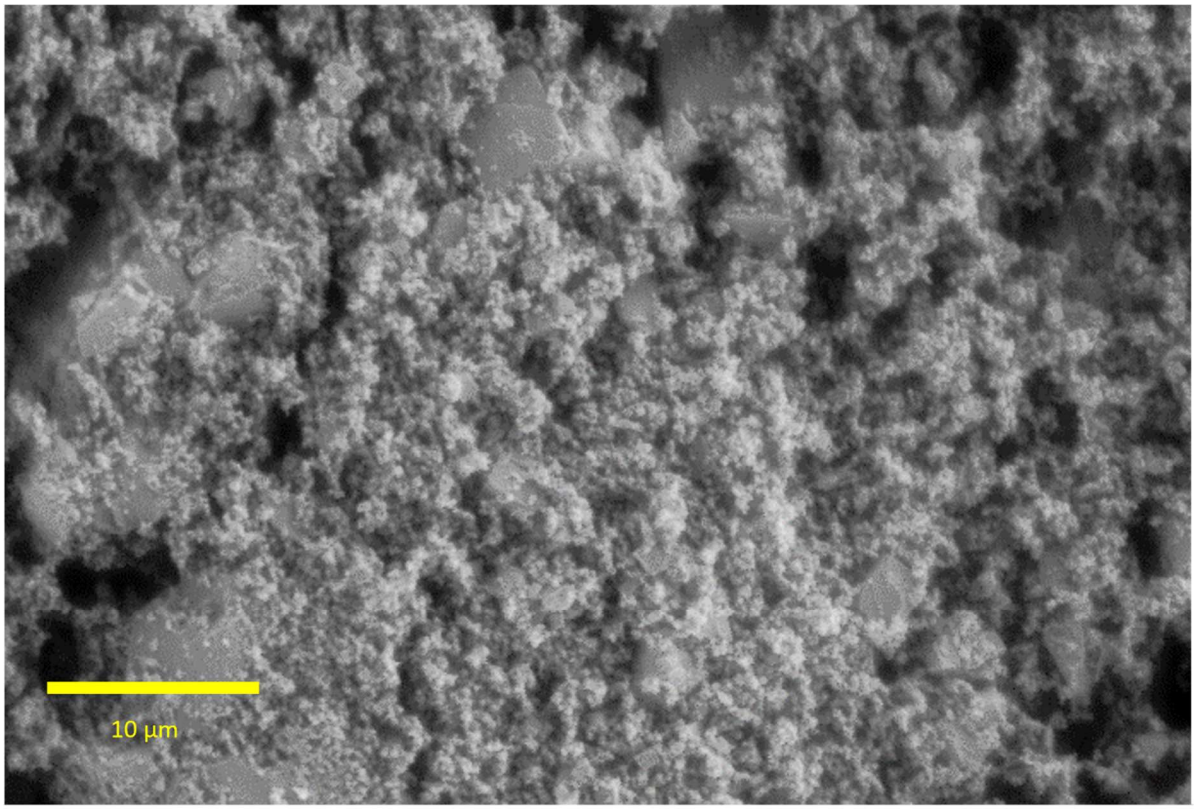

Figure 14 SEM of MnHCF powder, magnification 2010 X. Image taken using method outlined in section 2.2.3.2.

Table 9 provides the atomic % from the EDX of the SEM of the MnHCF powder.

Table 9 Atomic % from EDX of MnHCF powder SEM

Element	Atomic %
Fe	5.79
Mn	6.44
Na	16.05
N	28.08

The ratio of Fe:Mn from the results in **Table 9** is 1:1.1 which is as expected. For Fe:N the ratio is 1:4.85. This is lower than the expected 1:6 and does suggest we have some CN vacancies. Finally, the Fe:Na ratio is 1:2.77. This would suggest a formula of $Na_2Mn[Fe(CN)_6]$. With an excess amount of Na from the NaCl.

From **Table 10** the results of the elemental analysis of MnHCF are recorded.

Table 10 Elemental analysis results for MnHCF from MEDAC LTD

Element	H	C	N	Fe	Mn
Wt %	1.71	20.28	22.21	12.57	14.55
Theoretical Wt%	N/A	23.02	26.86	17.86	17.57
Ratio of $\frac{Wt\,\%}{Theoretical\,Wt\%}$	N/A	0.88	0.83	0.70	0.83

Once again, a low amount of Fe has been recorded by elemental analysis and suggests an issue with the sample measurements across all the samples.

2.2.5.4.2 Characterisation of MnHCF electrode

Figure 15 shows the SEM and EDX map of the MnHCF electrode. This electrode does not have the large sheets of materials with cracks and instead has a much rougher surface. From the EDX map in Figure 15 B we can see that the Mn distribution across the surface is not as uniform, especially when compared too Ni and Co.

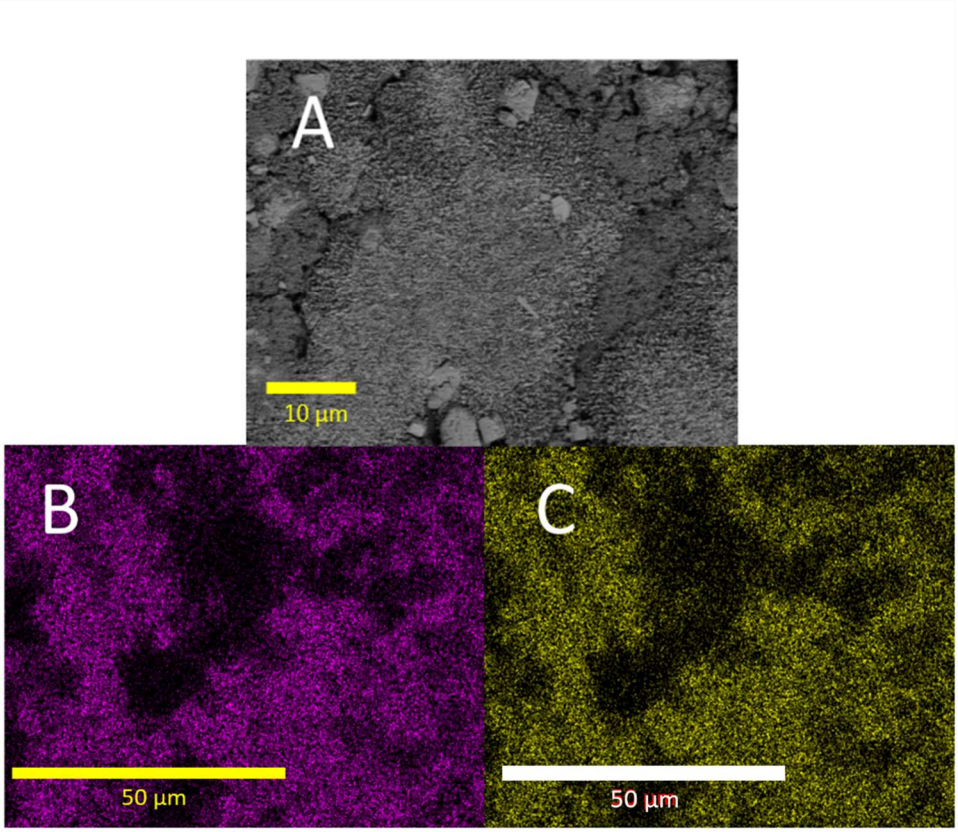

Figure 15 SEM of MnHCF electrode A) The SEM image of the MnHCF electrode B) EDX mapping showing Mn distribution across A and C) EDX mapping of Fe distribution across A. Image taken using method outlined in section 2.2.3.2.

2.2.5.5 Copper Hexacyanoferrate

2.2.5.5.1 Characterization of the synthesized CuHCF powder

Figure 16 shows the powder diffraction pattern for MnHCF synthesized according to the method outlined in section 2.2.2, analysis of which also leads to a space group of P 21/n corresponding to the monoclinic structure, with a unit cell length of a = 10.573 Å, B = 7.542 Å and c = 7.326 Å. These values are all in good agreement with literature sources. [80] Then in Figure 17 we see the SEM image of the CuHCF powder, magnified 2010 X. showing particle size of around 1 – 2 µm.

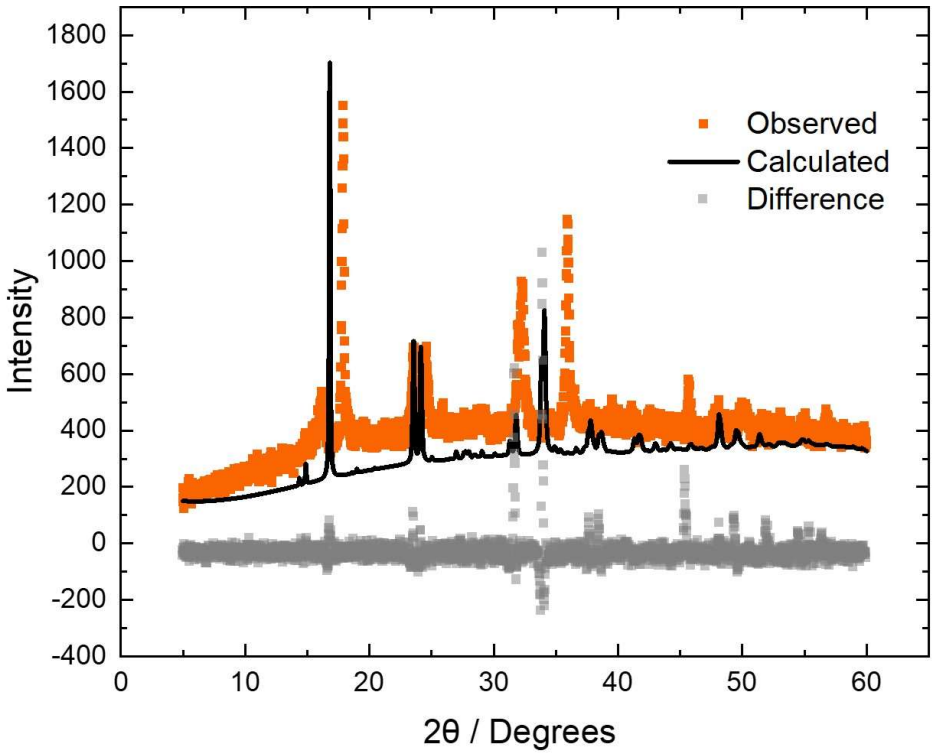

Figure 16 Diffraction pattern for CuHCF synthesised using the method mentioned in section 2.2.2. Showing the observed diffraction pattern (orange) and the calculated diffraction pattern (black line) along with the difference between the two (grey). Experimental procedure for XRD outlined in section 2.2.3.1.

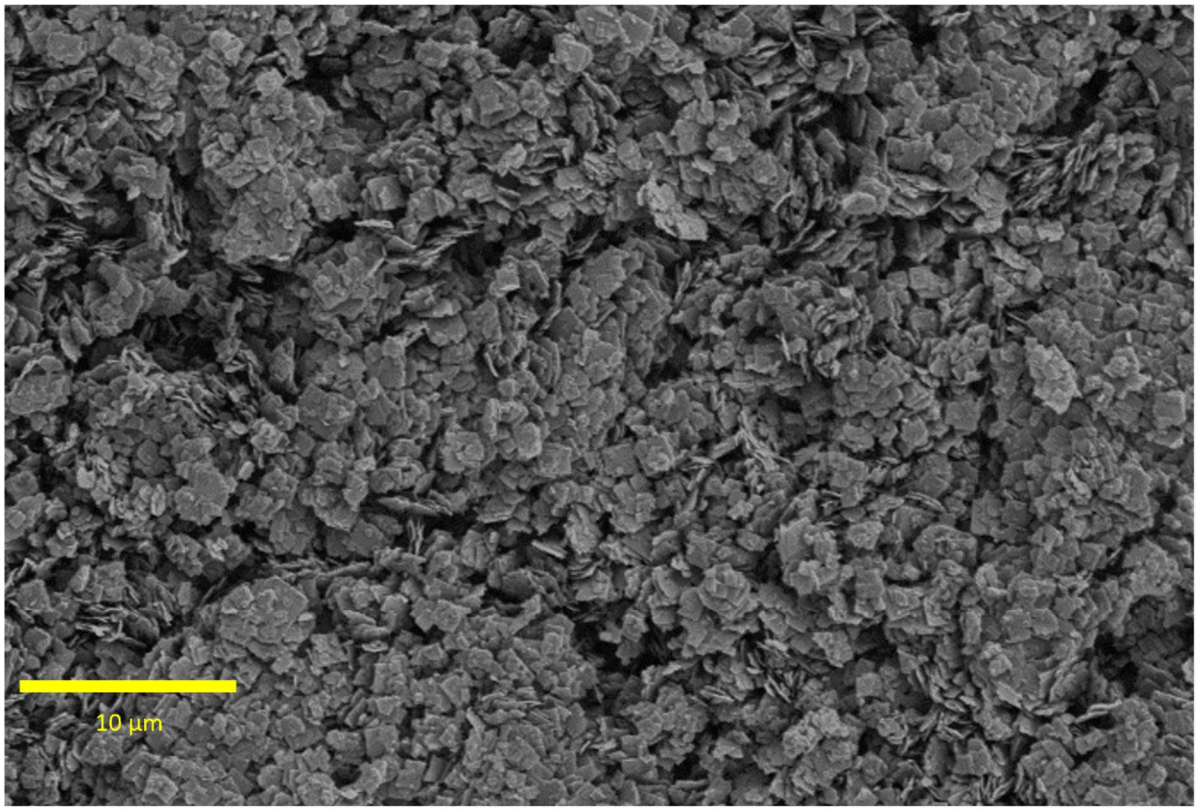

Figure 17 SEM image of CuHCF powder, magnification 2000 X. Image taken using method outlined in section 2.2.3.2.

Below in **Table 11** we have the EDX values from the SEM of the CuHCF powder.

Table 11 Atomic % from EDX of CuHCF powder SEM

Element	**Atomic %**
Fe	5.65
Cu	5.81
Na	10.72
N	34.69

From the data in **Table 11** the ratio of Fe:Cu is approximately 1:1, again this is the expected result. The ratio for Fe:N is 1:6.1 which is as expected for the PBA. Lastly the ratio of Fe:Na is 1:2. This all points to having synthesised the reduced form of CuHCF, with a formula of CuHCF $Na_2Cu[Fe(CN)_6]$.

Below in **Table 12** we have the results of the elemental analysis for CuHCF powder.

Table 12 Elemental analysis results for CuHCF from MEDAC LTD

Element	**H**	**C**	**N**	**Cu**	**Fe**
Wt %	1.46	15.62	17.29	13.23	9.74
Theoretical Wt%	N/A	22.40	26.14	17.38	19.77
Ratio of $\frac{Wt\,\%}{Theoretical\ Wt\%}$	N/A	0.70	0.66	0.76	0.49

Once again, the results for Fe seem to be under reported and do not match with the results from the EDX. Therefore, we can only look at the C:N ratio from this data which once again is in good order and aligned to what we expected 1:1.

2.2.5.5.2 Characterisation of CuHCF electrode

Figure 18 shows the SEM and EDX map of the CoHCF electrode. This electrode does not have the large sheets of materials with cracks and instead has a rougher surface. From the EDX map in Figure 18 B we can see that the Cu distribution across the surface is not as uniform, especially when compared too Ni and Co. However, there is a sufficient covering of Cu and Fe across the electrode to achieve reasonable XAFS results.

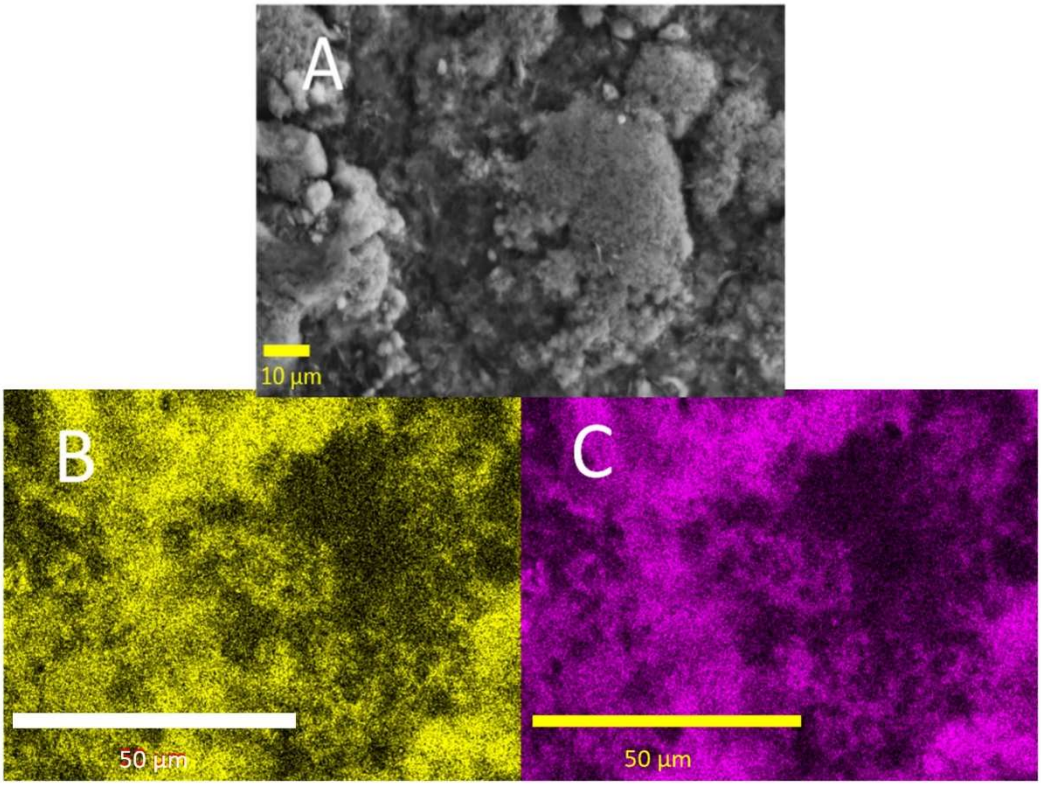

Figure 18 SEM of CuHCF electrode A) The SEM image with 500 X magnification B) EDX mapping showing Cu distribution across A and C) EDX mapping of Fe distribution across A. Image taken using method outlined in section 2.2.3.2.

2.2.5.6 Conclusion of material characterisation

In conclusion, the "one-pot" synthesis of FeHCF was a successful method at synthesising large quantities, > 5 mg, of FeHCF with a cubic structure and low fraction of CN vacancies. The PBAs/MHCFs where all synthesised using a metal nitrate and ferrocyanide. In each case we have synthesised the MHCFs in a reduced form with 2 Na ions present. The elemental analysis data has uniformly under recorded the amount of Fe compared to the EDX results and the theoretical amounts. Therefore, excluding this result, we can conclude that low vacancy high quality MHCFS have been synthesised.

From the SEM images of the electrodes, the homogeneity of the electrodes is not perfect. Although there is a good dispersion of active material across the electrode. However, this lack of uniformity will later cause issues with the spectroscopic results resulting in fluctuations in the absorbance of the sample.

In conclusion the methods of synthesis chosen where effective for making consistent MHCF samples and the method of electrode making produced electrodes of sufficient quality and loading to enable the electrochemical and *in situ* X-ray absorbance spectroscopic experiments to be conducted.

2.2.6 Thickness characterisation of electrodes

Figure 19 shows SEM images of both FeHCF (A) and CoHCF (B) electrode made using the procedure outlined in 2.2.4, showing the approximate thickness of 150 µm. To check the accuracy of this thickness an average was taken for a range of electrodes. This data will be further discussed in section 3.2.2.2.

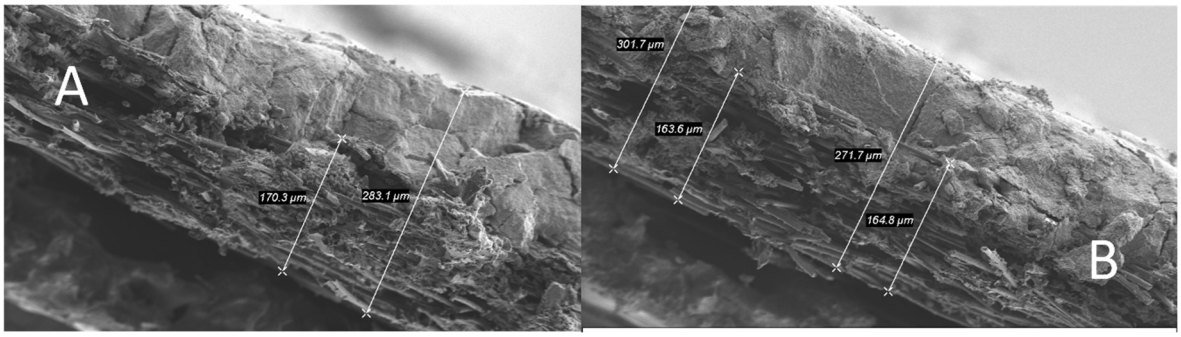

Figure 19 SEM images showing a cross section6 of A) FeHCF electrode and B) CoHCF electrode. Showing the thickness of the substrate and film and the thickness of the spray painted material. Image taken using method outlined in section 2.2.3.2.

2.3 Electrochemistry

2.3.1 *In situ* cell and electrochemical set up

The *in situ* cell was designed and made in house at diamond light source. The cell consists of a bulk electrolyte chamber of approximately 100 ml. A widow 1.5 cm in diameter was cut out in the centre of the cell on the front panel and in the back. The indent beam passes through the two Kapton windows and the electrode, which corresponds to a path length of 300 µm. Two 1 cm diameter holes in the top of the cell allow for the positioning of the counter and reference electrode. Figure 20 is a picture of the *in situ* cell set up for electrochemical experiments.

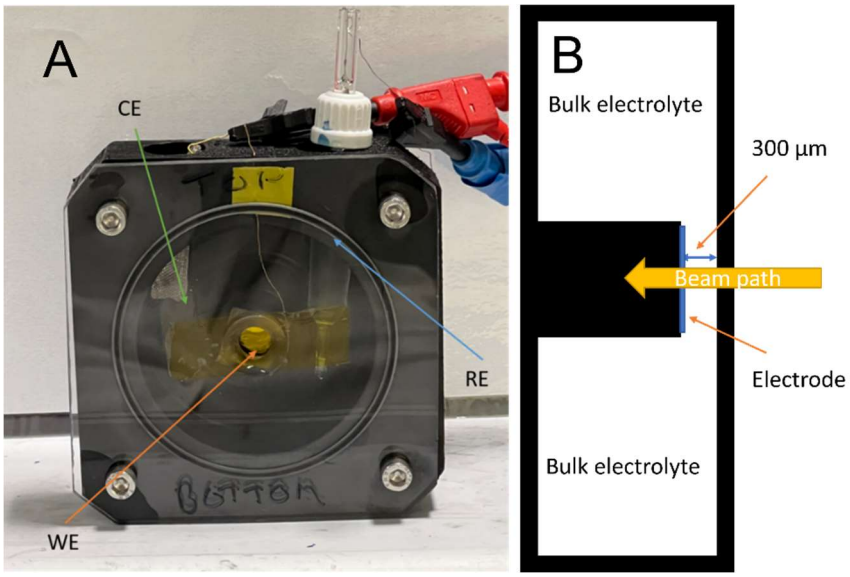

Figure 20 Picture of the *in situ* cell. A) showing the *in situ* cell with, electrode positions labelled, used and B) a schematic showing a profile view of the cell. With the 300 µm electrolyte paths labelled.

2.3.2 Electrochemical methods

2.3.3 Hardware and software used for electrochemical measurements and data analysis

The potentiostatic experiments where all carried out using a Metrohm Autolab PGSTAT101 operating NOVA 2.1 software. The electrochemical experiments performed were cyclic voltammetry (CV) and chronoamperometry.

All the acquired electrochemical data was analysed using Origin® 2019b graphing and analysis software and in-house made python scripts.

2.3.3.1 Cyclic voltammetry

Cyclic voltammetry (CV) is the main electrochemical method used throughout this work to analyse the materials and their electrochemistry. CV is an electrochemical technique that measures current that results from an applied linear potential sweeping between potential limits. CV is an important and useful technique as it gives insight into both thermodynamic and kinetic information about chemical systems. CV can be used to study a variety of redox processes, gain insight into the reversibility or a reaction, analyse electron transfer kinetics, and diffusion coefficients of transport ions and electroactive species.[45,102]

During a CV a potential is applied between a working and a reference electrode. This potential is ramped linearly at a fixed rate, known as a scan rate. The scan rate (υ) is normally applied in

mV s^{-1}. This is done between an upper and lower potential limit as a function of time. Figure 21 is a diagram showing how the potential is applied as a function of time.

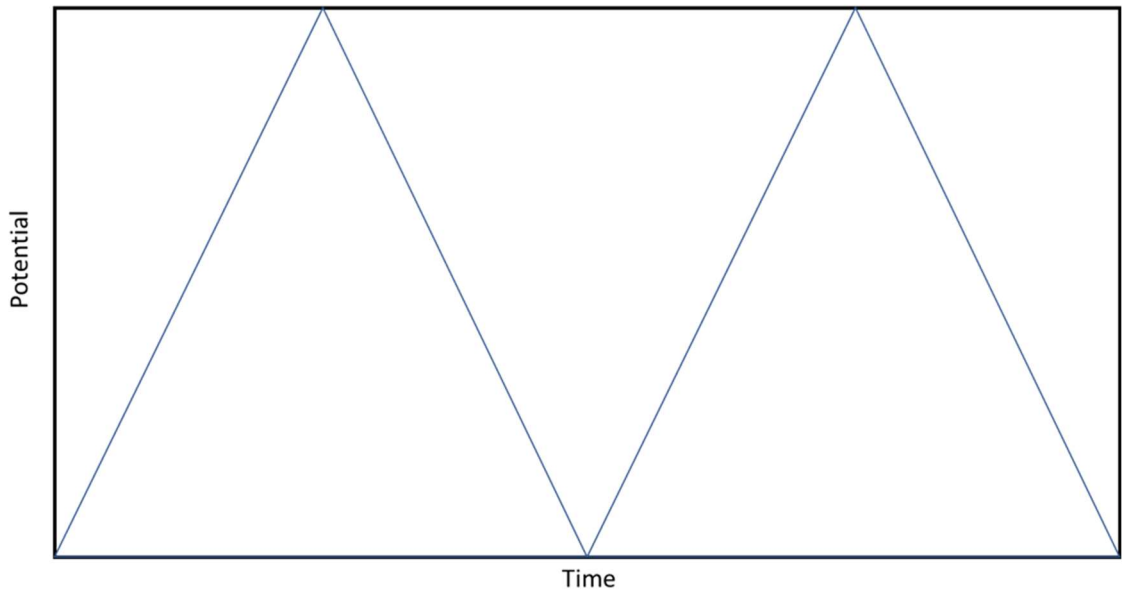

Figure 21 Diagram showing a CV waveform of potential *vs.* time.

2.3.3.1.1 Chronoamperometry

Chronoamperometry is an electrochemical technique where typically a square-wave potential is applied to the working electrode as a function of time. The resulting current is recorded and measured also as a function of time. Chronoamperometry is used to measure current-time dependent effects of a diffusion controlled process. Chronoamperometry will be used thought this work to test the kinetics across different potential widows based on the CVs.

2.3.4 *In situ* chronoamperometry experiments

For the purposes of the *in situ* and ex situ chronoamperometry studies a return potential E_1 is defined from the *CVs.* of the MHCFs as a point of non-Faradaic current at which the system is fully (de)intercalated. For example, FeHCF if the E_1 is chosen as 0.5 V *vs.* SCE, the driving potential E_2 is then pushed to increase the rate of (de)intercalation. The experiments are then carried out by first applying the E_2 potential for a set amount of time followed by the E_1 potential. This process is then repeated several times and then currents recorded. Figure 22 shows an example of the potential time profile being used during the *in situ* electrochemical experiments.

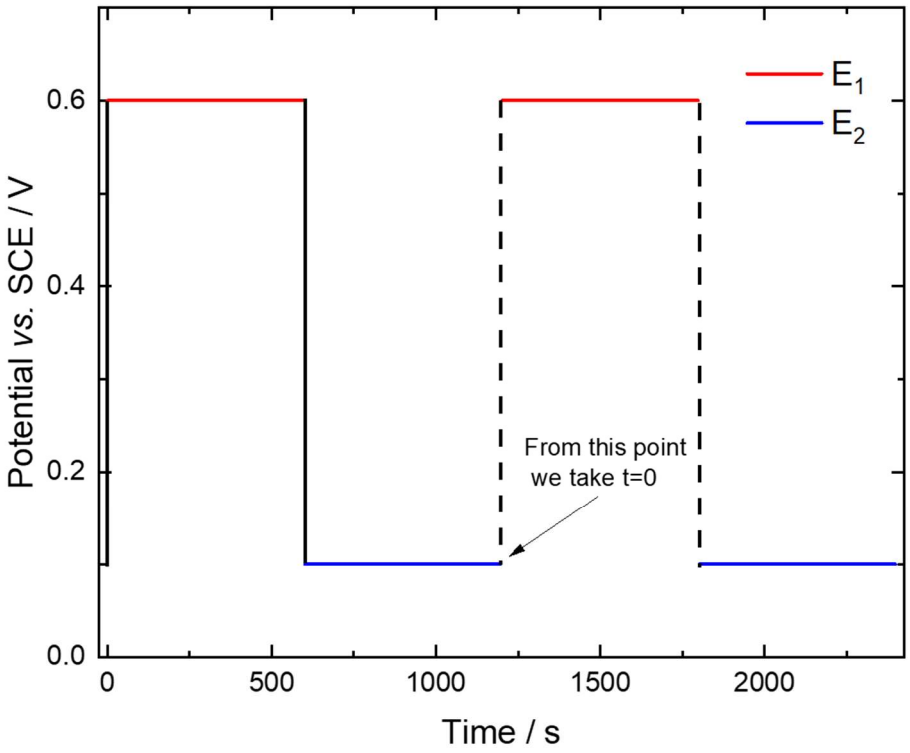

Figure 22 Schematic showing a potential time example from the chronoamperometry experiments. Showing the initial cycle of applying E_1 and E_2 and then the final cycle of applying E_1 and E_2 from where we take t = 0.

Shown in Figure 22 the E_1 and E_2 potentials are applied for multiple pulses. Using a trigger mechanism to initiate the XAFS start the start of each procedure, the XAFS data is then collected in real time during these pulses. In all cases unless otherwise specified the time resolution on the spectra is 0.1 ms or 10 spectra/second.

Figure 23 shows an example of the resulting current time response from the potential pulses.

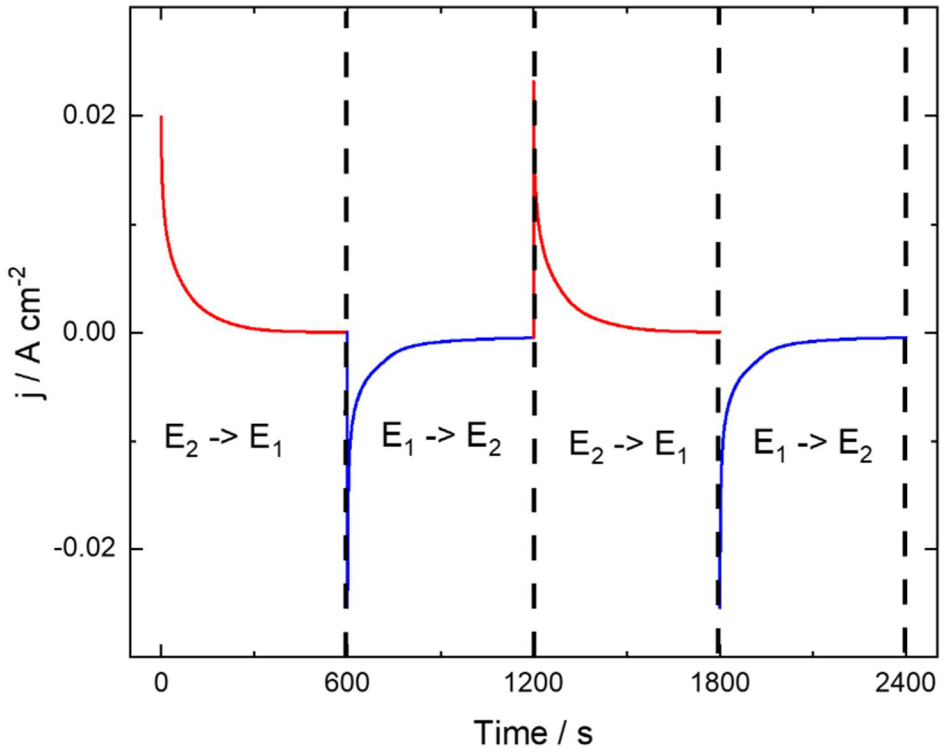

Figure 23 Example of the resulting current *vs.* time response of the *in situ* chronoamperometry. For MHCFS in 2 M $NaNO_3$ at a pH of 2. Each potential is held for 600 s. The red lines corresponding to the current from the application of E_2 to E_1 and the blue E_1 to E_2.

Table 13 Showing the E_1 and E_2 potentials used for each MHCFS for each electrolyte

Material	Cation	E_1 *vs.* SCE / V	Oxidation state at E_1	E_2 *vs.* SCE / V
FeHCF	Na	0.5	$Fe^{3+}[Fe^{2+}(CN)_6]$	0.4/0.3/0.2/0.0/-0.1
		-0.1	$Fe^{2+}[Fe^{2+}(CN)_6]$	0.1/0.2/0.3/0.4/0.5/0.6
	K	0.5	$Fe^{3+}[Fe^{2+}(CN)_6]$	0.4/0.3/0.2/0.1/-0.1
		-0.1	$Fe^{2+}[Fe^{2+}(CN)_6]$	0.1/0.3/0.5
NiHCF	Na	0	$Ni^{3+}[Fe^{2+}(CN)_6]$	0.4/0.6/0.8/1.0
MnHCF	Na	0.8	$Mn^{3+}[Fe^{3+}(CN)_6]$	0.6/0.4/0.4/0.0
		0.0	$Mn^{3+}[Fe^{2+}(CN)_6]$	0.2/0.4/0.6/0.8
CuHCF	Na	0	$Cu^{3+}[Fe^{2+}(CN)_6]$	0.4/0.6/0.8/1.0
CoHCF (dual edge)	Na	0.6	$Co^{3+}[Fe^{2+}(CN)6]$	0.5/0.4/0.3/0.2/0.1
		0.6	$Co^{3+}[Fe^{2+}(CN)_6]$	0.7/0.8/0.9/1.0/1.1
MnHCF (dual edge)	Na	0.8	$Mn^{2+}[Fe^{3+}(CN)_6]$	0.4/0.2/0.0
		0.8	$Mn^{2+}[Fe^{3+}(CN)_6]$	1.2/1.4/1.5

2.4 X-rays and X-ray techniques.

2.4.1 X-rays.

Vibrations between an electric field and magnetic field results in an electromagnetic wave (EM). These can allow for transmissions of energy through vacuums or without any medium. Both electric ($\hat{E}$) and magnetic ($\hat{B}$) fields can be expressed by the Maxwell equations:

$$\nabla^2 \hat{E} - \varepsilon_0 \mu_0 \frac{d^2 \hat{E}}{dt^2} = 0$$

Equation 6

$$\nabla^2 \hat{B} - \varepsilon_0 \mu_0 \frac{d^2 \hat{B}}{dt^2} = 0$$

Equation 7

Where ε_0 is the dielectric constant and μ_0 is the magnetic permeability in a vacuum.

The result of these equations is that both the electric and magnetic fields move at the speed of light c ($\frac{1}{\sqrt{\varepsilon_0 \mu_0}} \approx 3.10^8 m\, s^{-1}$). The vectors that describe the electric and magnetic field are not independent of each other. They are orthogonal, oscillate in phase and have a defined amplitude of c. For a plane wave, the Maxwell equations can be re-written in the following form:

$$\hat{E} = \hat{E}_0 e^{j(kr-\omega t)}$$

Equation 8

$$\hat{B} = \hat{B}_0 e^{j(kr-\omega t)}$$

Equation 9

Where $\hat{E}_0$and $\hat{B}_0$ give the direction of the oscillating electric and magnetic fields and their modulus provides the amplitude of the oscillation. k is the wave vector, with the direction of the propagation of the plane wave. The modulus of k is related to the wavelength, λ, of the radiation.

$$k = \frac{2\pi}{\lambda}$$

Equation 10

Finally, ω is angular frequency.

$$\omega = 2\pi\nu$$

Equation 11

Where ν is the frequency of radiation.

The following expression shows the relationship between wavelength and frequency.

$$c = \lambda \nu$$

Equation 12

Electromagnetic radiation with a wavelength between $10^{-2} < \lambda < 10^{2}$ Å is known as X-rays. This comparable to atomic sizes and sort interatomic distances. It is due to this reason that X-rays can be used to investigate systems on an atomic scale, with applications to spectroscopic, diffraction and imagine techniques. The energy related to X-rays can range from hundreds of electronvolts (eV) to thousands of eV. 1 eV is defined as the energy needed to accelerate a particle carrying a unit electronic charge across a potential of 1 V.

Interactions of X-rays with matter can be divided into three different processes. Firstly coherent (or elastic) scattering. This occurs when the energy of the X-ray photon is small compared with the ionization energy of the atom. This will result in a change of direction of the photon, known as a scatter. With $\nu_{\text{in}} = \nu_{\text{out}}$. Secondly incoherent scattering occurs when the energy of the photon is lost after interaction with core electrons. In this case $\nu_{\text{in}} > \nu_{\text{out}}$. Finally, the photoelectric effect, this is the ejection of a core electron (photo electron) because of absorbed energy. In this case the difference in energy between the incident beam (E_{in}) and the core electron energy (E_0) will determine the kinetic energy of the photo electron. This is defined by the following equation.

$$E_{in} = E_0 + \frac{mv^2}{2}$$

Equation 13

2.4.2 X-ray sources.

The conventional source of X-rays is known as an X-ray tube. These work by accelerating electrons at high velocities using a high voltage field and causing them to collide with a metal target, this is known as an anode plate. The source of electrons is known as a cathode. The anode is typically made of tungsten. A typical voltage applied is in the range of 30 to 100 kV.

Below in Figure 24 we see a spectrum that is generated from a standard X-ray source. The spectrum consists of intense peaks, these are characteristic of the target material. A background, known as white radiation or *Bremsstrahlung*. This is generated by photons from a range of energies and not connected to the anode material.

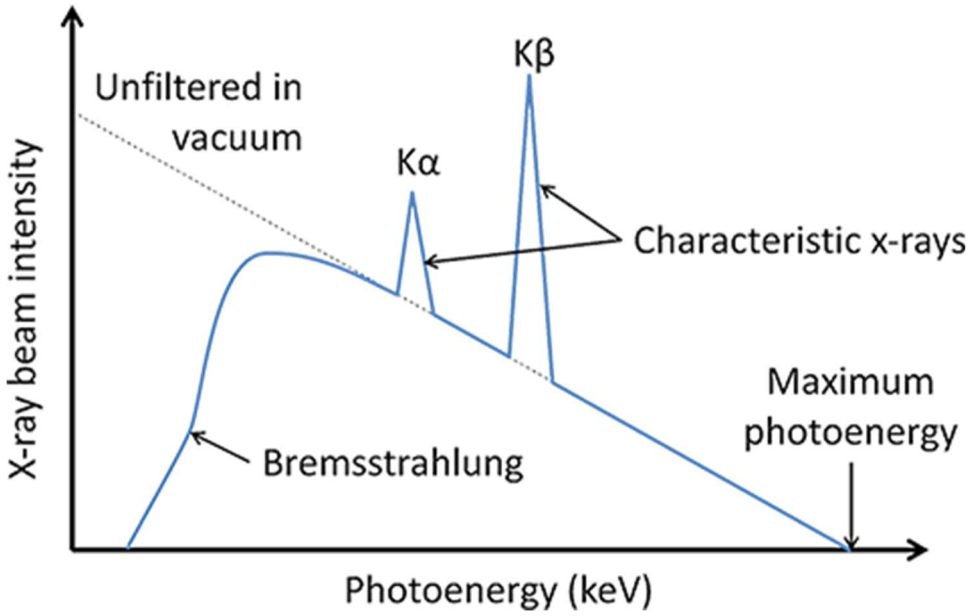

Figure 24 X-ray emission spectrum from a conventional source. Image from PhysicsOpenLab. © Copyright 2021.

The characteristic lines are label as K_α and K_β, these correspond to transitions from L and M shells to the K shell respectively. K corresponds to the shell with the quantum number n = 1, L n = 2 and M n=3.

Another source of X-ray radiation is synchrotron radiation. When electrons travel close to the speed of light, they are forced to curve their trajectories when a magnetic field is applied. During this process an amount of their energy is converted into radiation, this is known as synchrotron. Synchrotron radiation ranges from an extended infrared to X-ray radiation. Synchrotrons work by accelerating charged particles, in this case electrons, through a sequence of magnets until they almost reach the speed of light. These now fast-moving electrons produce a very bright light, this is known as synchrotron bright light. Below in Figure 25 we see a schematic of Diamond light source synchrotron. Firstly, the electrons are accelerated in a linear accelerator (Linac). Once the electron energy reaches several MeV a booster further increases their energy to GeV. After this the electrons are stored in a storage ring.

Each time the electrons change path as a response to a magnet the emitted radiation it goes to the beamline. Energy lost by the electrons as synchrotron radiation is restored by radio frequency electric fields which accelerates the electrons along a linear section.

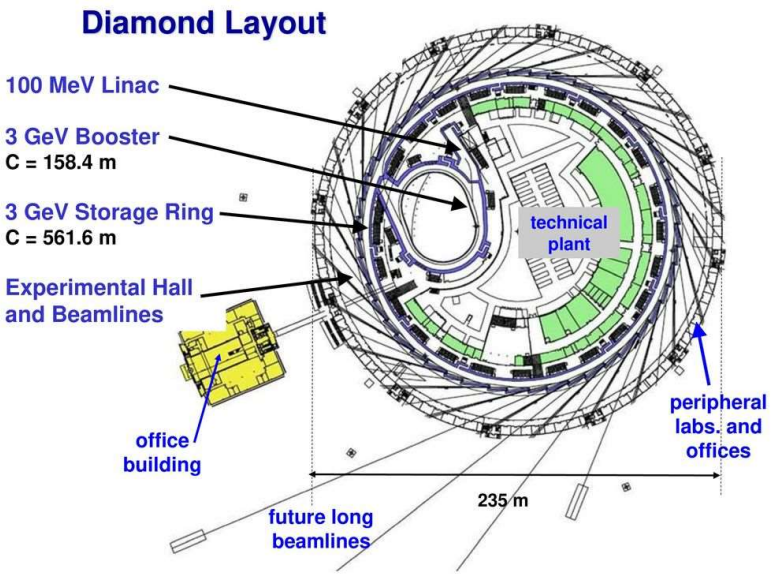

Figure 25 Schematic of synchrotron facility. Image taken from Diamond light source.

2.4.3 X-ray absorption fine structure.

X-ray absorption fine structure (XAFS) is a spectroscopic technique that is based on the principles of the photoelectric effect. When an X-ray photon of an appropriate energy is absorbed by an atom a core electron of the sample atom is excited to a higher energy state and if given enough energy possibly ejected into the continuum. XAFS techniques can be used to investigate both crystalline and amorphous samples, making XAFS a powerful analytical tool for many scientific fields. As electron transitions take place at specific energy values depending on the element XAFS is tuneable to the specific element under investigation.

During the XAFS experiment the absorption coefficient, μ, is measured as a function of energy, E. As E increases μ generally decreases. This means that as the X-rays increase in energy the sample becomes more transparent. The exception to this is the absorption edge energy. This is characteristic for each material and relates to where the energy of the X-ray matches the core electron binding energy.

The linear absorption coefficient μ (cm^{-1}), is given in:

$$\mu x = ln\frac{I_0}{I}$$

Equation 14

Where x is the sample length (cm), I_0 is the incident beam and I the transmitted beam. This equation is expressed in Figure 26.

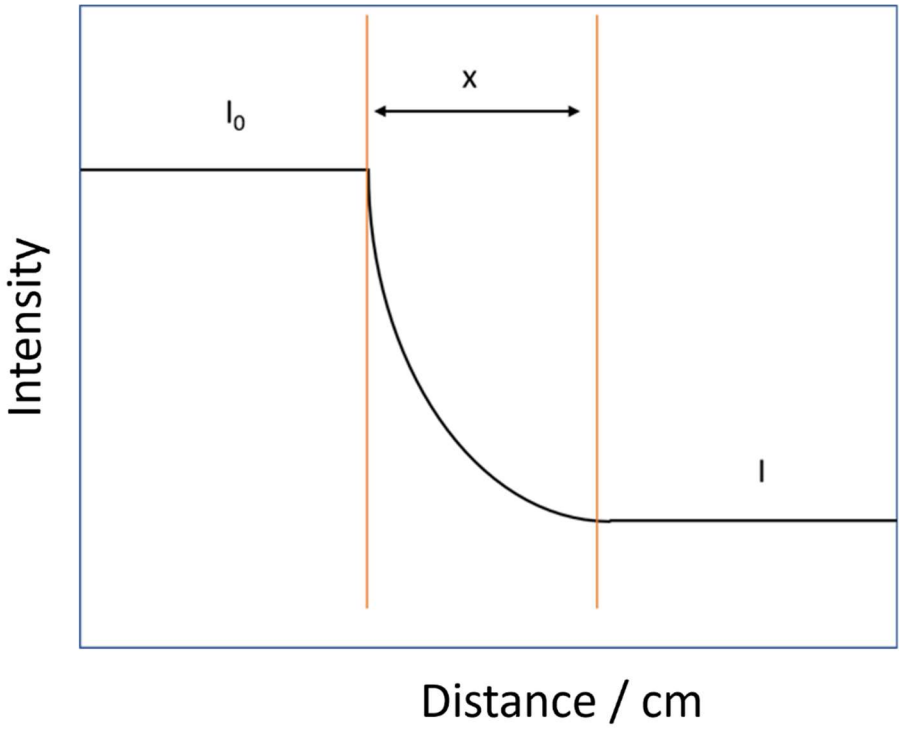

Figure 26 Transmission through a sample.

After absorption of X-ray energy, the excited electron can relax into a core hole filled by a higher energy electron. The energy difference between I_0 and I is released as a secondary photon. A secondary electron, Auger, electron may be free after absorbing the second photon.

The resulting XAFS spectrum is divided into two parts, as shown in Figure 27. The X-ray absorption near edge structure (XANES) and the extended X-ray absorption fine structure (EXAFS).

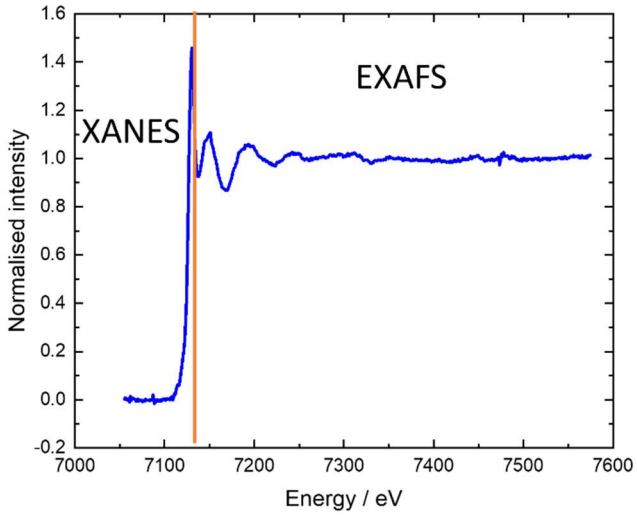

Figure 27 XAS spectrum of PB showing the XANES below roughly 7150 eV and the EXAFS region above 7150 eV.

The XANES region is affected by several factors effecting the element of interest.

- The oxidation states
- The electronic configuration
- The spin configuration
- Local geometry

The EXAFS region gives information about.

- The environment of the atom
- Interatomic distances and angles
- Structural and thermal disorders.

The resulting signal from EXAFS is commonly described as a wave. This wave has a given amplitude and phase. The first approximation of this wave results from the coordination number and type of atom and on the distances. The wave is expressed in the following equation.

$$x(k) = \sum_j^{shell} A(R_j, k) * \sin[2kR_j + \varphi(k)]$$

Equation 15

The final signal is expressed as the sum of all the sinusoidal contributions. Where each atom at a distance R_j accounts to the signal. The photo electron wavenumber k is expressed in the following equation.

$$k = \sqrt{\frac{2m(E - E_0)}{\hbar^2}}$$

Equation 16

In the case of the plane wave approximation and only a single scattering, the EXAFS equation can be expressed as follows,

$$x(k) = \sum_j \frac{N_j F_j(k) e^{-2k^2\sigma_j^2}}{kR_j^2} * sin[2kR_j + \delta_j(k)]$$

Equation 17

Where $F_j(k)$ and $\delta_j(k)$ are photoelectron scattering properties of neighboring atoms. If these properties are known we can then find, R_j, the distance to the neighbouring atom. N_j, the

coordination number of the neighboring atom and σ_j^2, the mean-square disorder of the neighboring atom. σ_j^2 is also known as the Debye-Waller factor.

2.4.4 Energy dispersive XAFS.

Energy dispersive EXAFS (EDE) is a technique that uses the diffraction of non-monochromatic X-rays by a polychromator crystal (bent crystal). This beam is focused onto the sample and then diverges towards a position sensitive detector. The beam position is then correlated to the energy. This leads to two distinct advantages of EDE. Firstly, because of the whole x-ray spectrum being collected simultaneously the technique can be used to investigate fast processes. Secondly the beam when focused on a sample is very small and stable. The stability results from the fact there is no movement of the optical elements during the spectrum collection.[103]

EDE will be used to study the kinetics of the charge/discharge process for MHCFSS based cathodes. The EDE data provides a separate measure of the change in oxidation state of the metal centres. Alongside this the electrochemical data will provide information regarding the alkali metal ion transport.

In Figure 28 we see a schematic of the i20-EDE beamline at Diamond light source. The beam starts with a wiggler. A wiggler is an insertion device in a synchrotron, made up of a series of magnets. These magnets deflect the beam of charged particles, this causes a change in acceleration which then leads to the production of a broad synchrotron radiation curve.

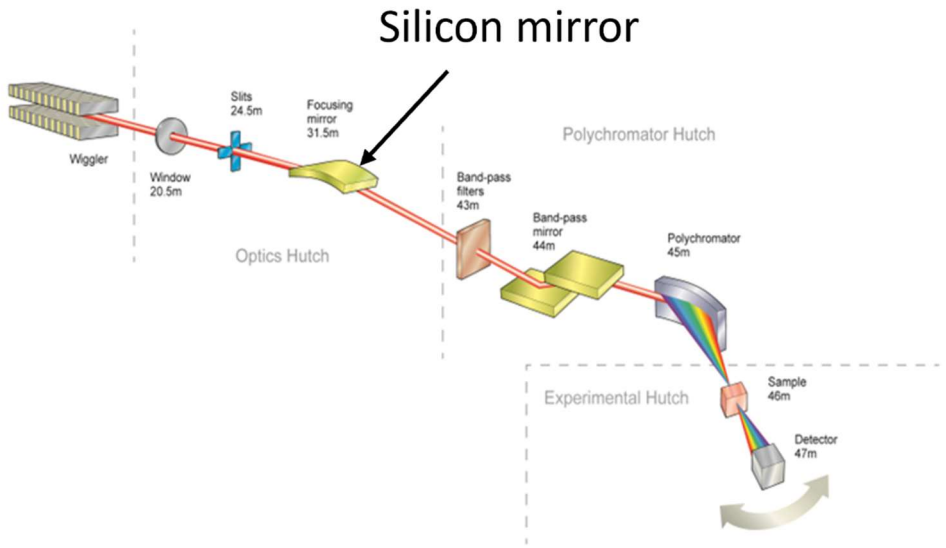

Figure 28 Schematic showing i20-EDE beam line. Image taken from Diamond light source.

The silicon mirror is an optical element in the beam. This acts as a vertical focussing mirror. The mirror is operated at 3 mrad incident angle and is coated with Rh and Pt strips. The purpose of this mirror is to focus the beam on the vertical direction towards the sample. A band pass mirror is another vertical deflecting mirror that alongside the upstream filters removes the heat load and the selection of sufficient wide bandpass that is accepted by the polychromator. Finally, the polychromator crystal is a thin bent silicon crystal. Either Si(111) or Si(311) which allows use of the entire beamline energy. [104,105]

2.5 Energy Dispersive EXAFS

2.5.1 Beamline and beamline set up

All energy dispersive EXAFS (EDE) experiments took place on I20-EDE at Diamond light source (UK). Using a Si (311) polychromator crystal or a Si (111), with a ring energy of 3.0 GeV and an average ring current of 300 mA. By changing to the Si (111) a larger range of X-rays is achieved for the dual edge experiments. The X-ray absorption spectra (XAS) were measured in transmission mode with air acting as the I_0 using an XH detector with a germanium window.[106] Al foil, between 180 µm and 240 µm thick, was used for attenuation. This prevented the beam from burning through the electrode during longer experiments and reduced the fluctuation of intensity of the spectroscopy results. By attenuating the beam with aluminium foil this fluctuation effect can be minimalised. This would cause an influx of Na ions at the point where the beam was on the sample and artificially increase the background absorption.

The XAS data was calibrated using the a reference foil of the K-edge under investigation. The calibration process converts the pixels on the detector using a polynomial. The calibration used a an ideal XAFS spectrum taken on B18 to reference the pixel for the edge position. For the simultaneous dual edge experiments both the polynomials for the Fe and Co foils were plotted in Origin and then a third polynomial was plotted combining the two. This was used to calibrate the data as it was collected.

2.5.2 *In situ* electrochemical experiment set up

The *in situ* electrochemical cell is placed on the beam line so that the sample is at the focal point of the beam. XAS spectra were collected during five charge and discharge cycles carried out for each potential range, E_1 and E_2, applied. A minimum of 3 repetitions of these charge/discharge cycles were carried out on different positions on the electrode.

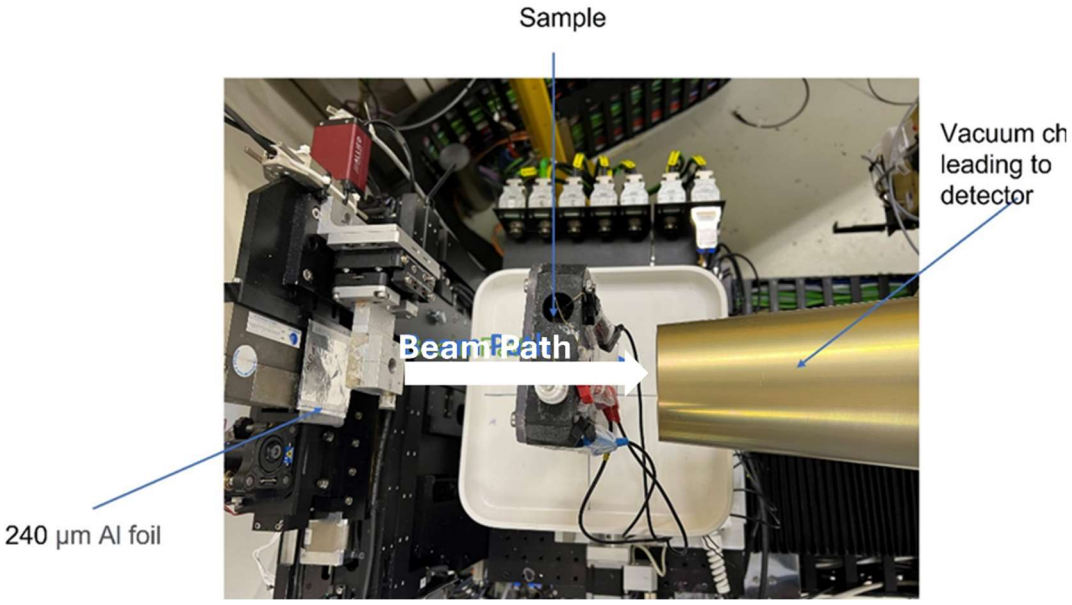

Figure 29 Top view of *in situ* cell on the i20-EDE beam line. Showing the beam path going from through the aluminium foil, through the *in situ* cell and then too the detector.

Above in Figure 29 we see an image of the *in situ* cell placed in the beam path.

2.5.3 Data processing

The XAS spectra were processed to analyse the changes in edge position. All data analysis is carried out using DAWN and python codes written in house. The edge position is defined by the energy at given by the 0.5 normalised intensity. This was found to give the most consistent and reproducible value for the edge position compared to other definitions of edge position, such as the peak of the first derivative.[107,108]

An example of the dual edge collected data is shown in Figure 30 where data was recorded at the Fe and Co K-edges simultaneously. For each dual-edge measurement, the first step in the data processing is to split the data into separate K-edges for each element. This is demonstrated in Figure 32 A and B. This data is then normalised.

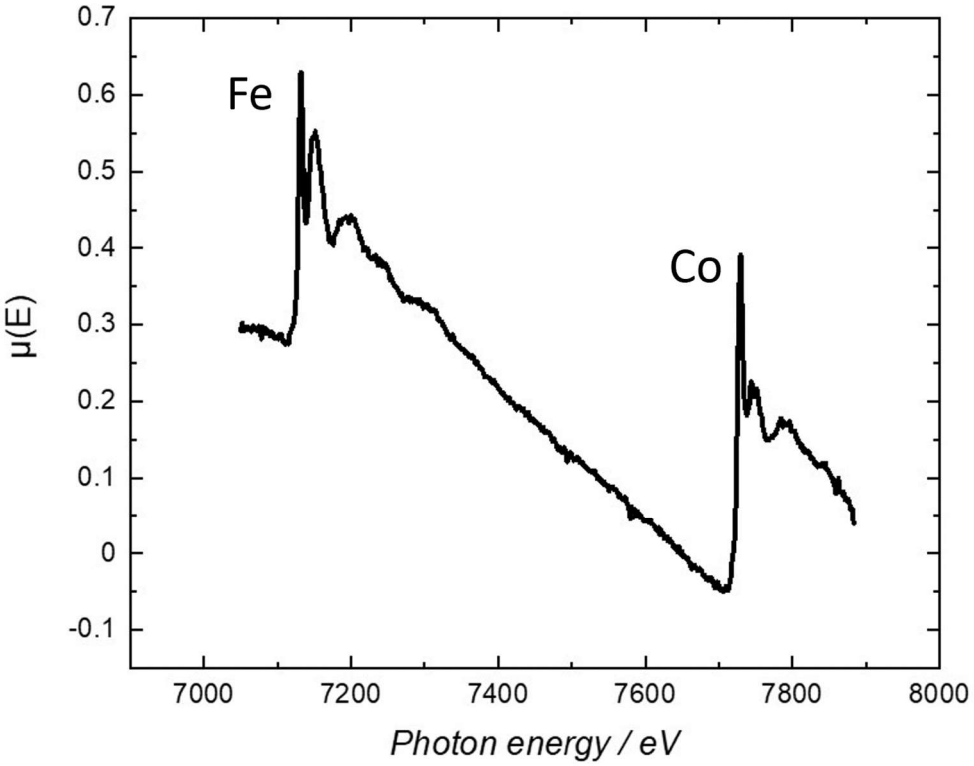

Figure 30 CoHCF dual edge XAS, dry electrode (loading 8 mg cm^{-2}) in the *in situ* cell.

2.5.4 Normalisation of the XAS data

The normalisation process converts the raw XAS data to a per-atom basis. This removes the effects on the spectrum resulting from sample preparation total absorption or instrument setting. The process of normalisation is carried out, in DAWN, following three steps; step 1 is to subtract a

pre-edge line; step 2 normalising the edge step and finally step 3 flattening the post-edge line to y = 1. As shown in Figure 31.

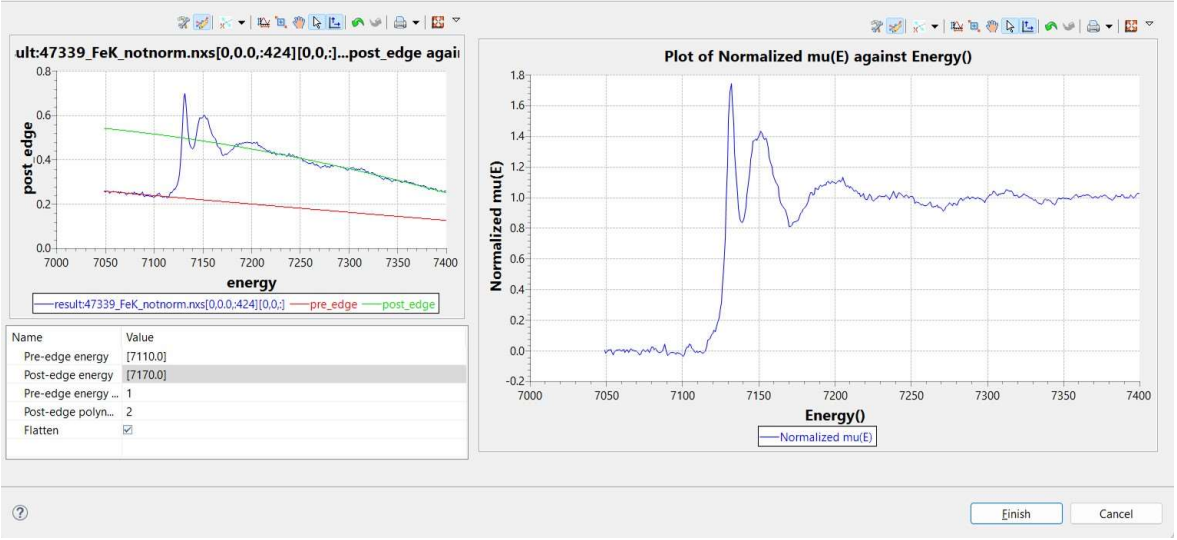

Figure 31 Example of the Normalisation process carried out using DAWN. Showing the pre-edge and post-edge values used in the normalisation process. The figure on the right shows the normalisation process and on the left the result of the normalisation.

Figure 32 shows the results before (Figure 32 A/B) the normalisation process. Then after (Figure 32 C/D) the normalisation process for both the Fe and Co K-edges.

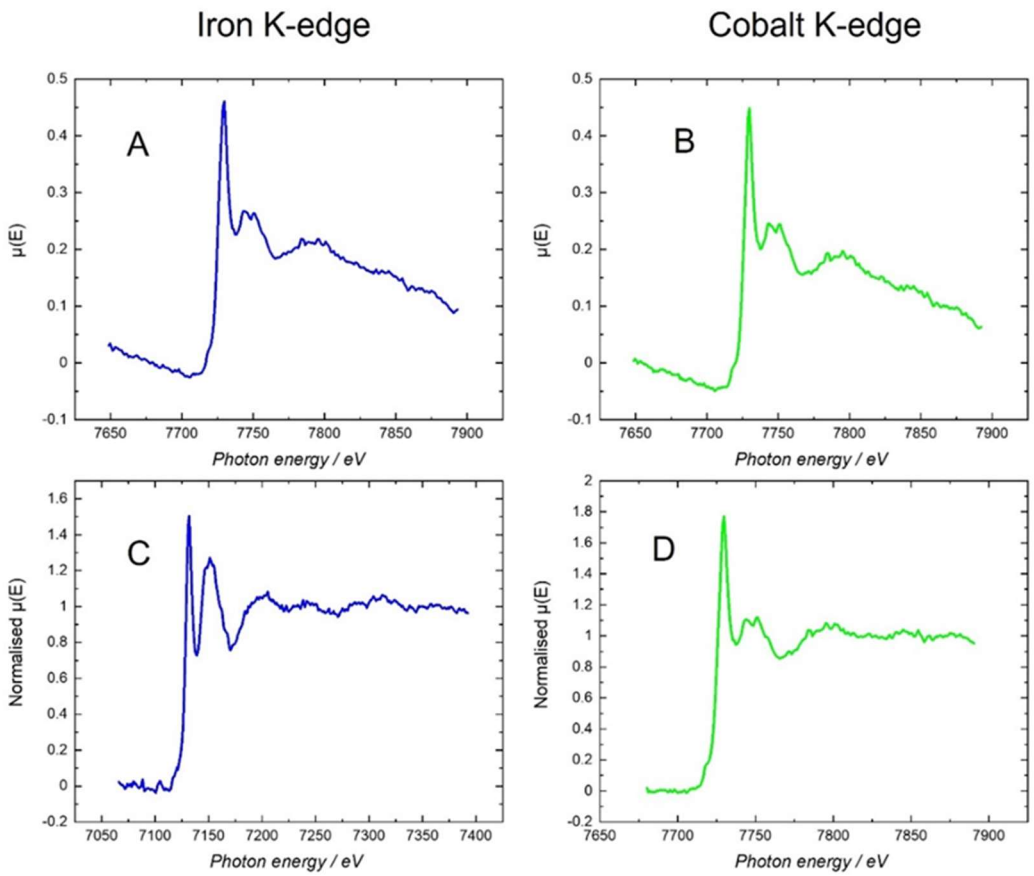

Figure 32 Comparing the collected raw data for the cropped Fe K-edge (A) and Co K-edge (B) and the normalised Fe K-edge (C) and Co K-edge (D).

2.5.5 Defining the edge position

The final stage of processing is to then calculate a value of the edge position from the normalised spectra as a function of time. For this the photon energy at 0.5 intensity of the normalised spectrum is chosen for the value of the edge position.[109] A python script was written to calculate this value from the normalised spectra. The 0.5 intensity of the normalised spectra was chosen as it was found to be much less affected by fluctuations in the experimental data from lack of homogeneity from the electrode.

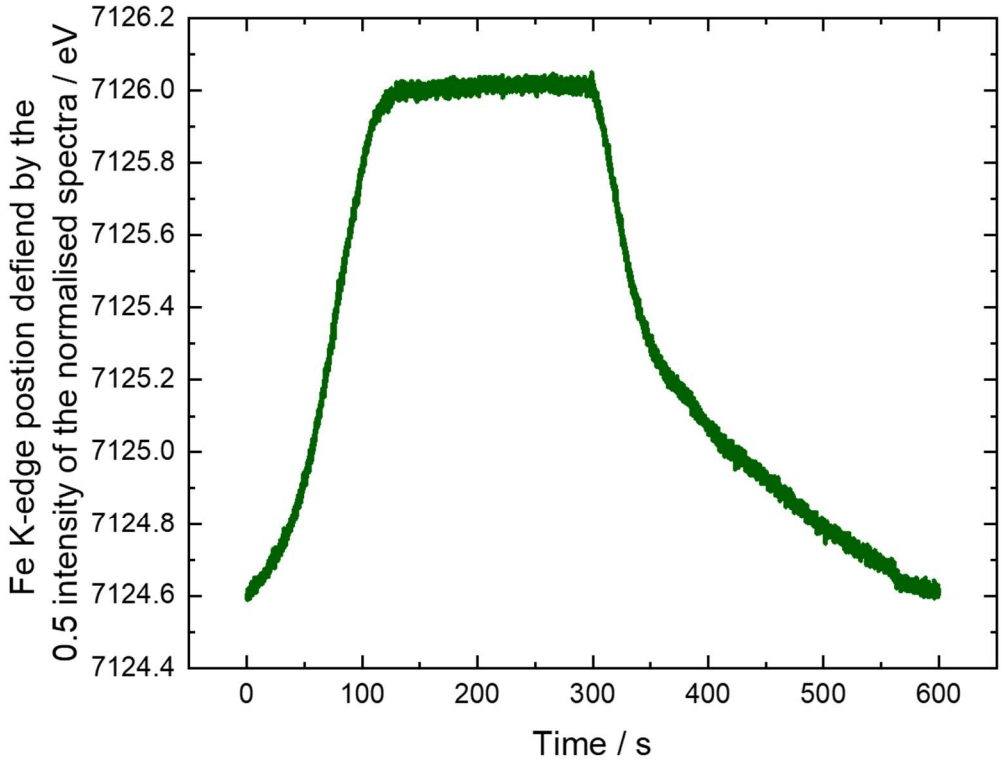

Figure 33 Example of the edge position defined by the 0.5 intensity of the normalised spectra *vs.* time plot.

2.5.6 Linear combination fitting

Linear combination fitting was carried out using DAWN software. The reference samples used for each linear combination were taken from within each experimental data set using the extremes of the data corresponding to the fully reduced or oxidise species. Thus, all the data analysed herein is in terms of the fraction of the metal atoms that change oxidation state and not the average oxidation state which would include the metal atoms that are not electrochemically active.

2.5.7 Time constants from exponential fits

The exponential responses of the edge position, current, and/or charge (y) as a function of time (x) were fitted using Origin® 2019b to Equation 18 to enable determination of the characteristic time constants.

$$\mathrm{y} = Ae^{\frac{x}{\tau}}$$

Equation 18

Where τ , the time constant, is defined by Equation 19.

$$\tau = \frac{1}{k}$$

Equation 19

and k, s^{-1}, is the rate of exponential decay or growth. Therefore, the time constant is inversely proportional to the rate of decay/growth of the exponential. Meaning a larger value of τ, s, corresponds to a slower rate of decay/growth.

Chapter 3 Study of sodium and potassium ion (de)intercalation in FeHCF at the Fe K-edge.

3.1 Introduction

3.1.1 Aim of this chapter

The aim of this chapter is to bring together several methods for the analysis the kinetics of ion (de)insertion and charge transfer in FeHCF electrodes. The rate of charge/discharge of FeHCF electrodes is limited by either the cation or electron transport or both. The first part of this chapter will focus on electrochemical methods to characterise the diffusion in the form of an effective diffusion coefficient for both Na^+ and K^+ ions. Cyclic voltammetry (CV), large amplitude potentials step voltammetry (LAPS) and potential iteration titration potentiometry (PITT) we will be able to derive different values of the diffusion coefficient of the Na^+ and K^+ cations and compare these results. The rate of transport of the cation into and out of the FeHCF lattice is limited by diffusion. To limit the contribution of mass transfer of cation to the electrode surface our system is designed with a large bulk concentration of cation. This leaves only diffusion within the FeHCF lattice and the electrode.

The second part of the chapter the electron transfer kinetics are explored. The kinetics can be limited by resistance in the electrode and/or by the rate of the fundamental electron transfer step. Using the results from LAPS, we can derive a rate constant for the oxidation and reduction processes. With the EDE data we will be able to see a response coming from just the redox reaction of the Fe within the FeHCF, from which we can calculate the resulting charge from this redox couple and compare this with the charges from the electrochemically derived charges from the experiments carried out during the beam time.

3.2 Results and Discussion

All experiments both electrochemical and spectroscopic were carried out in the static *in situ* cell described in section 2.3.4. With electrodes of loading of 8 mg cm^{-2}, of total mass of ink. This loading was used to ensure an edge jump of 1 for the spectroscopy experiments and includes the total mass of the whole ink, approximately 70% active material.

3.2.1 Electrochemical investigation into (de)intercalation of Na and K ions into Iron(III) hexacyanoferrate

3.2.1.1 Cyclic Voltammetry (CV) of FeHCF in Na^+ or K^+ electrolyte.

The CV for FeHCF is shown in Figure 34. The voltammetry was performed in a 2 M $NaNO_3$ electrolyte at a pH of 2. The voltammogram shows two distinct redox peaks. These two peaks are the result of the two Fe centres present in FeHCF. The first redox couple between -0.2 and 0.5 V *vs.* SCE (I/II) is attributed to the redox reaction of the iron bound to the nitrogen from the CN bridging ligand (Fe-N) and corresponds to reaction Equation 20:

$$XFe^{III}[Fe^{II}(CN)_6] + e^- + X^+ \rightleftharpoons X_2Fe^{II}[Fe^{II}(CN)_6]$$

Equation 20

The peak between 0.5 and 1.1 V *vs.* SCE (III/IV) in **Error! Reference source not found.** results from the redox couple of the carbon bound iron in the CN bridging ligand (Fe-C) shown in Equation 21:

$$Fe^{III}[Fe^{III}(CN)_6] + e^- + X^+ \rightleftharpoons XFe^{III}[Fe^{II}(CN)_6]$$

Equation 21

The sweep-rate dependent voltammograms are shown in Figure 35. As the sweep rate is increased the resolution of the sets of peaks decreases and it becomes hard to separate the two. Furthermore, the effect of uncompensated resistance from the *in situ* cell becomes more prominent as the scan rate increases.

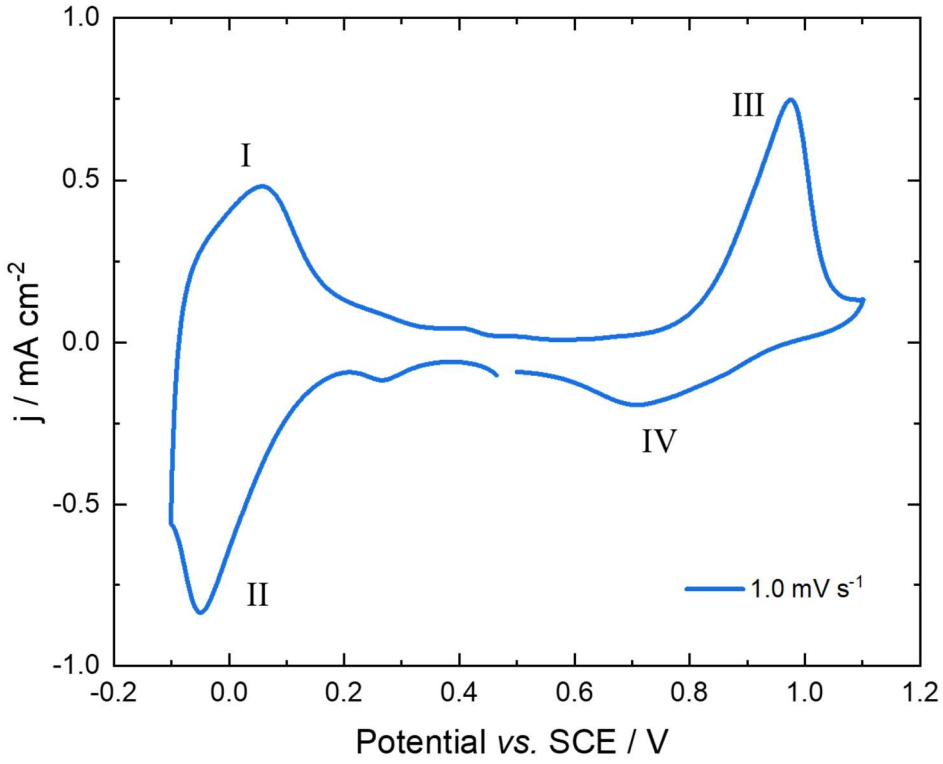

Figure 34 Cyclic voltammetry of an 8 mg cm^{-2} FeHCF on Toray carbon paper electrode in 2 M $NaNO_3$ at pH 2. With a scan rate of 0.1 mV s^{-1}. Start potential at 0.5 V and initial sweep to -0.1 V. Peaks I/II showing the Fe-N redox couple and III/IV the Fe-C redox couple. Carried out at room temperature (around 22 °C – 25 °C) in the *in situ* cell (see Figure 20).

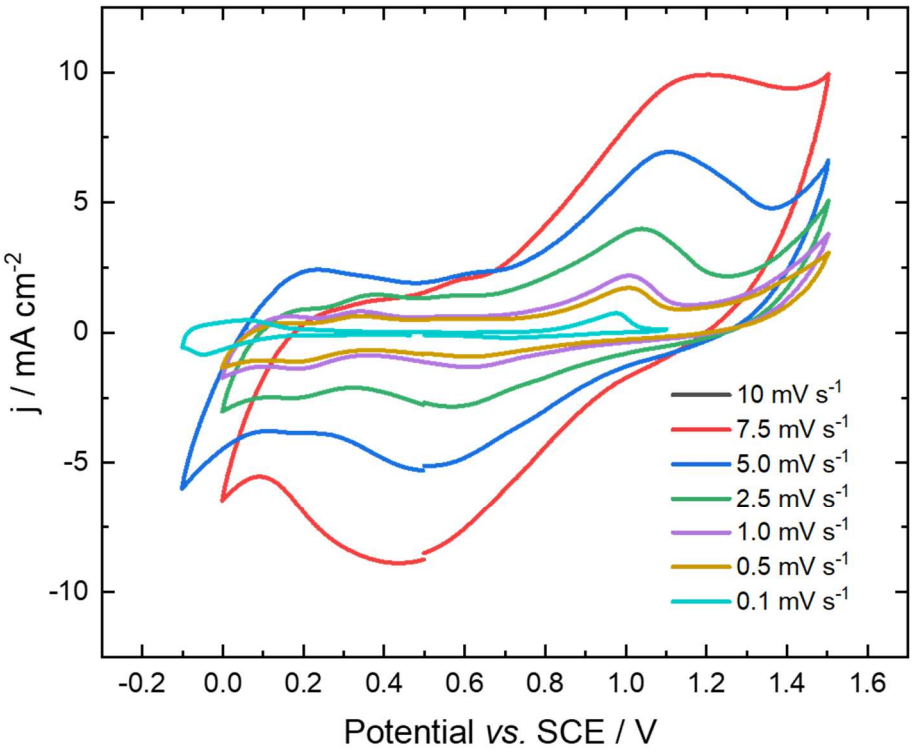

Figure 35 Sweep rate dependant cyclic voltammogram of the electrode shown in Figure 34. Starting at 0.5 V *vs.* SCE sweeping down to -0.1 V and up to 1.5 V vs SCE. Carried out at room temperature (around 22 °C – 25 °C) in the *in situ* cell (see Figure 20).

Figure 36 shows voltammetry of FeHCF in a 2 M KNO_3 electrolyte at a pH of 2, which also shows the two set of redox peaks typical for a voltammetry of FeHCF. The peak between -0.2 and 0.5 V *vs.* SCE corresponding to the Fe-N redox couple (V/VI, Equation 20). With the peak between 0.5 and 1.2 V *vs.* SCE resulting from the Fe-C redox couple (VII/VIII, Equation 21).

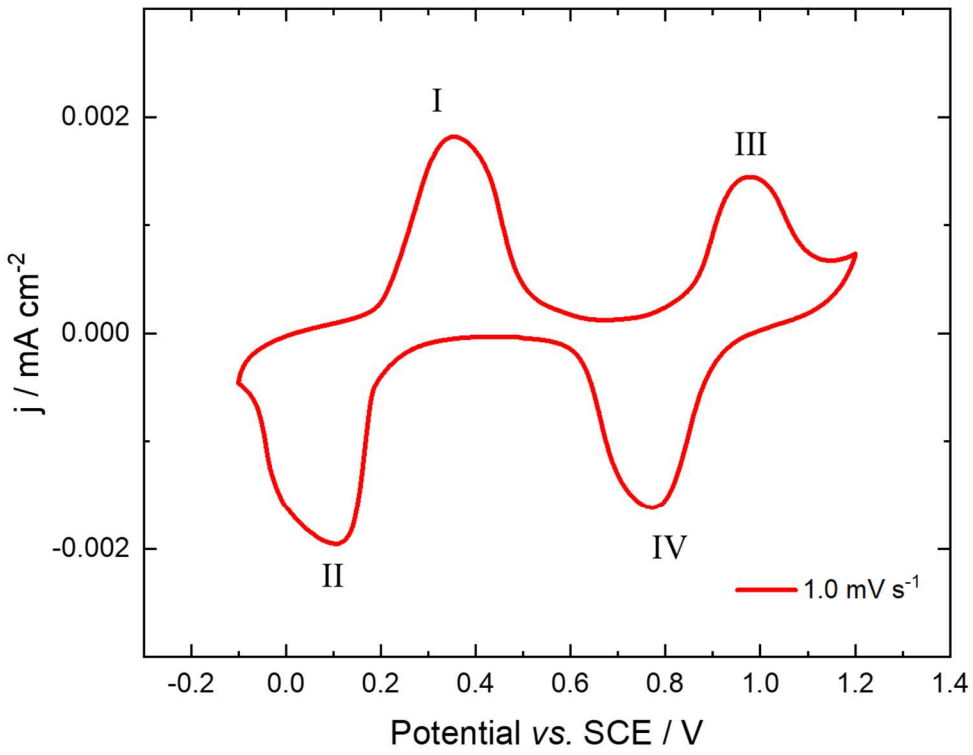

Figure 36 Cyclic voltammetry of an 8 mg cm^{-2} FeHCF on Toray carbon paper electrode in 2 M KNO_3 at pH 2. With a scan rate of 0.1 mV s^{-1}. Start potential at 0.5 V initially sweeping to -0.1 V. Peaks V/VI showing the Fe-N redox couple and VII/VII the Fe-C redox couple. Carried out at room temperature (around 22 °C – 25 °C) in the *in situ* cell (see Figure 20).

The oxidation state of the Fe present will influence the colour of the FeHCF. The fully reduced form $Na_2Fe^{II}[Fe^{II}(CN)_6]$, which is known as Prussian White is fully intercalated with Na^+. Therefore, for every Fe there is one Na. The more common form of FeHCF known as Prussian blue (PB), $NaFe^{III}[Fe^{II}(CN)_6]$ where is now a ratio of 1:0.5 for Fe:Na and the most oxidised form Prussian green (PG or sometimes Berlin green), $Fe[Fe(CN)_6]$. In PG all Na^+ should have been removed from the FeHCF lattice. The redox peak I/II (Figure 34) or V/VI (Figure 36) correspond to the change in colour from PB to PW. Peaks III/IV (Figure 34) and VII/VIII (Figure 36) relate to the change from PB to PG.

From Figure 35 the poor cycling stability of the redox peak between 0.5 and 1.1 V *vs.* SCE is clearly demonstrated, as the peak becomes more and more distorted at higher scan rates. This lack of stability is well recorded in the literature and results from side reactions forming H_2O_2.[110] The formation of H_2O_2 causes the electrolyte to become acidic and break down the CN bridging

ligands. This makes analysis and comparison of the Fe-C peak difficult. Therefore, for the rest of this chapter only the Fe-N redox peak will be used to investigate the effect of the cation on the electrochemistry of FeHCF.

3.2.1.2 Scan rate dependence of the cyclic voltammetry of FeHCF in both Na^+ and K^+ ion electrolytes

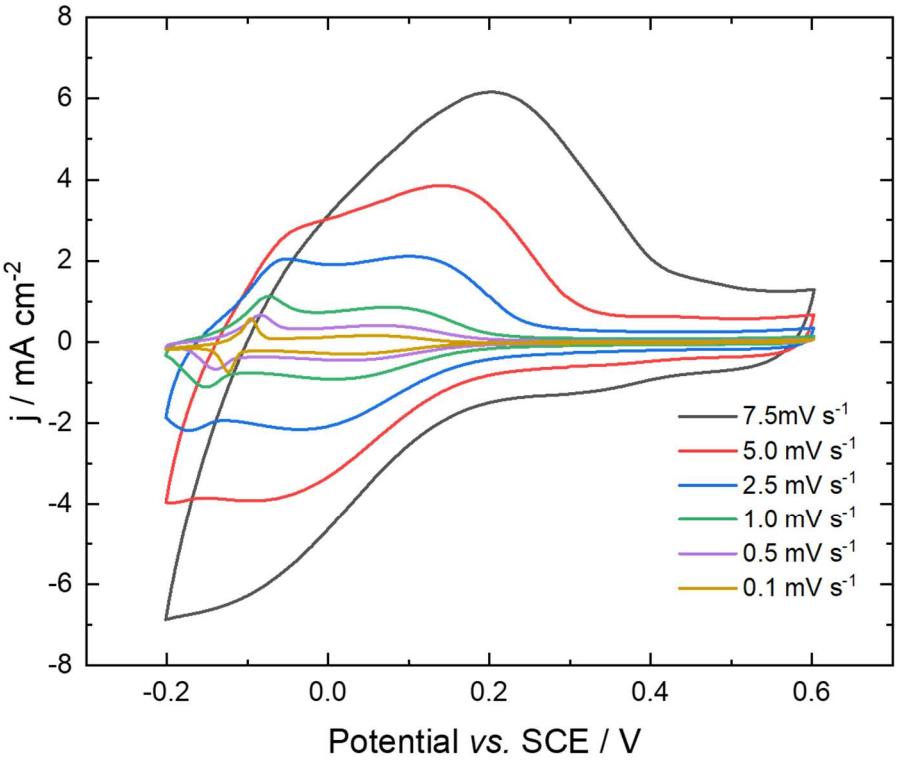

Figure 37 Cyclic voltammetry of an 8 mg cm^{-2} FeHCF on Toray carbon paper electrode in 2 M $NaNO_3$ at pH 2. Showing just the Fe-N redox couple for a range of scan rates from 10 mV s^{-1} to 0.1 mV s^{-1}. Carried out at room temperature (around 22 °C – 25 °C) in the *in situ* cell (see Figure 20).

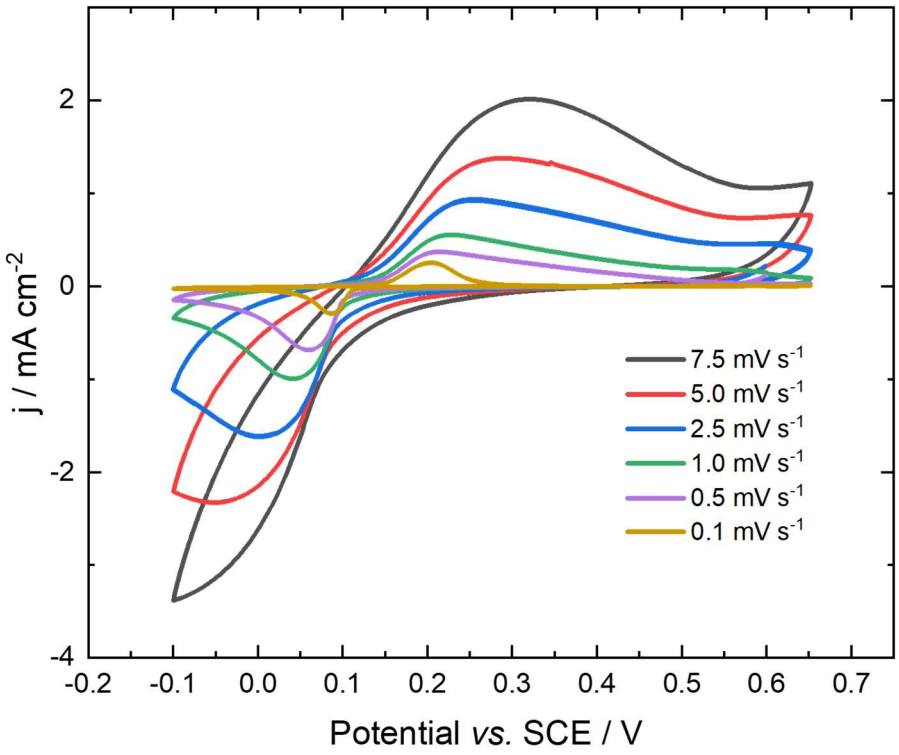

Figure 38 Cyclic voltammetry of an 8 mg cm^{-2} FeHCF on Toray carbon paper electrode in 2 M KNO_3 at pH 2. Showing just the Fe-N redox couple for a range of scan rates from 10 mV s^{-1} to 0.1 mV s^{-1}. Carried out at room temperature (around 22 °C – 25 °C) in the *in situ* cell (see Figure 20).

.

The voltammetry of just the Fe-N redox couple of FeHCF in a Na^+ electrolyte is shown in Figure 37 and in K^+ in Figure 38. The CV's show the response at several different scan rates ranging from 10 mV s^{-1} to 0.1 mV s^{-1}. The main difference between the CV's in Figure 37 and Figure 38 is that in the Na^+ ion electrolyte the peak is much broader. In studies found in the literature this broadness of peaks in an Na^+ ion electrolyte compared to a K^+ electrolyte is argued as resulting from the hydration radius of the corresponding cation. The hydration radius of Na^+ (3.58 Å) being larger than that of K^+ (3.31 Å) results in much slower kinetics for (de)intercalation.[111]

The XRD of the FeHCF (Figure 4) corresponds to a cubic structure. Previous studies have shown that the cubic structure has a much better cycling stability. [112,113] It has also been well documented that the (de)intercalation of K^+ is a much more facile process compared to Na^+. the difference in the facility of these reactions is attributed to a phase shift seen for FeHCF in Na^+

electrolyte. A shift from the cubic structure to rhombohedral is seen when Na^+ is intercalated to accommodate the larger size of cation.[114]

The CV of FeHCF in both Na^+ and K^+ ion electrolytes can now be analysed as a function of the scan rates shown in Figure 37 and Figure 38. To achieve this, we shall need to assume that the concentration of electrolyte is the same inside the electrode as it is in the bulk solution, 2 mol dm^{-3}. This assumption is made based on the saturation steps that were carried out before the experiments took place, as described in the experimental chapter. A geometric area of 3.8 cm^2 was used for each calculation and semi-infinite linear diffusion conditions are assumed, to allow for better comparison between the electrodes. Furthermore, due to time restrictions resulting from the COVID-19 pandemic proper ECSA studies were not carried out. A geometric area was used to all for better comparability between the results. Furthermore, due to time restriction resulting from COVID-19 proper study on the electrochemical area was not possible. Based on these assumptions we can use the Randles-Sevcik (RS) equation (Equation 22) to find an effective diffusion coefficient, D_{eff}, from the CV's: [115]

$$i_p = 2.69\ x\ 10^5 n^{\frac{3}{2}} \mathrm{A C_0 D}_{eff}^{\frac{1}{2}} \nu^{\frac{1}{2}}$$

Equation 22

were i_p is the peak current in amps, A; n is the number of electrons transferred in the reaction (n = 1); A the apparent area of the working electrode (3.8 cm^2); D_{eff} the diffusion coefficient $cm^2\ s^{-1}$; ν the scan rate in V s^{-1} and C_0 the concentration of electrolyte (2 mol dm^{-3}). A plot of i_p *vs.* $\nu^{1/2}$ should yield a straight line and the diffusion coefficient determine from the gradient. Although alternative analysis for irreversible reaction is available in order for better comparison with the literature, these systems where still modelled as reversible.

As the voltammetry for FeHCF in $NaNO_3$ over just the Fe-N region shows two peaks at -0.1 V and a second at 0.1 V both were analysed. As seen in Figure 39 the relationship between the peak anodic and cathodic current for the $\nu^{1/2}$ is linear at the lower scan rates for the lower peak of the Fe-N redox couple in Na^+. This result is expected and seen frequently in studies of MHCFS materials. [116]

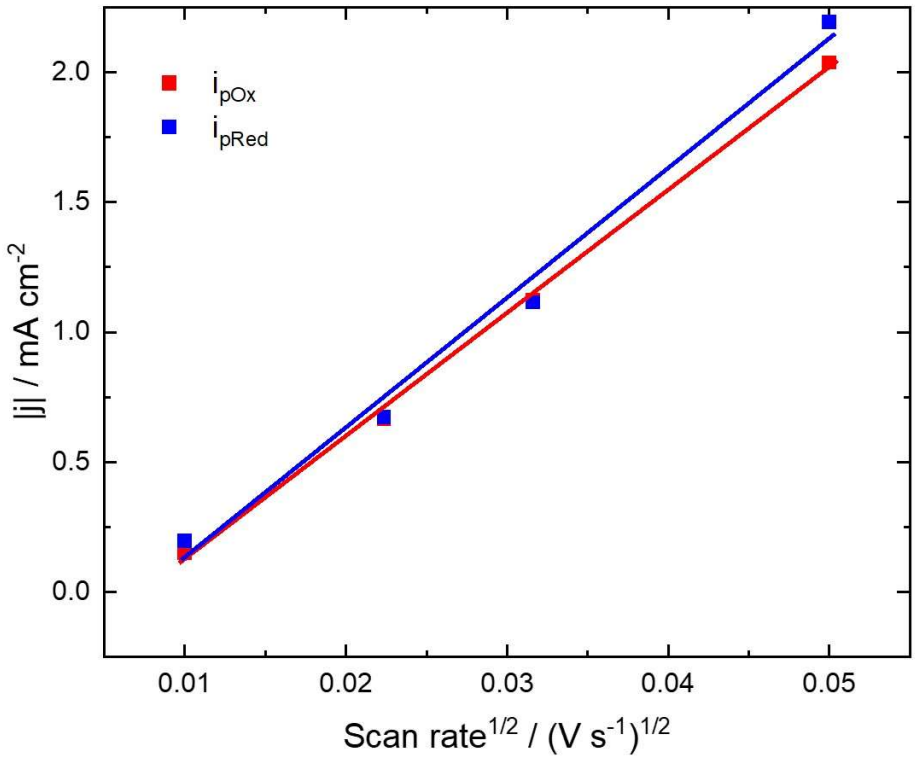

Figure 39 Analysis peak current *vs.* (scan rate)$^{1/2}$ for the CV of FeHCF in 2 M $NaNO_3$ at pH 2 between -0.2 and 0.65 V *vs.* SCE. Looking at just the Fe-N redox couple, lower peak E_p = 0.23 V *vs.* SCE.

The diffusion coefficient for the (de)intercalation process was calculated from the gradient of the plots in Figure 39. For the deintercalation we calculate a diffusion coefficient of (0.54 ± 0.03) x 10^{-9} cm^2 s^{-1}. Whilst for the intercalation process (0.60 ± 0.09) x 10^{-9} cm^2 s^{-1}. Thus, the diffusion coefficient from the CV is within error of each other for both (de)intercalation. The upper peak (approximately 0.1 V *vs.* SCE) for the Fe-N redox couple the peak current analysis is presented in Figure 40.

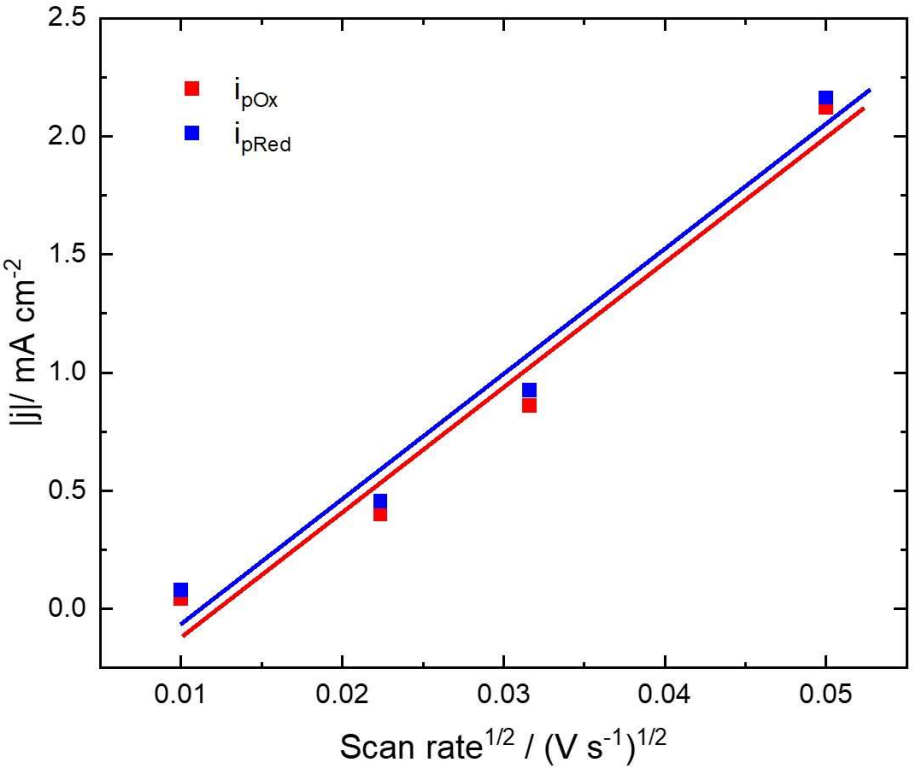

Figure 40 Analysis peak current *vs.* (scan rate)$^{1/2}$ for the CV of FeHCF in 2 M $NaNO_3$ at pH 2 between -0.2 and 0.65 V *vs.* SCE. Looking at just the Fe-N redox couple, higher peak E_p = 0.36 V.

Again, we derive a diffusion coefficient from the gradient. For the deintercalation process we obtain a value of (0.67 ± 0.12) x 10^{-9} cm ^{2} s^{-1}. For the intercalation (0.67 ± 0.14) x 10^{-9} cm^2 s^{-1}. In this case the value for the diffusion coefficient for both processes are the same.

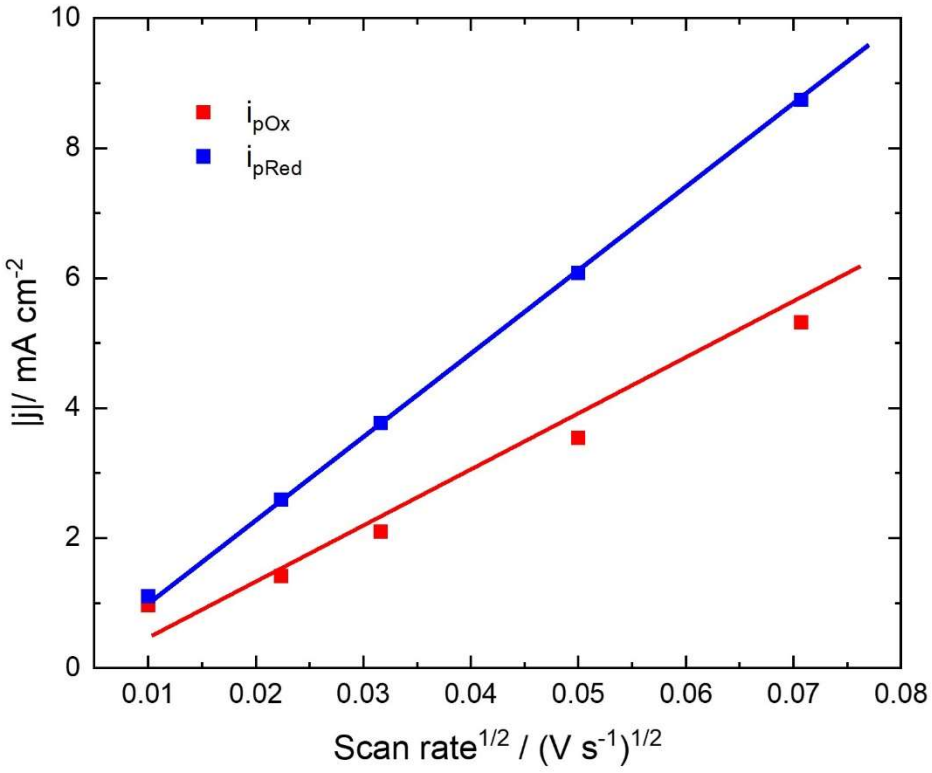

Figure 41 Analysis peak current *vs.* (scan rate)$^{1/2}$ for the CV of FeHCF in 2 M KNO_3 at pH 2 between -0.2 and 0.65 V *vs.* SCE. Looking at just the Fe-N redox couple.

The results in K^+ electrolyte is given in Figure 41. From the gradients of both lines, we derive a diffusion coefficient for the deintercalation (1.8 ± 0.29) x 10^{-9} cm^2 s^{-1} and the intercalation (3.5 ± 0.48) x 10^{-9} cm^2 s^{-1}.

In both electrolytes the deintercalation of either Na^+ or K^+ has a larger diffusion coefficient compared with the intercalation. This is confirmed by the peaks seen in the voltammetry, as the intercalation is always the broader peak, suggesting slower diffusion of the cation.

Using these diffusion coefficients, we can further our analysis of the voltammograms and derive a rate constant using the Nicholson-Shain method. Going further in this thesis the diffusion coefficient calculated from the intercalation will be used when needed in calculations for convenience of comparison with later experiments.

3.2.1.3 Determination of rate constant from cyclic voltammetry of FeHCF in Na^+ and K^+ electrolytes

To derive a rate constant from the CV's above the Nicholson-Shain (NS) method is used.[117,118] This method is widely used for estimating k^0 for Quasi reversible systems. Where k^0 is the rate

constant for the reaction. The NS method is based on the assumption that the system is quasi-reversible therefore, can only be applied where the peak to peak separation is in the range of 50 to 200 mV. The analysis is based on the kinetic parameter Ψ using the following equation:

$$\Psi = k^0 \left[\frac{n\mathrm{D}\pi\mathrm{F}}{\mathrm{RT}}\right]^{-\frac{1}{2}} v^{-\frac{1}{2}}$$

Equation 23

Where n is the number of electrons, D the diffusion coefficient $cm^2\ s^{-1}$, F Faraday's constant 96485 $C\ mol^{-1}$, R ideal gas constant 8.314 $J\ K^{-1}\ mol^{-1}$, T temperature 298 K. Ψ is calculated from Equation 24.

$$\Psi = \frac{-0.6288 + 0.0021\ X}{1 - 0.017\ X}$$

Equation 24

Where X:

$$X = \Delta\mathrm{E_p}\ x\ n$$

Equation 25

Where $\Delta\mathrm{E_p}$ is the difference in peak energy in mV for the oxidation and reduction peak. This then produces a working curve of Ψ *vs.* $\Delta\mathrm{E_p}$, from which we can deduced. The NS analysis is used for the voltammetry of FeHCF in 2 M $NaNO_3$ at pH 2 and the results are given in Figure 42.

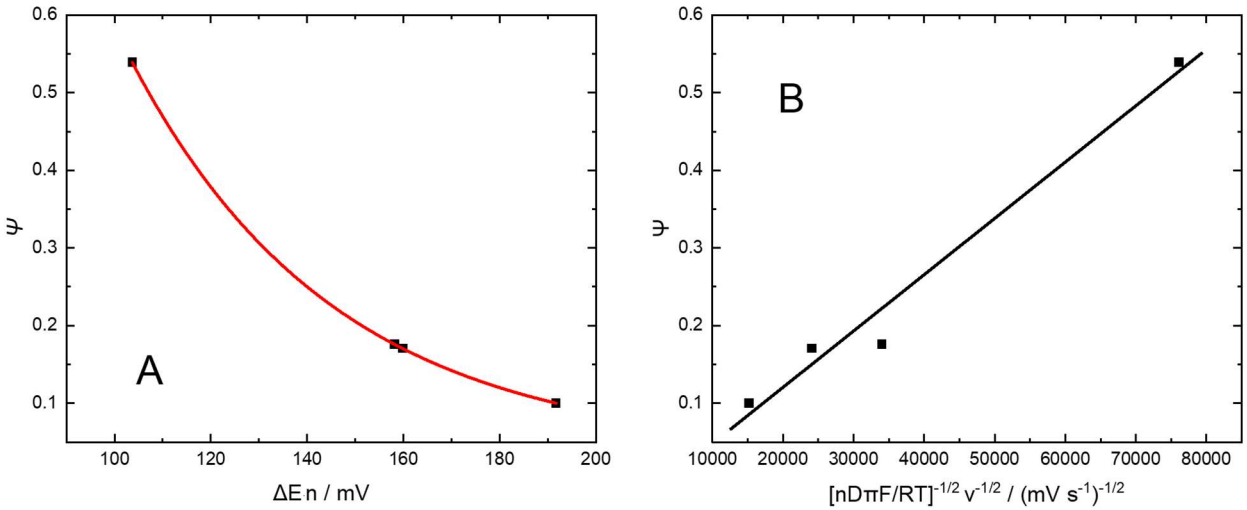

Figure 42 NS analysis for CV of FeHCF in 2 M $NaNO_3$ at pH 2. A) Ψ values calculated from Equation 24 *vs.* X, B) Ψ *vs.* $\left[\frac{n\mathrm{D}\pi\mathrm{F}}{\mathrm{RT}}\right]^{-\frac{1}{2}} v^{-\frac{1}{2}}$.

Figure 42 A shows how the Ψ varies with the peak potential difference. We see an exponential relationship between the Ψ value and the peak potential difference which is expected based on the literature sources.[119] Then in Figure 42 B the relationship between is given by Ψ and $\left[\frac{n\mathrm{D}\pi\mathrm{F}}{\mathrm{RT}}\right]^{-\frac{1}{2}} v^{-\frac{1}{2}}$ is given. When calculating $\left[\frac{n\mathrm{D}\pi\mathrm{F}}{\mathrm{RT}}\right]^{-\frac{1}{2}}$ part of Equation 23 for the Na^+ ion experiments the value of 24076.8 $cm^2\ s^{-1}$,is calculated using the diffusion coefficient from the RS analysis, from the voltammetry in Figure 37. As Ψ *vs.* $\left[\frac{n\mathrm{D}\pi\mathrm{F}}{\mathrm{RT}}\right]^{-\frac{1}{2}} v^{-\frac{1}{2}}$ has a linear relationship a value for k^0 of 7.25 x 10^{-6} m s^{-1} can be taken from the gradient. When comparing this value to literature examples where the NS analysis for reversible system has been used for MHCFS systems we are within the same order of magnitude as the literature sources.

Now the same analysis is applied to the voltammetry of FeHCF in KNO_3 at pH 2, with the results presented in Figure 43.

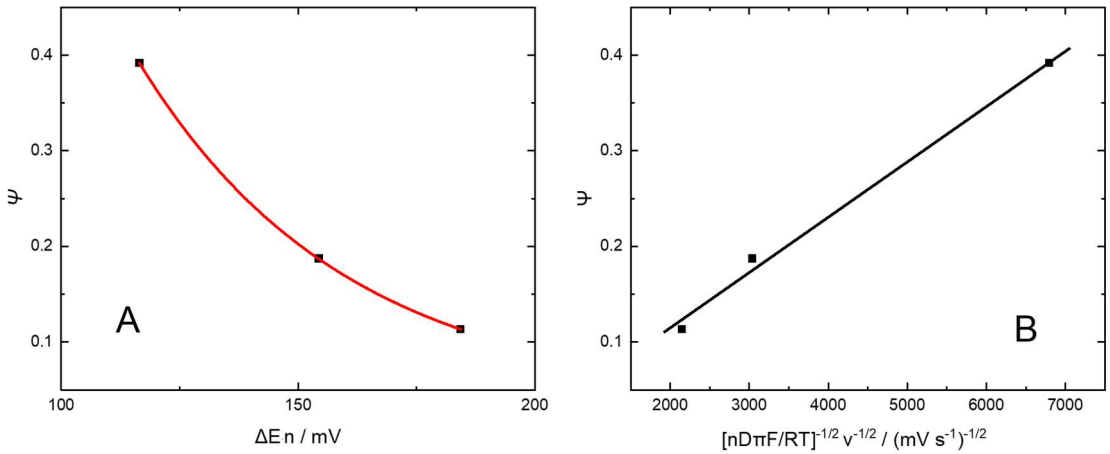

Figure 43 NS analysis for CV of FeHCF in 2 M KNO_3 at pH 2. A) Ψ values calculated from Equation 24 *vs.* X, B) Ψ *vs.* $\left[\frac{n\mathrm{D}\pi\mathrm{F}}{\mathrm{RT}}\right]^{-\frac{1}{2}} v^{-\frac{1}{2}}$.

Again in Figure 43 A an exponential relationship between Ψ and the peak potential difference as expected. Then Figure 43 B the linear relationship between Ψ and $\left[\frac{n\mathrm{D}\pi\mathrm{F}}{\mathrm{RT}}\right]^{-\frac{1}{2}} v^{-\frac{1}{2}}$ is linear means we can derive a value of 5.83 x 10^{-5} cm s^{-1} for k^0.

When comparing the values of k^0 for each of the two cations, 7.25 x 10^{-6} m s^{-1} for Na^+ and 5.83 x 10^{-5} m s^{-1} for K^+, a faster rate is calculated in the rate of ion transfer for K^+ is given. This is confirmed by the sharper peaks given for the Fe-N redox couple in the voltammogram.

3.2.2 Large amplitude potential step

The cation diffusion coefficient may also be determined using potential step (PS) experiments. As mentioned in the previous section the redox peak between 0.5 V and 1.2 V was not investigated as this peak is too susceptible towards side reactions. Therefore, going forward the reaction in Equation 26 is investigated.

$$NaFe^{3+}[Fe^{2+}(CN)_6] + e^- \rightleftharpoons Na_2Fe^{2+}[Fe^{2+}(CN)_6]$$

Equation 26

To carry out the large amplitude potential step (LAPS) experiment the potential is first held at a position where no Faradic response is recorded, and the oxidation state of iron in our material corresponds to PB. The main benefit of suing the LAPS method over the more conventional smaller steps is that during the smaller potential step any changes in the spectroscopic response are hard to determine. This is demonstrated in 3.2.5. From the voltammogram of FeHCF in 2 M $NaNO_3$ at pH 2 a holding potential (E_1) of 0.5 V is chosen for the reduction process. At this potential half of the sodium from within the FeHCF structure should have been deintercalated. Then to investigate the intercalation process a potential lower than our E_1 known as E_2 for is held for a period of time, long enough to see changes in the spectroscopic response. After which returning to E_1 and holding at this potential before jumping to a lower E_2 value as described in section 2.3.4. The E_1 and E_2 selected for the measurements in Na^+ and K^+ electrolyte is shown in **Table 14**. By using this method, we can study the effect that applying a greater magnitude of driving force (a larger potential step) has on the (de)intercalation process. Similarly, by selecting E_1 = -0.1 V (Na^+) and E_1 = 0.0 V (K^+) the deintercalation process can be studied.

Table 14 showing the potentials used for the large amplitude potential step experiments

Electrolyte	Process	E_1 *vs.* SCE / V	E_2 *vs.* SCE / V
2 M $NaNO_3$ at pH 2	Intercalation/ Reduction	0.5	0.4/0.3/0.2/0.0/-0.1
	Deintercalation/Oxidation	-0.1	0.1/0.2/0.3/0.4/0.5
2 M KNO_3 at pH 2	Intercalation/ Reduction	0.5	0.4/0.3/0.2/0.1/-0.1
	Deintercalation/Oxidation	0.0	0.1/0.3/0.5

The time frame of the potential holds, and the magnitude of the jump was dictated somewhat by the *in situ* EDE experiments. To see notable changes in the spectroscopic response larger jumps in potential where needed and these had to be held for a longer time.

The chronoamperometric response for the application of intercalation E_2 potentials *vs.* SCE from the E_1 value of 0.5 V for FeHCF in Na^+ is given in Figure 44 and those for the deintercalation (from E_1 = -0.1 V) in Figure 45. As anticipated, the magnitude of the current flowing increases as the of ΔE increases.

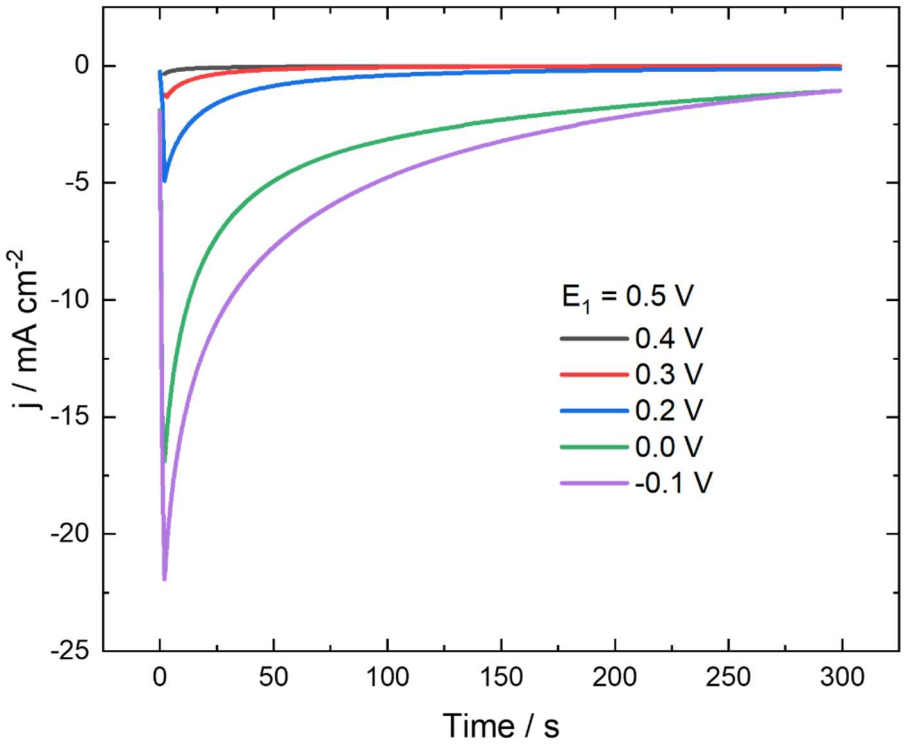

Figure 44 Chronoamperometric response for the large-amplitude potential step voltammetry for the intercalation of Na^+ ions. Showing the applied potential E_2 from the E_1 potential of 0.5 V *vs.* SCE.

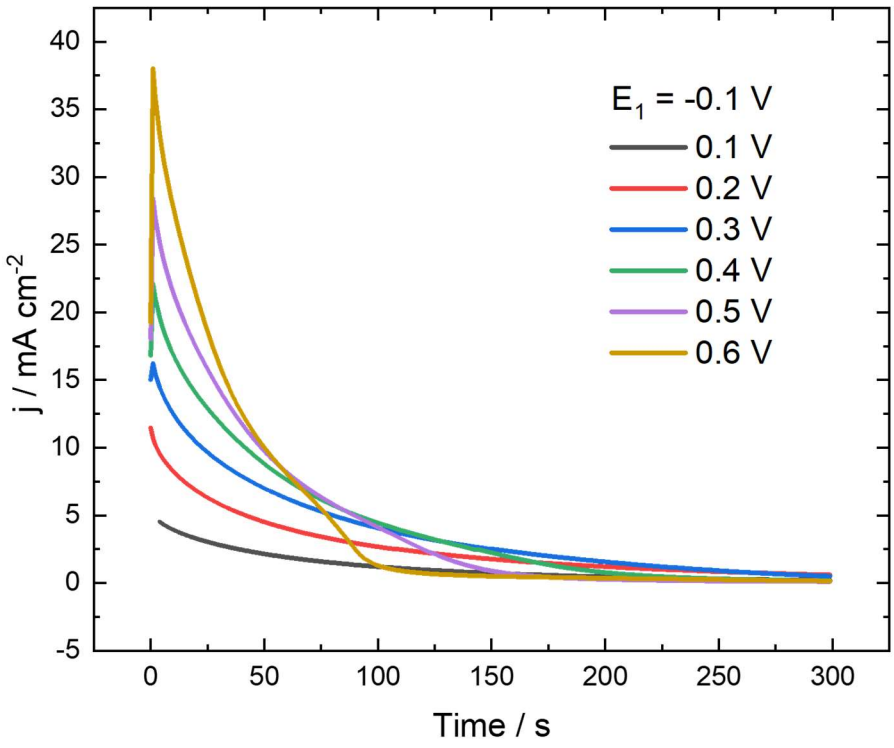

Figure 45 Chronoamperometric response for the large-amplitude potential step voltammetry for the deintercalation of Na^+ ions. Showing the applied potential ,E_2, from the E_1 potential of -0.1 V *vs.* SCE.

3.2.2.1 Cottrell analyses of LAPS *in situ* EDE experiment for FeHCF electrodes in Na^+ and K^+ ion electrolyte

The standard analytical approach for this experiment relies on the relationship between the current density, j, and time as shown in the Cottrell equation. (Equation 27)

$$\mathrm{j} = k\mathrm{t}^{-\frac{1}{2}}$$

Equation 27

Where:

$$k = \frac{\mathrm{nFC_0D_j^{\frac{1}{2}}}}{\pi^{\frac{1}{2}}}$$

Equation 28

Here, n is the number of electrons transferred (assumed 1); F is Faraday's constant; C_0 the initial concentration of electrolyte (2 M) and D_j the diffusion coefficient of the cation. Corresponding

plots of j *vs.* $t^{-\frac{1}{2}}$ should yield a linear relationship with a gradient equal to k, as defined in Equation 28.

The result of the Cottrell analysis on the chronoamperometric response for the intercalation of Na^+ into the FeHCF lattice is given in Figure 46 and the deintercalation of Na^+ in Figure 47.

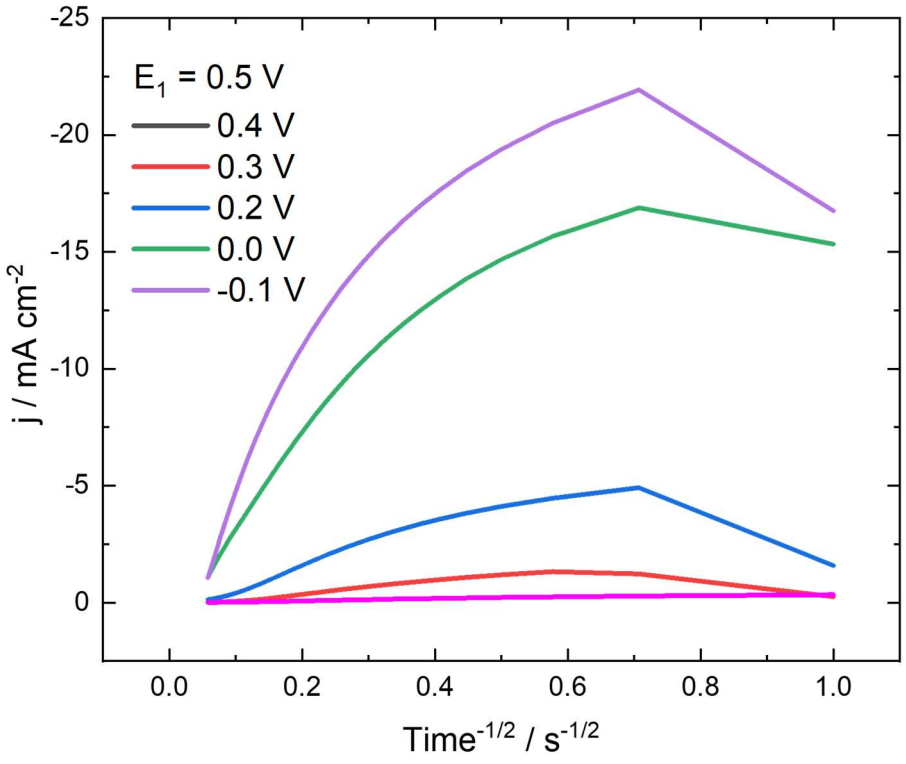

Figure 46 Cottrell analysis of the chronoamperometric response for the intercalation of Na^+ ions into the FeHCF lattice, from Figure 44.

As seen in Figure 46 there is an initial period where the magnitude of the current density increases linearly before decreasing. This increase lasts for approximately 3 seconds and is attributed to the double layer charging of the electrode and/or the change in conductivity of the FeHCF particles that accompany the transition of PB (an insulator) to PW (a conductor) and is therefore removed in the future data analysis. After the double layer charging, the current density *vs.* time is exponential throughout the rest of the experiment time. This suggests that the response does not correspond to linear diffusion. i.e., non-Cottrell based diffusion. Thus, a non-linear diffusion (NLD) model for these materials should be applied.

Figure 47 shows the corresponding result of the Cottrell analysis for the deintercalation of Na^+ from the FeHCF lattice for each E_2 potential applied from the E_1 of -0.1 V *vs.* SCE. Also, in agreement with the intercalation process, a non-linear response is observed for the deintercalation process and a NLD diffusion model used for further analysis.

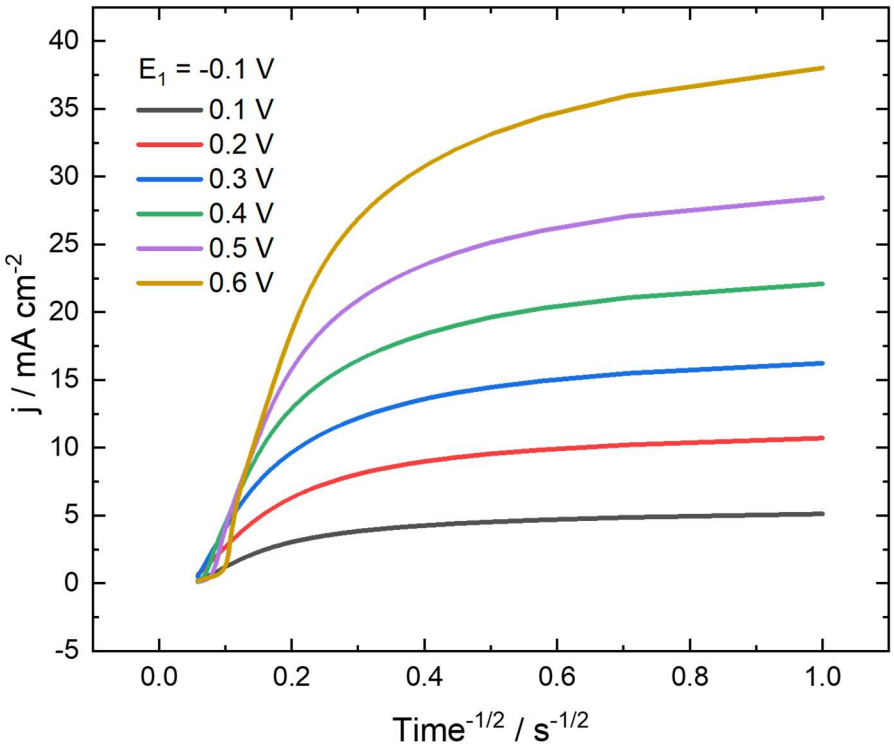

Figure 47 Cottrell analysis of the chronoamperometric response for the deintercalation of Na^+ ions into the FeHCF lattice, from Figure 45.

In Figure 48 the result of the LAPS experiments for K^+ intercalation into the FeHCF lattice from an E_1 of 0.5 V applying reduction potential *vs.* SCE is shown. With Figure 49 showing the result of the LAPS experiment for the deintercalation of K^+ form the FeHCF lattice by applying oxidation E_2 potentials from an E_1 of 0.0 V *vs.* SCE. Once again for the (de)intercalation of K^+ the expected effect of greater current density for a larger ΔE is observed.

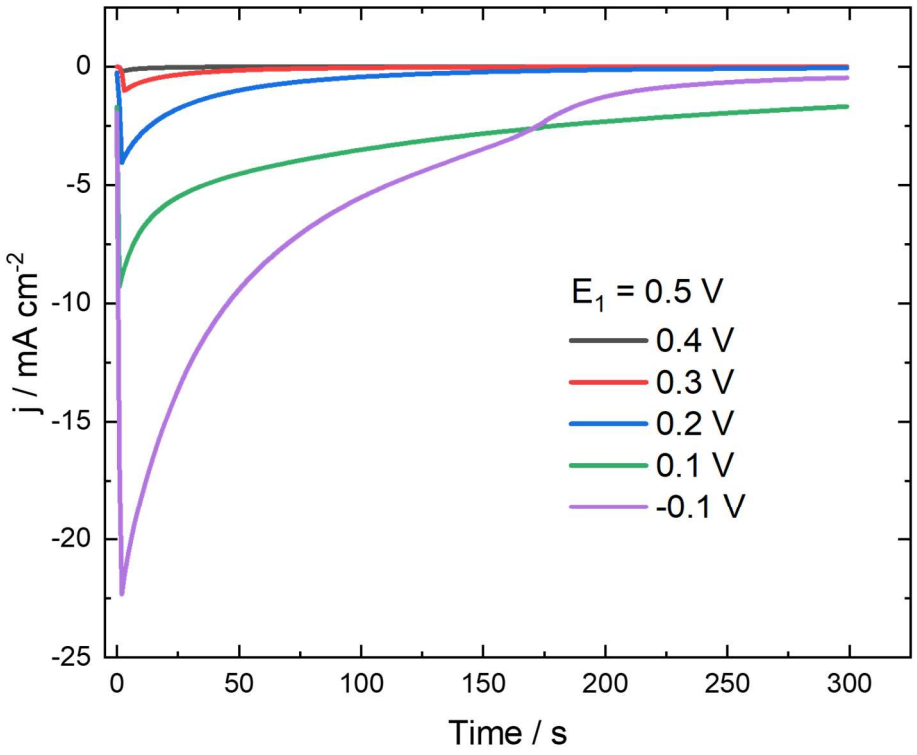

Figure 48 Chronoamperometric response for the large-amplitude potential step voltammetry for the intercalation of K^+ ions into the FeHCF lattice. Showing the applied potential (E_2) from the E_1 potential of 0.5 V *vs.* SCE.

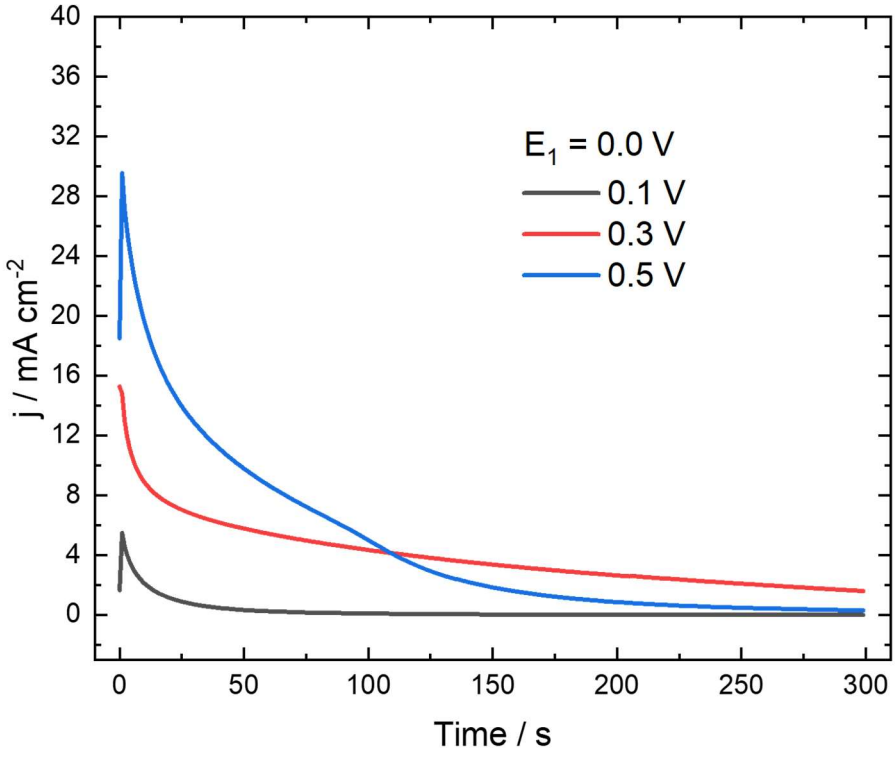

Figure 49 Chronoamperometric response for the large-amplitude potential step voltammetry for the deintercalation of K^+ ions from the FeHCF lattice. Showing the applied potential (E_2) from the E_1 potential of 0.0 V *vs.* SCE.

The Cottrell analysis was also performed on the LASP responses for the (de)intercalation of K^+ ion. Figure 50 shows the result of the Cottrell analysis for the intercalation of K^+ ions into the FeHCF lattice for the different E_2 potentials from the E_1 value of 0.5 V *vs.* SCE. With Figure 51 the results of the Cottrell analysis on the LAPS experiment for the deintercalation of K^+ ions for each E_2 potential from the E_1 value of 0.0 V *vs.* SCE.

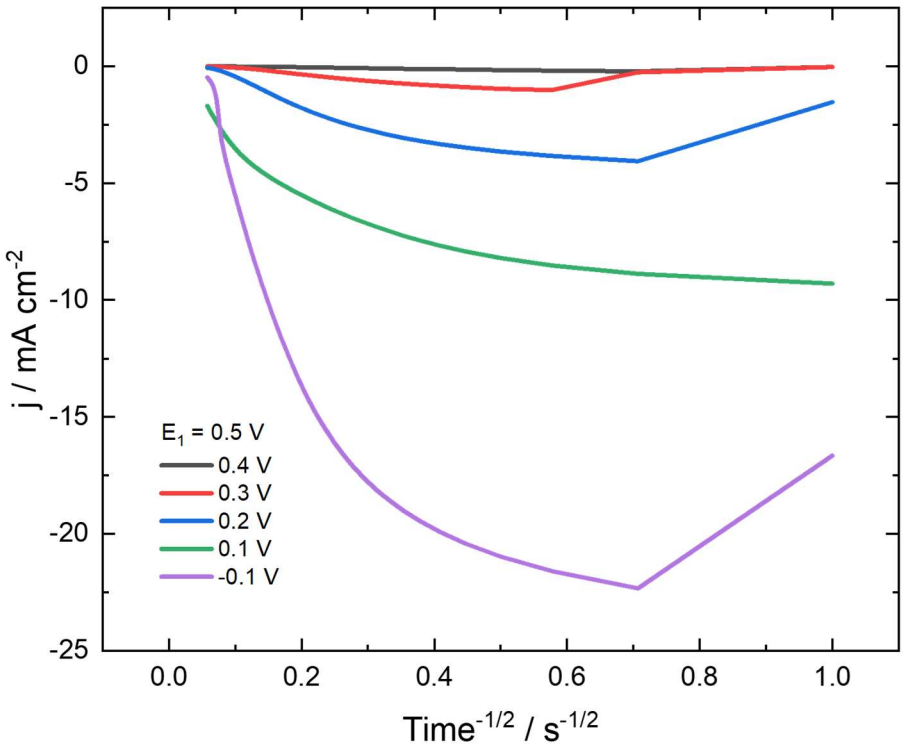

Figure 50 Cottrell analysis of the chronoamperometric response for the intercalation of K^+ ions into the FeHCF lattice, from Figure 48.

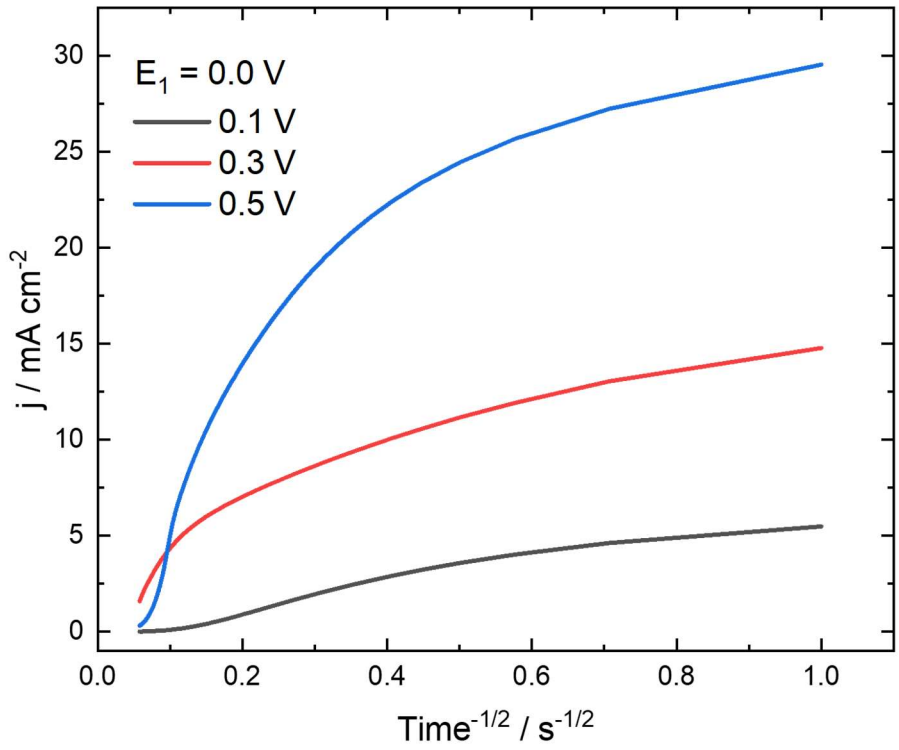

Figure 51 Cottrell analysis of the chronoamperometric response for the deintercalation of K^+ ions into the FeHCF lattice, from Figure 49.

As in the case of Na^+ intercalation, the first 3 s of K^+ intercalation (Figure 50), are dominated by double layer charging and/or the insulator (PB) to conductor (PW) transition. Whilst for K^+ deintercalation the Cottrell plot is smooth and follows an exponential throughout (Figure 51), in agreement with the Na^+ data.

Across all four LAPS experiments a non-Cottrell response is observed for the diffusion of cations. We therefore shall explore other methods to derive a diffusion coefficient for these data sets.

3.2.2.2 Alternate diffusion coefficient analysis

The diffusion coefficient of both Na^+ and K^+ ions for these systems, can also be determined by analysis of the chronoamperometric response using, Equation 29.

$$\ln(\mathrm{i}) = ln\left(\frac{2\mathrm{nFAD\Delta C}}{h}\right) - \left(\frac{\pi^2 \mathrm{D}}{4\mathrm{h}^2}\right)\mathrm{t}$$

Equation 29

Where i is the current, A. n is number of electrons involved in the redox reaction, in our case 1. F Faradays constant, 96485 C mol^{-1}. A the geometric area of the electrode, 3.8 cm^2. D the diffusion coefficient, cm^2 s^{-1}. C the concentration of electrolyte and h the thickness of the electrode. Therefore, by taking the ln of the current and plotting this as a function of time there should be a linear region in which the gradient is proportional to $\left(\frac{\pi^2 D}{4h^2}\right)$. This linear region should be present beyond a certain time according to Equation 30. [120,121]

$$t \gg \frac{h^2}{\pi^2 D}$$

Equation 30

To estimate this time the diffusion coefficient from the cyclic voltammetry is used. Based on the SEM images, given in 2.2.6, the average thickness of the electrode material is around 150 µm. Therefore, using Equation 30 we calculate that for t ≥ 150 s, Equation 29 is appliable.

This analysis of the LAPS experiments for Na^+ ion (de)intercalation using Equation 29 is plotted in Figure 52 (intercalation) and Figure 53 (deintercalation).

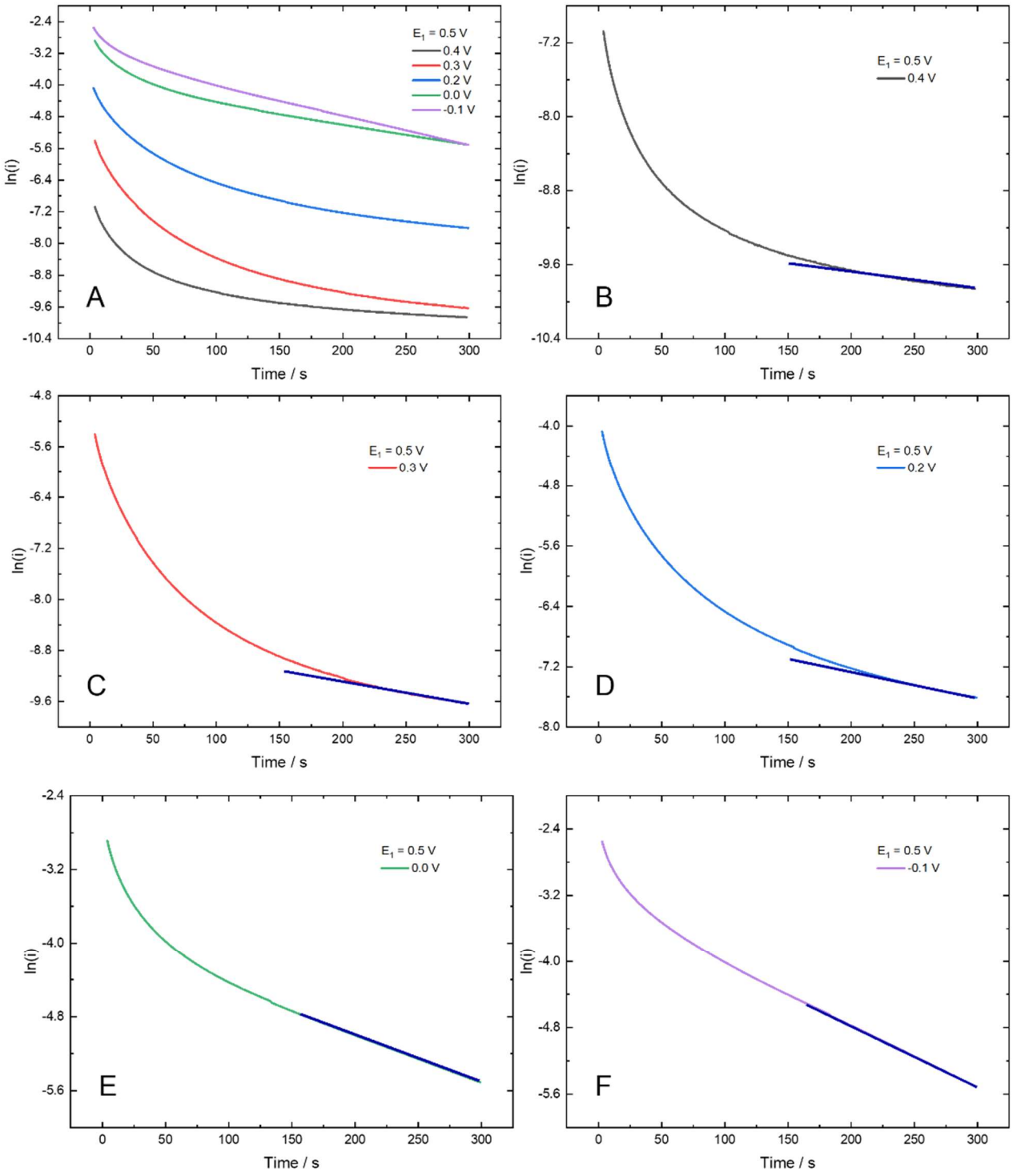

Figure 52 Potential dependent diffusion coefficient for the intercalation of Na^+ ions into the FeHCF lattice. Showing A) the ln(i) *vs.* t plots for all E_2 values applied from E_1 = 0.5 V B-F) the individual plots for each E_2 and the linear region, all potentials are *vs.* SCE.

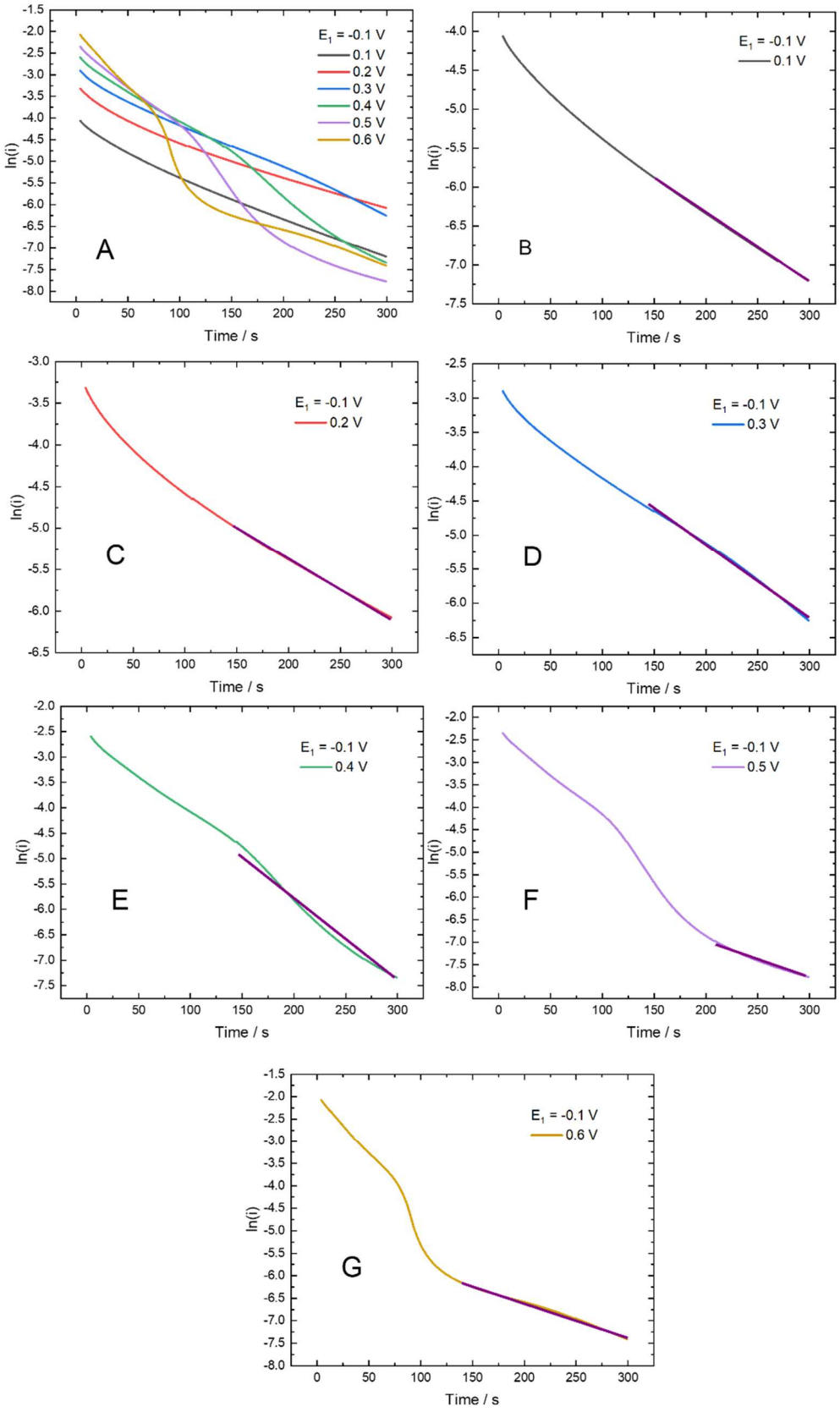

Figure 53 Potential dependent diffusion coefficient for the deintercalation of Na^+ ions from the FeHCF lattice. Showing A) the ln(i) *vs.* t plots for all E_2 values applied from E_1 = -0.1 V B-G) the individual plots for each E_2 and the linear region, all potentials are *vs.* SCE.

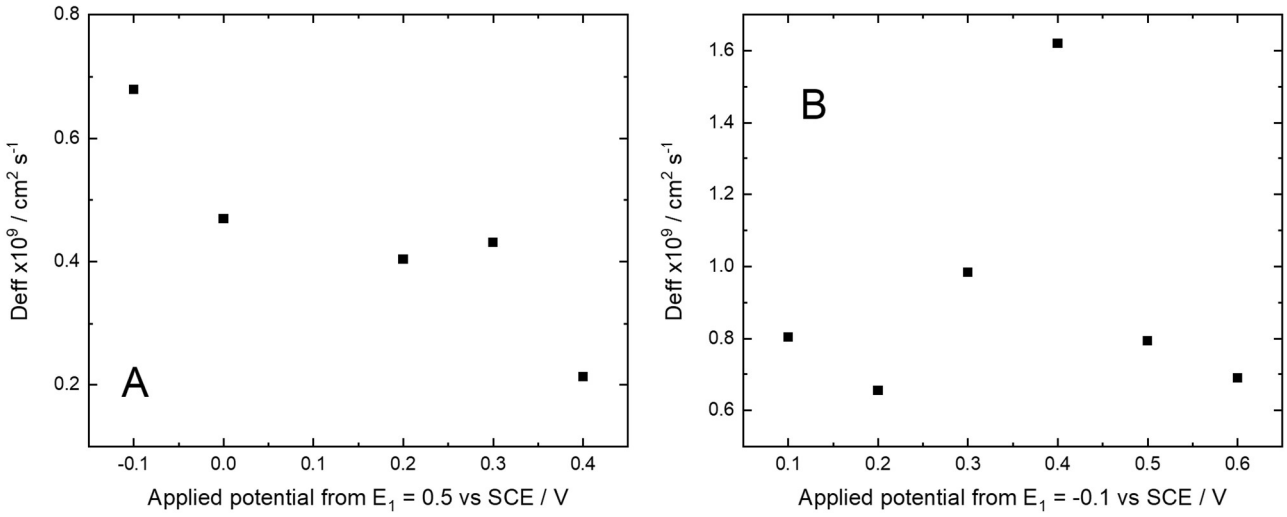

Figure 54 Comparison of the calculated diffusion coefficients from the linear region in the alternative diffusion coefficient analysis for the LAPS experiments on A) Intercalation of Na^+ cation and B) deintercalation of Na^+ cation.

Figure 54 shows the potential (E_2) dependence of the diffusion coefficient extracted from the data for the intercalation (Figure 54 A) and the deintercalation (Figure 54 B) process. In both cases a diffusion coefficient of the order of 10^{-9} cm^2 s^{-1} is calculated. This order of magnitude is in good agreement with literature sources that record values in the range of 10^{-9} to 10^{-12}.[122–124] At this longer time domain of above 150 s the process should be largely diffusion controlled. As observed for the cyclic voltammetry the diffusion coefficient obtained for the deintercalation are larger than the intercalation.

This same alternative diffusion coefficient analysis is carried out for the LAPS experiments of the (de)intercalation of K^+ ions, Figure 48 and Figure 49, for a FeHCF electrode. The results are given in Figure 55 (intercalation) and Figure 56 (deintercalation).

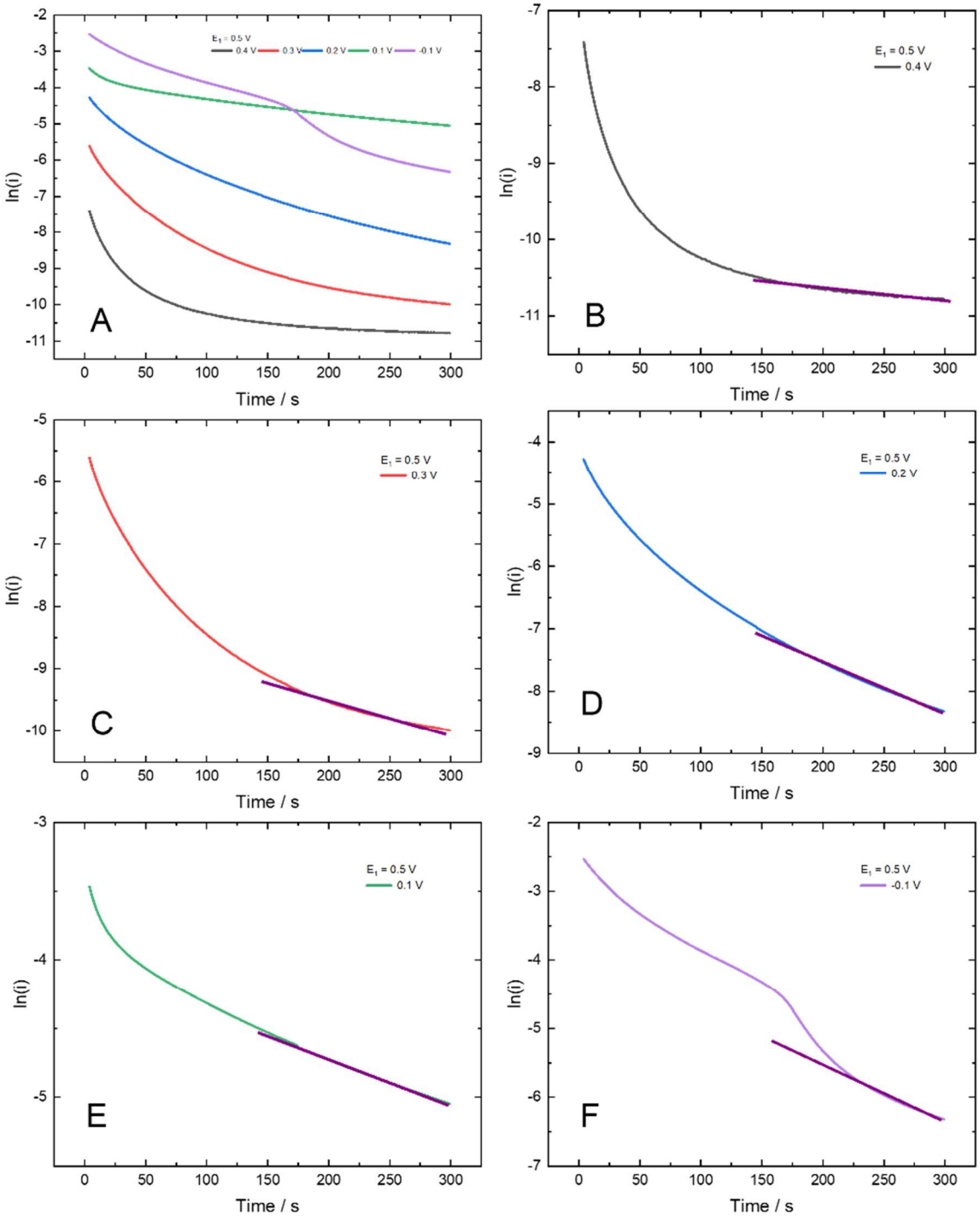

Figure 55 Potential dependent diffusion coefficient for the intercalation of K^+ ions into the FeHCF lattice. Showing A) the ln(i) *vs.* t plots for all E_2 values applied from E_1 = 0.5 V B-F) the individual plots for each E_2 and the linear region, all potentials are *vs.* SCE.

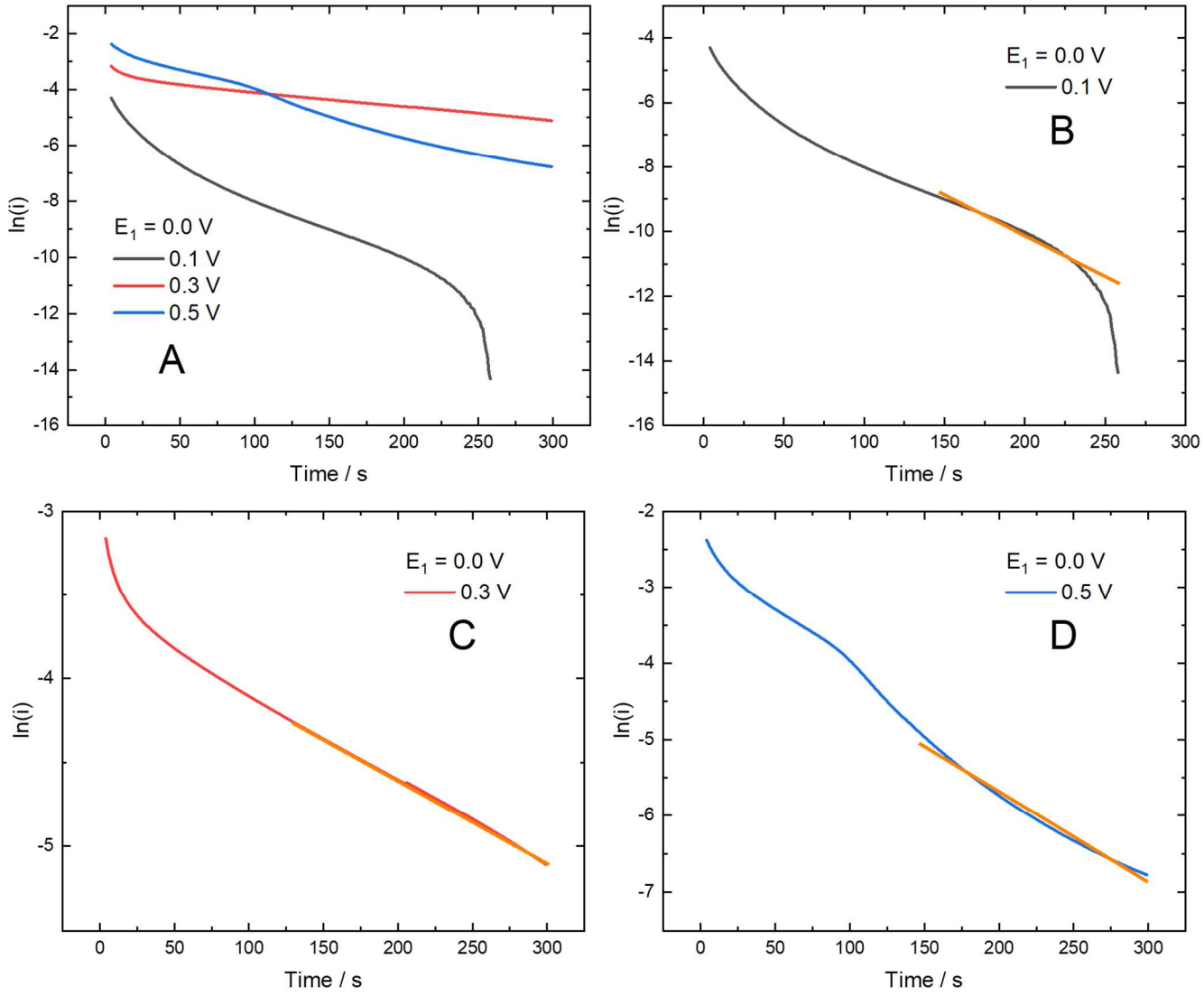

Figure 56 Thickness dependent diffusion coefficient for the deintercalation of K^+ ions into the FeHCF lattice. Showing A) the ln(i) *vs.* t plots for all E_2 values applied from E_1 = 0.0 V B-C) the individual plots for each E_2 and the linear region E) comparison of the derived diffusion coefficients from the linear regions, all potentials are *vs.* SCE.

As with the diffusion coefficients calculated for Na^+ ions with an FeHCF electrode the calculated diffusion coefficients for K^+ ions are also potential dependent, shown in Figure 57.

With Figure 57 A showing the diffusion coefficients for the intercalation of K^+ ions and Figure 57 B the diffusion coefficients for the deintercalation of K^+ ions, as a function of the applied E_2 potential. This is showing that the rate of diffusion is a function of the potential, more literally the driving force. It would be expected that diffusion would happen as a function of $t^{-1/2}$. However, due to the NLD seen in these systems this is not the case.

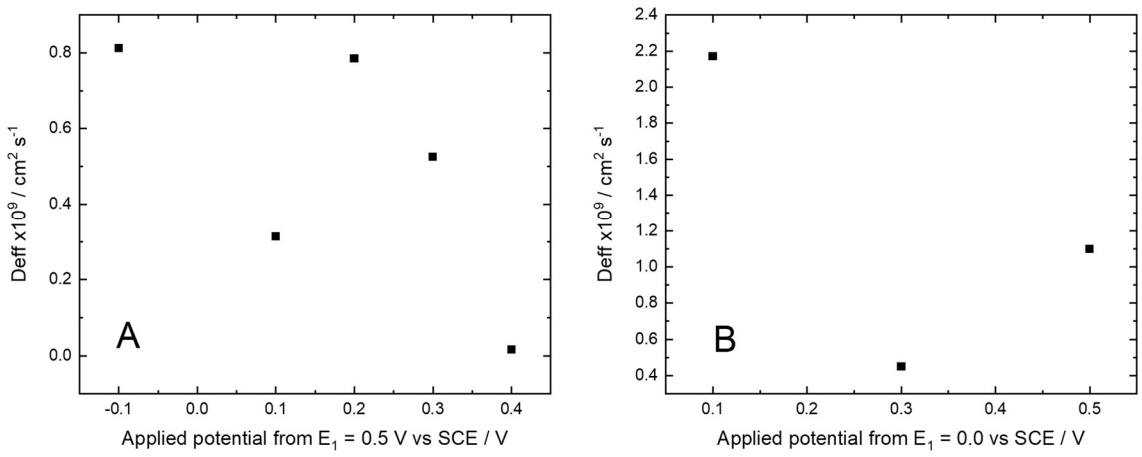

Figure 57 Comparison of the calculated diffusion coefficients from the linear region in the alternative diffusion coefficient analysis for the LAPS experiments on A) Intercalation of K^+ cation and B) deintercalation of K^+ cation.

The values calculated for the diffusion coefficient in this section are for the longer time frames, where diffusion is the dominating process of the electrochemical reaction. Now we shall look to the resulting charge from the LAPS experiments to obtain diffusion coefficients in the shorter time region.

3.2.3 Chronocoulometry

3.2.3.1 Integrated Cottrell equation

Another way to analyse the rate of diffusion for the (de)intercalation of Na/K ions into FeHCF electrodes is to look at the charge corresponding to the processes. By looking at the charge the shorter time effects that distort the current response are removed, as the current response in shorter time frames comes from the capacitive response. The charge is also more associated with the actual amount of intercalated cation.

To do this, we use the integrated Cottrell equation:[73]

$$\int \mathrm{i}\, dt = k \int \mathrm{t}^{-1/2}\, dt$$

Equation 31

Where k is as defined in Equation 28. By integrating the Cottrell equation with respect to time we yield the following equation:

$$\mathrm{Q} = 2k\mathrm{t}^{\frac{1}{2}}$$

Equation 32

We can now produce plots of Q *vs.* $\mathrm{t}^{\frac{1}{2}}$. To gain an even more understandable plot squaring the integrated Cottrell equation leads to:

$$\mathrm{Q}^2 = 4k^2\mathrm{t}$$

Equation 33

Where the time axis is now linear leading to a much better comparison with the original current transients.

Plots of Q^2 *vs.* t should be linear as predicted by Equation 23. With a gradient of $4k^2$ which contains the diffusion coefficient of the cation for the shorter time frame.

Below in Figure 58, the chronocoulometric response for the intercalation of Na^+ ion into the FeHCF lattice is given for each of the applied E_2 potentials from the E_1 of 0.5 V *vs.* SCE and the charge response for the deintercalation of Na^+ for each E_2 potential with an E_1 of -0.1 V *vs.* SCE given in Figure 59.

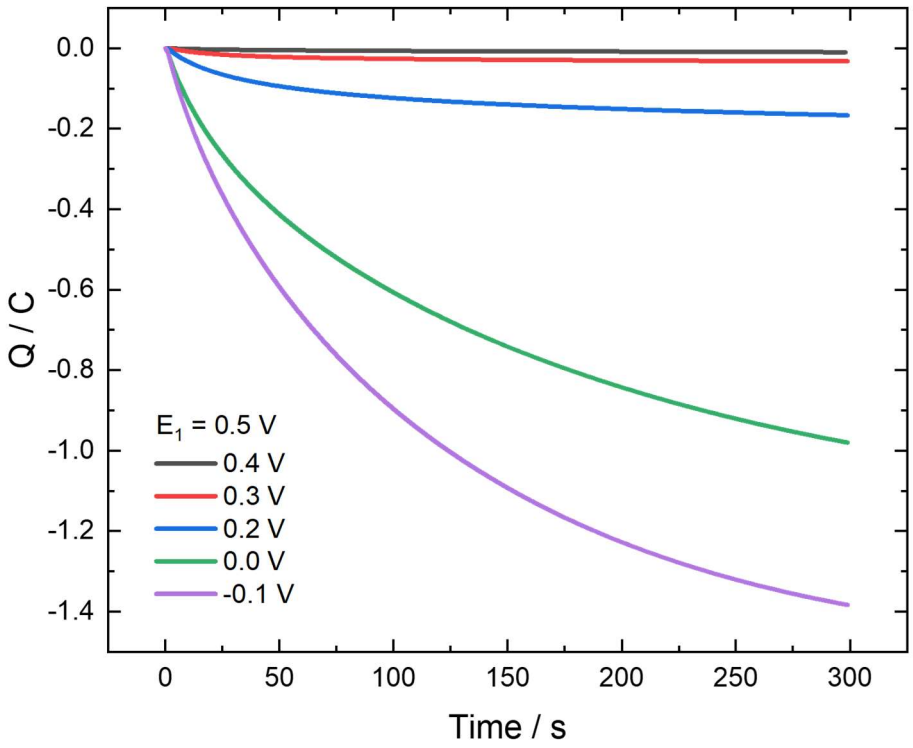

Figure 58 Chronocoulometric response for the large-amplitude potential step measurements for the intercalation of Na^+ ions. Showing the applied potential (E_2) from the E_1 potential of 0.5 V *vs.* SCE.

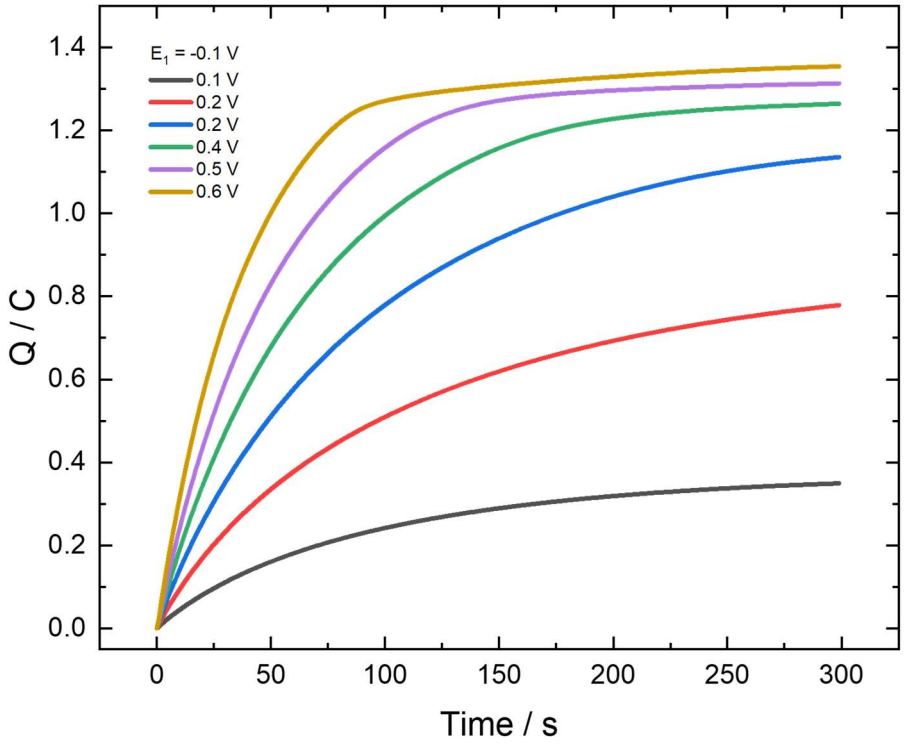

Figure 59 Chronocoulometric response for the large-amplitude potential step measurements for the deintercalation of Na^+ ions. Showing the applied potential (E_2) from the E_1 potential of -0.1 V *vs.* SCE.

Now we apply the integrated Cottrell analysis, Equation 23, to the charge response for the intercalation of Na^+ ions, Figure 60 and the charge response for the deintercalation of Na^+ ions, Figure 61.

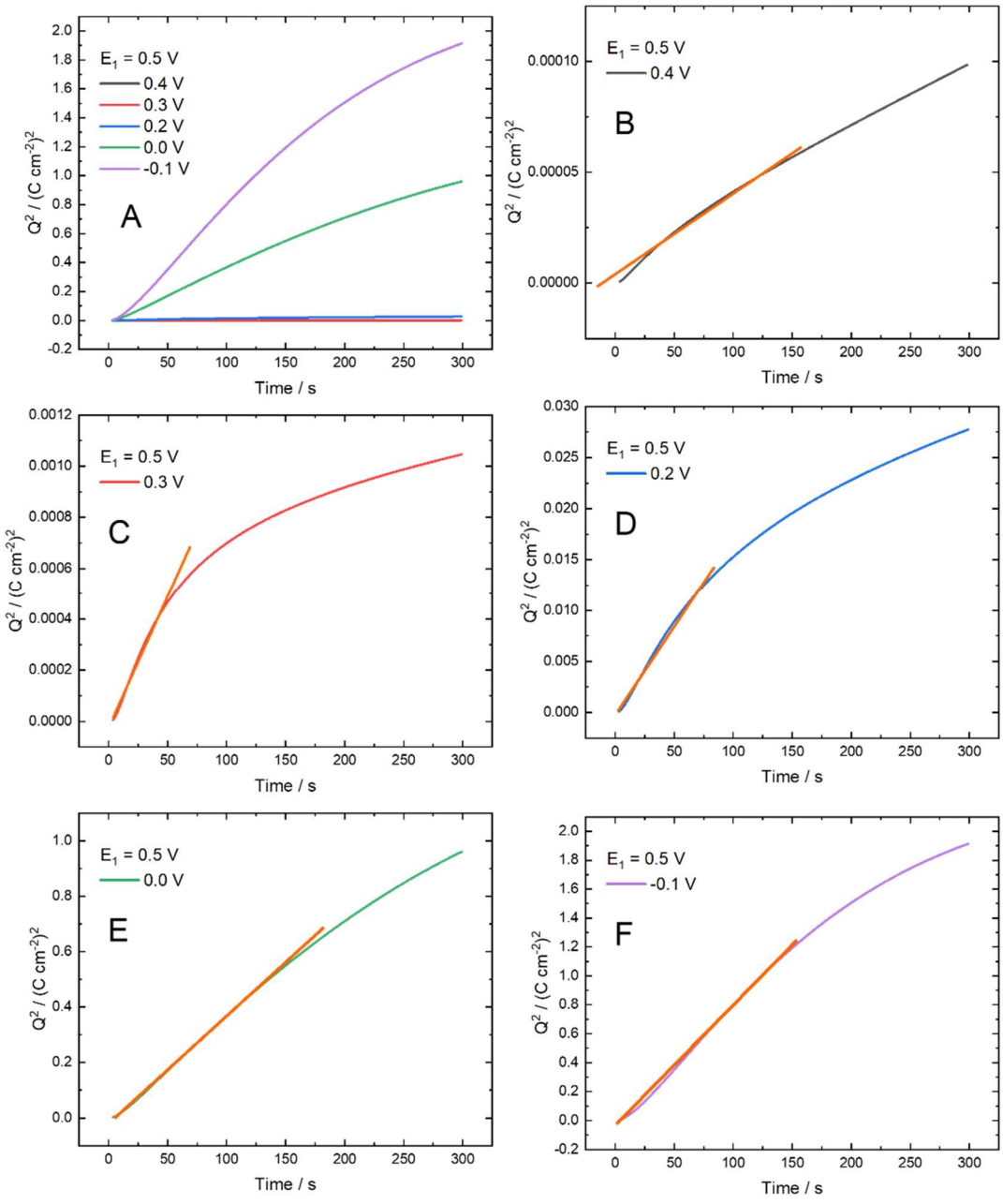

Figure 60 Integrated Cottrell analysis for diffusion coefficient for the intercalation of Na^+ ions into the FeHCF lattice. Showing A) the Q^2 *vs.* t plots for all E_2 values applied from E_1 = 0.5 V B-F) the individual plots for each E_2 and the linear region, all potentials are *vs.* SCE.

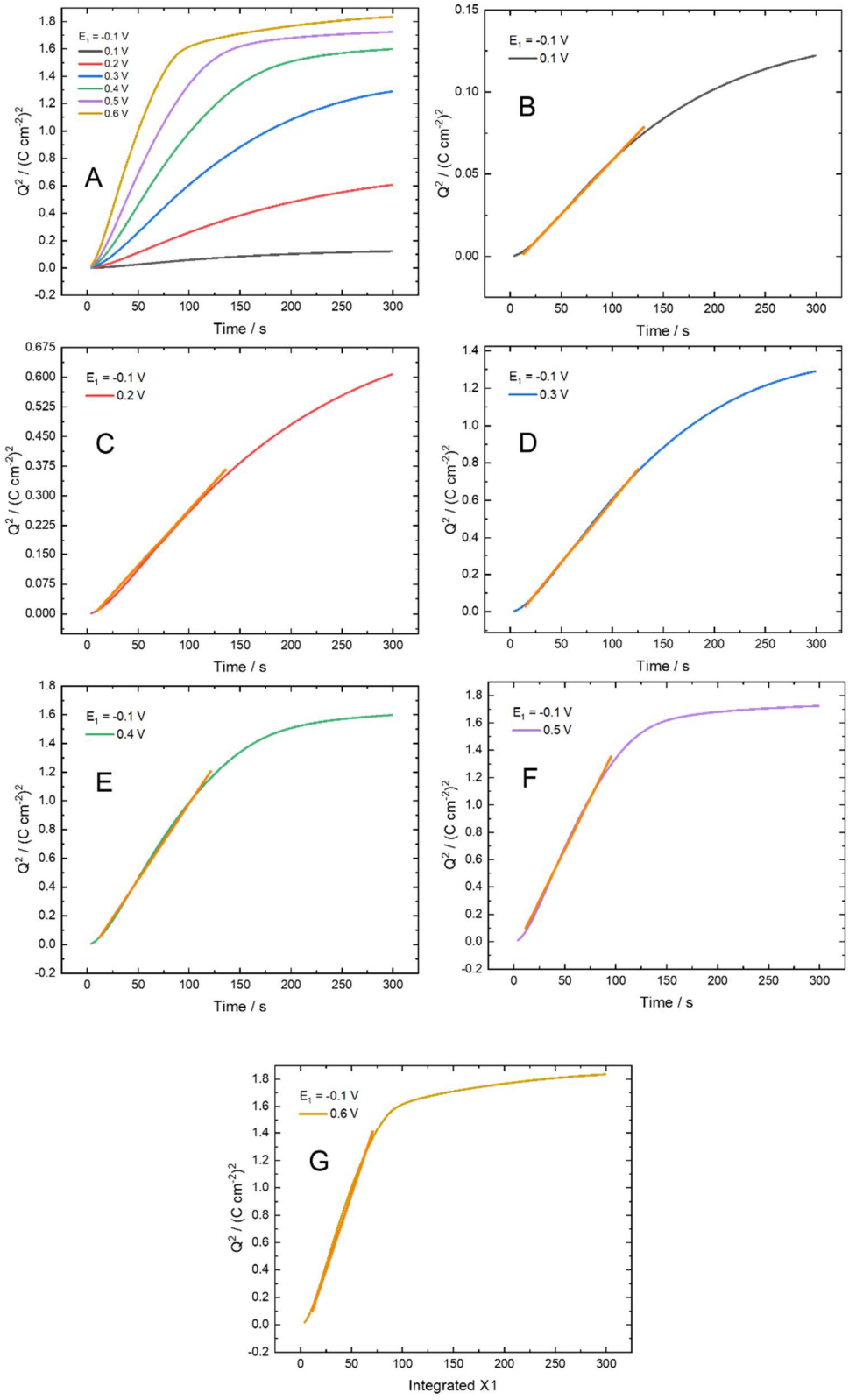

Figure 61 Integrated Cottrell analysis for diffusion coefficient for the deintercalation of Na^+ ions from the FeHCF lattice. Showing A) the Q^2 *vs.* t plots for all E_2 values applied from E_1 = -0.1 V B-G) the individual plots for each E_2 and the linear region H) comparison of the derived diffusion coefficients from the linear regions, all potentials are *vs.* SCE.

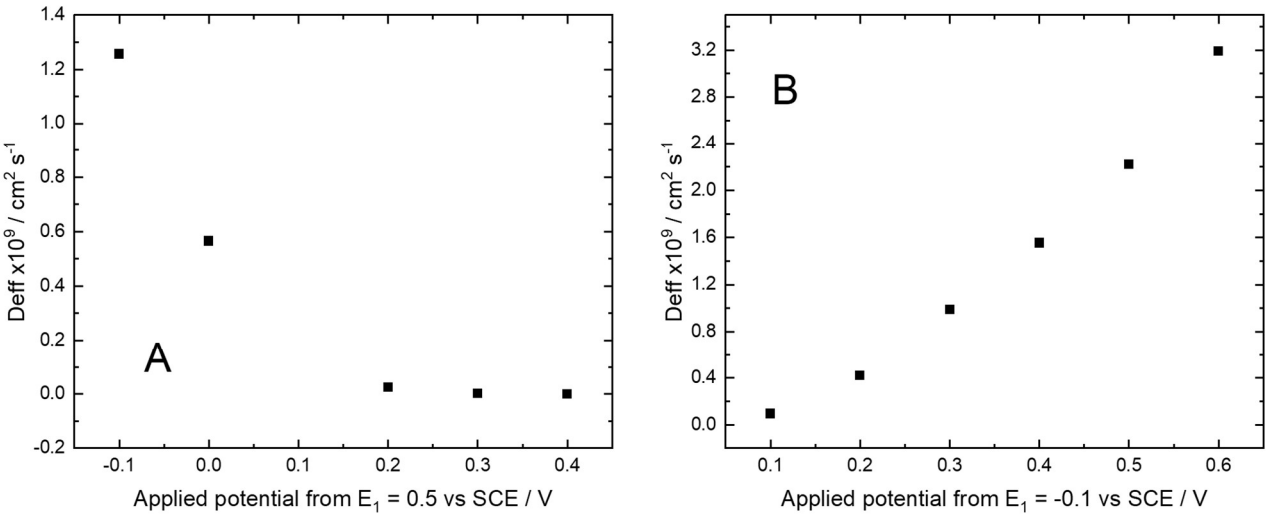

Figure 62 Comparison of the calculated diffusion coefficients from the linear region of the integrated Cottrell analysis of the LAPS experiments on A) Intercalation of Na^+ cation and B) deintercalation of Na^+ cation.

Looking at the results in Figure 60 and Figure 61, an initial linear region is seen when looking at the corresponding charges. This linear region as previously stated can lead to a diffusion coefficient for this initial period. Figure 62 shows the calculated diffusion coefficients, from the linear region, using the integrated Cottrell equation for the intercalation of Na^+ ions (Figure 62 A) and the deintercalation of Na^+ ions (Figure 62 B). From these plots as the magnitude of ΔE increases the value of D also increases. This suggests that the initial diffusion coefficient is proportional to the driving force applied. The faster the kinetics are driven the faster the cation diffuses into or out of the system. It is also worth noting that the calculated diffusion coefficients from the charge are of the same order of magnitude as the other previously calculated diffusion coefficients from the CV and alternative method.[125,126]

Figure 63 and Figure 64 record the corresponding charge for the LAPS experiment for the intercalation of K^+ ions and the deintercalation of K^+ ions into/ from the FeHCF lattice respectively.

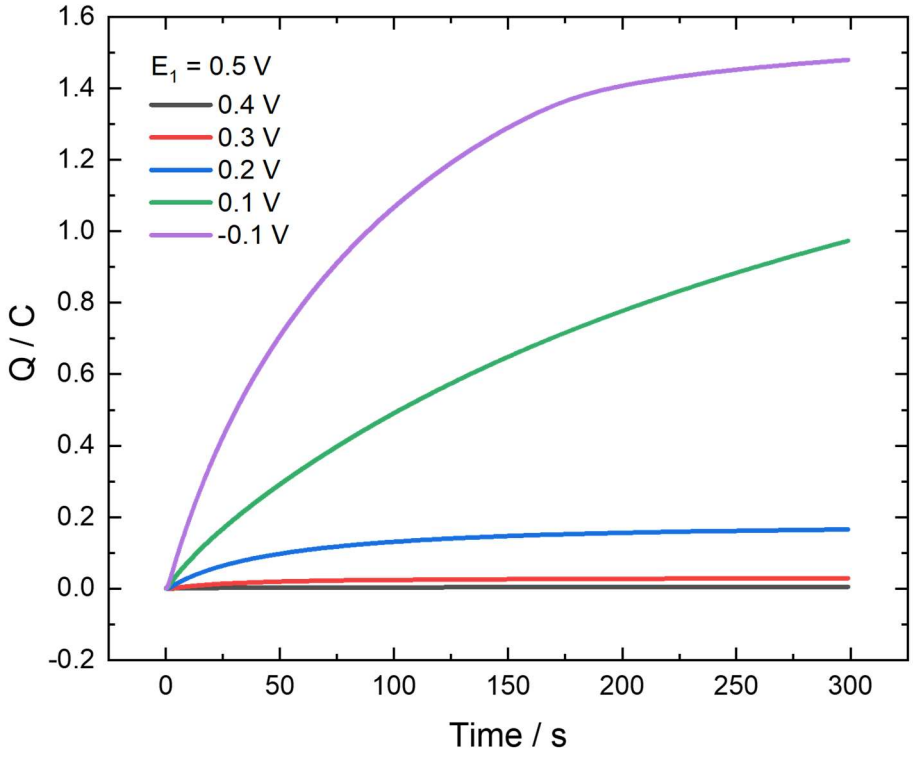

Figure 63 Chronocoulometry response for the large-amplitude potential step voltammetry for the intercalation of K^+ ions. Showing the applied potential (E_2) from the E_1 potential of 0.5 V *vs.* SCE.

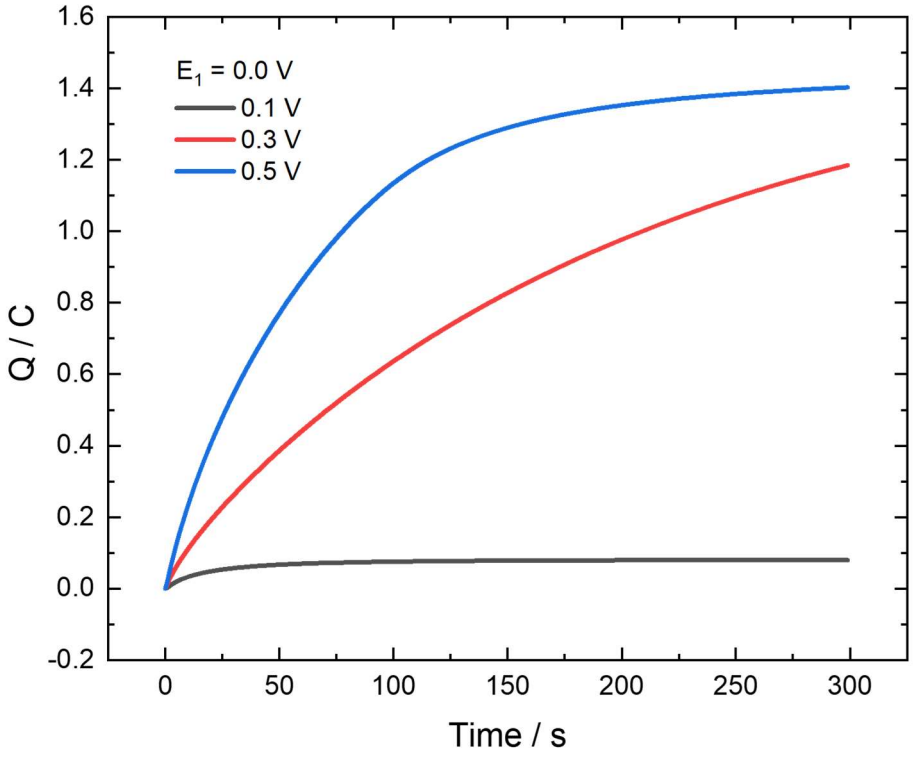

Figure 64 Chronocoulometry response for the large-amplitude potential step voltammetry for the deintercalation of K^+ ions. Showing the applied potential (E_2) from the E_1 potential of 0.0 V *vs.* SCE.

For both the results reported in Figure 63 and Figure 64 we carried out the same integrated Cottrell analysis, Equation 23 as done for Na^+ ion (de)intercalation for the (de)intercalation of K^+ ions from/to the FeHCF particles, shown in Figure 65 and Figure 66.

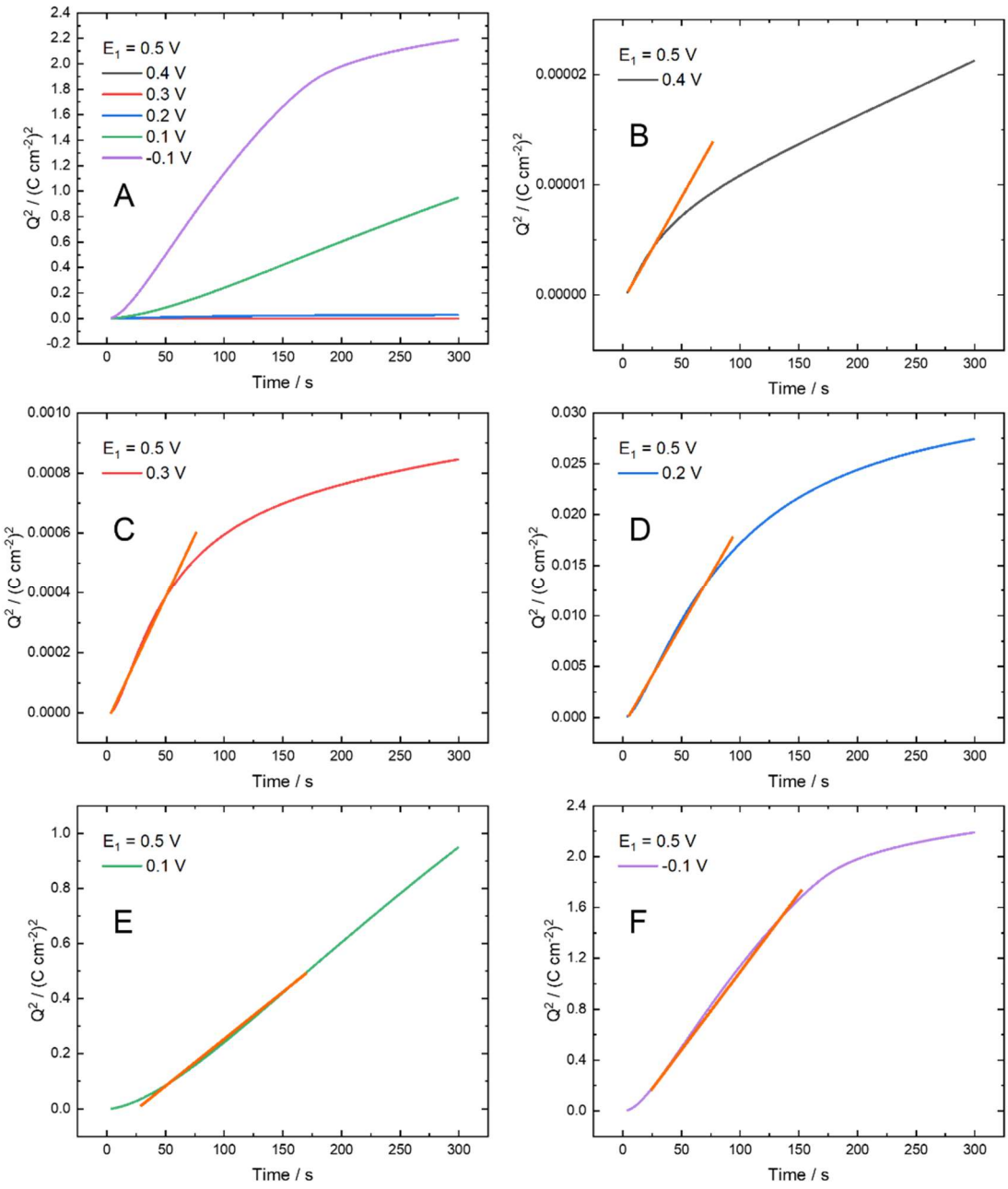

Figure 65 Integrated Cottrell analysis for diffusion coefficient for the intercalation of K^+ ions into the FeHCF lattice. Showing A) the Q^2 *vs.* t plots for all E_2 values applied from E_1 = 0.5 V B-F) the individual plots for each E_2 and the linear region, all potentials are *vs.* SCE.

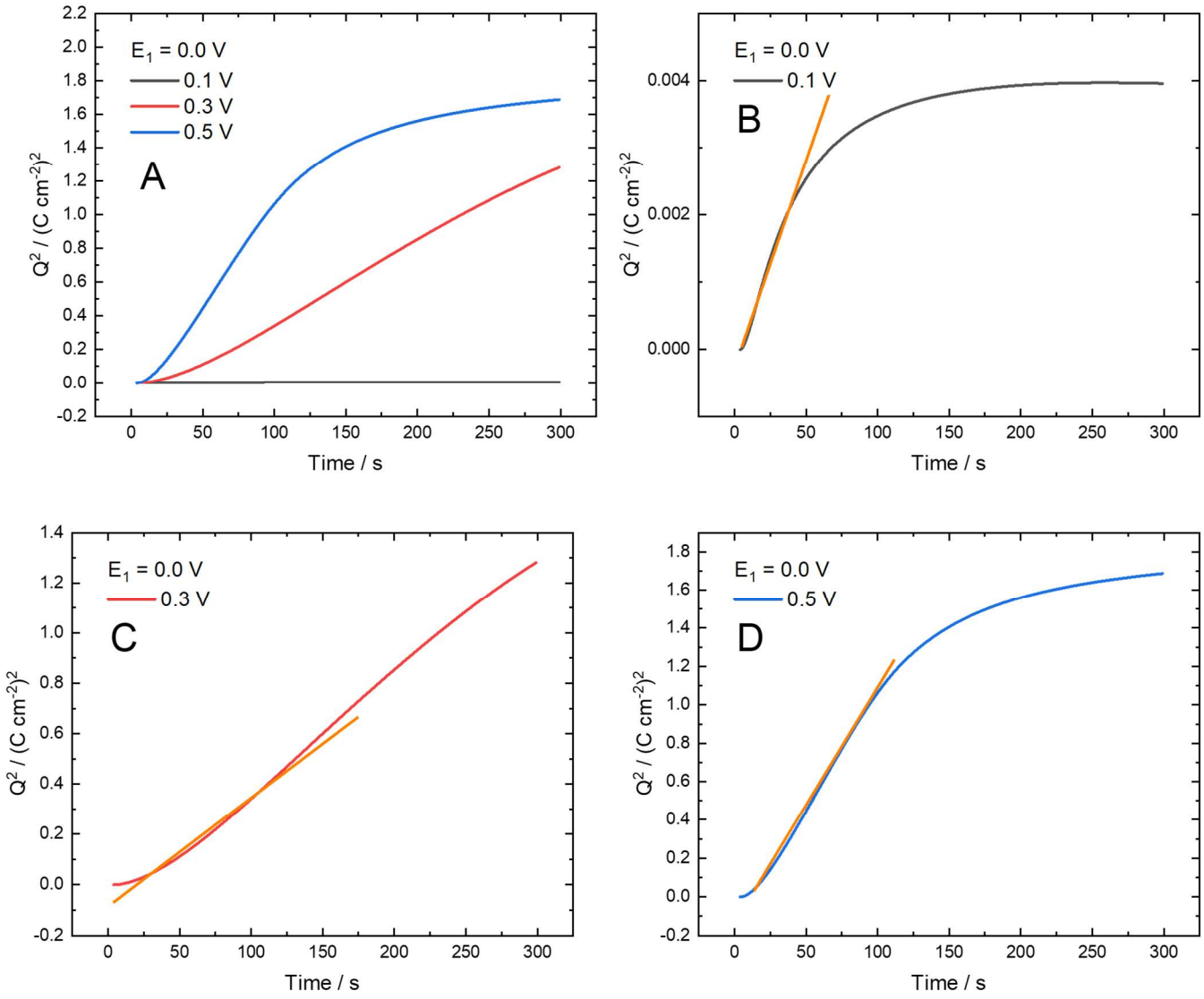

Figure 66 Integrated Cottrell analysis for diffusion coefficient for the intercalation of K^+ ions into the FeHCF lattice. Showing A) the Q^2 *vs.* t plots for all E_2 values applied from E_1 = 0.0 V B-D) the individual plots for each E_2 and the linear region, all potentials are *vs.* SCE.

Figure 67 shows the calculated diffusion coefficients, from the linear region, using the integrated Cottrell equation for the intercalation of K^+ ions (Figure 67 A) and the deintercalation of K^+ ions (Figure 67 B). Once again showing that the value of the diffusion coefficient is potential as seen for the (de)intercalation of Na^+ ions.

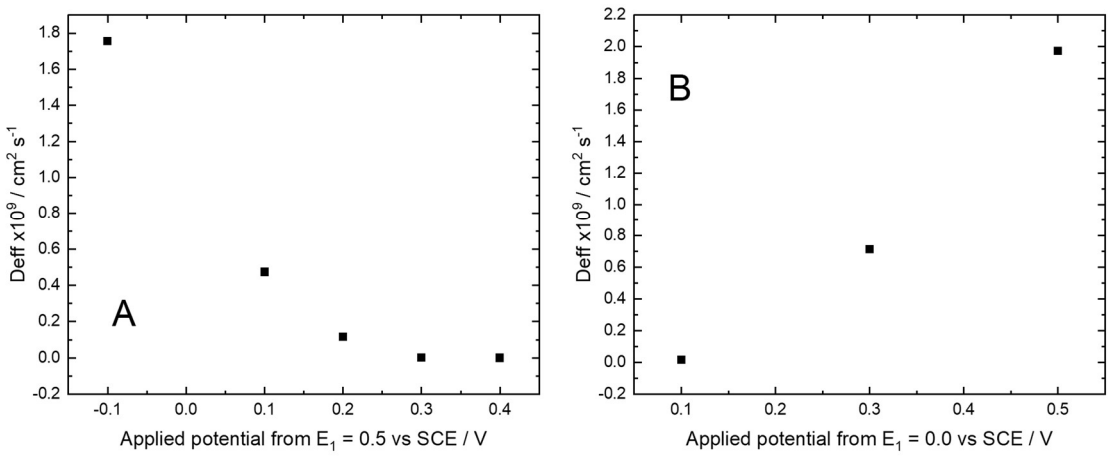

Figure 67 Comparison of the calculated diffusion coefficients from the linear region of the integrated Cottrell analysis of the LAPS experiments on A) Intercalation of K^+ ions and B) deintercalation of K^+ ions.

3.2.4 EDE results and kinetics

All the electrochemical results and analysis presented above contain contributions from the coupled ion and electron transport. To unmask the pure redox behaviour of the metal centres in FeHCF time resolved energy dispersive XAFS (EDE) was used.

The average data provides a measurement of the average oxidation state of the Fe in the electrode. An average oxidation state of $Fe_{ave}^{2.5+}$, should be present around 0.5 V and Fe_{ave}^{2+} at -0.1 V. To simplify the discussion, the $Fe_{ave}^{2.5+}$ will be referred to as the oxidised and the Fe_{ave}^{2+} the reduced.

3.2.4.1 Change in edge position as a function of time

The *in situ* EDE experiment carried out followed the same process as the LAPS experiments (section 3.2.2). A potential is applied at the E_1 value for either the reduction (intercalation) or oxidation (reduction). This is followed by a jump to the E_2 potential. Each potential is held for the same period. The time frame selected for each potential hold was dictated by the spectroscopic response. The E_1 potential had to be held long enough to see a return to the original edge position and the E_2 long enough to see a change in the edge position.

Repeating the potential applications and returning to the E_1 potential for a few cycles allows us to have a better idea of the history of the electrode and to see how repeatable the results are. When a new electrode is used for an *in situ* experiment a CV is run for 25 cycles at a scan rate of 100 mV

s^{-1}. This was done to condition the electrode to ensure the saturation of electrolyte within the electrode and to give the maximum capacity.

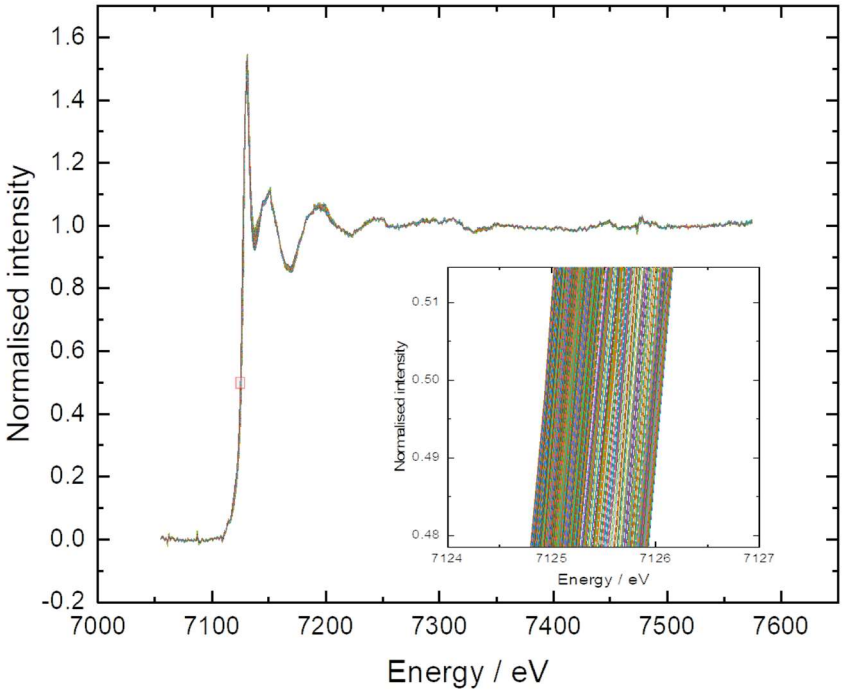

Figure 68 Example spectra from the *in situ* experiments for Na intercalation into FeHCF, showing a spectrum taken every 10 s. The insert shows the variation in edge position at the 0.5 normalised intensity for an experiment where E_1 = 0.5 V and E_2 = 0.0 V *vs.* SCE.

An example of the results from the *in situ* EDE experiments for FeHCF in Na^+ are given in Figure 68. Spectra are plotted for every 10 s whilst the E_2 potential was held for 300 s. The real time resolution of the experiment was 0.1 s per spectrum. To monitor the variation in edge position as a function of time the 0.5 intensity of the normalised spectrum was selected. In theory an approximate change in 1 eV should be seen between two different oxidation states.[127] For Fe^{3+} and Fe^{2+} literature sources state the difference should be in the region of 1.3 eV to 1.5 eV.[128]

The edge position was plotted as a function of time for the potential steps from 0.5 V and is shown in Figure 69 A and from -0.1 V in Figure 69 B. It is expected that when applying the E_1 potential from the different E_2 potentials (the first 300 s) that we would reach the same value for the edge position. However, variation in the focus on the sample due to movement of the electrode or thickness of the electrolyte means that returning to a defined point each time does not always occur. In agreement with the LAPS data as the magnitude of the applied potential from

the E_1 potential increasing the amount of change in edge potential increases (the final 300 s). It is only the data between 300 s and 600 s that is analysed going forward as the time where t < 300 s is a precursor step.

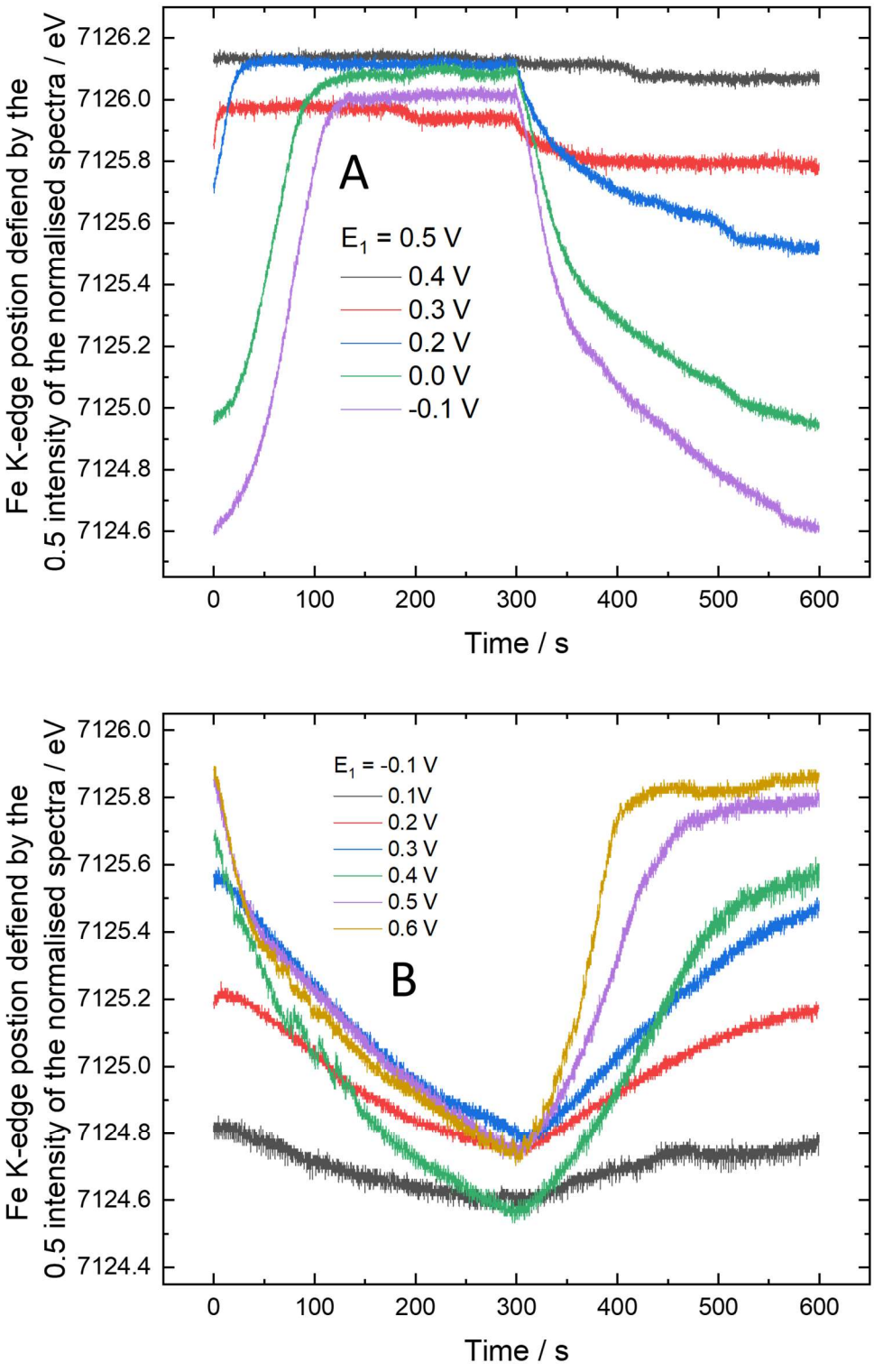

Figure 69 Change in edge position as a function of time from the *in situ* EDE experiments A) intercalation of Na^+ ions into FeHCF where E_1 = 0.5 V and the E_2 values are given in the figure, *vs.* SCE B) deintercalation of Na^+ ions from FeHCF where E_1 = -0.1 V and the E_2 values are given in the figure, *vs.* SCE. Each E is held for 300 s.

Figure 70 shows the Fe K-edge position defined by the 0.5 intensity of the normalised data is given for K+ ions for the during the potential step experiments. Figure 70 A shows the reduction of Fe-N (intercalation of K^+ ions) with an E_1 value of 0.5 V *vs.* SCE and E_2 values of 0.4/0.3/0.2/0.1/-0.1 V *vs.* SCE and Figure 70 B the oxidation of Fe-N (deintercalation of K^+ ions) with an E_1 of 0.0 V *vs.* SCE and E_2 potentials of 0.1/0.3/0.5 V *vs.* SCE. Owing to problems with the experiment at the beamtime, only three E_2 potential could be investigated for the oxidation in the available time.

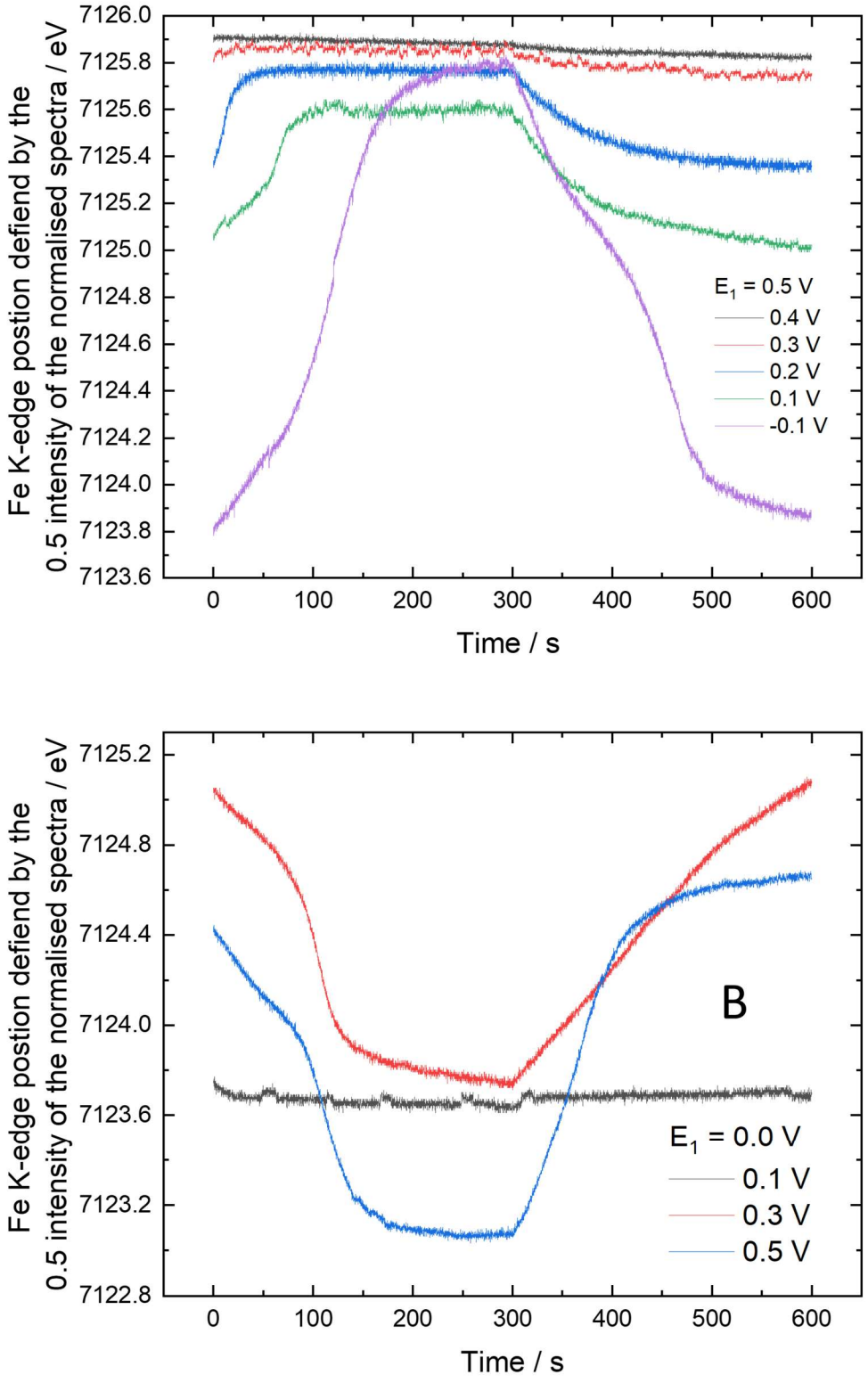

Figure 70 Graphs showing the change in edge position as a function of time from the *in situ* EDE experiments A) intercalation of K^+ ions into FeHCF where E_1 = 0.5 V and the E_2 values are given in the figure, *vs.* SCE B) deintercalation of K^+ ions from FeHCF where E_1 = 0.0 V and the E_2 values are given in the figure, *vs.* SCE. Each E is held for 300 s.

Across the results presented in Figure 69 and Figure 70, an average change in edge position of around 1.3 – 1.5 eV was observed. Most importantly these results are reversible. Each time the E_1 potential is applied we return to a similar value within error of the experimental set-up. Furthermore, the data presented is at least the third cycle of potential applications with a minimum of three successful repeats. Each of the data set above represents an averaging of three different experiments. Due to the nature of the *in situ* experiments repeating experiments is complex and these experiments have a low reproducibility. However, we were able to get at least three repeats of each experiment within reasonable limits of each other and therefore able to take an average. Reasonable limits were defined as not having an edge shift greater that 4 eV as this would be beyond the expected change and most likely resulting from issues with the experimental set up.

3.2.4.2 Linear combination analysis and kinetics

Linear combination analysis (LCA) was used to split the components of each experiment into the contributions from the oxidised and reduced species. To achieve this, we used the extremes from each experiment set. Normally standards would be used for LCA, but owing to fluctuations in the absolute edge position from different *in situ* EDE experiments this was not possible.

For example, from Figure 69 A investigating the Na^+ ion intercalation into FeHCF where E_1 = 0.5 V and E_2 = 0.4/0.3/0.2/0.0/-0.1 V *vs.* SCE. When E_1 is applied from E_2 an extreme is achieved in terms of oxidised species. The reverse is given when E_2 is applied from E_1, meaning we obtain an extreme for the reduced species. These extremities are demonstrated in Figure 71.

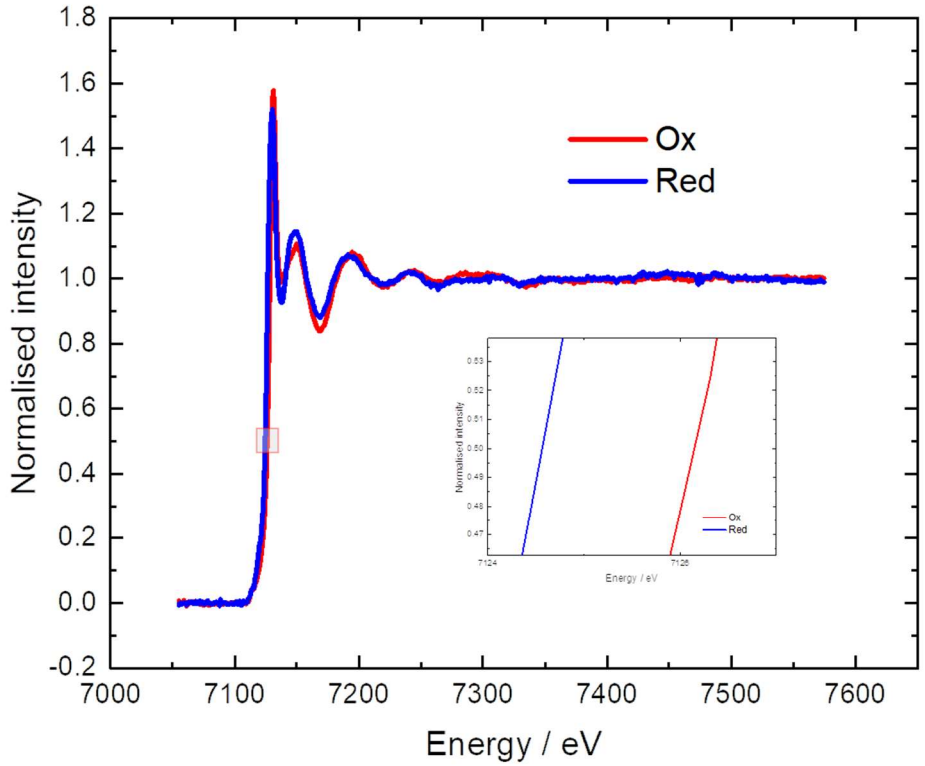

Figure 71 Showing the extreme spectra for the intercalation of Na^+ into FeHCF. Insert showing data in the taking of 0.5 normalised intensity.

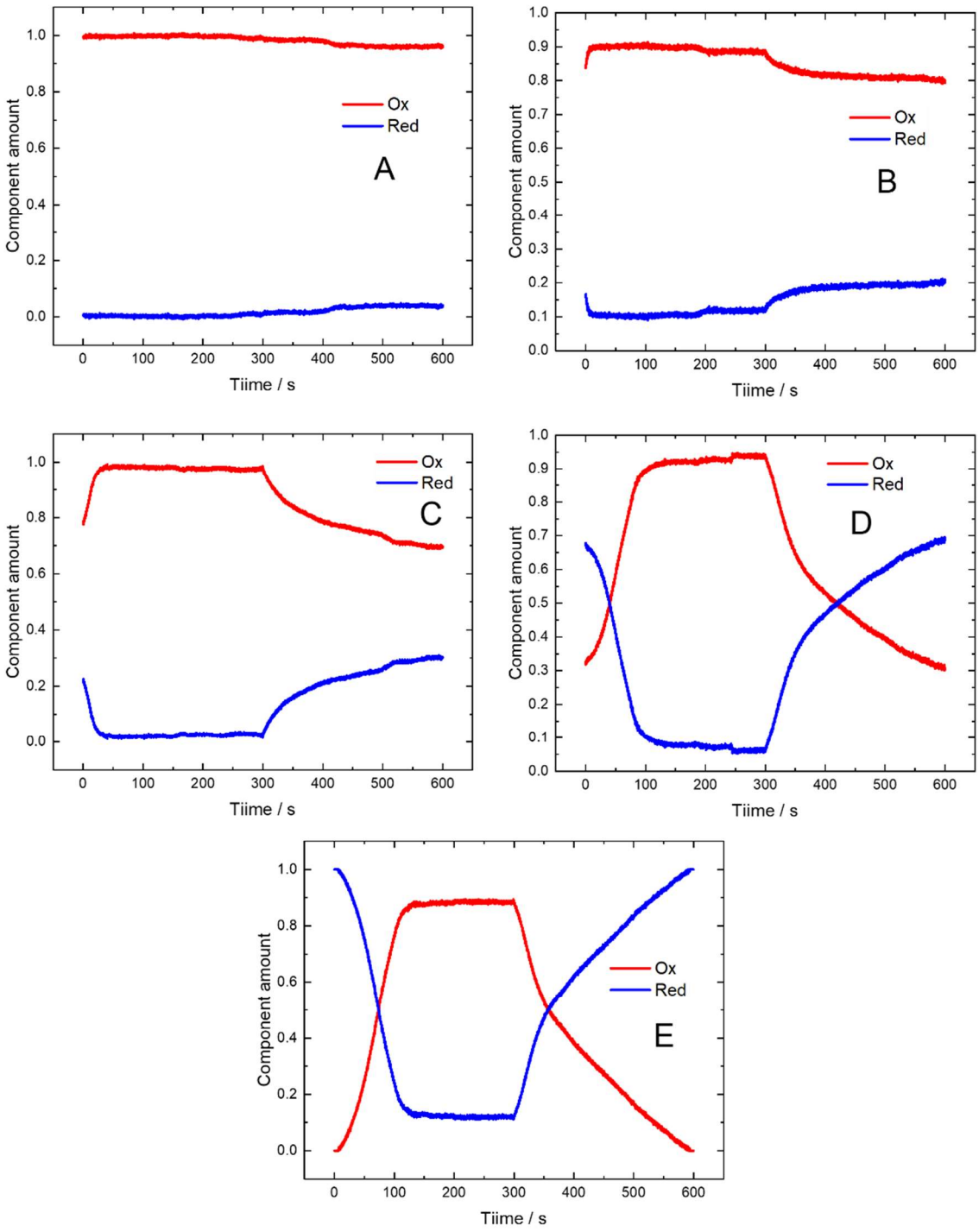

Figure 72 Linear combination results as a function of time for Na intercalation. Showing the application of E_1 = 0.5 V in each case for the first 300 s. Then for each E_2 value A) 0.4 V B) 0.3 V C) 0.2 V D) 0.0 V and E) -0.1 V for the final 300 s. Where red is the fraction of Fe^{3+} and blue the fraction of Fe^{2+}.

Figure 72 shows the results of the linear combination fitting for the reduction of Fe-N (Na^+ intercalation). For each E_2, data was also collected during the return (oxidation) step to E_1, but as this data does not present a consistent starting state they are not used in the subsequent

analysis. Thus, the results for t ≥ 300 s were extracted and t = 300 s was re-set to t = 0 s as shown in Figure 73 A.

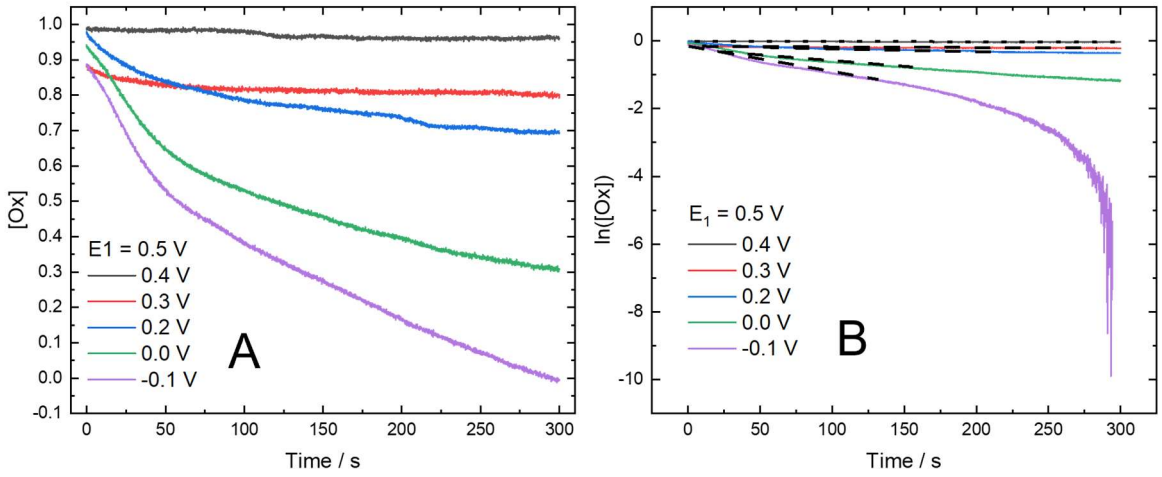

Figure 73 Kinetic analysis for the intercalation of Na^+ into FeHCF. A) showing the results of the change in concentration of the oxidised species B) the ln plot of A for 1st order kinetic analysis. Dashed line showing the linear region on the ln[Ox] *vs.* t plot.

The corresponding plots for the linear combination analysis of the oxidation of Fe-N (deintercalation of Na^+), where E_1 = 0.1 V *vs.* SCE, are shown in Figure 74. Extracted plots of the fraction of the reactant component as a function of time are given in Figure 75 A. With the rate constant obtained from the linear regions (shown by a dashed line) from Figure 75 B.

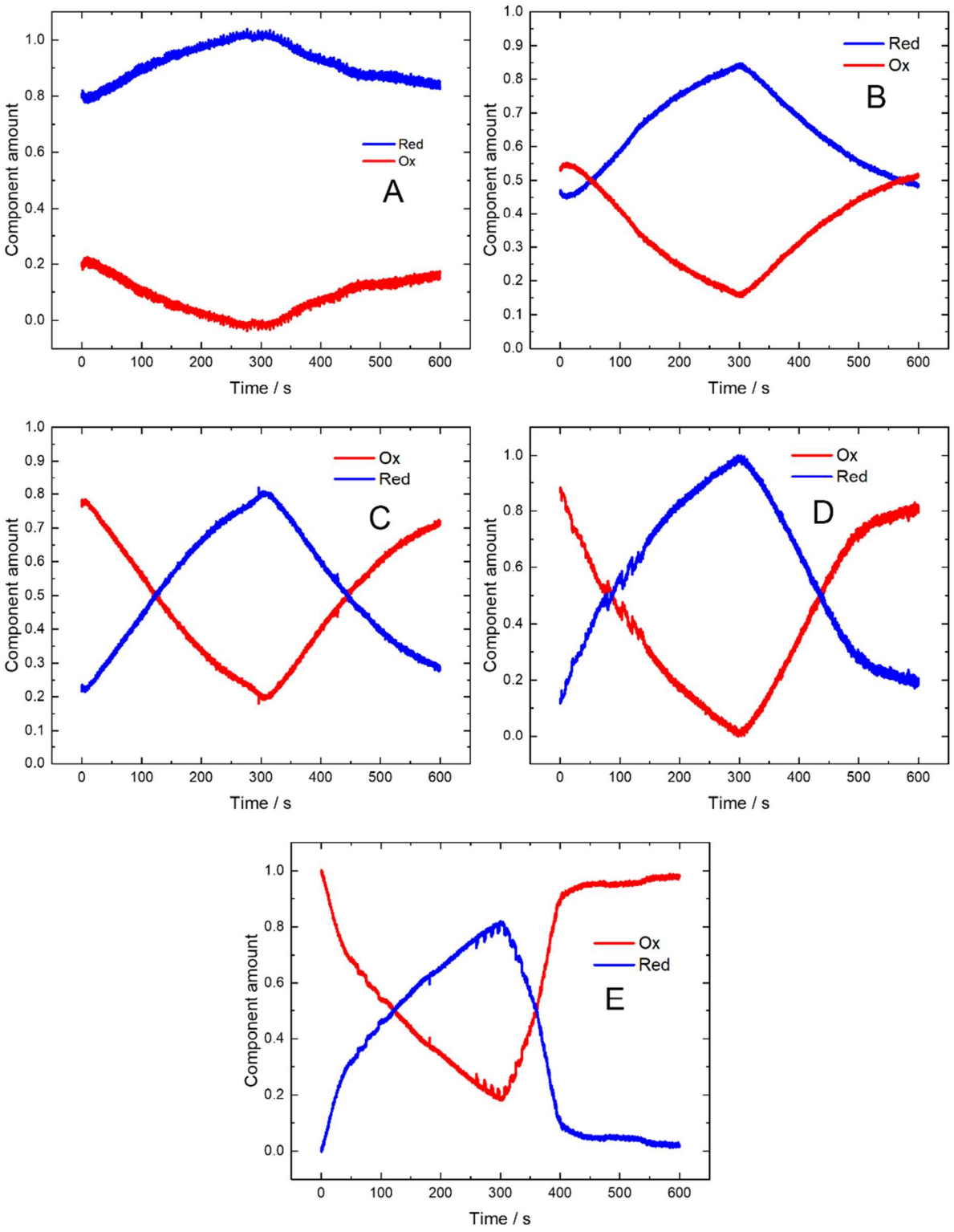

Figure 74 Linear combination results as a function of time for Na deintercalation. Showing the application of E_1 = -0.1 V in each case for the first 300 s. Then for each E_2 value A) 0.1 V B) 0.2 V C) 0.3 V D) 0.4 V and E) 0.5 V for the final 300 s. Where red is the fraction of Fe^{3+} and blue the fraction of Fe^{2+}.

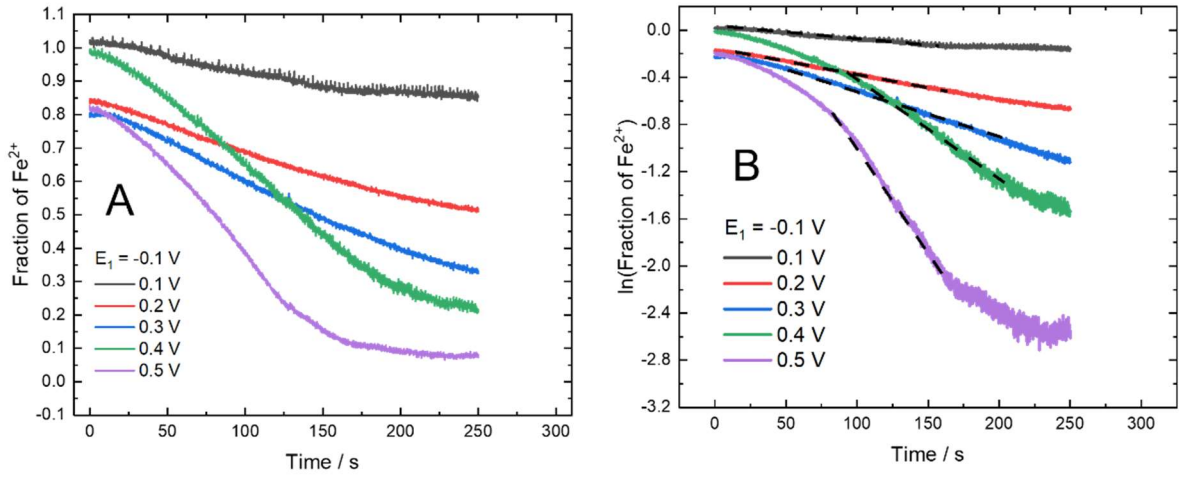

Figure 75 Kinetic analysis for the deintercalation of Na from FeHCF. A) showing the results of the change in concentration of the reduced species B) the ln plot of A for 1st order kinetic analysis.

The following figures correspond to the linear combination analysis of FeHCF during (de)intercalation of K^+ ions. Where Figure 76 and Figure 77 show the results of the linear combination analysis for the reduction of Fe-N (intercalation) and the oxidation of Fe-N (deintercalation) respectively. Figure 78 A, showing the extracted fraction of reactant as a function of time for the reduction. With Figure 78 B the corresponding linearised plot for the reduction, with the dashed line showing the linear region.

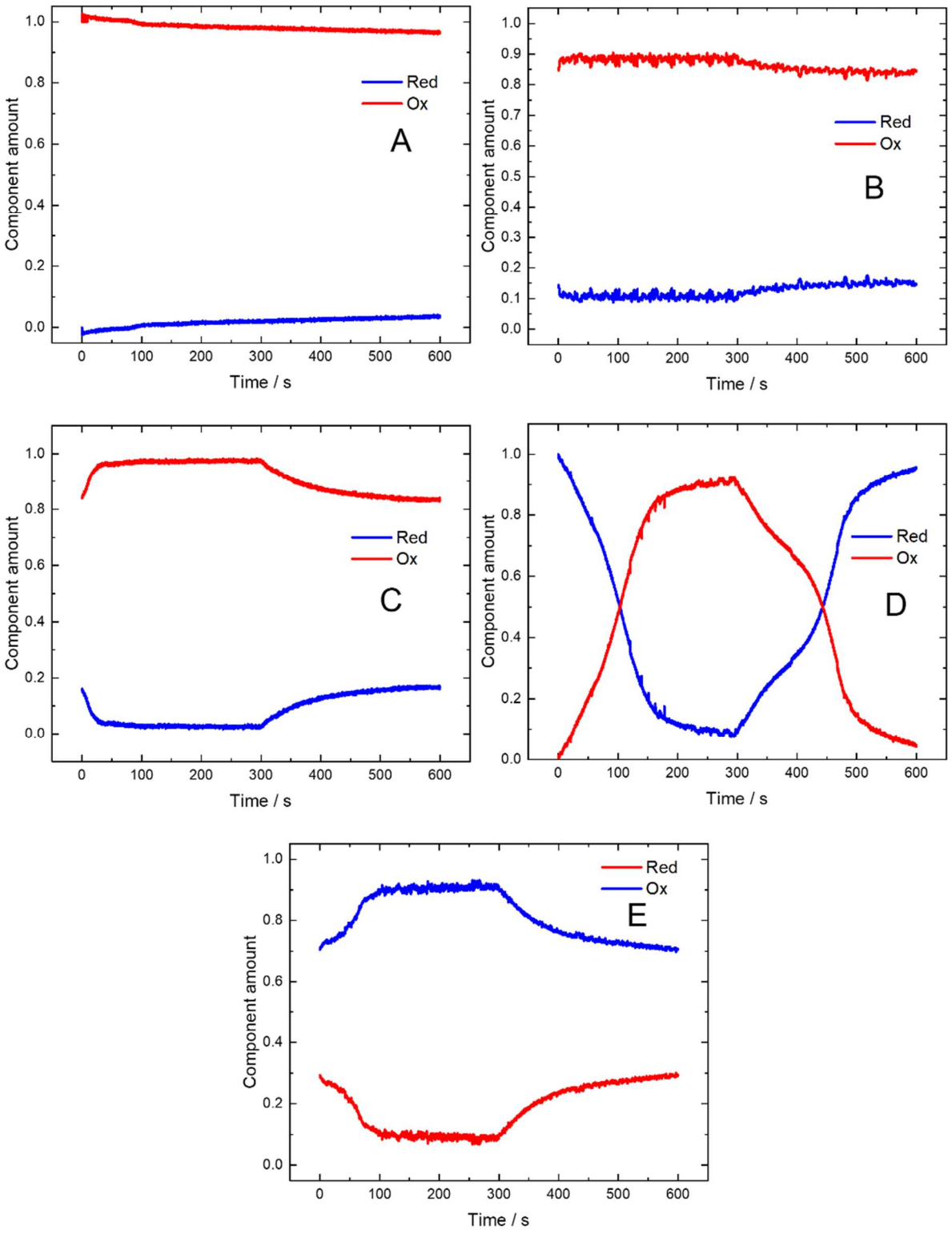

Figure 76 Linear combination results as a function of time for K intercalation. Showing the application of E_1 = 0.5 V in each case for the first 300 s. Then for each E_2 value A) 0.4 V B) 0.3 V C) 0.2 V D) 0.0 V and E) -0.1 V for the final 300 s. Where red is the fraction of Fe^{3+} and blue the fraction of Fe^{2+}.

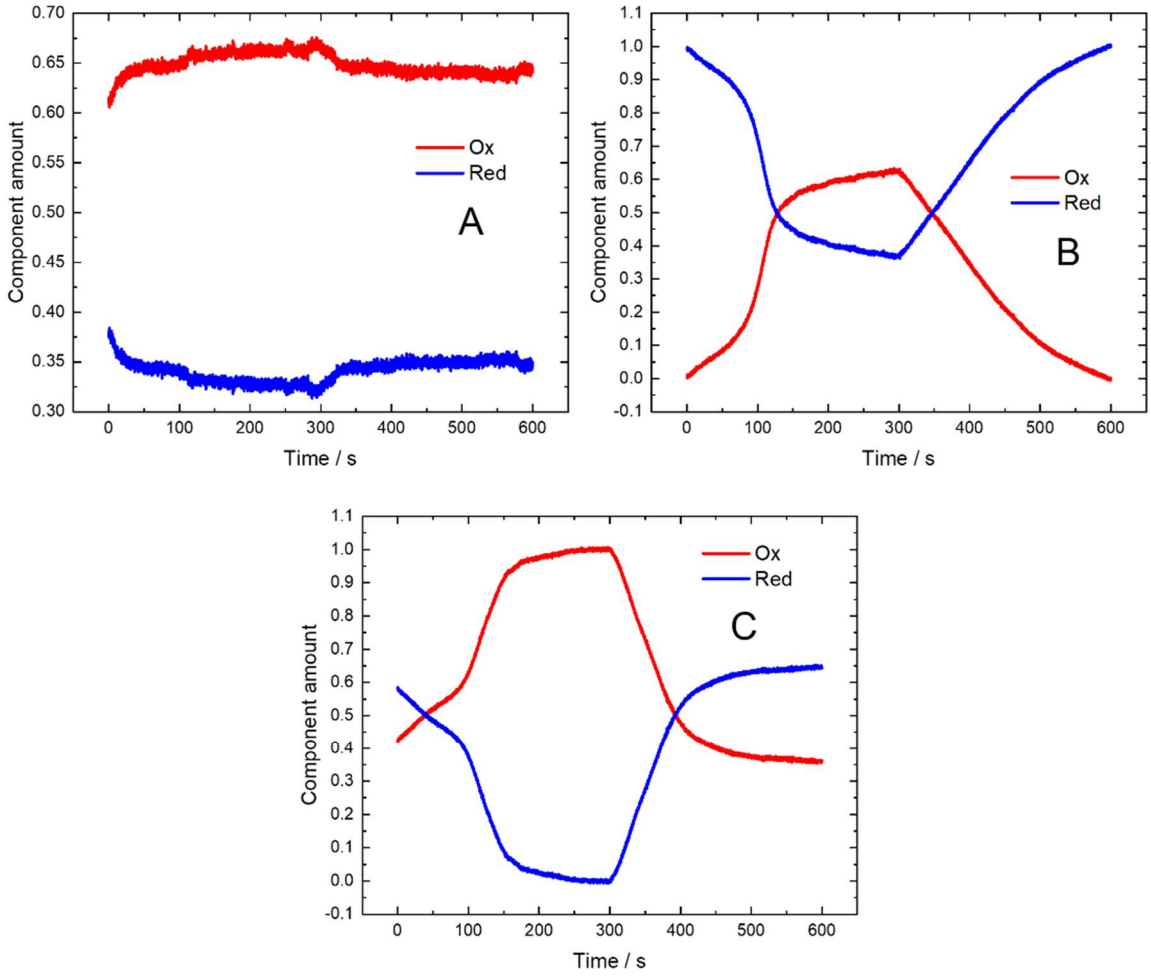

Figure 77 Linear combination results as a function of time for K intercalation. Showing the application of E_1 = - 0.1 V in each case for the first 300 s. Then for each E_2 value A) 0.1 V B) 0.3 V C) 0.5 V for the final 300 s. Where red is the fraction of Fe^{3+} and blue the fraction of Fe^{2+}.

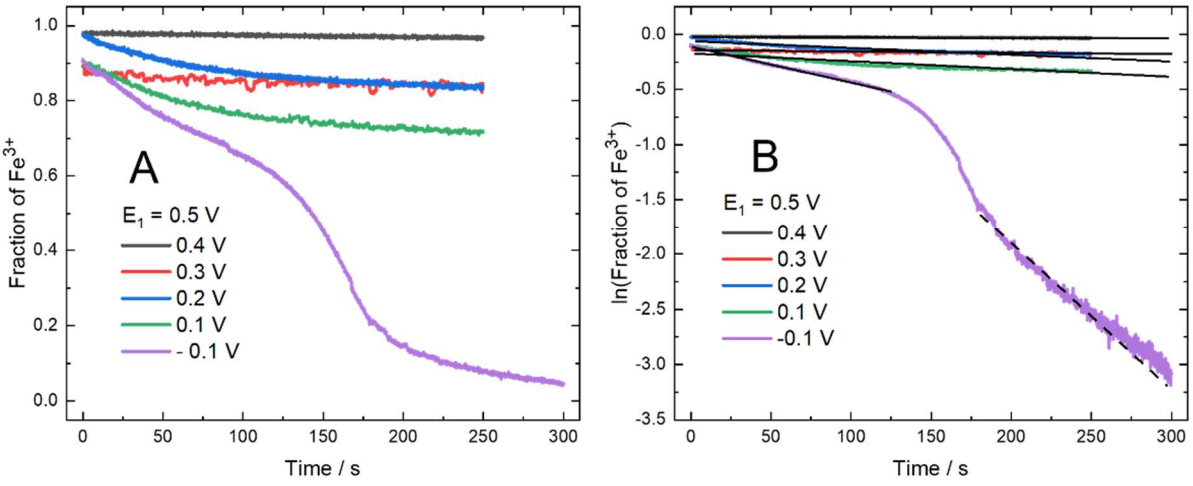

Figure 78 Kinetic analysis for the intercalation of K from FeHCF. A) showing the results of the change in concentration of the reduced species B) the ln plot of A for 1st order kinetic analysis.

Finally, not enough data is collected for the deintercalation of K^+ ions from FeHCF is collected to allow for appropriate further analysis. This was due to complications during the beam time experiment.

3.2.4.3 Reorganisation number

Treating the process as first order, the ln of the fraction of the oxidised component i.e., the reactant is plotted as a function of time in Figure 73 B.

$$\ln[A] = -kt + \ln[A_0]$$

Equation 34

A value for the rate constant, k, was obtained from the gradient of this linear region. The region fitted in each case is shown as the dashed black line in Figure 73 B. Marcus theory shows that the rate of an electrochemical reaction depends exponentially on the overpotential $\eta = E - E_0$. However, in the case of these experiments the overpotential is redefined as the driving force from E_1. Therefore, leading to $\Delta E = |E_2 - E_1|$. The exponential increase in k is observed in Figure 79 A in agreement with this theory, outlined in section 1.3. Accordingly, the ln(k) is plotted *vs.* the ΔE in Figure 79 B.

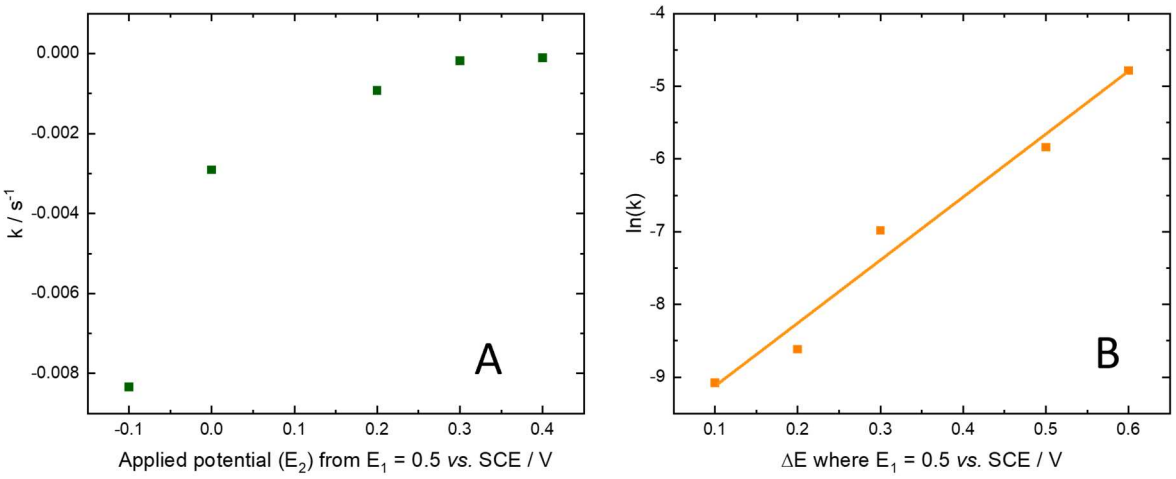

Figure 79 Comparison of the rate constants obtained from Na intercalation into FeHCF. A) rate constant as a function of applied potential B) ln of the rate constant *vs.* magnitude of applied potential.

Based on the results in the previous section from the semi log plots of ln(k) *vs.* ΔE (Figure 73 B, Figure 75 B, Figure 78 B) We can now consider our data in terms of Marcus theory.

Figure 75 also shows a linear relationship between the concentration of the reduced species as a function of time. However, in this case it appears there are two linear processes occurring. One process that up to approximately 150 s and then another from 150 s to 300 s, for the further analysis only the first 150 s will be considered. The values obtained for k are plotted against applied E_2 value in Figure 80 A. Again, a semi log plot is produced for the k values and plotted against the magnitude of the ΔE value, in Figure 80 B, which will be discussed at a later stage.

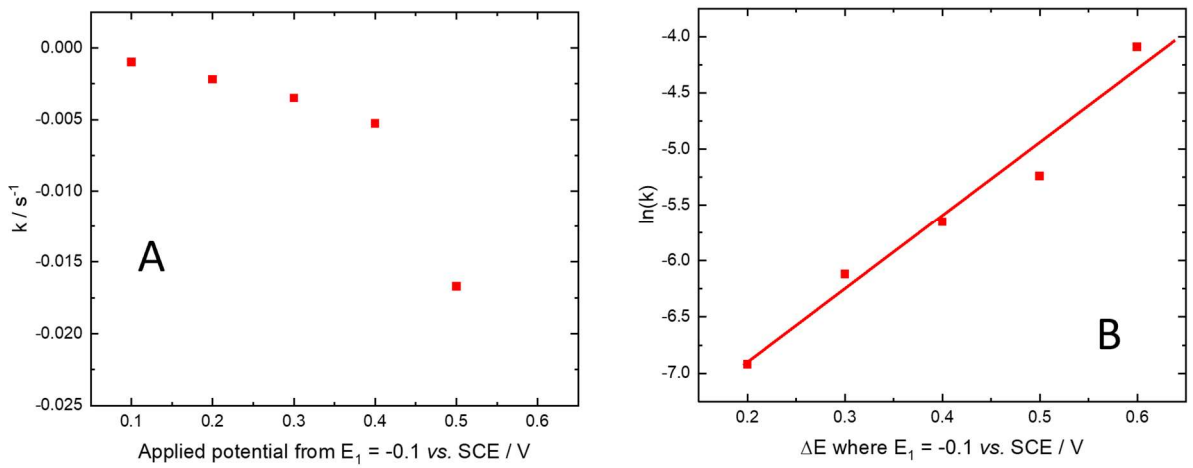

Figure 80 Comparison of the rate constants obtained from Na deintercalation into FeHCF. A) rate constant as a function of applied potential B) ln of the rate constant *vs.* magnitude of applied potential.

From the results of the reduction of Fe-N in a K^+ ion electrolyte, in Figure 78, The values for k, calculated from the linear regions (shown by black dash line) in Figure 78 B, are plotted against the E_2 in Figure 81 A and again a semi log plot of ln(k) *vs.* ΔE is produced, Figure 81 B .

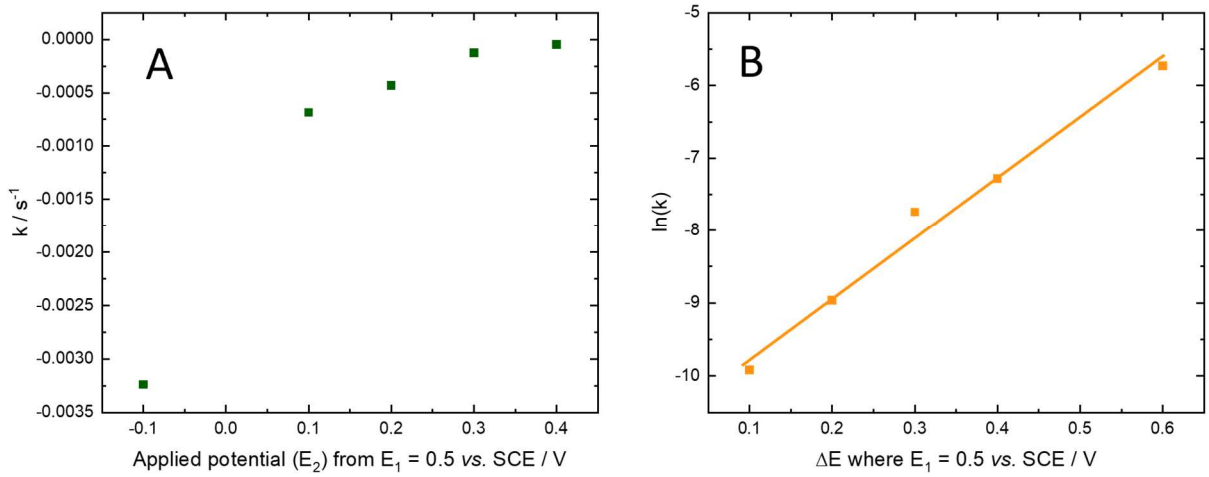

Figure 81 Comparison of the rate constants obtained from K intercalation into FeHCF. A) rate constant as a function of applied potential B) ln of the rate constant *vs.* magnitude of applied potential.

Below in **Table 15** we see a comparison of the calculated λ for each of the above kinetic results using Equation 3.

Table 15 Comparison of the reorganisation value calculated from the semi log plots of ln(k) *vs.* Δ E for each experiment

Cation	Reaction	Reorganisation number, λ / eV
Na	Reduction (intercalation)	0.629
	Oxidation (deintercalation)	0.602
K	Reduction (intercalation)	0.609

From this table we can again see that the oxidation process (the deintercalation of the cation) for both Na^+ and K^+ ions have a smaller value for λ compared to the reduction.

Most interestingly the value of λ for the oxidation when in an Na^+ electrolyte is higher that the λ for the reduction. Meaning the intercalation of Na^+ ions is more thermodynamically favourable compared to the deintercalation of Na^+ ions. The value for the intercalation of K^+ ions is also higher than the λ value for the deintercalation of Na^+ ions, again suggesting the intercalation process is more thermodynamically favourable.[129] This is most likely due to the intercalation process goes with the concentration gradient as a pose to deintercalation which is going from a place of low concentration too high.

3.2.5 Charge comparison

Finally using the results from the linear combination fitting and Faraday's law (Equation 35) we can calculate the resulting charge from the EDE data.

$$Q = mn\mathrm{F}$$

Equation 35

Where Q is the charge in C, m is the moles of active material, n the number of electrons and F is Faraday's constant. To do this, we must first calculate the average oxidation state at each point in time from the linear combination using the following equation:

$$Average\ oxidation\ state = (3\ \times\ Ox\%) + (2\ \times\ Red\%)$$

Equation 36

The difference between each point then allows the fractional accumulated charge to be determined for the spectroscopic data enabling direct comparison to the chronocoulometric data from the electrochemical data collected simultaneously. The comparison plot for intercalation (E_1 = 0.5 V) and deintercalation (E_1 = -0.1 V) for Na^+ are given in Figure 82 and Figure 83

respectively. In each case the spectroscopic and electrochemical charges follow the same trends, with the magnitude of the charge, Q increase as ΔE increases. However, especially for the larger values of ΔE, there is a poor overlap between the curves, suggesting different procedures are limiting the rates of the iron redox (spectroscopic data) and coupled ion-electron transport (electrochemical data) reactions.

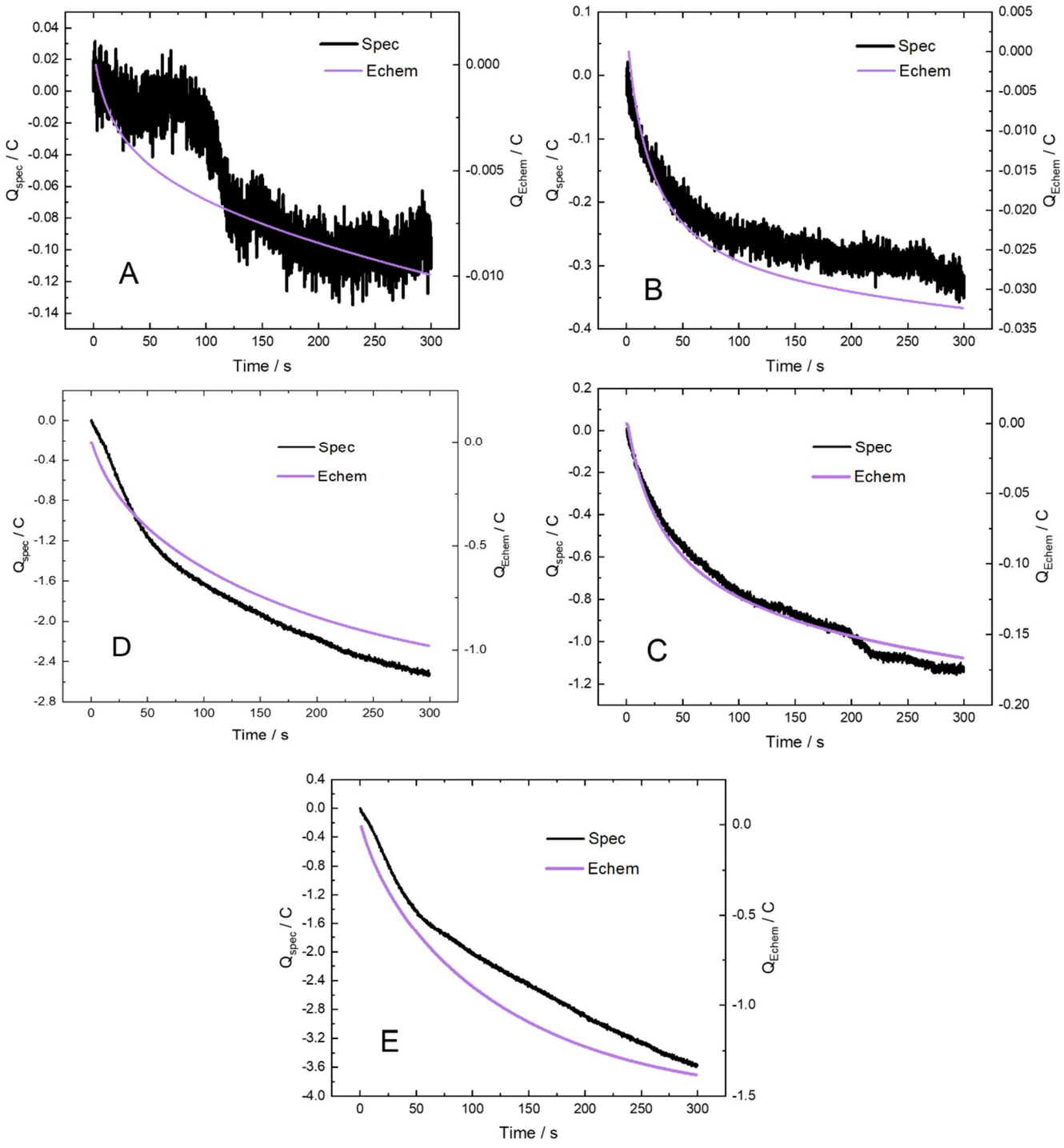

Figure 82 Comparison of calculated charges from the linear combination and electrochemical *in situ* EDE experiments, for Na^+ ion intercalation into FeHCF. In each case E_1 = 0.5 V with A) E_2 = 0.4 V, B) E_2 =0.3 V, C) E_2 = 0.2 V D) E_2 = 0.0 V and E) E_2 = -0.1 V.

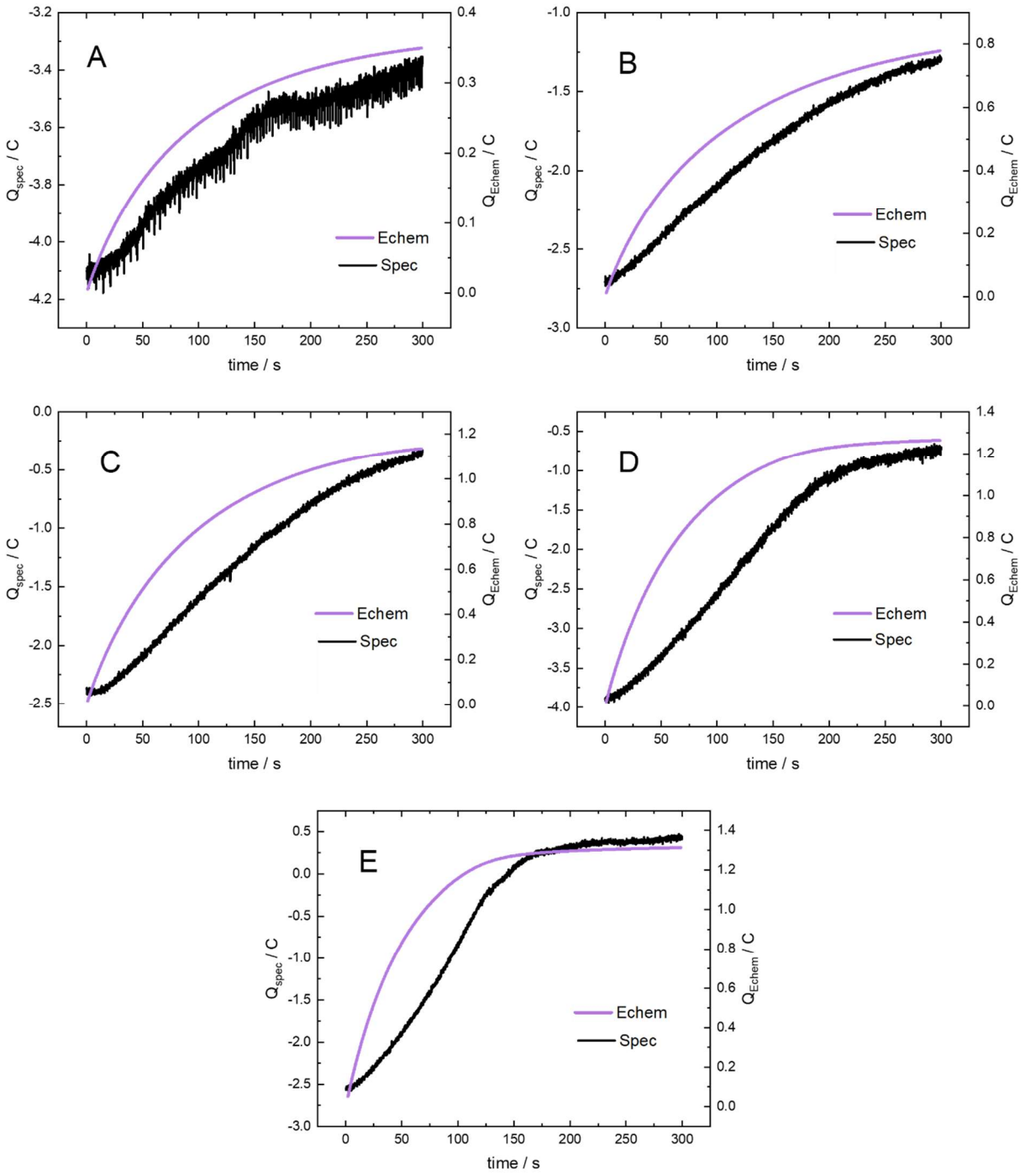

Figure 83 Comparison of calculated charges from the linear combination and electrochemical *in situ* EDE experiments, for Na^+ ion deintercalation into FeHCF. In each case E_1 = -0.1 V with A) E_2 = 0.1 V, B) E_2 =0.2 V, C) E_2 = 0.3 V D) E_2 = 0.4 V and E) E_2 = 0.5 V.

To further investigate the difference between the spectroscopic and electrochemical measurement, the data in Figure 82 and Figure 83 were fitted to exponentials. The time constants were extracted from the fits and are plotted in Figure 84. For both the intercalation (Figure 84 A) and the deintercalation (Figure 84 B). The constants for the spectroscopy are smaller than those

for the electrochemistry. This is even more pronounced for the deintercalation showing a much greater variation.

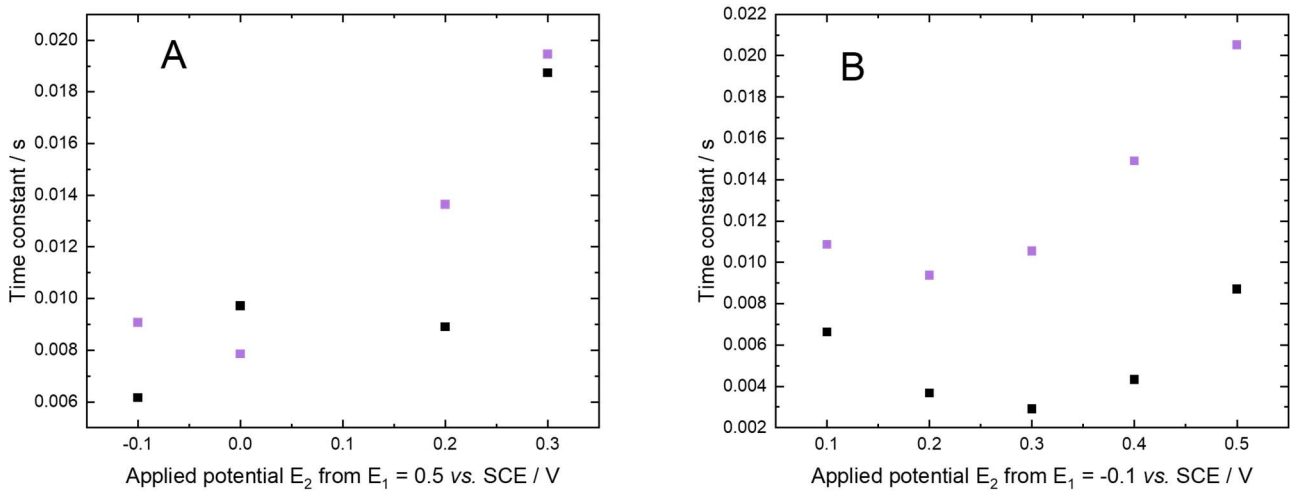

Figure 84 Time constants taken from the exponentials of both the calculated charge from the spectroscopy and the charge from the electrochemistry response. With A) time constants for the intercalation of Na^+ ions and B) the time constants for the deintercalation of Na^+ ions from FeHCF. Where black is the time constants from the spectroscopy and purple the time constants from the electrochemistry.

The spectroscopy results correspond directly to the redox reaction for the Fe centres in FeHCF, in this case specifically the Fe-N centre. This lag therefore suggests that the redox reaction of Fe is delayed compared the CIET or more specifically the IT.

To understand these results, we first need to understand the difference between Prussian blue (PB) the half intercalated form of FeHCF, $NaFe^{3+}[Fe^{2+}(CN)_6]$ and Prussian white (PW) the fully intercalated form of FeHCF, $Na_2Fe^{2+}[Fe^{2+}(CN)_6]$. Based on literature sources PB acts as more of an insulator compared to PW. In Figure 85 this difference is demonstrated schematically.[78]

As the electrode is reduced it becomes more conducting, thus the e^- transfer through the structure becomes more facile. We propose that this explains the smaller difference between the points in Figure 84 A. In contrast, upon oxidation (deintercalation), the PB particles become less conducting, making the e^- transfer through them more difficult, leading the Fe redox process becoming limited. A schematic outlining this process is given in Figure 85.

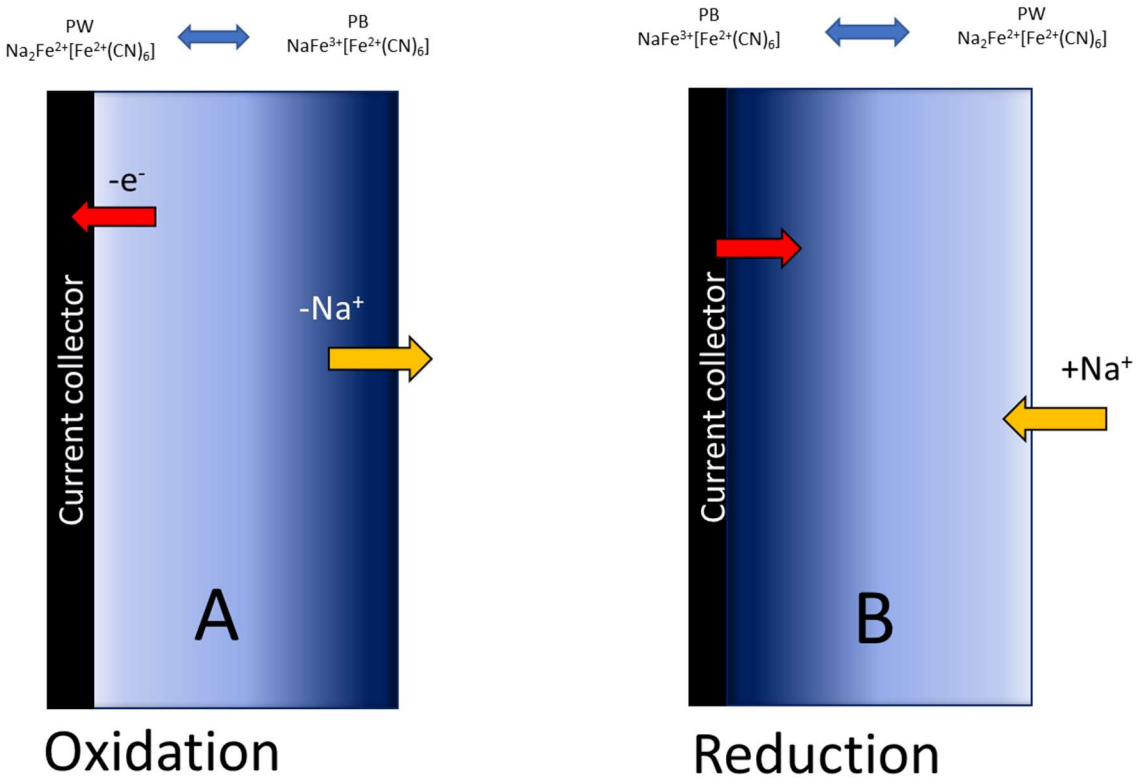

Figure 85 Effect of (de)intercalating cation on the electrode where the dark blue region is PB and the lighter white region PW A) deintercalation of Na^+ from the electrode B) intercalation of Na^+ into the electrode. The yellows arrows represent the difference of movement for the Na+ ions into/out of the electrode. The red arrows depict the direction of flow of the e- during the redox process shown in the figure.

The same process is carried out on the spectroscopy data for the (de)intercalation of K^+ ions into and from the FeHCF lattice. With the intercalation given in Figure 86 and the deintercalation in Figure 87.

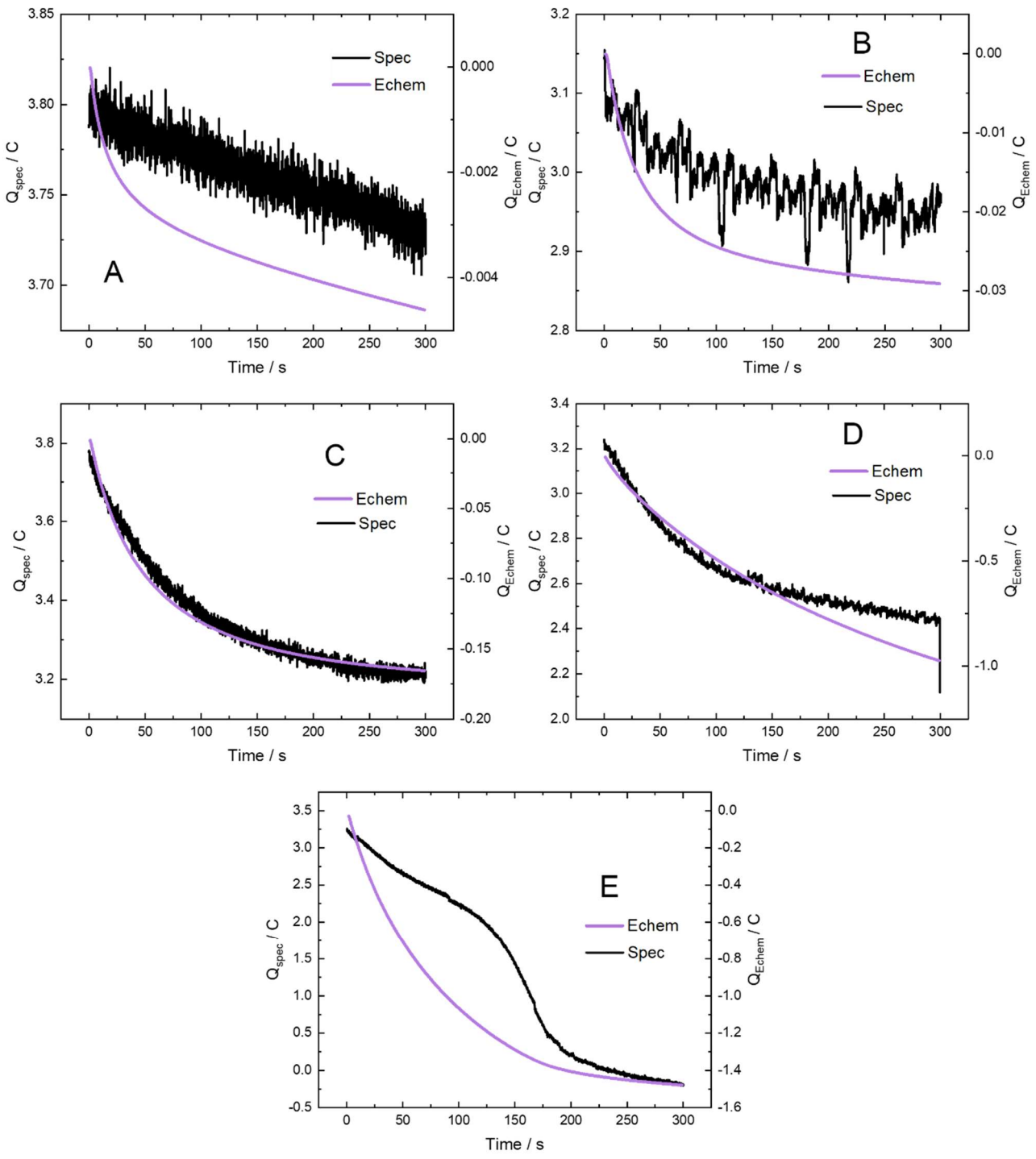

Figure 86 Comparison of calculated charges from the linear combination and electrochemical *in situ* EDE experiments, for K^+ ion intercalation into FeHCF. In each case E_1 = 0.5 V with A) E_2 = 0.4 V, B) E_2 =0.3 V, C) E_2 = 0.2 V D) E_2 = 0.1 V and E) E_2 = -0.1 V.

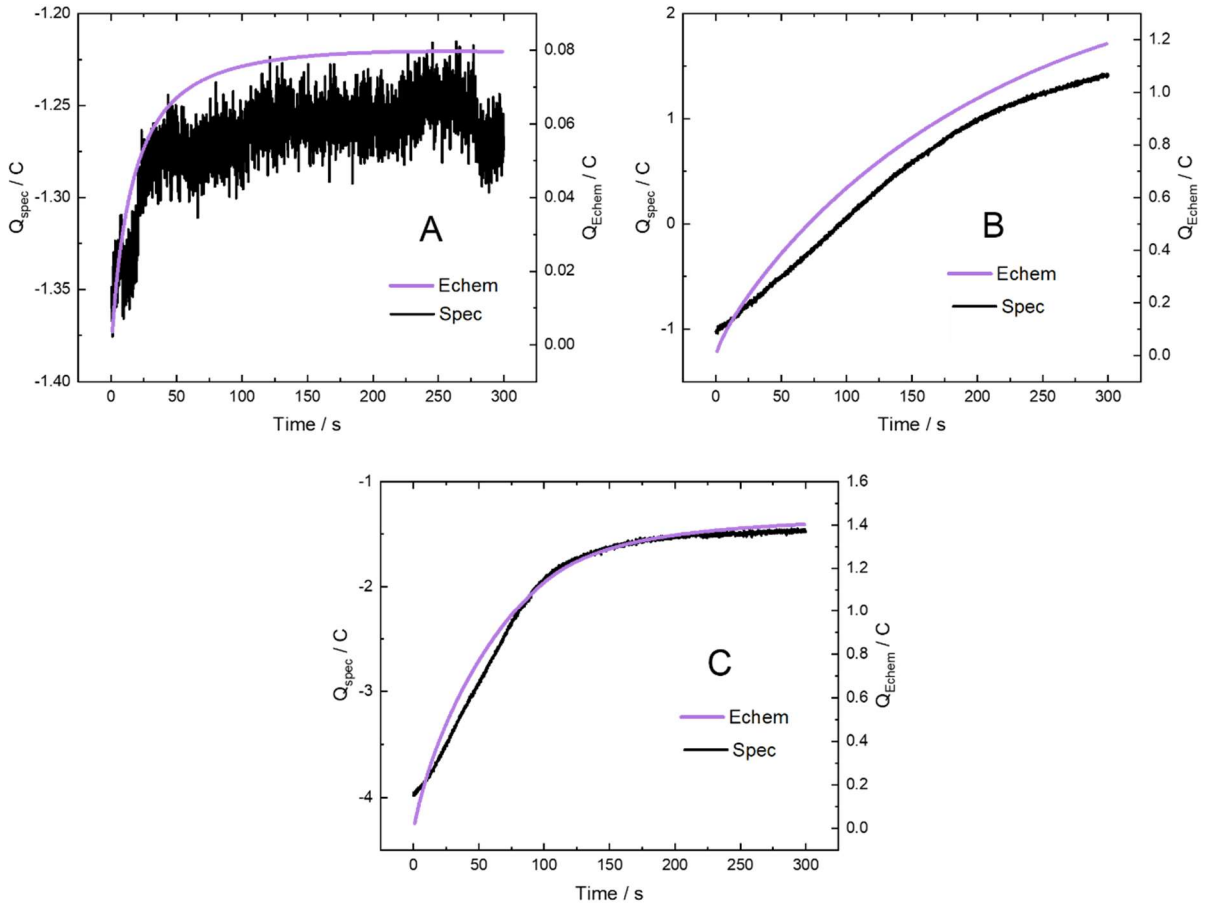

Figure 87 Comparison of calculated charges from the linear combination and electrochemical *in situ* EDE experiments, for K^+ ion deintercalation into FeHCF.
In each case E_1 = - 0.1 V with A) E_2 = 0.1 V, B) E_2 =0.3 V, C) E_2 = 0.5 V.

Figure 88 gives the comparison of the extracted time constants from Figure 86 and Figure 87. With Figure 88 A showing the time constants for the comparison of charges for the intercalation of K^+ ions and Figure 88 B the comparison for the intercalation of K^+ ions. Again, for both the (de)intercalation of K^+ ions there is a lag in the spectroscopy results (the ET) compared with the electrochemical. Suggesting that the transition from PB to PW plays a major role in the electrochemical mechanism for the (de)intercalation process for both cations.

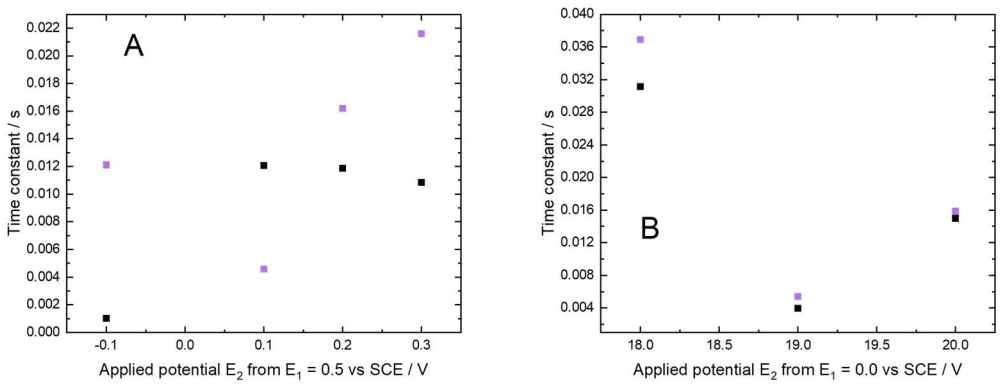

Figure 88 Time constants taken from the exponentials of both the calculated charge from the spectroscopy and the charge from the electrochemistry response. With A) time constants for the intercalation of K^+ ions and B) the time constants for the deintercalation of K^+ ions from FeHCF. Where black is the time constants from the spectroscopy and purple the time constants from the electrochemistry.

3.3 Conclusion

In this chapter a combination of electrochemistry and spectroscopy have been used to distinguish ET kinetics from CIET kinetics. Comparison was made on the rate of diffusion of the ions (CIET) through the FeHCF lattice in two separate electrolytes $NaNO_3$ and KNO_3. Three methods for determining diffusion coefficients have been demonstrated for both the (de)intercalation of Na^+ ions and K^+ ions. **Table 16** shows a comparison of these derived diffusion coefficients. In all cases the deintercalation of the ion is faster than the intercalation. Furthermore, the movement of K^+ ions in both (de)intercalation are faster than that of Na^+. This is explained by the size of each of the ions, with the hydration radius of Na^+ being larger than that of K^+.

Table 16 Comparison of derived diffusion coefficients for (de)intercalation into/from FeHCF for Na^+ and K^+ ions.

Technique	Intercalation/deintercalation	Diffusion coefficient for Na^+ x 10^9/ cm s^{-1}	Diffusion coefficient for K^+ x 10^9/ cm s^{-1}
Cyclic voltammetry	Intercalation	0.67 ± 0.12	1.8 ± 0.29
	Deintercalation	0.67 ± 0.14	3.5 ± 0.48
Alternative diffusion coefficient	Intercalation (range)	0.2 – 0.8	0.01 – 0.8
	Deintercalation (range)	0.6 - 10	0.4 – 2.2
Chronocoulometry	Intercalation (range)	0.01 – 1.3	0.01 – 1.8
	Deintercalation (range)	0.01 – 3.2	0.01 – 2.2

Through the analysis of the diffusion coefficient insight is gained on the CEIT kinetics of the system, which in each case we see the rate being dependent on the applied potential, E_2. Most importantly from the CT its shown that a NLD mechanism is controlling the movement of the ions in the lattice.

From the NS analysis a value of k^0 for the CIET kinetics can be determined from the voltammograms in each ions electrolyte. For Na^+ ions a $k^0$of 7.25 x 10^{-6} m s^{-1} is calculated compared to a k^0 of 5.83 x 10^{-6} m s^{-1} for K^+. These values of k^0 fit perfectly with the results from the voltammograms as the reaction in the K^+ electrolyte is more facile in comparison to Na^+. All these results give insight into the CIET kinetics of for the (de)intercalation reaction in FeHCF.

EDE were used to attempt to separate the ET kinetics from the electrochemical CIET kinetics. The results (Figure 69 and Figure 70) clearly demonstrate that as the driving force increases the rate of change of oxidation state and the amount of change in the oxidation state increases. These results are then split into their oxidised and reduced components, from which a charge can be calculated for the spectroscopy results. This charge corresponds to the ET mechanisms. Comparing this charge derived from the spectroscopy (spectroscopic charge) with the electrochemical charge shows there is a difference in the respective time constants, with a longer time constant denoting a slower process.

During the intercalation process for both Na^+ and K^+ ions the lag decreases as the driving force increases. This is because PB acts as an insulator whilst PW is more conducting. This means that as the electrode is reduced, and the ions intercalated the electrode becomes more conducting

increasing the rate of ET. The opposite is seen when the ions are deintercalated and the electrode becomes more insulting, slowing down the rate of ET.

Moving into the next chapter looking at changing the M in the MHCFS material effects the overall coupled ion and electron transport kinetics and once again looking at just the electron transfer kinetics using the spectroscopy.

Chapter 4 Study of sodium ion (de)intercalation in NiHCF and CuHCF at the Fe K-edge.

4.1 Introduction

4.1.1 Aim of this chapter

In the previous chapter we analysed the effect of changing the (de)intercalating cation for FeHCF. For this chapter we shall look only at the intercalation of Na^+ cations but investigate the effect that changing the metal bound to the N, in the CN bridging ligand, has on the rate of (de)intercalation. For this the (de)intercalation of Na^+ cations in Nickel(III) hexacyanoferrate (NiHCF) and Copper(III) hexacyanoferrate (CuHCF) will be studied. Following the same structure as Chapter 3, we shall firstly investigate the cyclic voltammetry of each of these MHCFS materials. This will be followed by the results of the LAPS experiments and other methods of exploring diffusion coefficients for these materials. Then finally looking at the spectroscopic results to gain a comparison between the coupled ion and electron transport kinetics from the electrochemistry and the unmasked electron transport kinetics from the energy dispersive x-ray spectroscopy.

4.2 Results and Discussion

All experimental details for this chapter are given in Chapter 2 and the methods of analysis used outlined in Chapter 3.

4.2.1 Cyclic voltammetry

4.2.1.1 Cyclic voltammetry of NiHCF in CuHCF in Na^+ ion electrolyte

Voltammogram of an 8 mg cm^{-2} NiHCF electrode in 2 M $NaNO_3$ at pH 2 is given in Figure 89 as a function of the sweep rate.

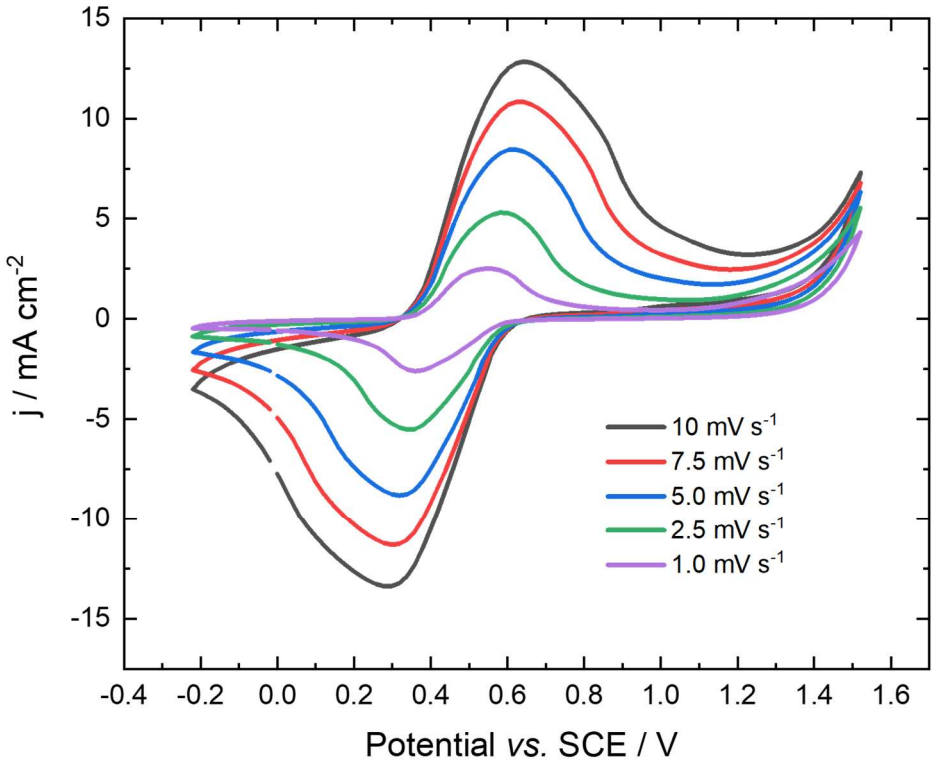

Figure 89 Cyclic voltammetry of an 8 mg cm^{-2} NiHCF on Toray carbon paper electrode in 2 M $NaNO_3$ at pH 2, for a range of scan rates from 10 mV s^{-1} to 1.0 mV s^{-1}, starting at 0.8 V and then initially sweeping to -0.2 V. Carried out at room temperature (around 22 °C – 25 °C) in the *in situ* cell (see Figure 20).

Unlike the CV's for FeHCF, NiHCF shows only a single redox couple corresponding to just the Fe-C redox reaction. The Ni-N redox couple is not electrochemically active in this region. A similar result is seen in the voltammogram for CuHCF, Figure 90.

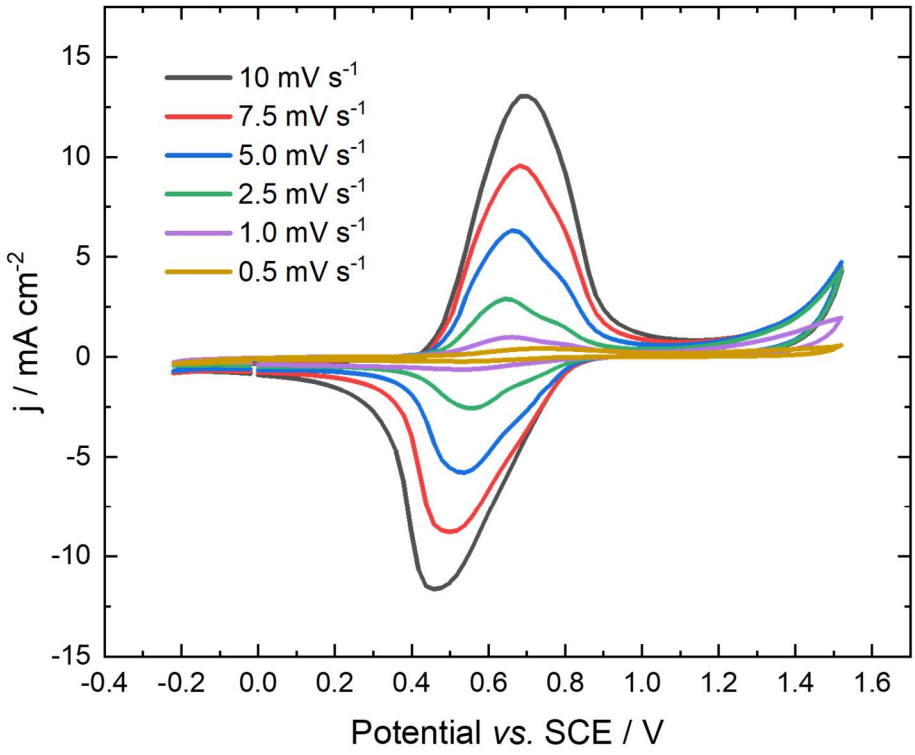

Figure 90 Cyclic voltammetry of an 8 mg cm^{-2} CuHCF on Toray carbon paper electrode in 2 M $NaNO_3$ at pH 2, for a range of scan rates from 10 mV s^{-1} to 0.5 mV s^{-1}, starting at 0.8 V and then initially sweeping to -0.2 V. Carried out at room temperature (around 22 °C – 25 °C) in the *in situ* cell (see Figure 20).

Therefore, when analysing these voltammograms, they follow the redox the redox reaction shown in Equation 37.

$$NaM^{II}[Fe^{III}(CN)_6] + e^- + Na^+ \rightleftharpoons Na_2M^{II}[Fe^{II}(CN)_6]$$

Equation 37

Where M is either Ni or Cu bound to the CN from the CN bridging ligand.

4.2.1.2 Scan rate dependency of Ni/Cu HCF voltammetry's in Na^+ electrolyte

The peak current dependence on scan rate for NiHCF in an Na^+ electrolyte is given in Figure 91 and for CuHCF in Na^+ electrolyte in Figure 92. A linear relationship is shown between the peak current and the square root of the scan rate.

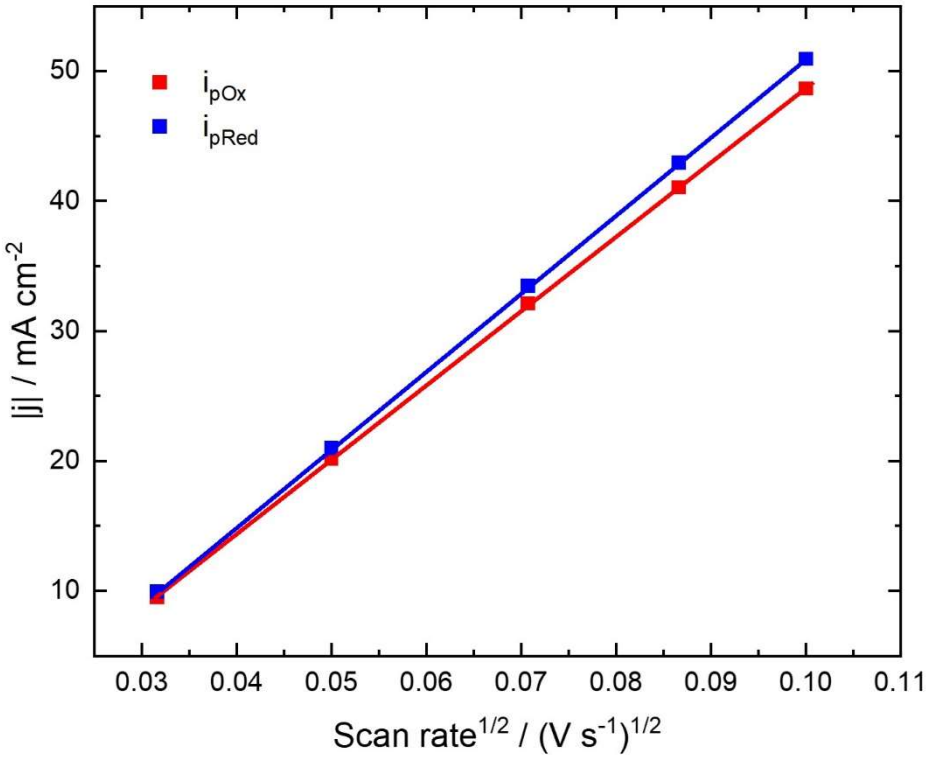

Figure 91 Analysis peak current *vs.* (scan rate)$^{1/2}$ for the CV of NiHCF in 2 M $NaNO_3$ at pH 2 for the Fe-C redox peak, Figure 89.

From these linear relationships a diffusion coefficient of (7.83 ± 5.9) x 10^{-9} cm^2 s^{-1} for the deintercalation and for the intercalation (8.61 ± 3.2) x 10^{-9} cm^2 s^{-1} in NiHCF. These values for the diffusion coefficient again show the intercalation being the faster process as it has the larger value for the diffusion coefficient. The values do have a large error associated with them, most likely from these systems showing a quasi-reversible behaviour. However, again to keep consistency with the reported literature we have chosen to model these as reversible systems.

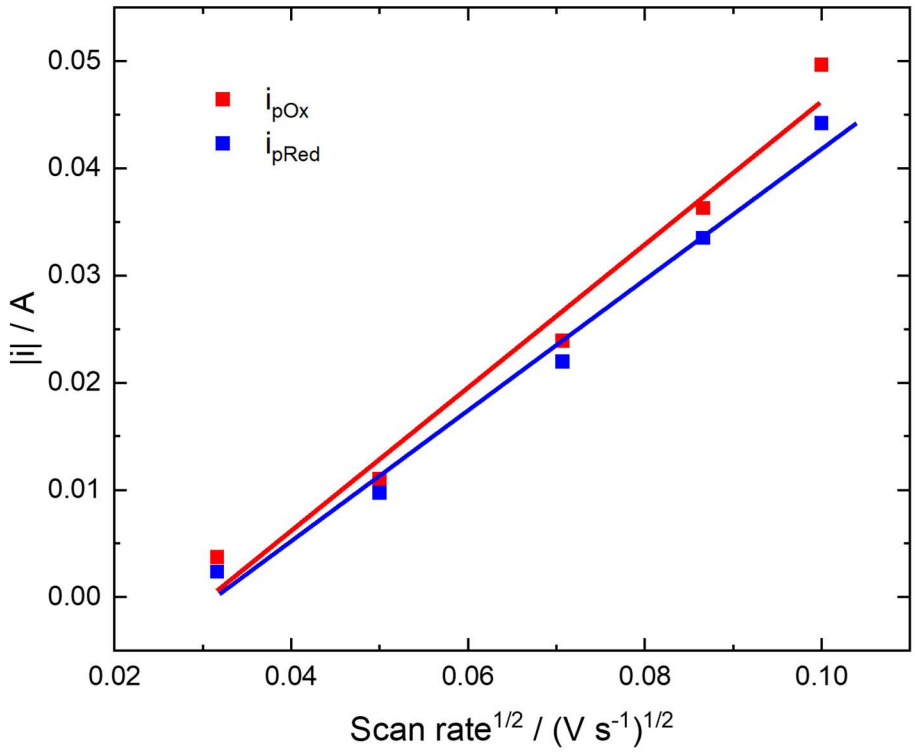

Figure 92 Analysis peak current *vs.* (scan rate)$^{1/2}$ for the CV of CuHCF in 2 M $NaNO_3$, Figure 90.

From the gradient we obtain a diffusion coefficient of (10.0 ± 1.9) x 10^{-9} cm^2 s^{-1} for the deintercalation and (9.1 ± 1.23) x 10^{-9} cm^2 s^{-1} for the intercalation in CuHCF.

All the derived diffusion coefficients for Ni/Cu HCF are all agreement with those found in literature sources. [29,30] In each case the diffusion coefficient for the deintercalation is lower and therefore faster for the deintercalation than the intercalation.

4.2.1.3 Determination of a rate constant from the voltammetry's of Ni/Cu HCF in Na^+ electrolyte

The Nicholson-Shain (NS) method, outlined in section 3.2.1.3, is once again used to derive a value of the rate constant from the respective voltammograms of Ni/Cu HCF in Na^+ electrolyte.

Firstly, the results from applying the NS method to the voltammetry for NiHCF in 2 M $NaNO_3$ are given in Figure 93. Where Figure 93A gives the calculated Ψ value as a function of the peak separation and Figure 93 B the plot for Equation 23, where the gradient gives the k^0 value.

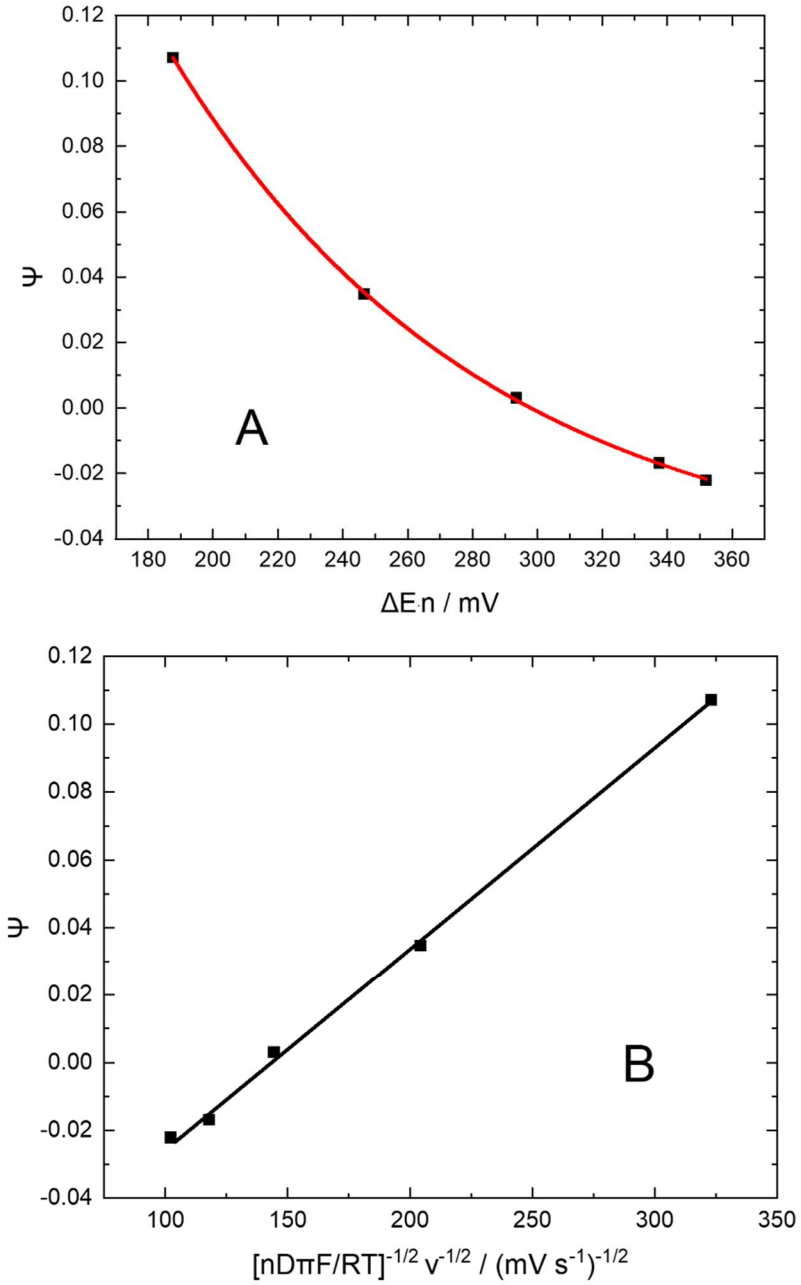

Figure 93 NS analysis for CV of NiHCF in 2 M $NaNO_3$ at pH 2. A) Ψ values calculated from Equation 25 *vs.* X, B) Ψ *vs.* $\left[\frac{n\mathrm{D}\pi\mathrm{F}}{\mathrm{RT}}\right]^{-\frac{1}{2}} v^{-\frac{1}{2}}$.

Figure 94 shows the NS analysis for the cyclic voltammetry's of CuHCF (Figure 90). Figure 94 A gives the calculated Ψ values *vs.* the peak to peak separation for the respective voltammetry. With the gradients from Figure 94 B giving the value for k^0.

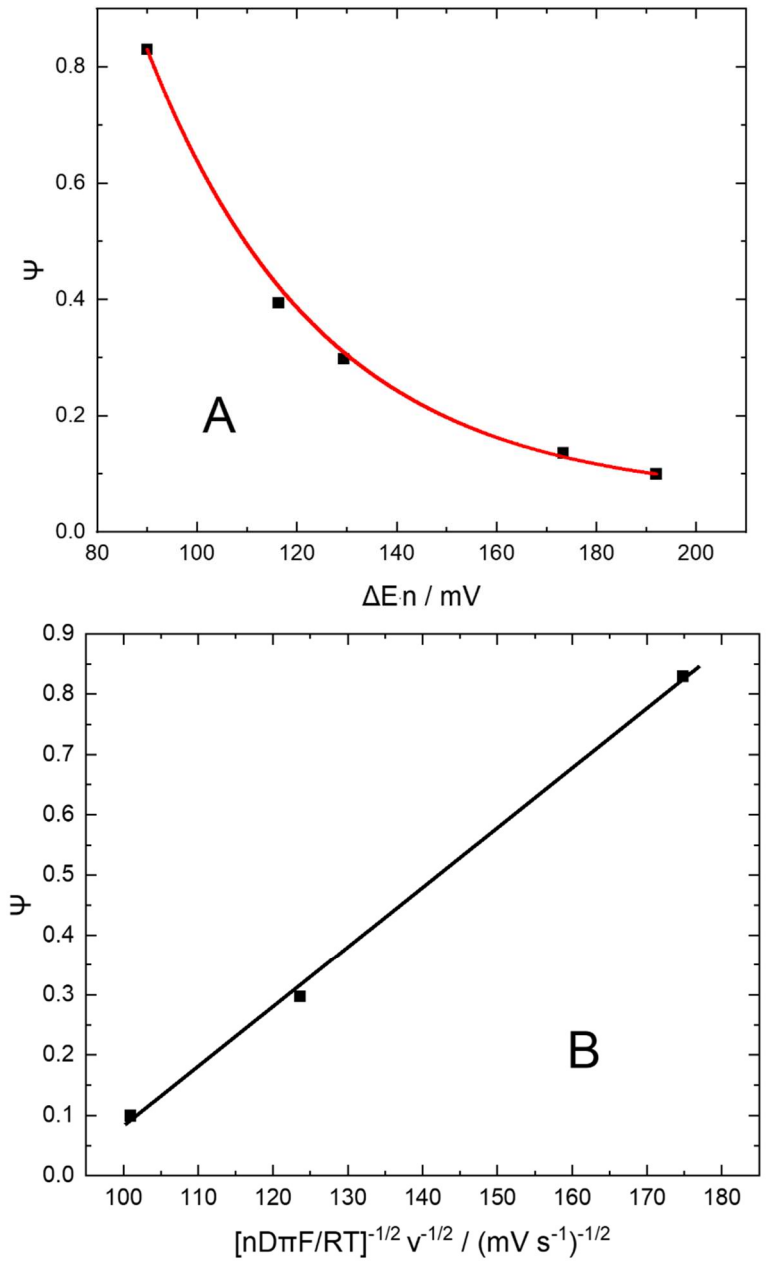

Figure 94 NS analysis for CV of CuHCF in 2 M $NaNO_3$ at pH 2. A) Ψ values calculated from Equation 25 *vs.* X, B) Ψ *vs.* $\left[\frac{n\mathrm{D}\pi\mathrm{F}}{\mathrm{RT}}\right]^{-\frac{1}{2}} v^{-\frac{1}{2}}$.

The derived rate constant for NiHCF is 5.90 x 10^{-6} m s^{-1} and for CuHCF 9.97 x 10^{-5} m s^{-1}. These values for k^0 are in terms of order of magnitude in agree with literature sources, which record values for k^0 around 10^{-6}.[31] A faster rate, therefore, is calculated for the deintercalation of Na^+ ions from NiHCF than for CuHCF.

These values will be further discussed in comparison with the other k^0 values calculated for the different MHCFS in the conclusion chapter (Chapter 6)

4.2.2 Large amplitude potential step experiments

For each of the MHCFS the deintercalation of Na^+ ions were investigated during the *in situ* EDE experiment. In this section the resulting LAPS experiment carried out during the EDE experiments are recorded. Below in **Table 17** the applied E_1 and E_2 values for each MHCFS are summarised.

Table 17 showing the applied potentials (E_2) and the return potential (E_1) for each of the *in situ* LAPS EDE experiments for the Ni/Cu/Mn HCF electrodes

Electrode material	Process	E_1 potential *vs.* SCE / V	E_2 potential *vs.* SCE / V
NiHCF	Deintercalation	0.0	0.4/0.6/0.8
CuHCF	Deintercalation	0.0	0.4/0.6/0.8/1.0

In Figure 95 the results of the LAPS experiment for the deintercalation of Na^+ from the NiHCF lattice during the EDE experiment. Showing the E_1 potential of 0.0 V and the applied E_2 potentials *vs.* SCE. In Figure 96 the results of the *in situ* LAPS/EDE experiment for the deintercalation of Na^+ from the CuHCF lattice showing the E_2 potential applied from the E_1 potential of 0.0 V *vs.* SCE. In both cases similar currents are recorded with both achieving a maximum of approximately 0.055 A cm^{-2}.

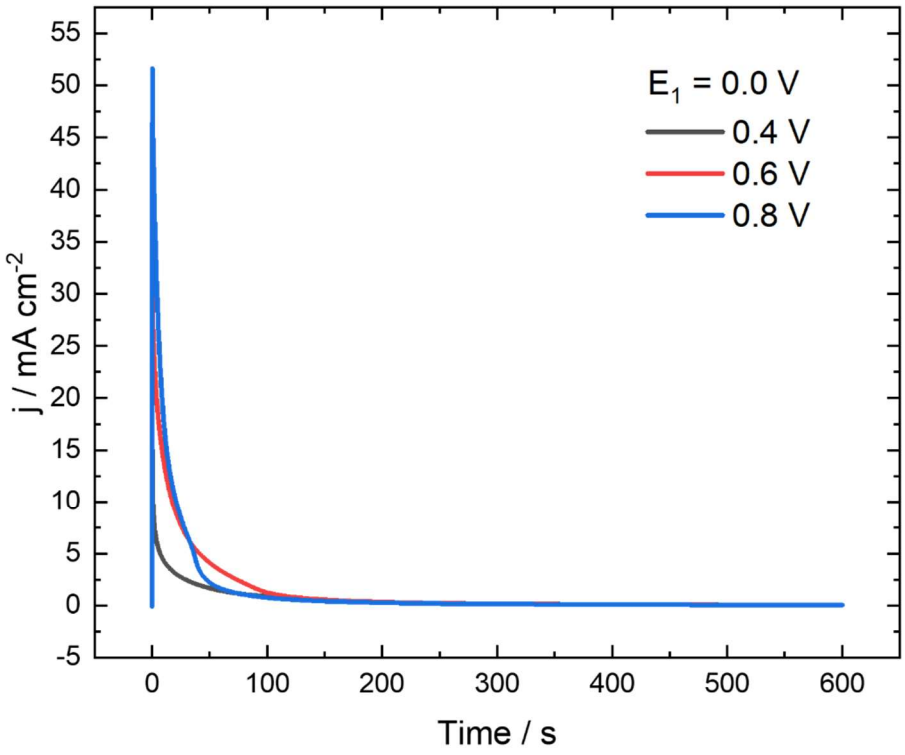

Figure 95 Chronoamperometric response for the large-amplitude potential step voltammetry for the deintercalation of Na^+ ions from NiHCF. Showing the applied potential (E_2) from the E_1 potential of 0.0 V *vs.* SCE.

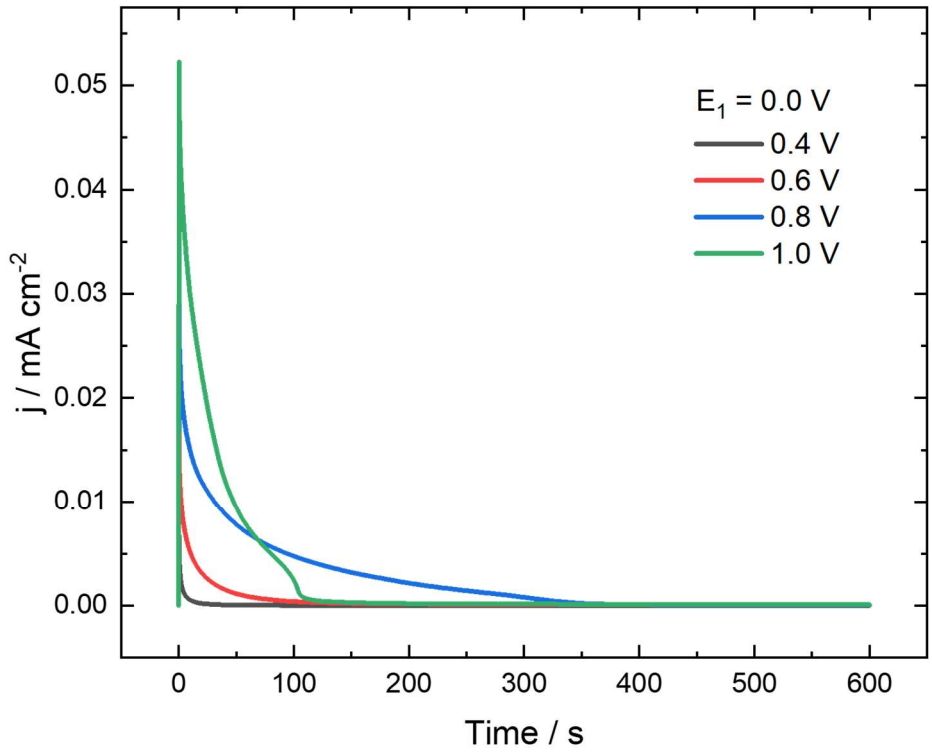

Figure 96 Chronoamperometric response for the large-amplitude potential step voltammetry for the deintercalation of Na^+ ions from CuHCF. Showing the applied potential (E_2) from the E_1 potential of 0.0 V *vs.* SCE.

As with the LAPS *in situ* EDE experiments for Na^+ and K^+ ions (de)intercalation for FeHCF electrode we shall use the Cottrell analysis to investigate the LAPS data for Ni/Cu deintercalation of Na^+.

4.2.2.1 Cottrell analysis of *in situ* LAPS EDE experiments for Ni/Cu HCF electrodes

Using the same method of analysis shown in section 3.2.2.1, the Cottrell analysis of the *in situ* LAPS EDE experiments for NiHCF and CuHCF in an Na^+ ion electrolyte will be presented in this section.

The CT analysis of the LAPS experiments for NiHCF are in Figure 97 and for CuHCF in Figure 98. The resulting CT analysis gives an initial period of linearity followed by a non-linear curve for the bulk of the experimental time. Again, this initial period is removed for future analysis.

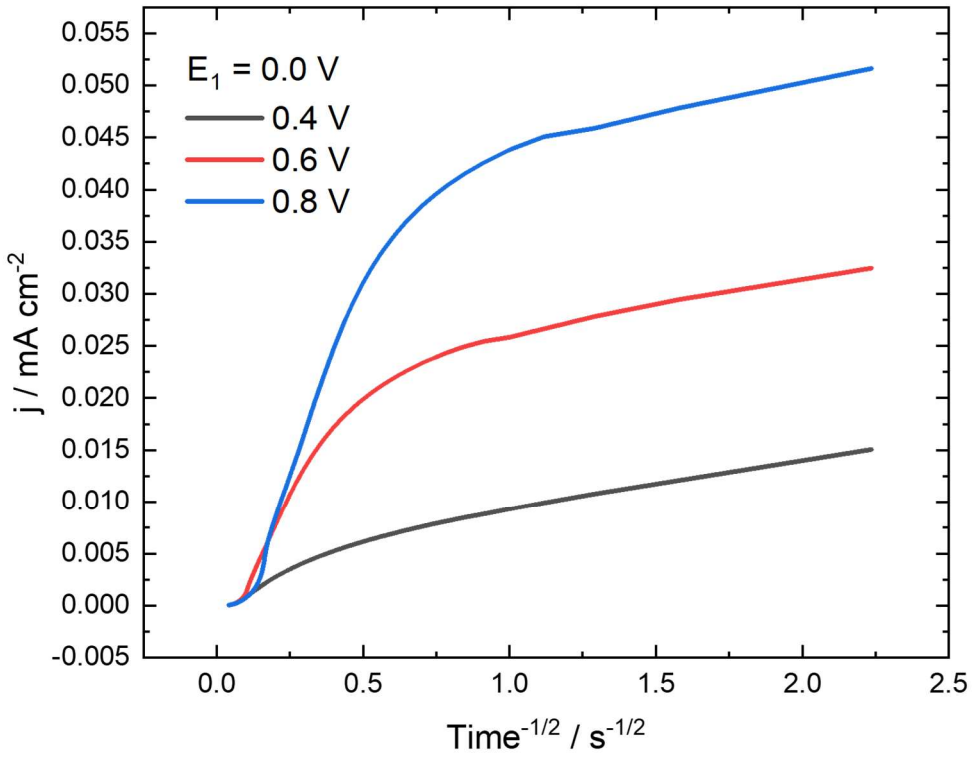

Figure 97 Cottrell analysis of the chronoamperometric response for the deintercalation of Na^+ ions from the NiHCF lattice. Showing the E_1 potential of 0.0 V and the applied potential E_2 *vs.* SCE, from Figure 95.

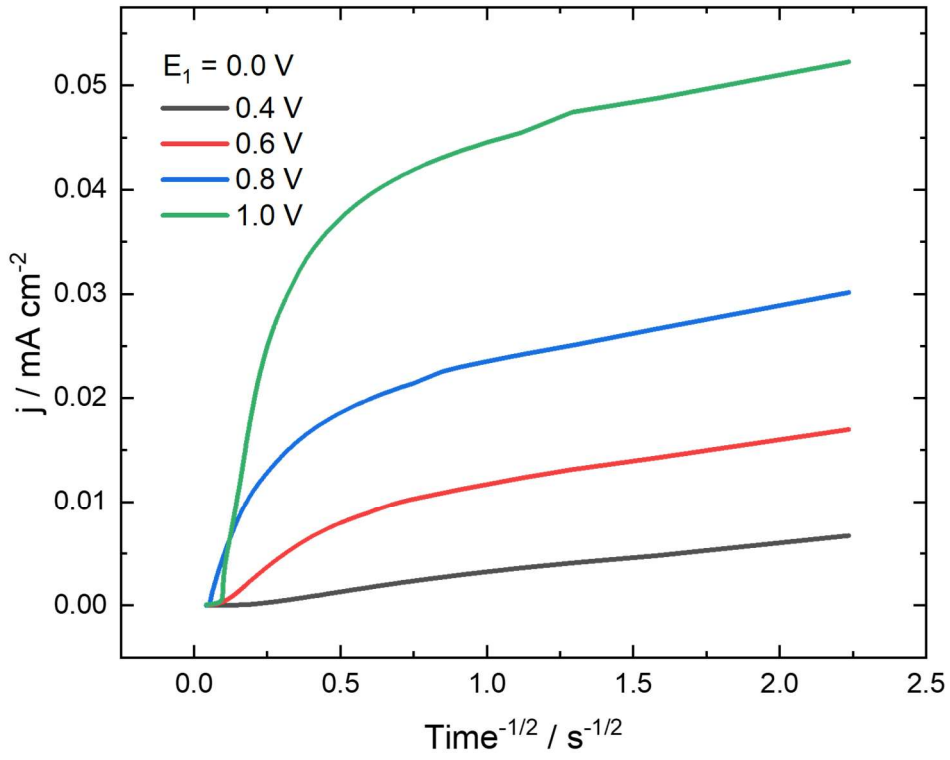

Figure 98 Cottrell analysis of the chronoamperometric response for the deintercalation of Na+ ions from the CuHCF lattice. Showing the E_1 potential of 0.0 V and the applied potential E_2 *vs.* SCE, from Figure 96.

4.2.2.2 Alternative time diffusion coefficient analysis

Now, using the same method outlined in section 3.2.2.2, diffusion coefficients were determined from the LAPS experiment for NiHCF and CuHCF, Figure 95 and Figure 96 respectively, using Equation 29. Using the same assumption and thickness for the FeHCF electrode, to maintain consistency, the analysis is applied to $t \geq 150$ s.

The results of the analysis on the LAPS experiment for NiHCF are given in Figure 99 and Figure 100 for the LAPS experiments on CuHCF.

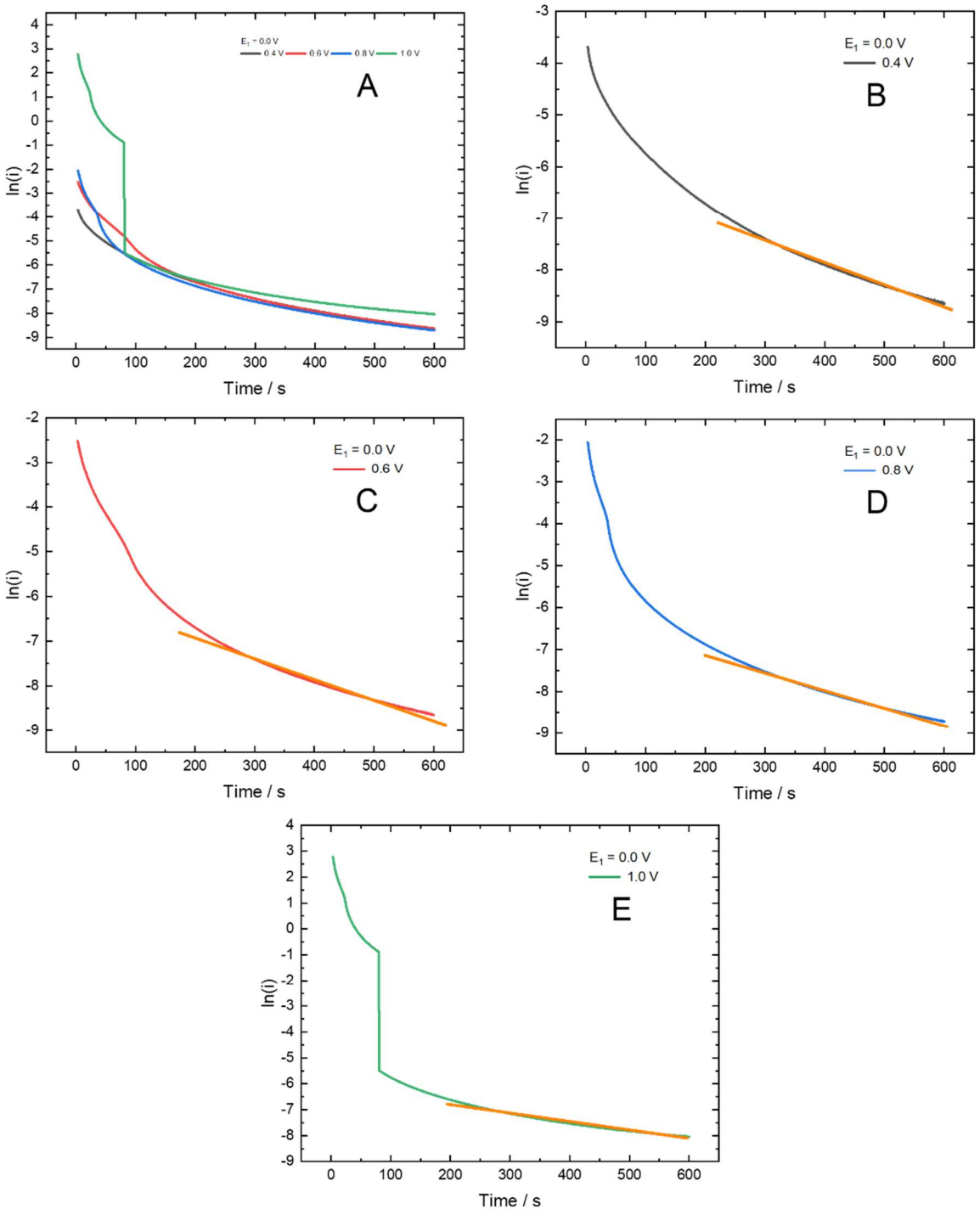

Figure 99 Potential dependent diffusion coefficient for the deintercalation of Na^+ ions into the NiHCF lattice. Showing A) the ln(i) *vs.* t plots for all E_2 values applied from E_1 = 0.0 V B-E) the individual plots for each E_2 and the linear region, all potentials are *vs.* SCE.

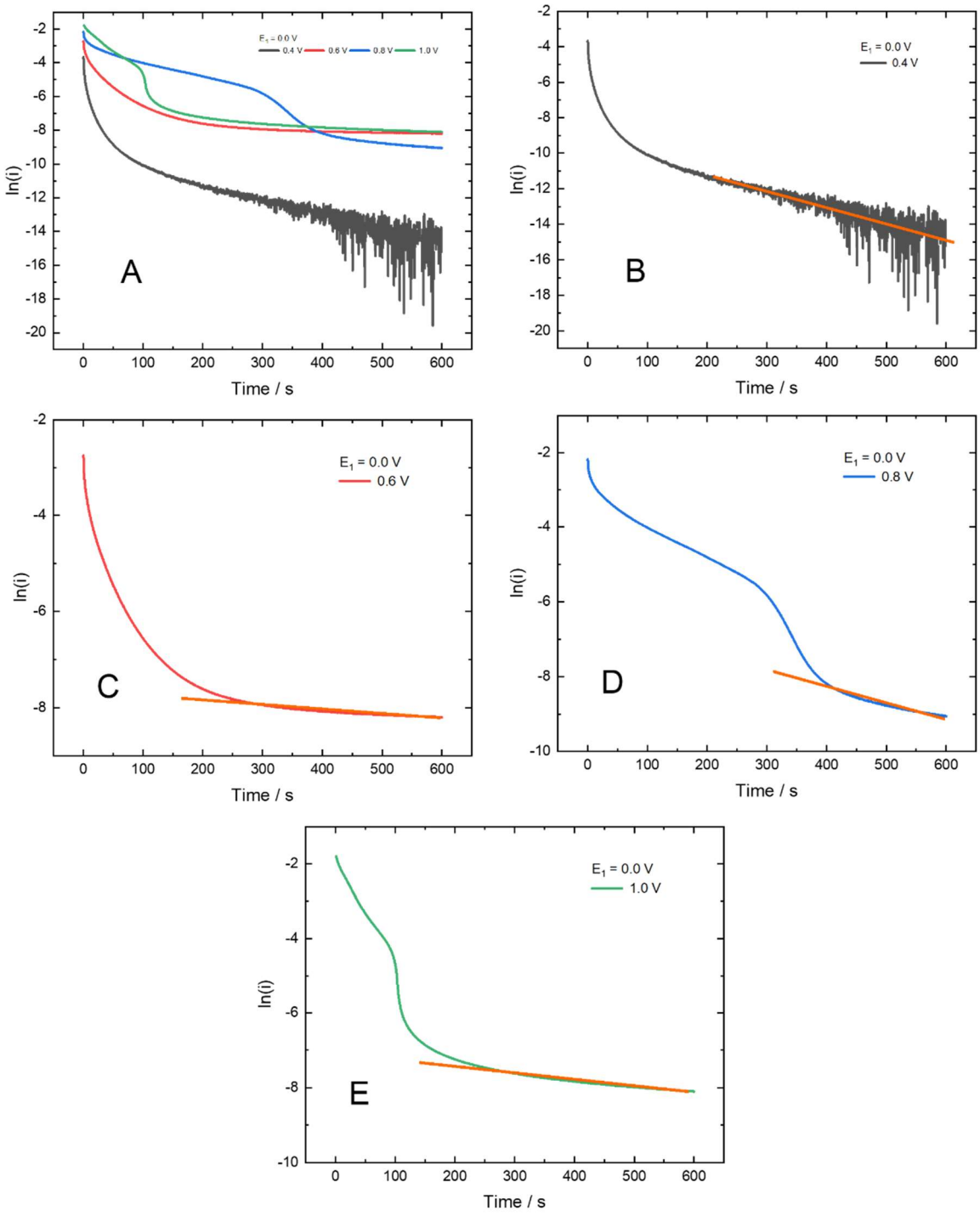

Figure 100 Potential dependent diffusion coefficient for the deintercalation of Na^+ ions into the CuHCF lattice. Showing A) the ln(i) *vs.* t plots for all E_2 values applied from E_1 = 0.0 V B-E) the individual plots for each E_2 and the linear region, all potentials are *vs.* SCE.

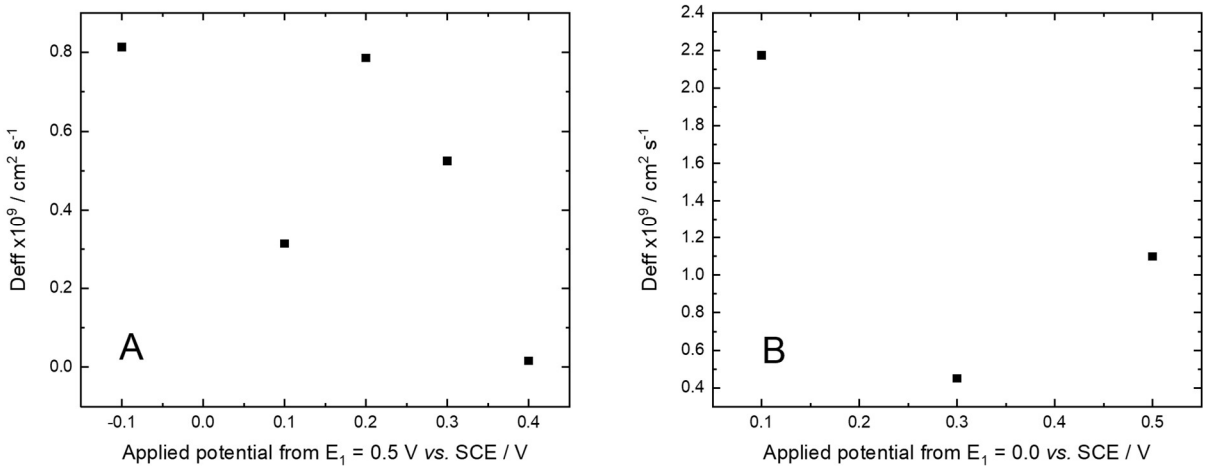

Figure 101 Comparison of the calculated diffusion coefficients from the linear region in the alternative diffusion coefficient analysis for the LAPS experiments on A) NiHCF and B) CuHCF.

The diffusion coefficient obtained for the loner time frame for both NiHCF and CuHCF are given in Figure 101 A and B respectively. The values for D_{eff} are all the order of magnitude of x 10^{-9} cm^2 s^{-1} and again in good agreement with the literature sources.[32] In both cases the value of D is varies as a function of the applied ΔE, reaching a lower value for the diffusion coefficient at a higher E_2 value. Suggesting that at these higher E_2 values we are under a diffusion control. This is also supported in both cases as we have gone past the maximum peak on the voltammetry and would therefore expect to be limited (controlled) by diffusion.

4.2.3 Chronocoulometry

The charge response from the LAPS experiments on NiHCF and CuHCF are given in Figure 102 and Figure 103,respectively.

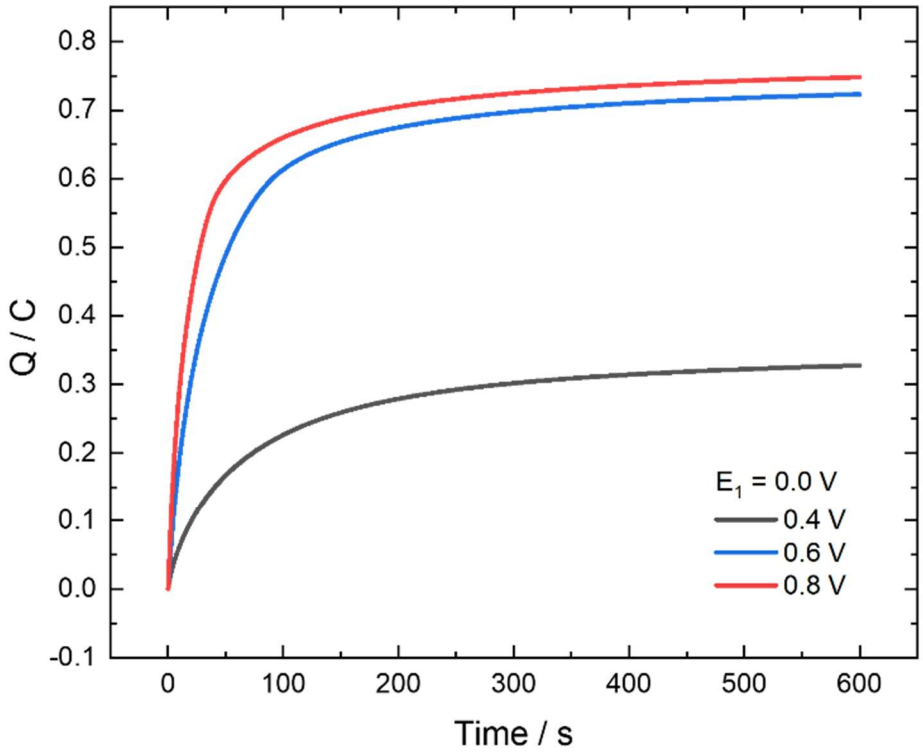

Figure 102 Chronocoulometry response for the large-amplitude potential step voltammetry for the deintercalation of Na^+ ions from NiHCF electrode. Showing the applied potential (E_2) from the E_1 potential of 0.0 V *vs.* SCE.

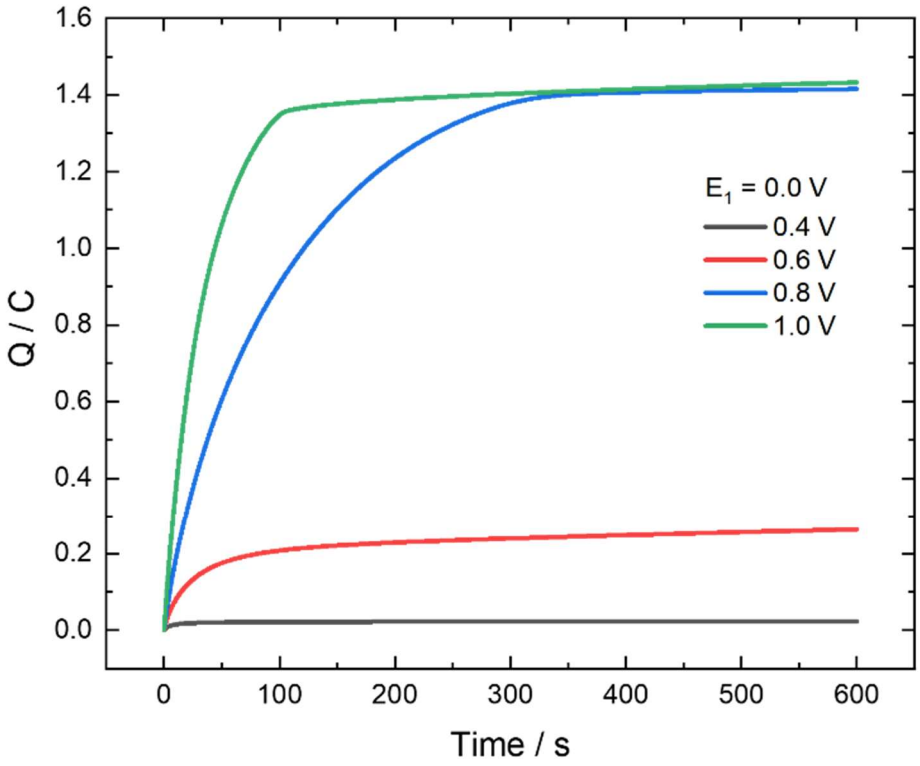

Figure 103 Chronocoulometry response for the large-amplitude potential step voltammetry for the deintercalation of Na^+ ions from CuHCF electrode. Showing the applied potential (E_2) from the E_1 potential of 0.0 V *vs.* SCE.

Following the integrated Cottrell analysis, Equation 23 yields the following results, for NiHCF Figure 104 and for CuHCF Figure 105.

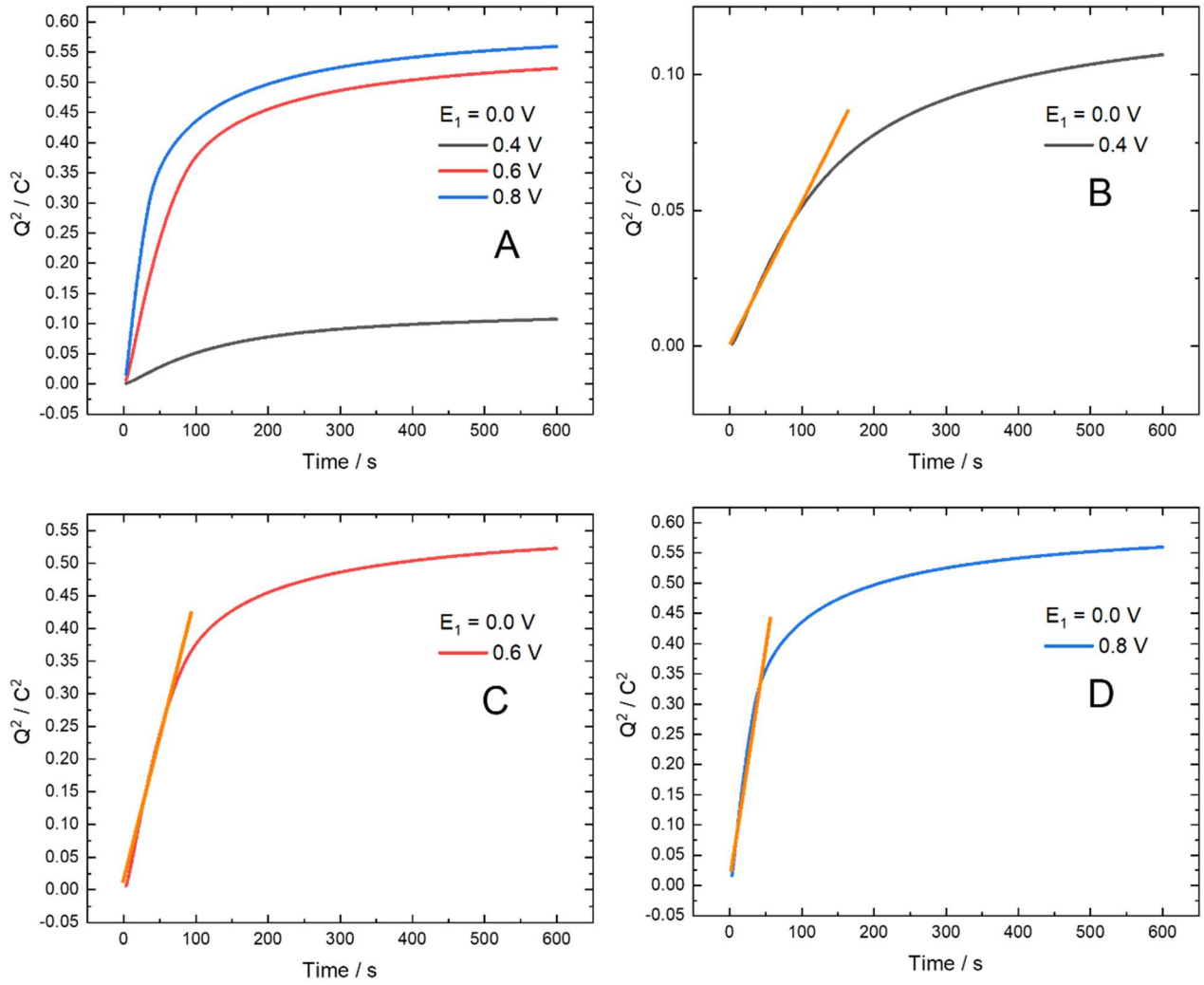

Figure 104 Integrated Cottrell analysis for diffusion coefficient for the deintercalation of Na^+ ions from the NiHCF lattice. Showing A) the Q^2 *vs.* t plots for all E_2 values applied from E_1 = 0.0 V B-D) the individual plots for each E_2 and the linear region, all potentials are *vs.* SCE.

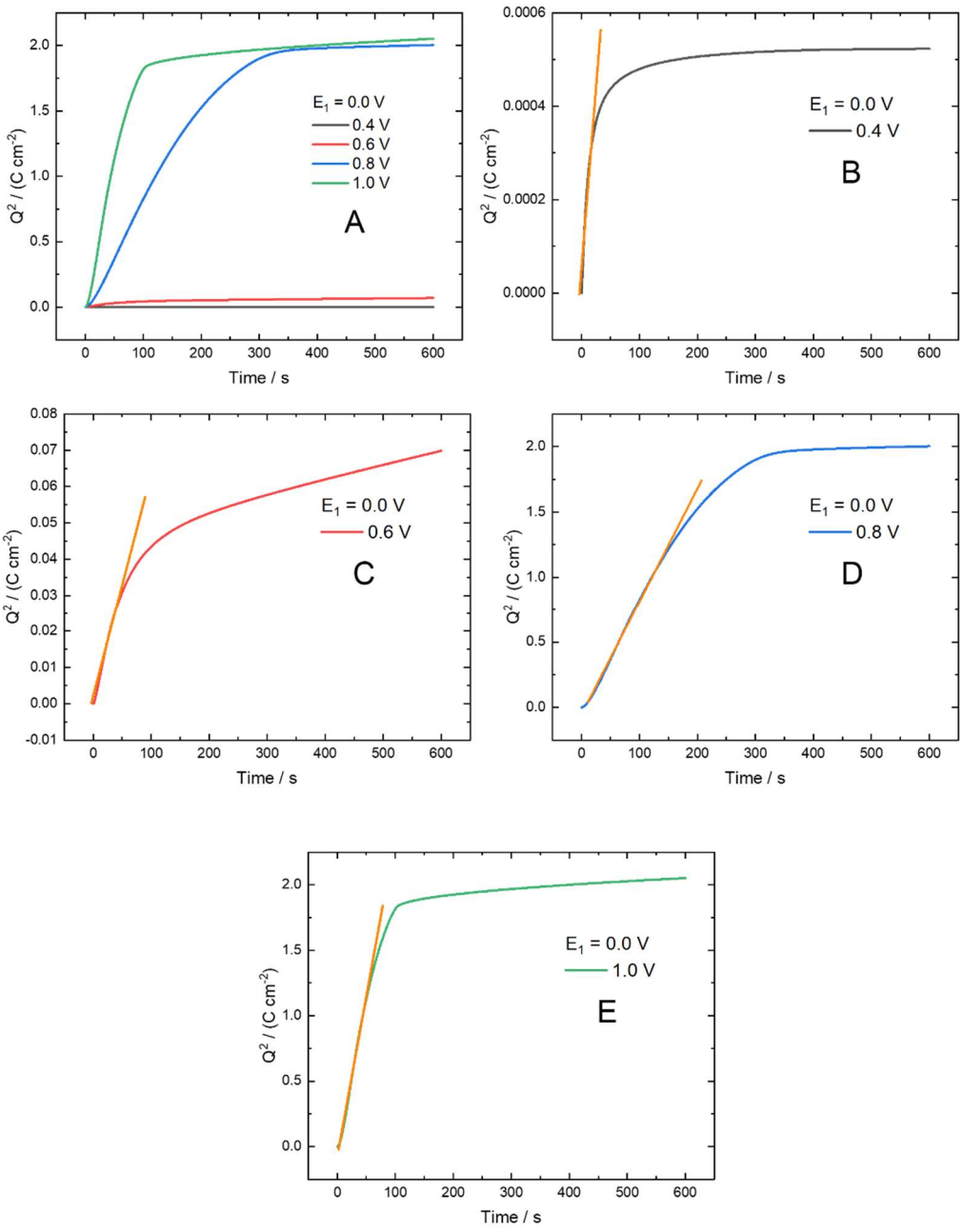

5

.

Figure 105 Integrated Cottrell analysis for diffusion coefficient for the deintercalation of Na^+ ions from the CuHCF lattice. Showing A) the Q^2 *vs.* t plots for all E_2 values applied from E_1 = 0.0 V B (E_2 = 0.4 V),C (E_2 = 0.6 V),D (E_2 = 0.8 V),E (E_2 = 1.0 V)) the individual plots for each E_2 and the linear region, all potentials are *vs.* SCE with the E_2 potential shown on the plot.

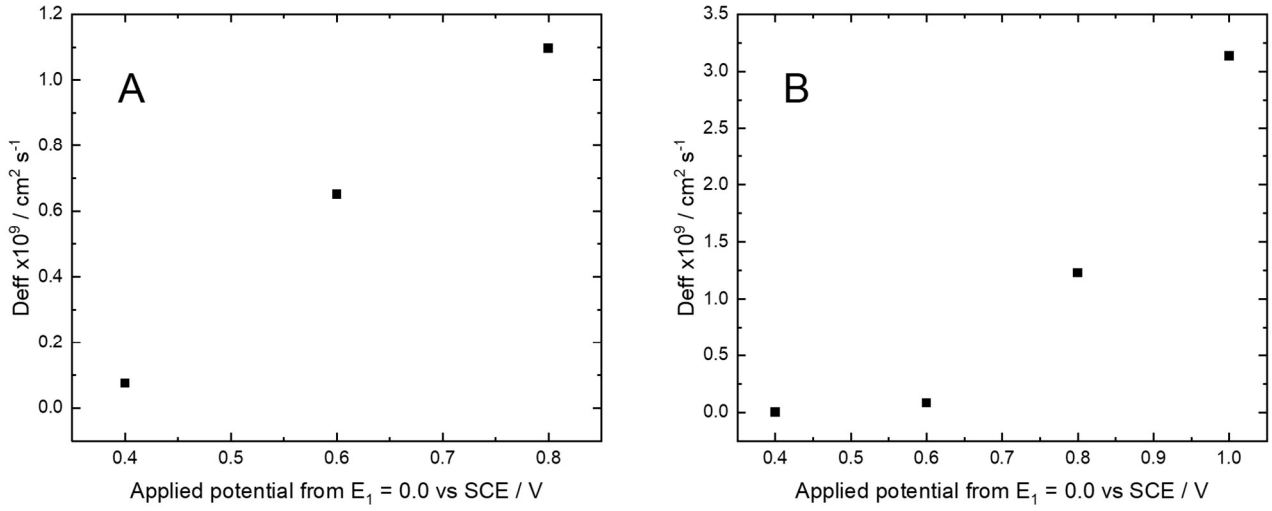

Figure 106 Comparison of the calculated diffusion coefficients from the linear region of the integrated Cottrell analysis of the LAPS experiments on A) NiHCF and B) CuHCF.

Figure 106 gives the calculated D_{eff} value or each E_2 value for NiHCF (Figure 106 A) and CuHCF (Figure 106 B). In each case the values are within the expected order of magnitude, x 10^{-9} cm^2 s^{-1}. The values are again potential dependant, reaching a maximum at the highest magnitude of ΔE. Furthermore, much like the deintercalation of Na^+ and K^+ from FeHCF (Figure 62 and Figure 67 B respectively) the rate of diffusion for the deintercalation is linear with respect to the driving force. This is to say the large the value of ΔE the faster the deintercalation. This suggests that in the initial period the kinetics of the reaction are limiting an the diffusion coefficient is responding to a grater driving force of the redox reactions.

4.2.4 EDE results and kinetics

The *in situ* spectroscopic results that follow focus on the Fe-C redox couple from Ni/Cu/Mn HCF. In each case the Fe K-edge position is defined by the 0.5 intensity of the normalised spectra.

4.2.4.1.1 Edge position as a function of time

Figure 107 and Figure 108 give the change in Fe K-edge position as a function of time for both NiHCF and CuHCF respectively. In both cases an E_1 of 0.0 V *vs.* SCE is used applying E_2 potentials for the oxidation of the Fe-C redox couple (deintercalation of Na^+). For each experiment Two cycles of E_2 to E_1 and the E_1 to E_2 are recorded, with each potential hold lasting for 600 s. Again, in accordance with the LAPS experiments the EDE results show a larger change in the oxidation state of Fe for greater magnitudes of ΔE. The high level of noise shown in the edge position results in

several different ways from bending of the cell window to beam damage of the sample to movement of the beam on the sample.

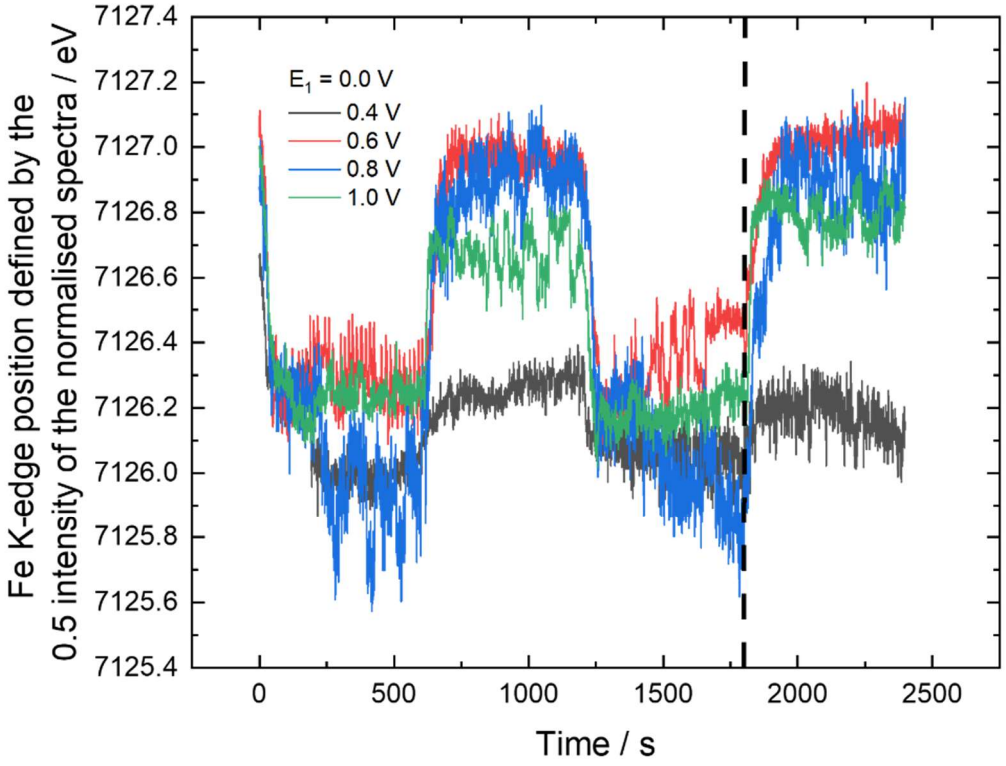

Figure 107 Change in edge position as a function of time from the *in situ* EDE experiments for Na^+ deintercalation from NiHCF. Showing the application of E_1 = 0.0 V from 0 – 600 s and 1200 to 1800 s. E_2 from 600 – 1200 s and 1800 to 2400 s for each E_2 potential applied.

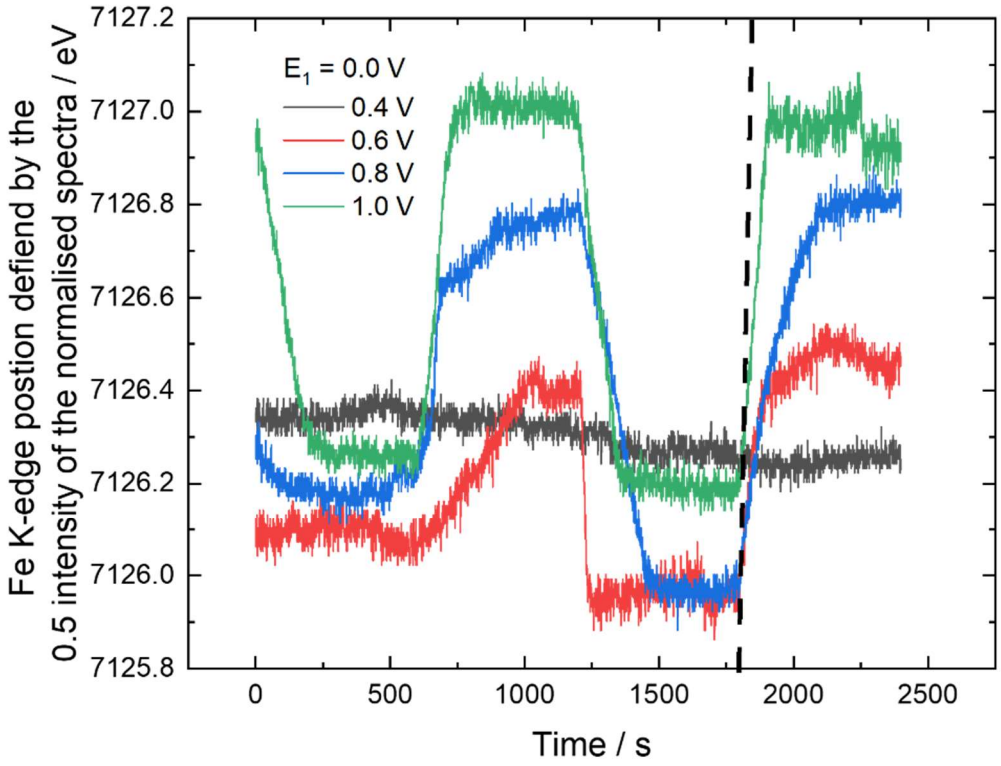

Figure 108 Change in edge position as a function of time from the *in situ* EDE experiments for Na^+ deintercalation from CuHCF. Showing the application of E_1 = 0.0 V from 0 – 600 s and 1200 to 1800 s. E_2 from 600 – 1200 s and 1800 to 2400 s for each E_2 potential applied.

4.2.4.1.2 Linear combination

Once again linear combination analysis was used to split the spectroscopy data into the oxidised and reduced components. For the case of NiHCF and CuHCF we have only investigated the oxidation process, due to complications during the beam time, the reduced species will act as the reactant and the oxidised the product. Below in Figure 109 and Figure 110 are the results of the LCA for NiHCF and CuHCF, respectively.

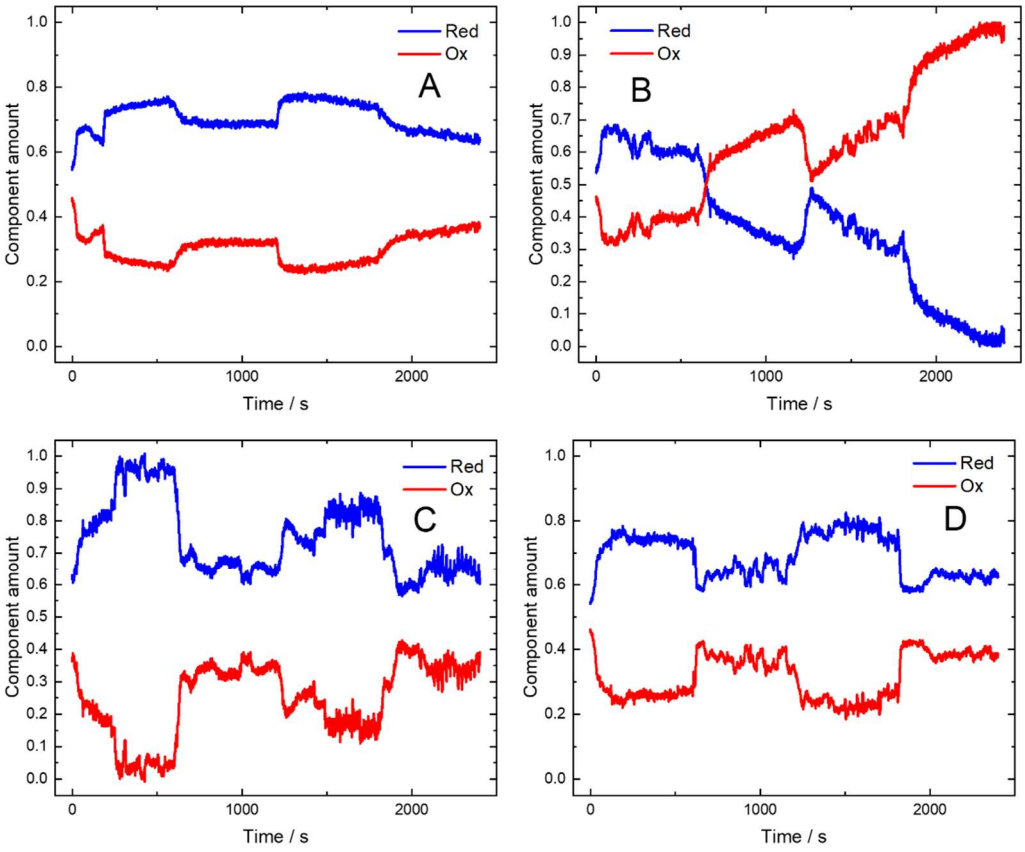

Figure 109 Linear combination analysis results as a function of time for Na^+ deintercalation from NiHCF. Showing the application of E_1 = 0.0 V in each case from 0 – 600 s and 1200 to 1800 s. Then for each E_2 value A) 0.4 V B) 0.6 V C) 0.8 V D) 1.0 V from 600 – 1200 s and 1800 to 2400 s. Where red is the fraction of Fe^{3+} and blue the fraction of Fe^{2+}.

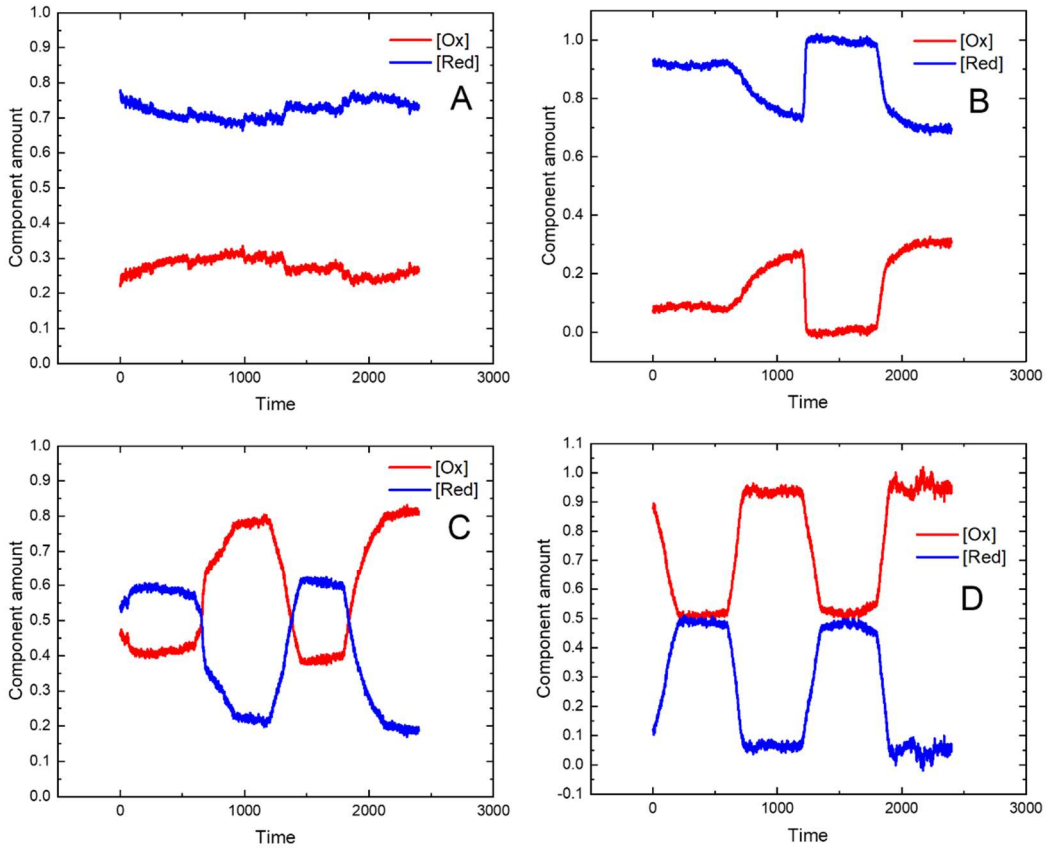

Figure 110 Linear combination analysis results as a function of time for Na+ deintercalation from NiHCF. Showing the application of E_1 = 0.0 V in each case from 0 – 600 s and 1200 s to 1800 s. Then for each E_2 value A) 0.4 V B) 0.6 V C) 0.8 V D) 1.0 V from 600 – 1200 s.

The results from the LCA will be used in the next section to calculate the charge resulting from the change in oxidation state of the Fe.

4.2.5 Charge comparison

Figure 111 and Figure 112 show the charge *vs.* time plots from both the spectroscopic results and the electrochemical results of the deintercalation of Na^+ ions for, NiHCF and CuHCF respectively. These plots were produced using the method outlined in section 3.2.4.

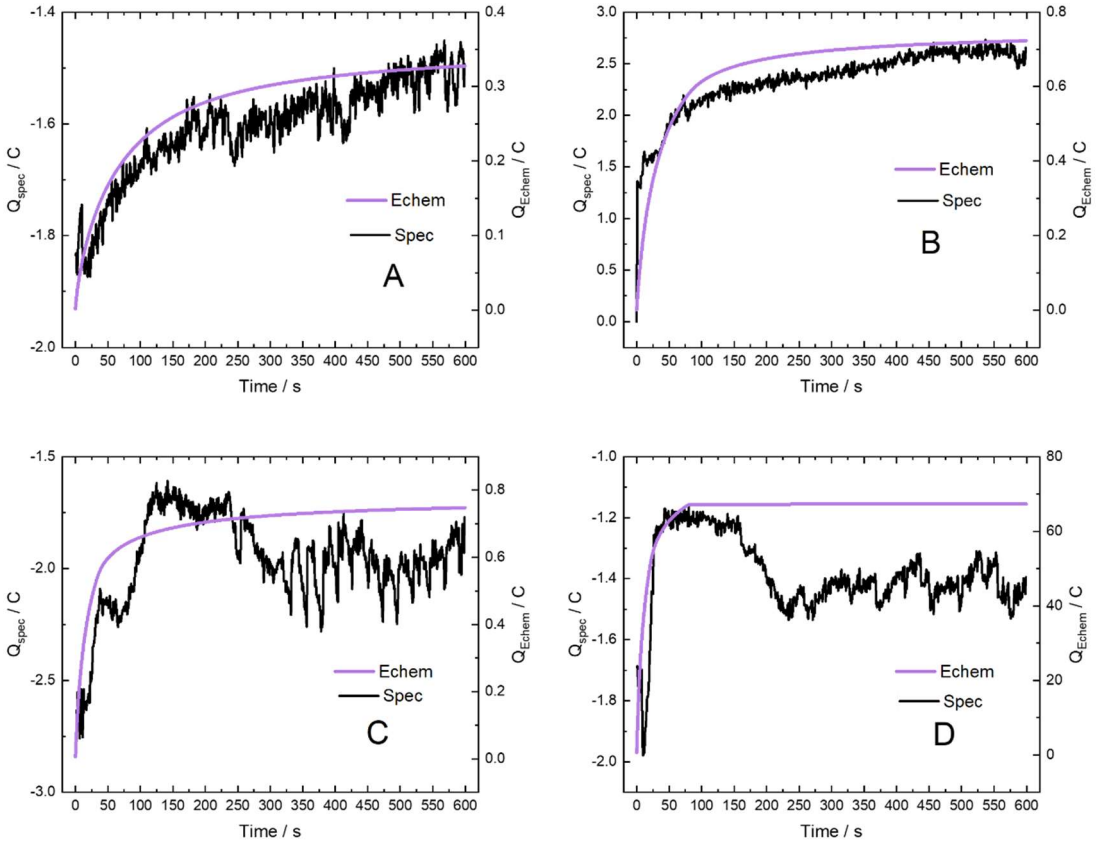

Figure 111 Comparison of calculated charges from the linear combination and electrochemical *in situ* EDE experiments, for Na^+ ion deintercalation from NiHCF. In each case E_1 = 0.0 V with A) E_2 = 0.4 V, B) E_2 =0.6 V, C) E_2 = 0.8 V, D) E_2 = 1.0 V *vs.* SCE.

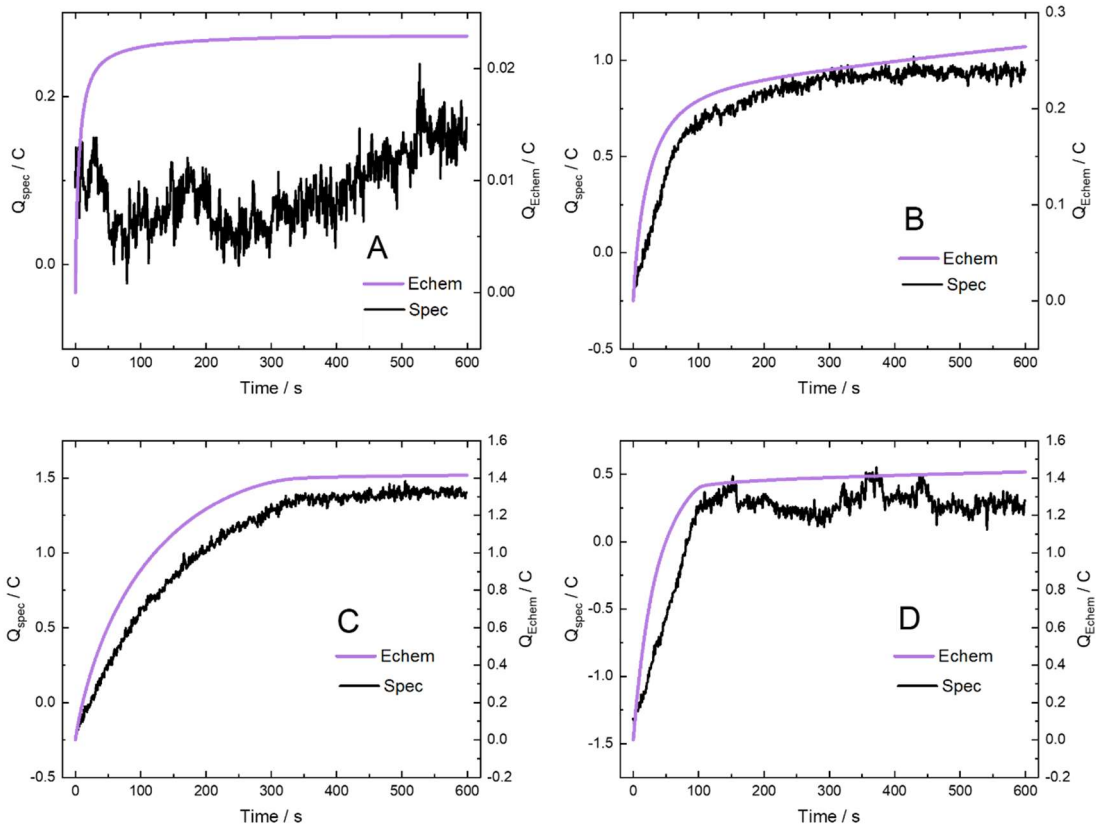

Figure 112 Comparison of calculated charges from the linear combination and electrochemical *in situ* EDE experiments, for Na^+ ion deintercalation from CuHCF. In each case E_1 = 0.0 V with A) E_2 = 0.4 V, B) E_2 =0.6 V, C) E_2 = 0.8 V, D) E_2 = 1.0 V *vs.* SCE.

In both cases exponentials are fitted to the Q *vs.* time curves for the spectroscopy. and electrochemical currents, giving the results shown in Figure 113. Where Figure 113 A corresponds to the intercalation of Na^+ form the NiHCF lattice and Figure 113 B the deintercalation from the CuHCF lattice.

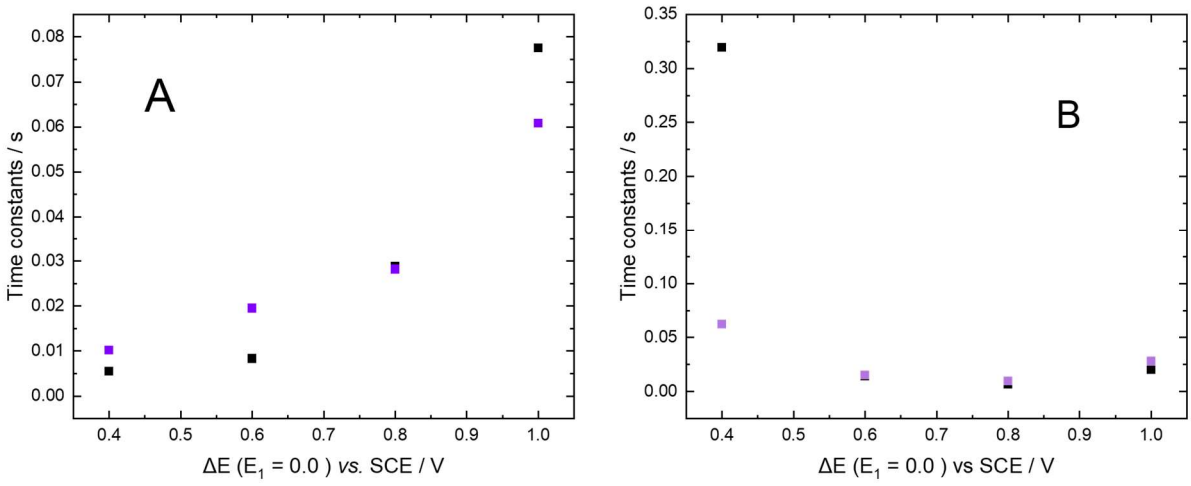

Figure 113 Time constant comparison from the Q *vs.* t plots for A) NiHCF and B) CuHCF. Where black is the time constants from the spectroscopy and purple the time constants from the electrochemistry.

In both cases the time constants for both charges are very similar. Except for the initial value in Figure 113 B where ΔE = 0.4 V, this larger difference results from the small change in edge position seen for this small magnitude of ΔE, suggesting that most of the current response comes from other processes not the redox of Fe-C. These data sets contrast with the time constants seen for the electrochemistry and spectroscopy. For the deintercalation process in FeHCF of Na^+ ions as we do not see a the lagging of the spectroscopic response. This suggests that the conductivity of the Ni and Cu HCF electrodes is less effected by the removal of cation.

As discussed in section 1.3 and section 1.4, it is recorded throughout the literature the importance that the C coordinated metal has on the conductivity of MHCF materials electrodes.[75,79] Therefore in the case of NiHCF and CuHCF as there is no change to the C coordinated metal (remains Fe) and as Ni and Cu are inactive during the redox reaction it comes to no surprise that we see similar results for these materials when looking at the charge comparisons.

What is interesting when comparing these results with those of the deintercalation of Na^+ from FeHCF across the Fe-N redox couple (Figure 84 B) there is less difference in the ET (from the spectroscopy) and the CEIT (from the electrochemistry) for Ni/Cu HCF than there is for FeHCF, during the transition from PW to PB. This confirms that the effect of the overall conductivity of the material is less determined by Fe-C redox couple compared to the Fe-N redox couple, as less to no lag is seen in these results.

4.3 Conclusions

In this chapter the deintercalation of Na+ ions from NiHCF and CuHCF is investigated. Again, the diffusion coefficients for the deintercalation process were found to be potential dependent and therefore correspond to the driving force. The calculated diffusion coefficient from each method is summarised in **Table 18**. From these values it is clear to see that the deintercalation process from CuHCF is faster than that from NiHCF. These values are supported by the value for the rate of the redox reaction, derived using the NS method. Which for NHCF is 5.90×10^{-6} m s^{-1} and for CuHCF is 9.97×10^{-5} m s^{-1}. Showing that CuHCF has the faster redox reaction.

Table 18 Comparison of derived diffusion coefficients for deintercalation of Na^+ ions from NiHCF and CuHCF.

Technique	Diffusion coefficient for NiHCF x 10^{-9}/ cm s^{-1}	Diffusion coefficient for CuHCF x 10^{-9}/ cm s^{-1}
Cyclic voltammetry	Intercalation: 8.61 ± 3.2 Deintercalation: 7.83 ± 5.9	Intercalation: 9.1 ± 1.23 Deintercalation: 10.0 ± 1.9
Alternative diffusion coefficient	0.32 – 0.44	0.1 – 0.85
Chronocoulometry	0.1 – 1.1	0.01 - 3.25

Then the spectroscopy results are analysed to separate the ET from the CIET kinetics. What we see is little difference in time constant between electrochemical charge and the charge resulting from the change in oxidation state. This suggests that unlike in FeHCF where the conductivity of the material was influencing the rate of ET, the redox mechanism of the Fe-C couple is not affected by the conductivity of the material and varies as a function of the driving force becoming more insulting as the ions are deintercalated from the lattice. Low-spin iron has fewer unpaired electrons compared with the high-spin iron, meaning that low-spin iron will have a larger band gap and therefore be more insulating. These different spin states effect the band gap of the material and therefore the conductivity of the material changes. The mix of spin states from Fe^{2+}/Fe^{3+} therefore leads to less conductive behaviour in FeHCF compared with other MHCFs.[79]

Chapter 5 Dual edge study of sodium ion (de)intercalation in CoHCF and MnHCF.

5.1 Aim of this chapter

As mentioned in the introduction XAFS is an important tool in the investigation of battery materials, especially those that contain multiple transition metals.[130] There are many examples of using XAFS to study these materials ranging from Lithium iron phosphates (LIPs) to Lithium nickel manganese cobalt oxides (NMCs).[131–135] In these studies XAFS has been used as a powerful tool to better understand the complicated reaction mechanisms occurring during battery cycling. This is because XAFS can provide information on the valance states during the cycling of various elements and on the local structure, such as coordination number and bond length, of those elements. Most of the current XAFS studies of battery materials focus on one transition metal at a time. Some examples do attempt to measure multiple edges at once but due to the limitations of scanning beamlines, a true simultaneous measurement is impossible, and each metal edge is measured separatly.[87] However, polychromatic beam used on EDE enables us to truly measure multiple edges simultaneously. Spectra for a wide energy range can be obtained instantaneously. In the case of CoHCF and MnHCF the K-edge positions for Co (7716 eV), Mn (6539 eV) and Fe (7112 eV) are close enough to allow them to be measured at the same time. An example of the instantly collected dual edge spectra is given in Figure 114. Where Figure 114 A is a dual edge spectra for CoHCF showing the Fe (blue line) and Co (green line) K-edges and Figure 114 B a dual edge spectra from MnHCF showing the Mn (brown line) and Fe (blue line) K-edges.

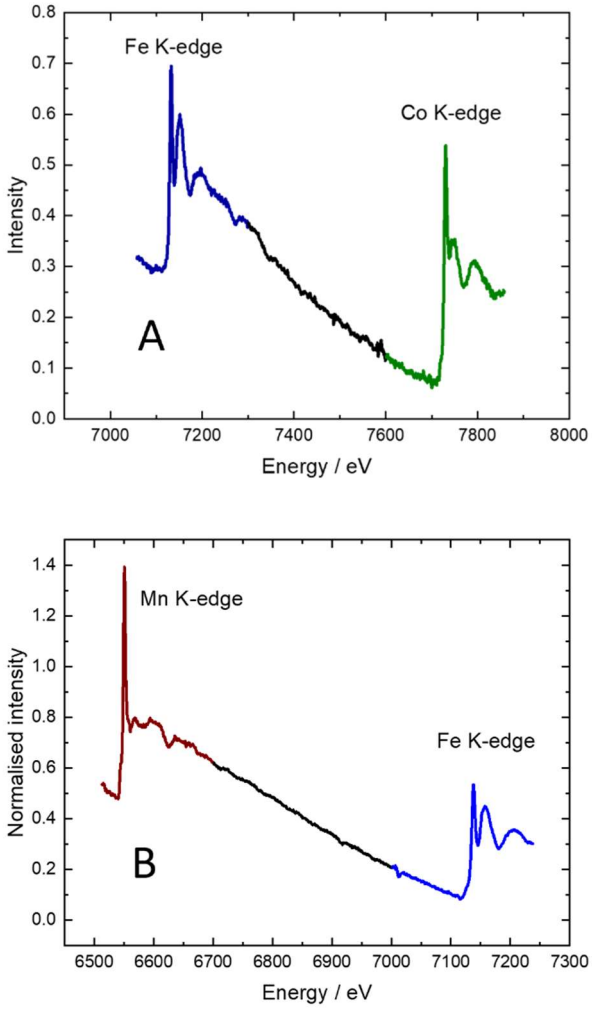

Figure 114 Example of dual edge spectra taken during *in situ* EDE experiments. A) showing a dual Fe (blue line) and Co (green line) K-edge and B) showing a dual Mn (brown line) and Fe (blue line) K-edge spectrum.

This technique therefore allows the investigation of both metal sites at the same time during cycling. However, the method is not without issues, due to collecting such a wide energy range resolution on the XANES region for the metal with the K-edge at the lower range is lost. As well as the EXAFS resolution on the transition metal at the higher K-edge. Furthermore, maintaining the focal point on the sample becomes even more important when attempting to measure two edges simultaneously. However, experimental aspects such as window pulsing caused by pumping of the solution (when used) and heating of the sample make this more difficult. Aside from these drawbacks this technique does allow for an insightful investigation into the relative changes in oxidation state of each metal during oxidation and reduction in a truly simultaneous manner.

5.2 Cobalt hexacyanoferrate

As mentioned above CoHCF is an excellent candidate for the simultaneous dual edge EDE study, due to the K-edges of Co and Fe being close in range. In Figure 115 the voltammogram of CoHCF in 2 M $NaNO_3$ at pH 2, taken in the *in situ* cell, is given. With a start potential of 0.6 V *vs.* SCE sweeping down to 0.0 V *vs.* SCE at a scan rate of 1.0 mV s^{-1}. The first redox peak between 0.1 and 0.6 V *vs.* SCE (I/II) is attributed to the Co-N redox couple. Whilst the redox peak between 0.6 and 1.1 V *vs.* SCE (III/IV) is attributed to the Fe-C redox couple. [21]From the voltammogram an E_1 potential of 0.6 V *vs.* SCE is chosen, with the corresponding oxidation states $NaCo^{3+}[Fe^{2+}(CN_6)]$. From this potential we can study the reduction of the Co-N redox couple (intercalation of Na^+) and the oxidation of the Fe-N redox couple (deintercalation of Na^+) by applying lower or higher E_2 potentials respectively.

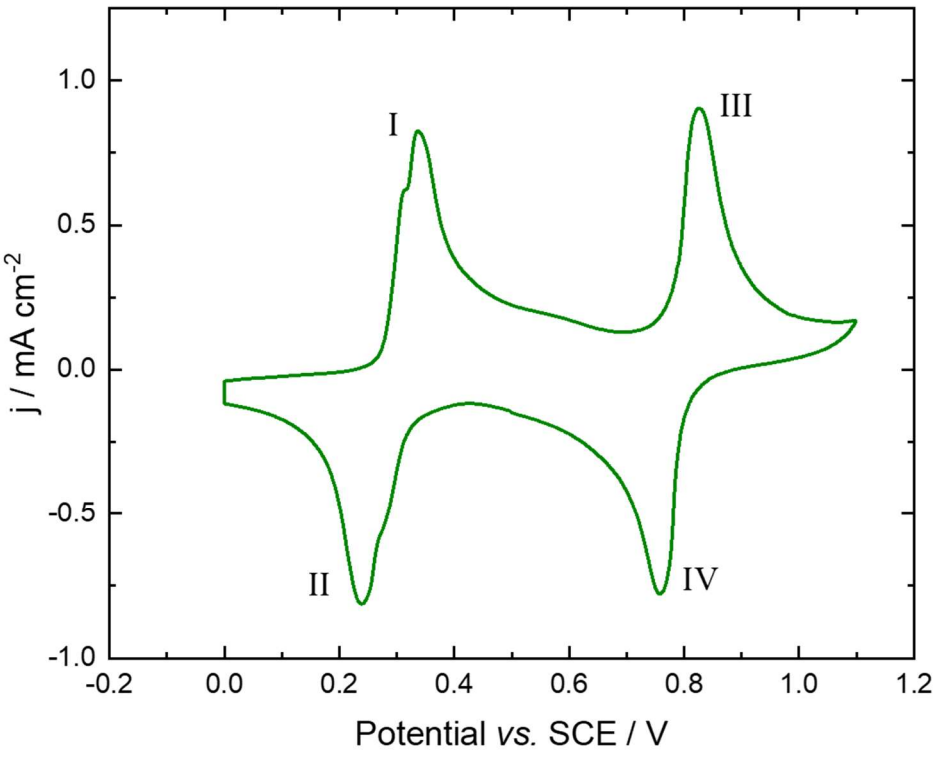

Figure 115 Cyclic voltammetry of an 8 mg cm^{-2} CoHCF on Toray carbon paper electrode in 2 M $NaNO_3$ at pH 2. With a scan rate of 0.5 mV s^{-1}. Carried out at room temperature (around 22 °C – 25 °C) in the *in situ* cell (see Figure 20).Peaks I/II showing the Co-N redox couple and III/IV the Fe-C redox couple. Starting at 0.5 V *vs.* SCE.

Once again, we used the LAPS experiments to investigate the effect of driving force (potential) on the rate of change of oxidation compared with the electrochemical response. **Table 19** gives a summary of the applied potentials for each redox couple.

Table 19 Showing the E_1 and E_2 potentials for the LAPS experiments of CoHCF.

Material	Redox couple investigated	E_1 *vs.* SCE / V	E_2 *vs.* SCE / V
CoHCF	Co-N	0.6	0.5/0.4/0.3/0.2/0.1
	Fe-N	0.6	0.7/0.8/0.9/1.0/1.1

5.2.1 Chronocoulometry

The charge response for the *in situ* LAPS experiments for CoHCF are given in Figure 116 and Figure 117. With Figure 116 corresponding to the intercalation of Na^+ ions and the reduction of Co-N and Figure 116 the deintercalation of Na^+ ions and the oxidation of Fe-C. Figure 118 and Figure 119 corresponds to the integrated Cottrell analysis of the LAPS experiments for the reduction of Co-N and the oxidation of Fe-C respectively. Figure 120 compares the derived diffusion coefficients from the integrated Cottrell analysis, with Figure 120 A showing the diffusion coefficients as a function of the applied potential for the intercalation of Na^+ ions (reduction of Co-N) and Figure 120 B the deintercalation of Na^+ ions (oxidation of Fe-C). Again, a clear link is seen between the magnitude of the driving force and the rate of diffusion, with the diffusion coefficient being potential dependant. The range of diffusion coefficients for both (de)intercalation of Na^+ ions to/from CoHCF are lower than those seen for the (de)intercalation of Na^+ ions to/from FeHCF, suggesting that the diffusion is more limiting in the case of CoHCF.

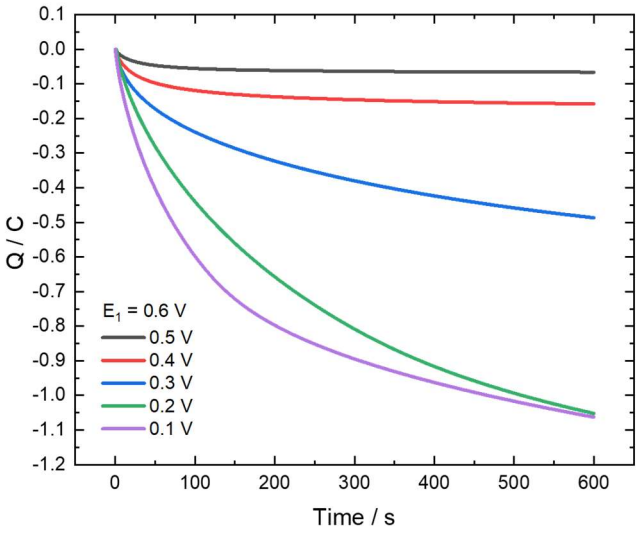

Figure 116 Chronocoulometry response for the large-amplitude potential step voltammetry for the intercalation of Na^+ ions into CoHCF electrode. Showing the applied potential (E_2) from the E_1 potential of 0.6 V *vs.* SCE.

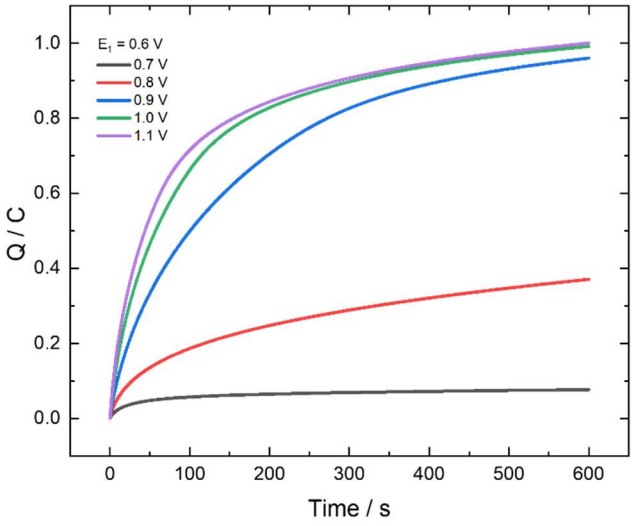

Figure 117 Chronocoulometry response for the large-amplitude potential step voltammetry for the deintercalation of Na^+ ions into CoHCF electrode. Showing the applied potential (E_2) from the E_1 potential of 0.6 V *vs.* SCE.

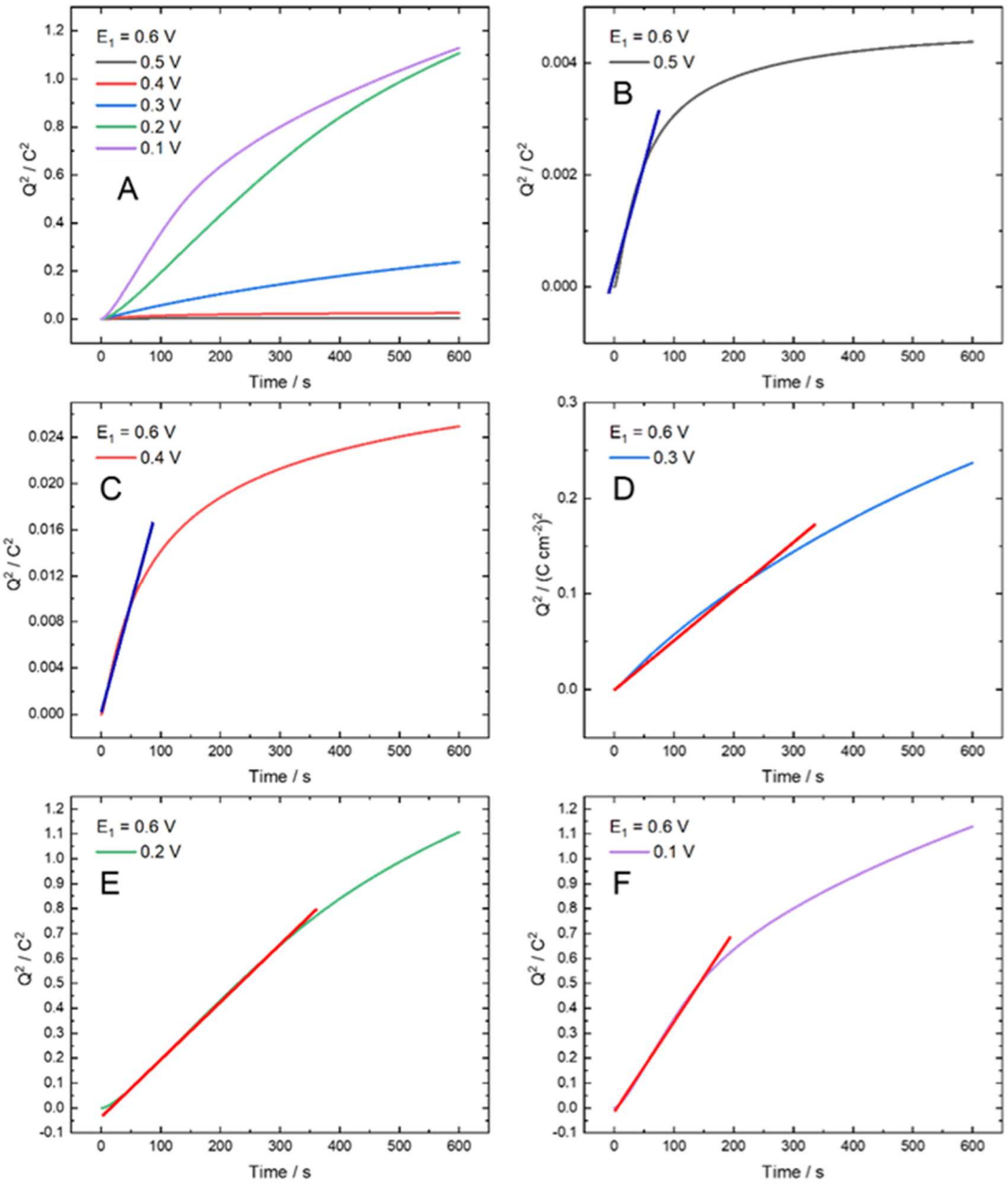

Figure 118 Integrated Cottrell analysis for diffusion coefficient for the intercalation of Na^+ ions from the CoHCF lattice. Showing A) the Q^2 *vs.* t plots for all E_2 values applied from E_1 = 0.0 V B-F) the individual plots for each E_2 and the linear region, all potentials are *vs.* SCE.

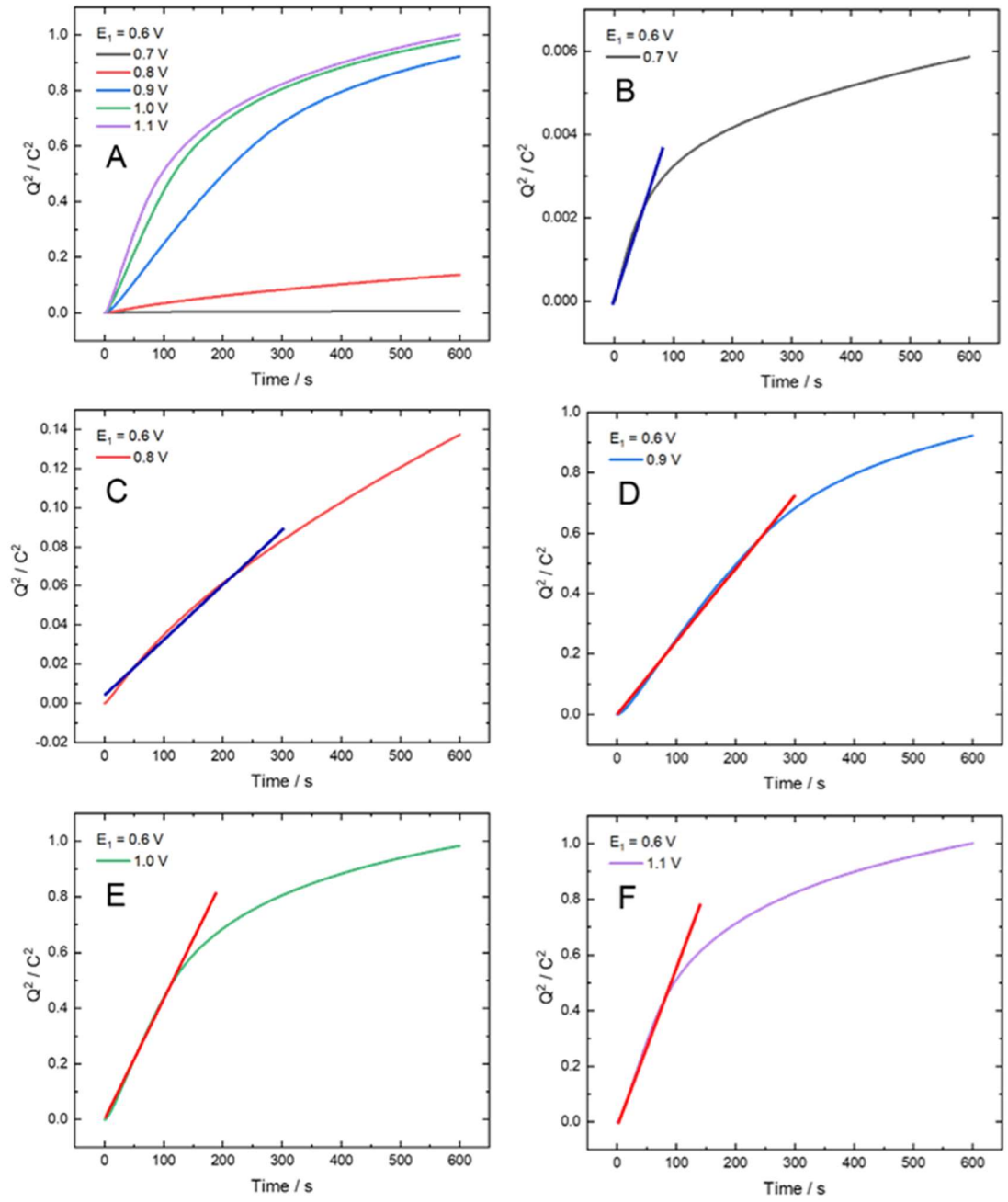

Figure 119 Integrated Cottrell analysis for diffusion coefficient for the deintercalation of Na^+ ions from the CoHCF lattice. Showing A) the Q^2 *vs.* t plots for all E_2 values applied from E_1 = 0.6 V B-F) the individual plots for each E_2 and the linear region, all potentials are *vs.* SCE.

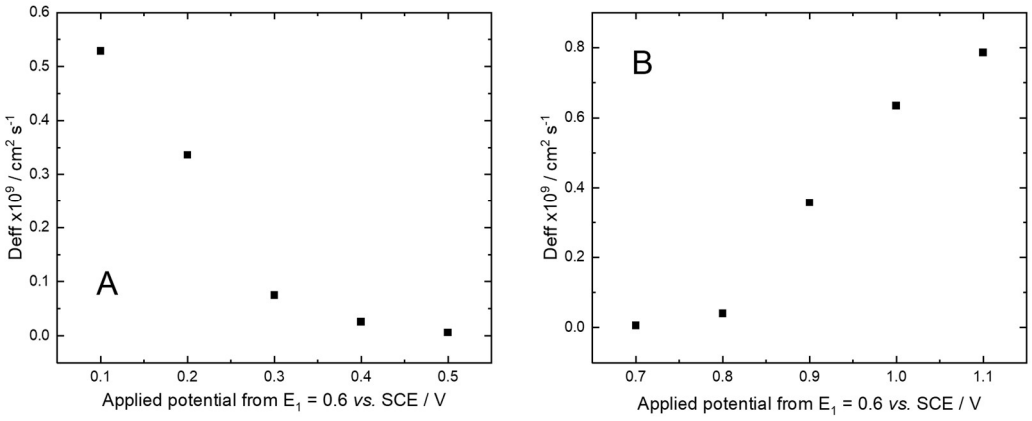

Figure 120 Comparison of the calculated diffusion coefficients from the linear region of the integrated Cottrell analysis of the LAPS experiments on A) Intercalation of Na^+ ions and B) deintercalation of Na^+ ions into/from the CoHCF lattice.

5.2.2 Simultaneous dual edge EDE experiment

For the analysis of the XAFS results in this section it is important to note due to drifting in the intensity of the XAFS response, resulting from gas formation in the sample, fluctuation of the path length due to window benign or sample degradation, LCA analysis is no longer possible. Therefore, the results will now be discussed in terms of ΔeV which corresponds to the change in the energy of the K-edge, still defined by the energy at the 0.5 intensity of the normalised spectra. This ΔeV value directly corresponds to the change in oxidation state of the metal and can therefore be discussed as the charge resulting from the application of E_2 from E_1.

Figure 121 shows the results of the LAPS experiments carried out *in situ* during the EDE experiment for CoHCF, investigating the reduction of Co-N in an Na^+ electrolyte. Figure 121 A gives the corresponding Chronocoulometry from the LAPS experiments, showing that as we increase ΔE we obtain a large value for the corresponding charge. Figure 121 B shows how the Co K-edge varies as a function of time for each applied E_2 value and Figure 121 C the corresponding Fe K-edge taken simultaneously with the Co K-edge.

Across this potential range (0.6 V to 0.1 V *vs.* SCE) it is expected that the resulting charge will come mainly from the reduction of the Co-N, with a change of approximately 1.5 – 2.0 eV corresponding to the change of oxidation state i.e., Co^{3+} to Co^{2+}. Figure 121 B shows quite clearly that as we increase ΔE the amount and rate of change in the oxidation state of Co is affected, with a larger increase seen in ΔeV for larger ΔE. What is interesting in Figure 121 C that the Fe shows very little change in oxidation state (a change of around 1.0 to 1.5 eV would correspond to one unit of oxidation state as shown in Chapter 3 and Chapter 4) suggesting that most of the Fe has

already been reduced at 0.6 V *vs.* SCE. Figure 121 D gives a visual representation of how the change in ΔeV changes (faded line) alongside the charge resulting from the LAPS experiments. The quality of the Fe K-edge data given in Figure 121 and Figure 122 is compromised due to the limiting energy range of the Fe EXAFS data, resulting in the 0.5 intensity of the spectra being more sensitive to baseline drift and/or noise in the spectra. However, the reliability of the edge position at the Co K-edge data is better, as the larger energy range after this edge means the 0.5 intensity is better defined.

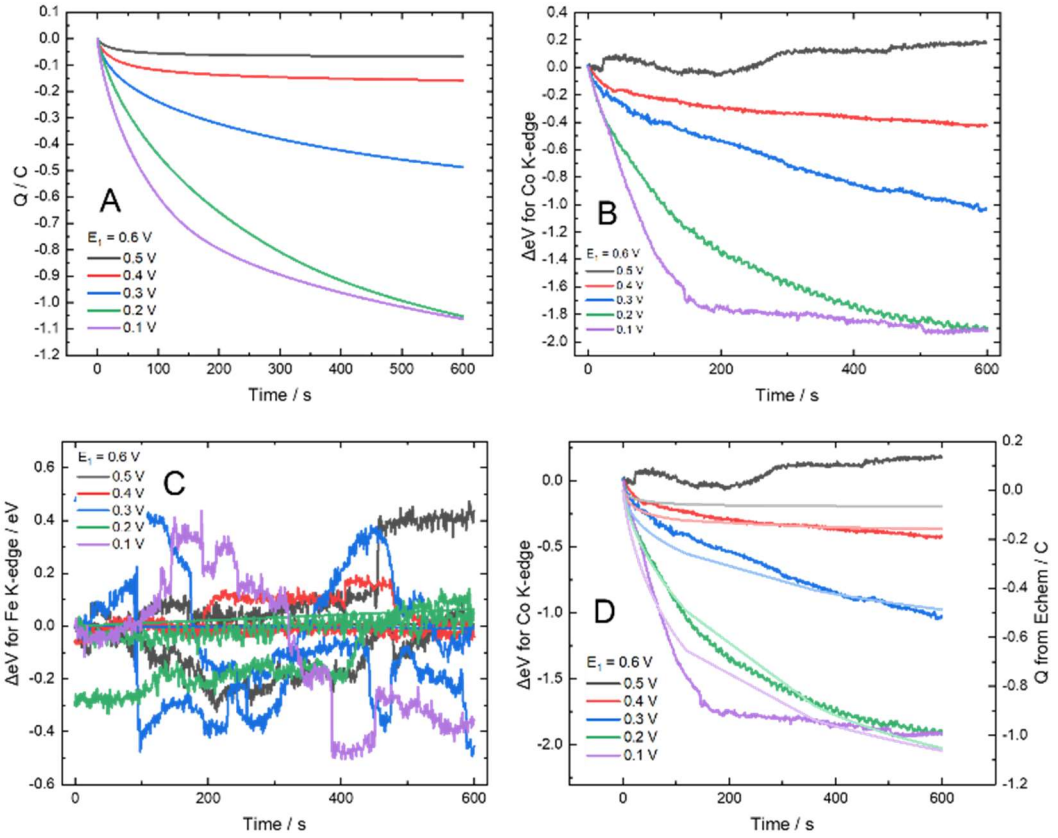

Figure 121 Results of the *in situ* EDE experiments for the reduction of Co-N in CoHCF. A) the charge *vs.* time results from the LAPS experiments. B) The amount of change in the Co K-edge for each applied E_2 (shown in figure) as a function of time. C) The amount of change in the Fe K-edge for each applied E_2 (shown in figure) as a function of time and D) showing a comparison of the ΔeV value for the Co K-edge *vs.* the charge resulting from the electrochemical result (faded line).

Figure 122 now shows the effect of applying oxidising E_2 potentials from 0.6 V *vs.* SCE, which specifically focusses on the Fe-C redox couple. This is confirmed by Figure 122 B which shows an insignificant change in the oxidation state of Co compared with Figure 122 C which at the larger ΔE gives a change in oxidation state of roughly 0.8 eV. Figure 122 D gives a visual representation of how the ΔeV changes alongside the charge from the electrochemistry, clearly showing less lag between the electrochemical (CIET) results and the spectroscopic results (ET). These results for the comparison (Figure 122 D) are in agreement with the results seen in section 4.2.5, looking at the charge comparison for NiHCF and CuHCF, showing less lag for the carbon bound iron at higher magnitudes of ΔE.

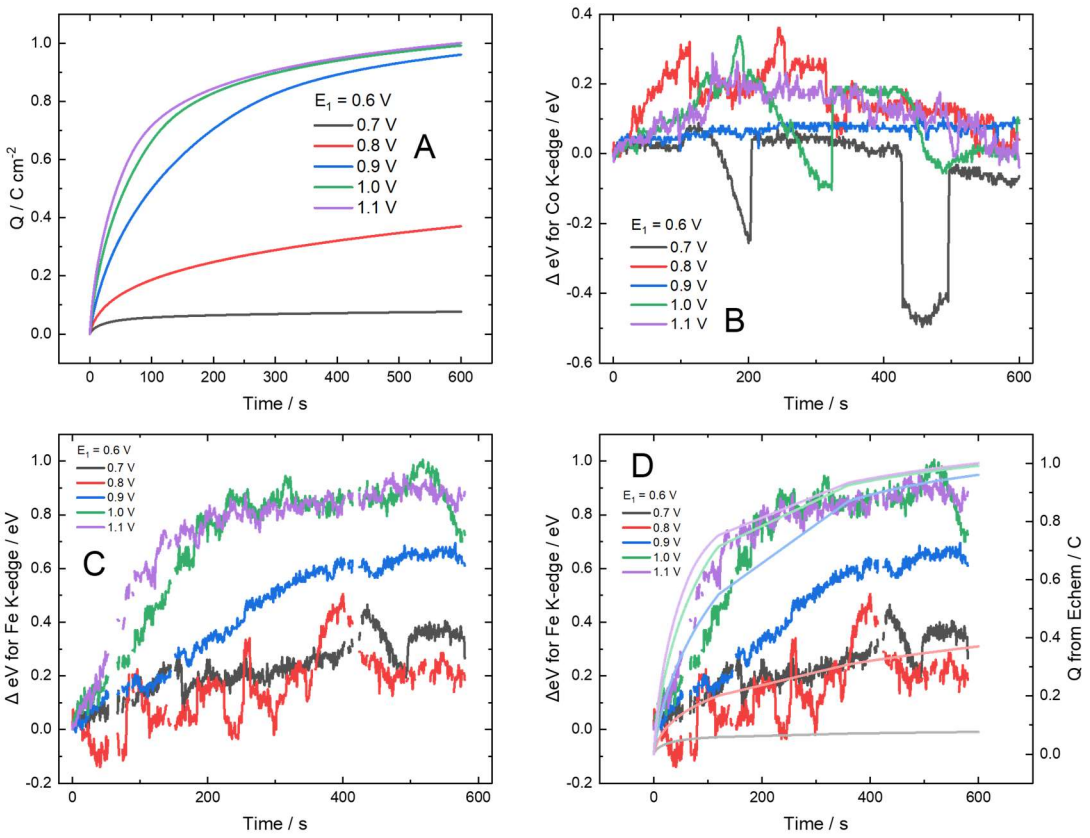

Figure 122 Results of the *in situ* EDE experiments for the oxidation of Fe-C in CoHCF. A) the charge *vs.* time results from the LAPS experiments. B) The amount of change in the Co K-edge for each applied E_2 (shown in figure) as a function of time. C) The amount of change in the Fe K-edge for each applied E_2 (shown in figure) as a function of time and D) showing a comparison of the ΔeV value for the Fe K-edge *vs.* the charge resulting from the electrochemical result (faded line).

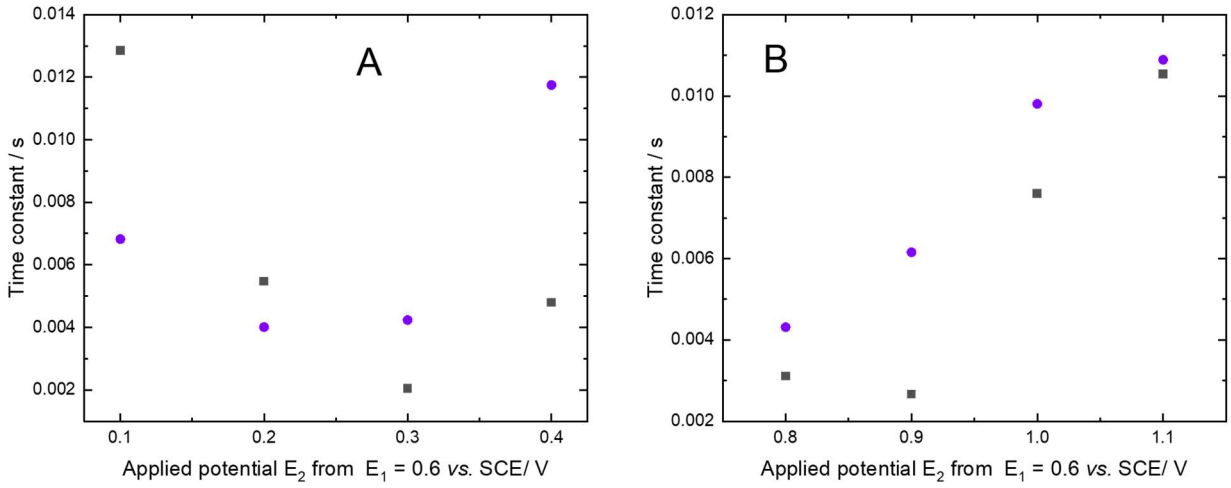

Figure 123 Time constant comparison of the charge from the LAPS experiments and change in ΔeV as a function of time. A) the time constant associated with the charge from the LAPS experiment and the time constant associated with ΔeV for the Co K-edge for the reduction of Co-N and B) the time constant associated with the charge from the LAPS experiment and the time constant associated with ΔeV for the Fe K-edge for the oxidation of Fe-C. Where black is the time constants from the spectroscopy and purple the time constants from the electrochemistry.

Once again, we can analyse the corresponding exponentials for each *in situ* EDE LAPS experiment. However, this time an exponential fitted to the ΔeV and charge transients , with Figure 123 showing the result for these fittings. Figure 123 A shows how the time constant for the Co K-edge (Figure 121 B) compares with that of the time constant for the charge (Figure 121 A) during the reduction of Co-N and Figure 123 B and how the time constant for the Fe K-edge (Figure 122 C) compared with the time constant from the charge (Figure 122 A). For the analysis of both sets of data the point corresponding to ΔE is equal to 0.1 was removed, as no change was seen in the ΔeV *vs.* time data. In both cases the reduction of Co-N and oxidation of Fe-C there is little difference in the time constants for the spectroscopy compared with the time constants for the electrochemistry. From the results in 4.2.5 for NiHCF and CuHCF we expect to see little difference during the oxidation process for the Fe-C redox couple (deintercalation of Na^+ ions), which is also shown in Figure 123 B. Showing the material becoming more insulating as Na^+ ions are removed from the structure and the rate of both CIET and ET slowing down. When comparing the results in Figure 123 A with those of the intercalation of Na^+ ions for FeHCF (Figure 84 A) where the material becomes more conductive and the rate of ET increases, moving from PB to PW for the reduction of Fe-N. The reduction of Co-N shows a decrease in the rate of ET as we move from Co^{3+} to Co^{2+}(greater magnitude of ΔE). This suggests that the fully reduced form of CoHCF

($Na_2Co^{3+}[Fe^{3+}(CN)_6]$) is more insulting compared to the half intercalated state $NaCo^{2+}[Fe^{3+}(CN)_6]$ which is more conducting, as there is faster ET. However, during the intercalation process the IT is the limiting step as the ET reaction is happening at a faster rate, this is also seen for the intercalation of Na^+ into FeHCF where the ET has the faster rate (smaller time constant). This is also supported by the diffusion coefficient data shown in Figure 120 A, where the range of diffusion coefficients is much smaller than that for the intercalation of Na^+ ion into FeHCF (Figure 62 A). From this data we believe that when the oxidation stated of the metal in the MHCF are the same the material is more conducting. To further understand this data, studies into the electronic conductivity of CoHCF at the different states of intercalation will be needed using four point probe or electrochemical impedance measurements, but due to time restraints resulting from COVID-19 this was beyond the scope of this work.

5.3 Manganese hexacyanoferrate

Finally, MnHCF is also studied using the same dual edge methods as CoHCF. An example of the voltammogram for MnHCF in 2 M $NaNO_3$ electrolyte at pH 2 is given in Figure 124.The voltammetry shows two redox peaks. Like the voltammetry of FeHCF. The first set of peaks (I/II) between -0.2 and 0.8 V *vs.* SCE is attributed to the Fe-C redox couple. The set of peaks between 0.8 and 1.6 V *vs.* SCE (III/IV) corresponds to the Mn-N redox couple.[21]

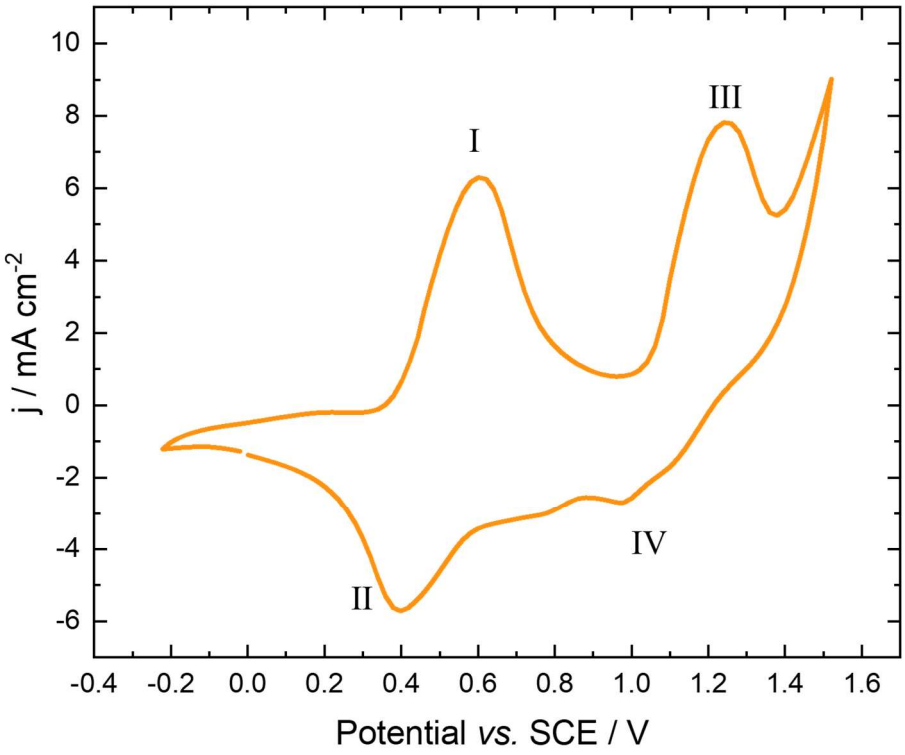

Figure 124 Cyclic voltammetry of an 8 mg cm^{-2} FeHCF on Toray carbon paper electrode in 2 M $NaNO_3$ at pH 2. With a scan rate of 0.5 mV s^{-1}, starting at 0.0 V *vs.* SCE. Carried out at room temperature (around 22 °C – 25 °C) in the *in situ* cell (see Figure 20). Peaks I/II showing the Fe-C redox couple and III/IV the Mn-N redox couple. Starting at 0.0 V *vs.* SCE.

From the voltammogram of MnHCF, Figure 124, an E_1 value of 0.8 V is selected to investigate both the reduction of Fe-C and the oxidation of Mn-N. **Table 20** summarises the E_1 and E_2 potentials used during the *in situ* LAPS EDE experiments.

Although MnHCF is an excellent candidate for the dual edge study, Mn and Fe have K-edges within a measurable range, the drawbacks of this material should be discussed. MnHCF is well documented to have poor cycling stability, and therefore difficult reproducibility, compared to the other MHCF materials discusse.[25,26,101,132,134] This poor cycling stability results from the change in the Jahn-Teller (JT) distortion on the oxidation of Mn^{2+} to Mn^{3+}, leading to an irreversible change in the structure of the MnHCF lattice. The initial issue resulting from the JT distortion is that during the saturation step used for the other MHCF the MnHCF will start to break down. Furthermore, this breakdown in the MnHCF lattice leads to greater inhomogeneity of the electrode affecting the overall conductivity of the material and the ability to get reproducible

XAFS data. Therefore, only a small number of E_2 values were investigated to give the best chance of reproducible data.

Table 20 Showing the E_1 and E_2 potentials for the LAPS experiments of CoHCF.

Material	Redox couple investigated	E_1 *vs.* SCE / V	E_2 *vs.* SCE / V
MnHCF	Fe-C	0.8	0.4/0.2/0.0
	Mn-N	0.8	1.2/1.4/1.5

5.3.1 Chronocoulometry

In Figure 125 and Figure 126, the charge response for the *in situ* LAPS experiments for the dual edge MnHCF are given. With Figure 125 giving the charge for the intercalation of Na^+ ions and the reduction of the Fe-C redox couple and Figure 126 the deintercalation of Na^+ ions and the oxidation of the Mn-N redox couple.

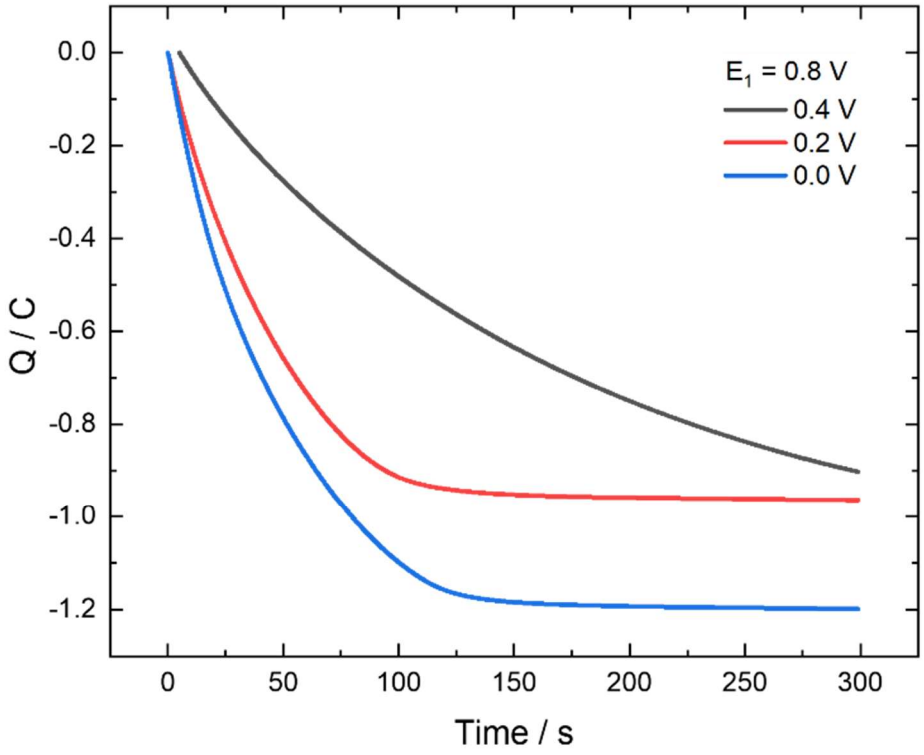

Figure 125 Chronocoulometry response for the large-amplitude potential step voltammetry for the intercalation of Na^+ ions into MnHCF electrode. Showing the applied potential (E_2) from the E_1 potential of 0.8 V *vs.* SCE.

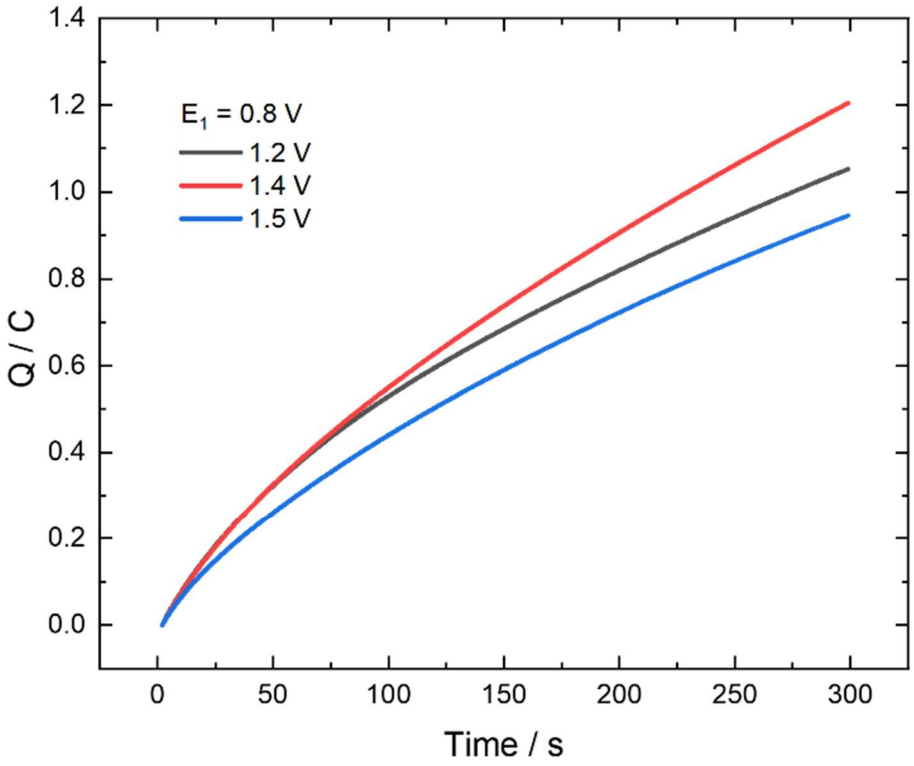

Figure 126 Chronocoulometry response for the large-amplitude potential step voltammetry for the deintercalation of Na^+ ions from MnHCF electrode. Showing the applied potential (E_2) from the E_1 potential of 0.8 V *vs.* SCE.

Figure 127 and Figure 128 show the results of the integrated Cottrell analysis for the reduction of Fe-C (intercalation of Na^+ ions) and the oxidation of Mn-N (deintercalation of Na^+ ions) respectively, showing the linear regions used to derive the diffusion coefficient for each E_2 potential applied. Figure 129 shows a comparison of the diffusion coefficients derived from the integrated Cottrell analysis, with Figure 129 A showing the intercalation of Na^+ and Figure 129 B the deintercalation of Na^+. Again in Figure 129 A as the magnitude of ΔE increases the rate of diffusion increases for the intercalation.

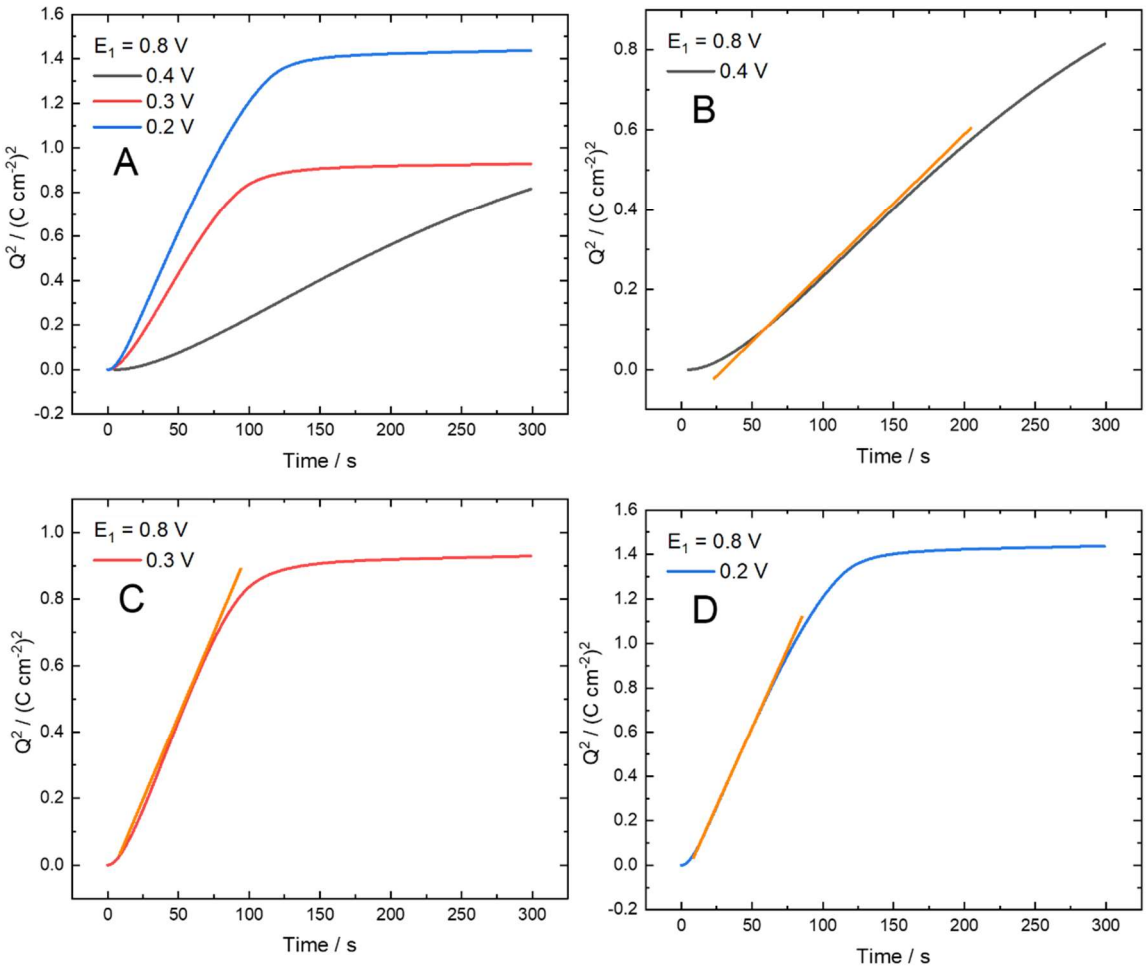

Figure 127 Integrated Cottrell analysis for diffusion coefficient for the intercalation of Na^+ ions into the MnHCF lattice. Showing A) the Q^2 *vs.* t plots for all E_2 values applied from E_1 = 0.8 V B-D) the individual plots for each E_2 and the linear region, all potentials are *vs.* SCE.

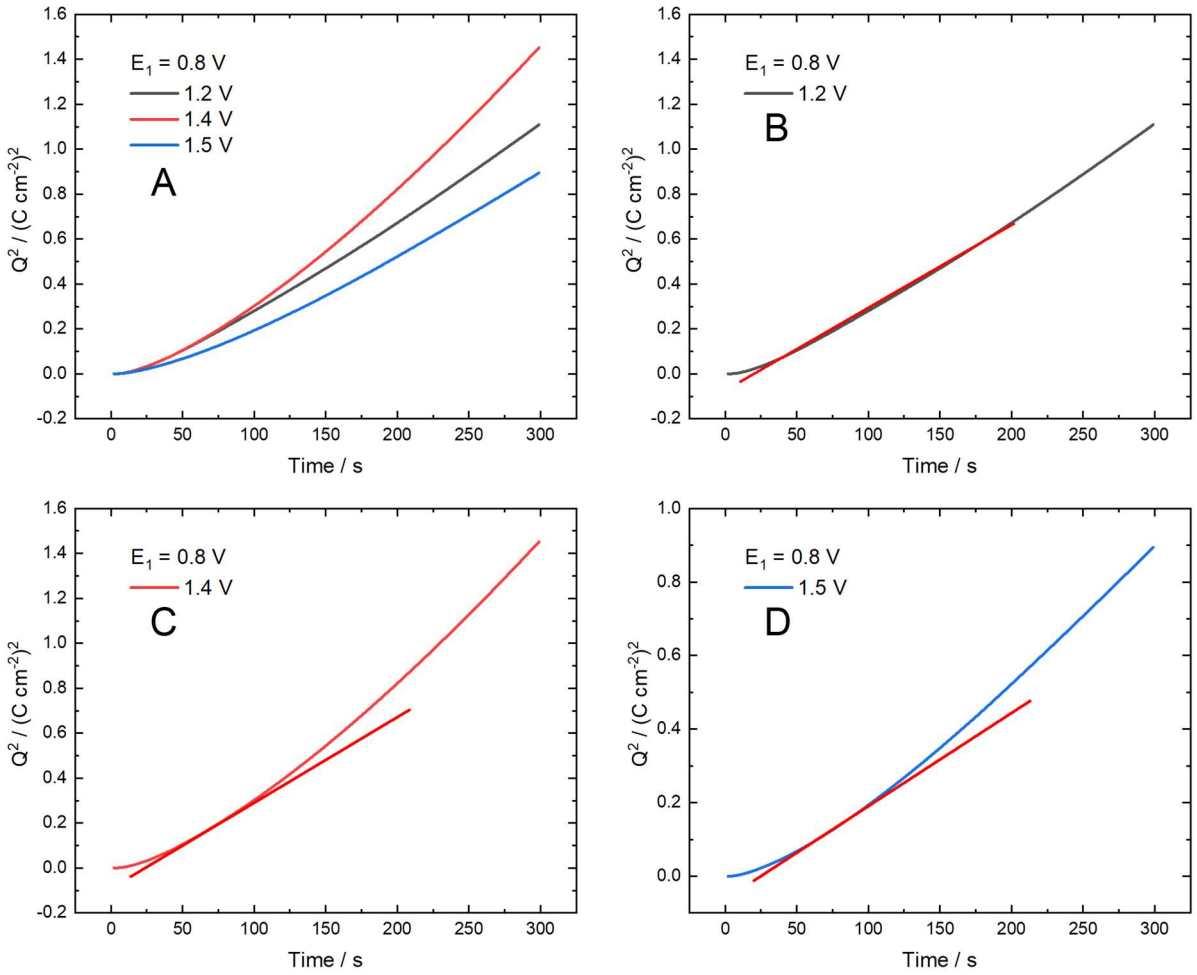

Figure 128 Integrated Cottrell analysis for diffusion coefficient for the deintercalation of Na^+ ions from the MnHCF lattice. Showing A) the Q^2 *vs.* t plots for all E_2 values applied from E_1 = 0.8 V B-D) the individual plots for each E_2 and the linear region, all potentials are *vs.* SCE.

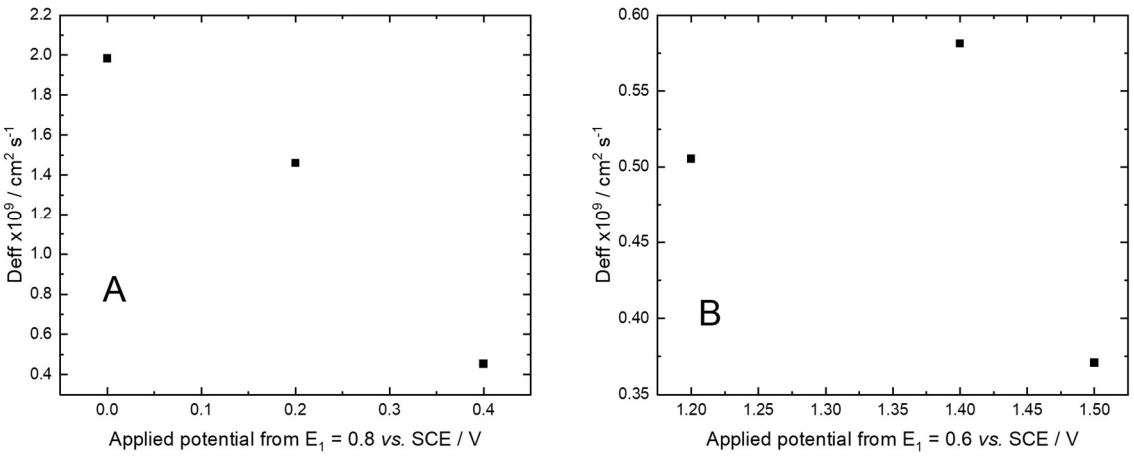

Figure 129 Comparison of the calculated diffusion coefficients from the linear region of the integrated Cottrell analysis of the LAPS experiments on A) Intercalation of Na^+ ions and B) deintercalation of Na^+ ions into/from the MnHCF lattice.

5.3.2 Simultaneous dual edge EDE experiment

Figure 130 gives the results from the *in situ* LAPS EDE experiments on MnHCF focussing on the reduction of Fe-C redox couple in MnHCF, i.e., the intercalation of Na^+. Figure 130 A gives the charge response from the LAPS experiments. Figure 130 B and C show the response of the change in ΔeV for the Mn K-edge and Fe K-edge respectively as a function of time. Across this potential range it is expected that only the Fe should change in oxidation state and the Mn to remain dormant. With an approximate change of around 0.8 eV for the Fe K-edge(Figure 130 C) and little to no change in the Mn K-edge (Figure 130 B), the data collected during the *in situ* LAPS experiment confirms this. Figure 131 shows the comparison of the time constants from the spectroscopic and electrochemical data for the reduction of Fe-C in MnHCF, showing a decrease in the rate of both ET (Spec) and CIET (Echem) as the magnitude of ΔE increases. However, the CEIT rate remains slower than the ET rate. These results suggest that $Na_2Mn^{2+}[Fe^{2+}(CN)_6]$ is more insulating than the half intercalated state ($NaMn^{2+}[Fe^{3+}(CN)_6]$), as was shown for CoHCF, the rate of ET slows down but the rate of the CIET is still slower. From this we can deduce that the IT is the limiting the CIET kinetics. Much more experimental work would need to be conducted on these samples to understand this data but due to COVID-19 restriction we were unable to do so.

Lastly, Figure 132 shows the results for the *in situ* LAPS experiments for the oxidation of the Mn-N redox couple. Figure 132 A shows the corresponding charge from the electrochemistry and Figure 132 B showing the results the change in oxidation state (ΔeV) *vs.* time for the Mn K-edge. The data for the simultaneously collected Fe K-edge is not presented here as the results are too

disrupted by noise to show any trend. As the oxidation of Mn is susceptible to JT distortion (see above) only the results from two of the E_2 potentials are presented as by the third step the data quality was too poor for inclusion. What we can see though in Figure 132 B is that there is a substantial change in the oxidation sate of the Mn for ΔE of 0.6 V (around 3.0 eV). No further analysis of the time constants was completed for the data shown in figure 132, as the limited nature of this data set meant that meaningful conclusions were not possible.

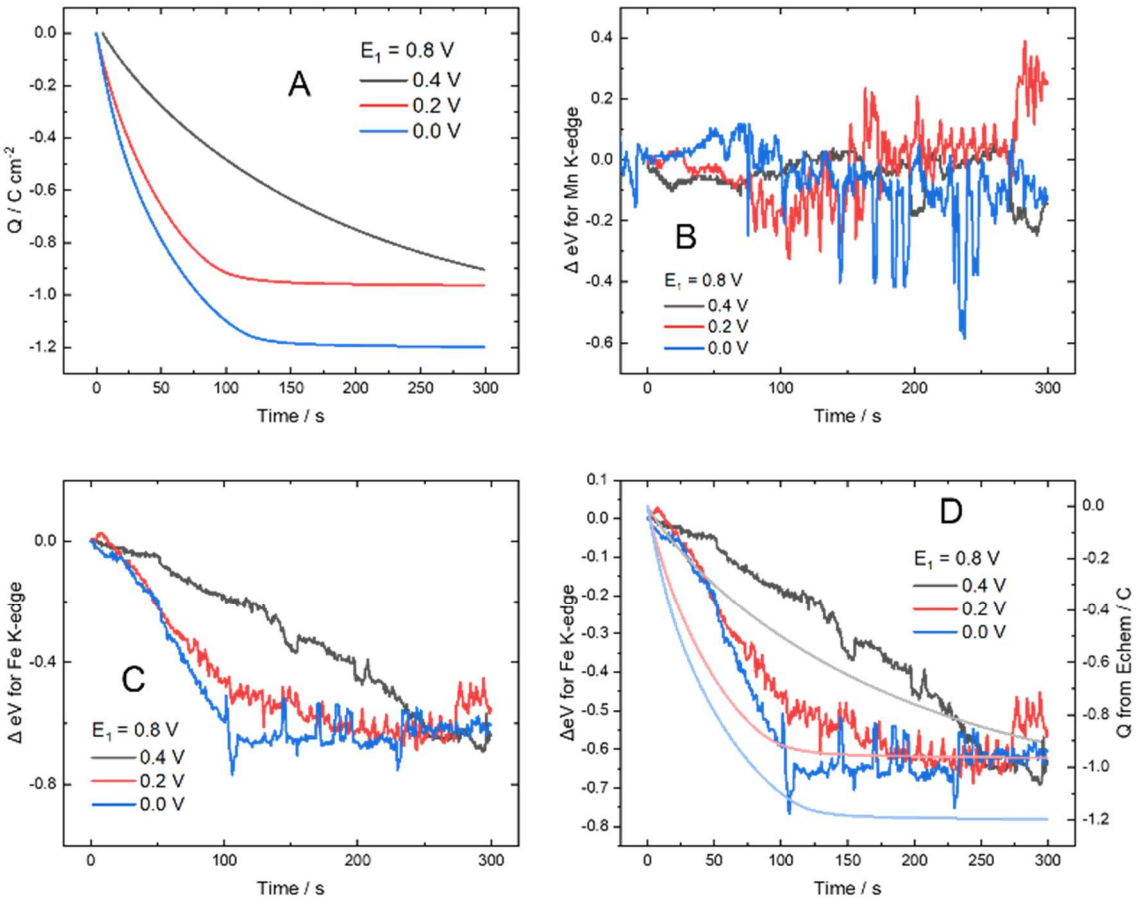

Figure 130 Results of the *in situ* EDE experiments for the reduction of Fe-C in MnHCF. A) the charge *vs.* time results from the LAPS experiments. B) The amount of change in the Mn K-edge for each applied E_2 (shown in figure) as a function of time. C) The amount of change in the Fe K-edge for each applied E_2 (shown in figure) as a function of time. D) showing a comparison of the ΔeV value for the Fe K-edge *vs.* the charge resulting from the electrochemical result (faded line).

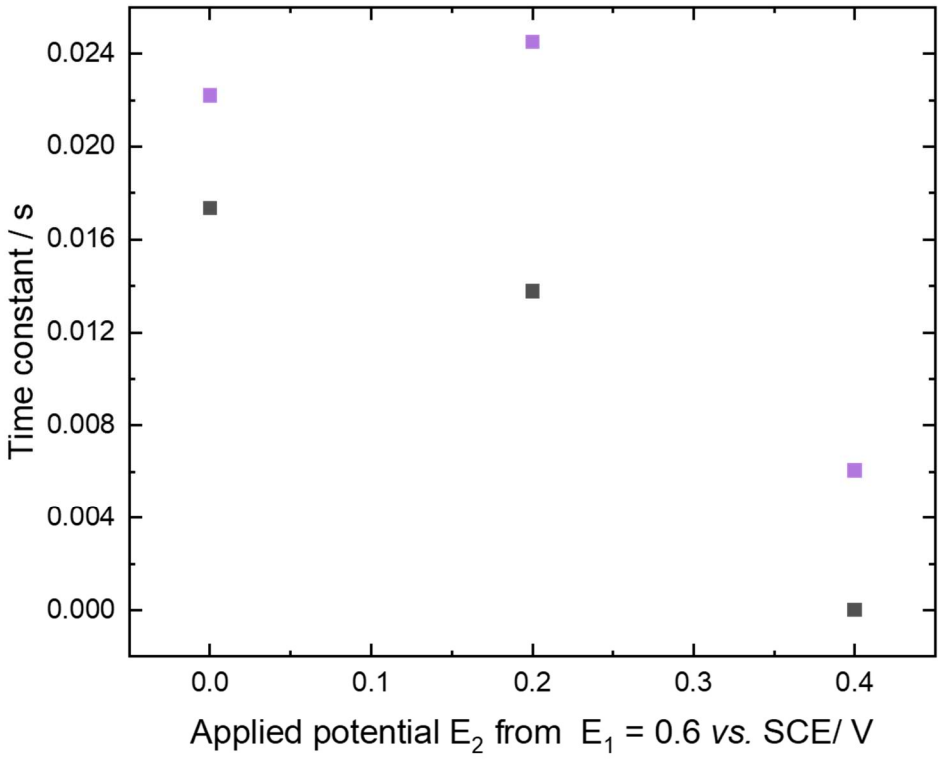

Figure 131 Time constant comparison for the intercalation of Na^+ (reduction of Fe-C) from MnHCF. Where black is the time constants from the spectroscopy and purple the time constants from the electrochemistry.

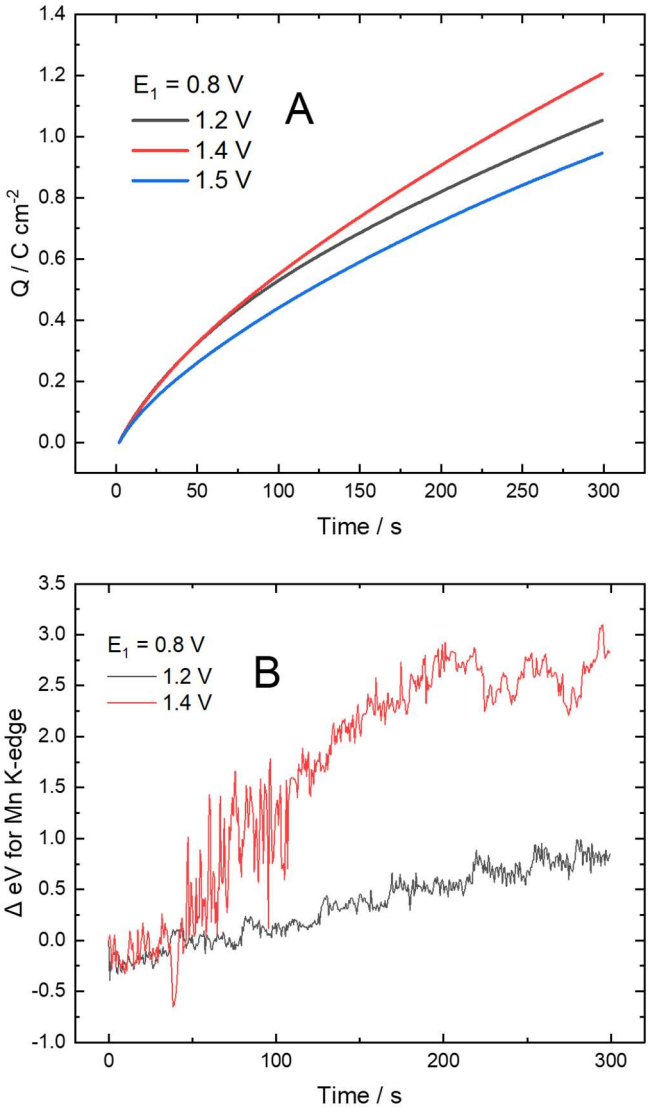

Figure 132 Results of the *in situ* EDE experiments for the oxidation of Mn-N in MnHCF. A) the charge *vs.* time results from the LAPS experiments. B) The amount of change in the Mn K-edge for each applied E_2 (shown in figure) as a function of time.

5.4 Conclusions

In this chapter the full capabilities of EDE have been demonstrated in terms of simultaneous measurements of multiple transition metal K-edges during electrochemical experiments, by using EDE to study the Fe and Co K-edges from CoHCF and the Fe and Mn K-edges from MnHCF in real time. Even with the complications resulting from either the technique itself e.g., loss of energy resolution due to a wide energy range, or issues from the materials, e.g., JT distortion, EDE can still provide insightful information regarding the ET kinetics of the metals during the redox reaction. This technique can be applied to other battery materials that contain multiple transition

metals, an example of which is work I carried out on I20-EDE on NMC 811 ($LiNi_{0.8}Mn_{0.1}Co_{0.1}O_2$) Li-ion battery cathodes in a collaboration with Rhodri Jervis' group from UCL, which is not included in this thesis.

In this chapter and in chapter 4, it has been shown that for the MHCF materials where the nitrogen bound metal is substituted for Fe, that the rate of IT appears to be the limiting factor. This is in direct contrast to the results seen in Chapter 3 where the conducting/insulting nature of the material was limiting the rate of ET. This work highlights the needs for more work to be completed to understand the effects of the spin states of the metal centres on the ionic conductivity of the Prussian Blue Analogue materials to further understand the limitations of CIET kinetics and to enable a better understanding of this data.

Chapter 6 Conclusion and Future work.

The first aim of this thesis was to synthesise MHCF compounds that would allow for effective electrochemical experiments to be conducted during *in situ* EDE experiments. It was shown in section 2.2.1 that the one-pot method used to synthesis FeHCF produced a cubic structure material, which as discussed is the ideal structure for cycling stability. Furthermore, the method used to synthesise Ni/Cu/Co and MnHCF (section 2.2.2) produced the desired MHCF materials that allowed for further electrochemical study.

The second aim was to design an *in situ* cell that would allow for *in situ* EDE and electrochemical experiments. The operando cell was designed to remove the need for electrolyte flow, without increasing the effect of mass transport on the electrochemistry. The flow needed to be removed as the movement of electrolyte through the beam path caused drifting in the spectroscopic results, as the background absorbance of the electrolyte varied. The results throughout this thesis demonstrate that the cell described in section 2.3.1 was sufficient for these types of experiments.

In this thesis we have shown that EDE can be used to aid the process of distinguishing the ET kinetics of a redox reaction from the CIET kinetics given during the analysis of an electrochemical experiment.

In Chapter 3, the rate of (de)intercalation of both Na^+ and K^+ ions is studies for FeHCF electrodes was studied in detail. The focus of the chapter being on the Fe-N redox couple of FeHCF. Various methods were used to measure an effective diffusion coefficient (IT). These diffusion coefficients were found to be dependent on the applied potential, with the intercalation having a slower rate of diffusion than the intercalation, for both Na^+ and K^+. By using *in situ* experiments on the EDE beamline, we have shown that during the reduction process the combined rate of the CIET is initially faster than the ET but as the magnitude of the driving force increases the difference between the two time constants reduces. We attributed this difference to the change from insulting PB to the more conducting PW. This change from an insulator led to a faster rate of ET, and this affect was seen for both Na^+ and K^+ ions. When investigating the oxidation for the same redox couple the reverse effect is seen, and the ET becomes slower as the magnitude of the driving force increases. We also see the combined rate of CIET slows down as the material becomes more insulting.

Chapter 4, focuses on the rate of deintercalation of Na^+ ions form NiHCF and CuHCF during electrochemical cycling of the Fe atoms, i.e., the Fe-C centres. Again, the diffusion coefficients were found to be potential dependant but for both these materials the deintercalation process is

much faster that than for FeHCF. Once again, a charge was calculated from the spectroscopic data, and when the time constants for these are compared with those of the charge from the electrochemical data very little difference is between the two. These data show that as the magnitude of the driving force increases so does the rate of reaction. Based on these results, we conclude that there was no change in the conductivity of the material as the oxidation state of the iron varied, in contrast to that in chapter 4 when the oxidation state of the Fe-N varied.

Chapter 5, demonstrates the capability of EDE to perform real time *in situ* simultaneous dual edge studies, i.e., the collection of data across two metal K-edges in one spectrum. For this CoHCF and MnHCF were used as the Co/Fe and Mn/Fe K-edges are close enough in range to collect them in the same spectrum, whilst retaining sufficient energy resolution to follow the changes in oxidation state. These materials also allowed investigation into the affected of changing the nitrogen bound metal in MHCF. Data of reasonable quality were obtained for CoHCF, showing the changes in oxidation states of both the Co-N and Fe-C metal centres, but the poor cycle stability of MnHCF limited the quality of the results that could be obtained.

6.1 Future work

Due to COVID19 there is still a large range of further experiments that were intended to be carried out using EDE on these materials. Firstly, instead of LAPS experiment's, which led to non-Cottrell like results and strain on the electrode, the use of the potential iteration titration (PITT) technique would provide an excellent alternative electrochemical experiment. PITT uses much smaller potential steps and allows for a better derivation of potential dependant diffusion coefficients. Furthermore, by using smaller potential steps more insight can be gained on the effect of driving force on the rate of change of oxidation state. For this thesis larger potential steps were used to see significant changes in the edge position and had been intended as the first set of investigations of each of the materials. If more time had been available these smaller steps may have provided greater insights. This technique could also be applied to a wider range of MHCF materials or other battery materials (NMC LIPs) with multiple redox centres. Other MHCF materials with the carbon centre doped such as iron(II) hexacobaltate, for example, where there is a Co bound to the carbon would be a good candidate.

Further investigation would also be focused on the making of the MHCF electrodes. As mentioned above (sections 2.2.5) the method of production of these electrodes (section 2.2.4) resulted in large cracks present in the electrode surface. Optimisation of the homogeneity of the electrodes would result in a more linear diffusion regime (as discussed in section 3.2.2). In addition to a more uniform diffusion through the electrode having a more homogeneous active layer would lead to

reversible kinetics that are more in line with what the literature shows for MHCF electrochemical reactions, as discussed in section 3.2.1.3. As discussed in this section and at other point in this thesis, although the electrochemical results presented are in line with a more quasi reversible system the mathematical analysis throughout has been based on the assumption of reversible kinetics in order to keep compatibility with literature sources. Furthermore, improving the homogeneity of the electrodes would enable better mapping during the *in situ* experiments as the assumption could be better made that the electrode is acting uniformly across the surface. Methods to improve the homogeneity of the electrode could be done using a K bar, doctors blade or spin coater, along with this more investigation into the solvent used to disperse the slurry would assist in producing uniform electrodes.[136]

Galvanostatic cycling would also be interesting investigation to carry out *in situ* and look at the rate of change of oxidation on a longer time scale. Although galvanostatic cycling does have drawback for *in situ* studies as the intense beam used, such as that on I20 interferes with the galvanostatic response, as reported by Sidrah Hussain in her thesis work titled "Advanced characterisation of next generation battery cathode materials using X-rays"[137], who found that during a scanning XAS measurement on the other branch of I20, that as the X-ray energy was scanned across the K-edge of the element undergoing oxidation the cell current was no longer limited by that set during the cycling and was in effect driven by the X-ray photons. Another important parameter to investigate further is the spin state ionic conductivity of the MHCF materials. Giving more insight into how the conductivity of the electrodes varies as a function of the oxidation state of the metals in the MHCF material. Further to this four point probe studies can be done to see how the conductivity varies across the electrode surface and therefore further support the mapping done during *in situ* experiments.

Chapter 7 References

1 T. M. Gür, *Energy Environ Sci*, 2018, **11**, 2696–2767.

2 J. O. G. Posada, A. J. R. Rennie, S. P. Villar, V. L. Martins, J. Marinaccio, A. Barnes, C. F. Glover, D. A. Worsley, and P. J. Hall, *Renewable and Sustainable Energy Reviews*, 2017, **68**, 1174–1182.

3 Y. Chen, Y. Kang, Y. Zhao, L. Wang, J. Liu, Y. Li, Z. Liang, X. He, X. Li, N. Tavajohi and B. Li, *Journal of Energy Chemistry*, 2021, **59**, 83–99.

4 G. Zampardi and F. La Mantia, *Curr Opin Electrochem*, 2020, **21**, 84–92.

5 A. Paolella, C. Faure, V. Timoshev*ski*i, S. Marras, G. Bertoni, A. Guerfi, A. Vijh, M. Armand, and K. Zaghib, *J Mater Chem A Mater*, 2017, **5**, 18919–18932.

6 A. Zhou, W. Cheng, W. Wang, Q. Zhao, J. Xie, W. Zhang, H. Gao, L. Xue and J. Li, *Adv Energy Mater*, 2021, **11**, 2000943.

7 H. Tomiyasu, H. Shikata, K. Takao, N. Asanuma, S. Taruta and Y.-Y. Park, *Scientific Reports 2017 7:1*, 2017, **7**, 1–12.

8 S. Phadke, R. Mysyk and M. Anouti, *Journal of Energy Chemistry*, 2020, **40**, 31–38.

9 B. J. Feldman and O. R. Melroy, *Journal of Electroanalytical Chemistry*, 1987, **234**, 213–227.

10 Y. Lu, L. Wang, J. Cheng and J. B. Goodenough, *Chemical Communications*, 2012, **48**, 6544–6546.

11 L. Wang, J. Song, R. Qiao, L. A. Wray, M. A. Hossain, Y. De Chuang, W. Yang, Y. Lu, D. Evans, J. J. Lee, S. Vail, X. Zhao, M. Nishijima, S. Kakimoto and J. B. Goodenough, *J Am Chem Soc*, 2015, **137**, 2548–2554.

12 Y. Lu, L. Wang, J. Cheng and J. B. Goodenough, *Chemical Communications*, 2012, **48**, 6544–6546.

13 Y. You, X. Yu, Y. Yin, K. Nam and Y. Guo, *Nano Res*, 2015, **8**, 117–128.

14 P. Arora, R. E. White and M. Doyle, *J Electrochem Soc*, 1998, **145**, 3647–3667.

15 P. J. Kulesza, M. A. Malik, M. Berrettoni, M. Giorgetti, S. Zamponi, R. Schmidt and R. Marassi, *Journal of Physical Chemistry B*, 1998, **102**, 1870–1876.

16 M. Qin, W. Ren, R. Jiang, Q. Li, X. Yao, S. Wang, Y. You and L. Mai, *ACS Appl Mater Interfaces*, 2021, **13**, 3999–4007.

17 C. Liu, Z. G. Neale, and G. Cao, *Materials Today*, 2016, **19**, 109–123.

18 A. Zhou, W. Cheng, W. Wang, Q. Zhao, J. Xie, W. Zhang, H. Gao, L. Xue and J. Li, *Adv Energy Mater*, 2021, **11**, 1–35.

19 L. Zhang, X. Li, M. Yang and W. Chen, *Energy Storage Mater*, 2021, **41**, 522–545.

20 J. Qian, C. Wu, Y. Cao, Z. Ma, Y. Huang, X. Ai and H. Yang, *Adv Energy Mater, 2018, **8**, 1702619*.

21 B. Haghighi, S. Varma, F. M. Alizadeh Sh., Y. Yigzaw and L. Gorton, *Talanta*, 2004, **64**, 3–12.

22 K. Itaya, K. Shibayama, H. Akahoshi and S. Toshima, *J Appl Phys*, 1982, **53**, 804–805.

23 L. Samain, F. Grandjean, G. J. Long, P. Martinetto, P. Bordet and D. Strivay, *J Synchrotron* Radiat, 2013, **117**, 9693 - 9712.

24 A. Kraft, *Bull. Hist. Chem*, 2008, **33**, 2.

25 S. F. A. Kettle, E. Diana, E. Boccaleri, P. L. Stanghellini, C. Ifm, V. Uni, V. P. Giuria, P. O. A, A. V and V. G. Bellini, *Inorg Chem*, 2007, **46**, 1747–1751.

26 C. Erinmwingbovo, M. S. Palagonia, D. Brogioli and F. La Mantia, *ChemPhysChem*, 2017, **18**, 917–925.

27 J. F. KEGGIN and F. D. MILES, *Nature*, 1936, **137**, 577–578.

28 H. J. Buser, A. Ludi, D. Schwarzenbach and W. Petter, *Inorg Chem*, 1977, **16**, 2704–2710.

29 Q. Wang, J. Li, H. Jin, S. Xin, and H. Gao, *InfoMat*, 2022, **4**, 12311.

30 K. Hurlbutt, S. Wheeler, I. Capone and M. Pasta, *Joule*, 2018, **2**, 1950–1960.

31 C. D. Wessells, S. V Peddada, R. A. Huggins and Y. Cui, *Nano Lett*, 2011, **11**, 5421–5425.

32 S. Yu, Y. Li, Y. Lu, B. Xu, Q. Wang, M. Yan and Y. Jiang, *J Power Sources*, 2015, **275**, 45–49.

33 Z. Jia, J. Wang and Y. Wang, *RSC Adv*, 2014, **4**, 22768–22774.

34 M. S. Wu, L. J. Lyu, and J. H. Syu, *J Power Sources*, 2015, **297**, 75–82.

35 M. Pasta, R. Y. Wang, R. Ruffo, R. Qiao, H. W. Lee, B. Shyam, M. Guo, Y. Wang, L. A. Wray, W. Yang, M. F. Toney and Y. Cui, *J Mater Chem A Mater*, 2016, **4**, 4211–4223.

36 P. J. Kulesza, M. A. Malik, S. Zamponi, M. Berrettoni and R. Marassi, *Journal of Electroanalytical Chemistry*, 1995, **397**, 287–292.

37 M. Takachi, T. Matsuda and Y. Moritomo, *Applied Physics Express*, 2013, **6**, 0–3.

38 H. Gao, S. Liu, Y. Li, E. Conte and Y. Cao, *Energies (Basel)*,2017, **10**, 1787.

39 Z. Shen, Y. Sun, J. Xie, S. Liu, D. Zhuang, G. Zhang, W. Zheng, G. Cao and X. Zhao, *Inorg Chem Front*, 2018, **5**, 2914–2920.

40 A. Mullaliu, M. Gaboardi, J. R. Plaisier, S. Passerini and M. Giorgetti, *ACS Appl Energy Mater*, 2020, **3**, 5728–5733.

41 S.-M. Chen, *J. Electroanal. Chem.*, 2002, **521**, 1-2.

42 S. Sriman Narayanan and F. Scholz, *Electroanalysis*, 1999, **11**, 465-469.

43 D. Fraggedakis, M. McEldrew, R. B. Smith, Y. Krishnan, Y. Zhang, P. Bai, W. C. Chueh, Y. Shao-Horn and M. Z. Bazant, *Electrochim Acta*, 2021, **367**, 137432.

44 E. J. F. Dickinson and A. J. Wain, *Journal of Electroanalytical Chemistry*,2020, **872**, 114154.

45 Allen J. Bard, Larry R. Faulkner, *Electrochemical Methods: Fundamentals and Applications*, 2000, **3rd Edition**, Chapter 3.

46 V. A. Nikitina, S. Y. Vassiliev and K. J. Stevenson, *Adv Energy Mater*, 2020, **10**, 1903933 .

47 R. A. Marcus, *J. Chem. Phys*, 1956, **24**, 966-978.

48 S. W. Feldberg, *Anal Chem*, 2010, **82**, 5176–5183.

49 T. P. Silverstein, *J Chem Educ*, 2012, **89**, 1159–1167.

50 M. Z. Bazant, *Acc Chem Res*, 2013, **46**, 1144–1160.

51 M. Z. Bazant, *Acc Chem Res*, 2013, **46**, 1144–1160.

52 R. Seeber, C. Zanardi and G. Inzelt, *ChemTexts*, 2015, **1**, 18.

53 T. P. Silverstein, *J Chem Educ*, 2012, **89**, 1159–1167.

54 J. H. Bombile, M. J. Janik and S. T. Milner, *Physical Chemistry Chemical Physics*, 2017, **20**, 317–331.

55 R. Ghosh and F. C. Spano, *Acc Chem Res*, 2020, **53**, 2201–2211.

56 K. Morita, M. J. Golomb, M. Rivera and A. Walsh, *Chem. Mater*, 2023, **35**, 3652-3659.

57 Allen J. Bard, Larry R. Faulkner , *Electrochemical Methods: Fundamentals and Applications*, 2000, **3rd Edition**, Chapter 4.

58 G. Zhang, A. S. Cuharuc, A. G. Güell and P. R. Unwin, *Phys Chem Chem Phys*, 2015, **17**, 11827–11838.

59 J. Hui, X. Zhou, R. Bhargava, A. Chinderle, J. Zhang, and J. Rodríguez-López, *Electrochim Acta*, 2016, **211**, 1016–1023.

60 S. Gutiérrez-Portocarrero, P. Roquero, M. Becerril-González and D. Zúñiga-Franco, *Diam Relat Mater*, 2019, **92**, 219–227.

61 I. Duo, A. Fujishima, and C. Comninellis, *Electrochem commun*, 2003, **5**, 695–700.

62 A. J. Slate, D. A. C. Brownson, A. S. Abo Dena, G. C. Smith, K. A. Whitehead and C. E. Banks, *Physical Chemistry Chemical Physics*, 2018, **20**, 20010–20022.

63 A. S. Ambolikar, S. K. Guin and S. Neogy, *New Journal of Chemistry*, 2019, **43**, 18210–18219.

64 H. Dong, S. Wang, J. J. Galligan and G. M. Swain, *Front. Biosci*, 2011, **3**, 518-540 .

65 X. Ji, C. E. Banks, A. Crossley, and R. G. Compton, *ChemPhysChem*, 2006, **7**, 1337–1344.

66 J. F. Cassidy, R. C. de Carvalho, and A. J. Betts, *Electrochem*, 2023, **4**, 313–349.

67 P. Bai and M. Z. Bazant, *Nat Commun*, 2014, **5**, 3585.

68 L.-C. Chen and K.-C. Ho, *J. Electrochem Soc*, 2002, **149**, E40.

69 L.-C. Chen and K.-C. Ho, *J. Electrochem Soc*, 2001, **148**, E282.

70 J. J. Garcia-Jarefio, A. Sanmatias, J. Navarro-Laboulais, D. Benito and F. Vicente, *Electrochemical Acta,* 1998, **43**, 3-4.

71 C. E. D. Chidsey and R. W. Murray, *J. Phys. Chem*, 1986, **90**, 1479-1484.

72 E. Czir, pj G. Kulesza Inzelt, A. Wolkiewicz and K. M. Miecznikowski Malik, *Journal of Nepal Chemical Society*, 2013, **30**, 1-4.

73 D. Xing, P. P. Bawol, A. E. A. A. A. Abd-El-Latif, L. Zan and H. Baltruschat, *ChemElectroChem*, 2021, **8**, 3726–3739.

74 A. Eftekhari, *J Power Sources*, 2003, **124**, 182–190.

75 K. Hurlbutt, F. Giustino, M. Pasta and G. Volonakis, *Chemistry of Materials*, 2021, **33**, 7067–7074.

76 A. Viehbeck and D. W. Deberry, *J. Electrochem Soc*, 1991, **12**, 3633-3640 .

77 D. Pajerowski, T. Watanabe, T. Yamamoto, and Y. Einaga, *Phys. Rev. B*, 2011, **81**, 223-8522.

78 F. S. Hegner, J. R. Galán-Mascarós and N. López, *Inorg Chem*, 2016, **55**, 12851–12862.

79 K. Hurlbutt, F. Giustino, M. Pasta and G. Volonakis, Chem. Mater, 2020, **32**, 7653-7661 .

80 P. Hosseini, K. Wolkersdö, M. Wark, E. Redel, H. Baumgart and G. Wittstock, *J. Phys. Chem*, 202, **124**, 16849-1689.

81 I. Oh, H. Lee, H. Yang and J. Kwak, *Electrochemistry Communications*, 2001, **3**, 274-280 .

82 S. Saeed, S. Boyd, W.-Y. Tsai, R. Wang, N. Balke and V. Augustyn, *this journal is Cite this: Chem. Commun*, 2021, **57**, 6744.

83 J. Nordstrand, E. Toledo-Carrillo, S. Vafakhah, L. Guo, H. Y. Yang, L. Kloo and J. Dutta, *ACS Appl Mater Interfaces*, 2022, **14**, 1102–1113.

84 M. Qin, W. Ren, R. Jiang, Q. Li, X. Yao, S. Wang, Y. You and L. Mai, *Cite This: ACS Appl. Mater. Interfaces*, 2021, **13**, 4007.

85 H. Li, J. Huang, K. Yang, Z. Lu, S. Yan, H. Su, C. Liu, X. Wang and B. Ren, *Journal of Physical Chemistry Letters*, 2022, **13**, 479–485.

86 M. Giorgetti and M. Berrettoni, *Inorg Chem*, 2008, **47**, 6001–6008.

87 M. Giorgetti, S. X. Dou, F. M. Labajos, Z. Luo, and Y. Masuda, *ISRN Materials Science*, 2013, **2013**, 22.

88 A. Mullaliu, G. Aquilanti, P. Conti, J. R. Plaisier, M. Fehse, L. Stievano and M. Giorgetti, Radiation Physics and Chemistry, 2020, **175**, 108252.

89 J. Seok, S. H. Yu and H. D. Abrunã, *J. Phys. Chem C*, 2020, **124**, 16332–16337.

90 Z. Wang, M. T. Sougrati, Y. He, P. N. Le Pham, W. Xu, A. Iadecola, R. Ge, W. Zhou, Q. Zheng, X. Li and J. Wang, *Nano Energy*, 2023, **109**, 108256.

91 J. Sottmann, F. L. M. Bernal, K. V. Yusenko, M. Herrmann, H. Emerich, D. S. Wragg and S. Margadonna, *Electrochem Acta*, 2016, **200**, 305–313.

92 Y. Moritomo, M. Takachi, Y. Kurihara and T. Matsuda, *Advances in Materials Science and Engineering*, 2013, **7**, 967285.

93 Q. Wang, N. Wang, S. He, J. Zhao, J. Fang and W. Shen, *Dalton Transactions*, 2015, **44**, 12878.

94 S. Kjeldgaard, I. Dugulan, A. Mamakhel, M. Wagemaker, B. B. Iversen and A. Bentien, *Coord. Chem. Rev*, 2017, **352**, 328-345.

95 B. H. Toby and R. B. Von Dreele, *J Appl Crystallogr*, 2013, **46**, 544–549.

96 M. B. Zakaria and T. Chikyow, , DOI:10.1016/j.ccr.2017.09.014.

97 L. Zhou, M. Zhang, Y. Wang, Y. Zhu, L. Fu, X. Liu, Y. Wu, and W. Huang, *Electro. Acta*, 2017, **232**, 106-113.

98 S.-M. Chen, *J. Electroanal. Chem*, 2002, **521**, 1-2.

99 C. D. Wessells, S. V. Peddada, R. A. Huggins and Y. Cui, *Nano Lett*, 2011, **11**, 5421–5425.

100 D. T. Schwartz, *Apply* Spec¸ 2002, **56**, 1021–1029.

101 J. Joseph, H. Gomathi and G. P. Rao, *J. Electroanal Chem*, 1991, **304**, 263–269.

102 Y. Q. Liu, Y. Yan and H. X. Shen, *Chin J Chem*, 2005, **23**, 1165–1172.

103 Derek Pletcher, *A First Course in Electrode Processes*, 2009, **2nd Edition**, Chapter 4.

104 A. B. Kroner, M. A. Newton, M. Tromp, O. M. Roscioni, A. E. Russell, A. J. Dent, C. Prestipino and J. Evans, Phys. *Chem. Phys. Chem*, 2014, **15**, 3049–3059.

105 M. Newville, *J. Sync. Rad*, 2005, **12**, 537-541 .

106 S. Calvin, *XAFS for Everyone*, 2013, **1st Edition**, Chapter 1.

107 E. Dispersive, J. Headspith, J. Groves, P. N. Luke, M. Kogimtzis, G. Salvini, S. L. Thomas, R. C. Farrow, J. Evans, T. Rayment, J. S. Lee, W. D. Goward, M. Amman, O. Mathon and S. Diaz-Moreno, *J. Sync. Rad*, 2016, **23**, 353-368.

108 J. E. Penner-Hahn, *Comprehensive Coordination Chemistry II*, 2003, **2**, 159–186.

109 M. Basham, J. Filik, M. T. Wharmby, P. C. Y. Chang, B. El Kassaby, M. Gerring, J. Aishima, K. Levik, B. C. A. Pulford, I. Sikharulidze, D. Sneddon, M. Webber, S. S. Dhesi, F. Maccherozzi, O. Svensson, S. Brockhauser, G. Náray and A. W. Ashton, *J Synchrotron Radiat*, 2015, **22**, 853–858.

110 K. Sakata and K. Amemiya, *Electrochem commun*, 2023, **157**, 107627.

111 A. A. Karyakin, E. E. Karyakina and L. Gorton, *ElecChem. Comms*, 1999, **1**, 78-82.

112 M. Asai, A. Takahashi, K. Tajima, H. Tanaka, M. Ishizaki, M. Kurihara and T. Kawamoto, *RSC Adv*, 2018, **8**, 37356–37364.

113 C. Li, W. Yan, S. Liang, P. Wang, J. Wang, L. Fu, Y. Zhu, Y. Chen, Y. Wu and W. Huang, *Nanoscale Horiz*, 2019, **4**, 991–998.

114 B. Xie, P. Zuo, L. Wang, J. Wang, H. Huo, M. He, J. Shu, H. Li, S. Lou and G. Yin, *Nano Energy*, 2019, **61**, 201–210.

115 L. Wang, J. Song, R. Qiao, L. A. Wray, M. A. Hossain, Y. De Chuang, W. Yang, Y. Lu, D. Evans, J. J. Lee, S. Vail, X. Zhao, M. Nishijima, S. Kakimoto and J. B. Goodenough, *J Am Chem Soc*, 2015, **137**, 2548–2554.

116 S. Muhammad, U. B. Zahra, A. Ahmad, L. A. Shah and A. Muhammad, *J. Chem. Soc. Pakistan*, 2020, **42**, 813–817.

117 H. Kahlert, U. Retter, H. Lohse, K. Siegler and F. Scholz, *Journal of Physical Chemistry B*, 1998, **102**, 8757–8765.

118 R. S. Nicholson, *Anal. Chem*, 1965, **37**,1351-1355

119 E. P. Randviir, *Electrochem Acta*, 2018, **286**, 179–186.

120 N. Elgrishi, K. J. Rountree, B. D. McCarthy, E. S. Rountree, T. T. Eisenhart, and J. L. Dempsey, *J. Chem. Ed*, 2017, **95**, 197-206.

121 A. Eftekhari, *J Power Sources*, 2003, **124**, 182–190.

122 A. Eftekhari, *Electro. Chem. Acta*, 2011, **47**, 495-499.

123 F. H. Ferreira Batista, L. J. Amaral Siqueira, L. T. Costa and T. L. Ferreira, *Journal of Physical Chemistry C*, 2018, **122**, 2717–2725.

124 Q. Yang, W. Wang, H. Li, J. Zhang, F. Kang, and B. Li, *Electrochim Acta*, 2018, **270**, 96–103.

125 W. Wang, Z. Hu, Z. Yan, J. Peng, M. Chen, W. Lai, Q. F. Gu, S. L. Chou, H. K. Liu and S. X. Dou, *Energy Storage Mater*, 2020, **30**, 42–51.

126 A. J. Bard and L. R. Faulkner, *Electrochemical Methods: Fundamentals and Applications*, 2001, **3nd Edition**, 156–225.

127 C. D. Wessells, S. V Peddada, M. T. McDowell, al -, Y. Xiong, Y. Lin, Q. Xue ,*J. Electrochem. Soc*, 2018, **165**, 1777.

128 B. D. Shrivastava, *Indian. Natn. Sci*, 2013, **4**, 921-966.

129 M. Grafe, E. Donner, R. N. Collins, and E. Lombi, *Analytica Chem Acta*, 2104, **822**, 1-22.

130 J. S. Zhou and M. A. J. Rodgers, *J. Am. Chem*, 1991, **113**, 7728-7734.

131 M. Chen, S.-L. Chou, and S.-X. Dou, *Nature Comms*, 2019, **10**, 1480.

132 T. Sano, R. Miyahara, M. Katayama, Y. Kobayashi, Y. Horiuchi, Y. Shibano and Y. Inada, *Energy Environ. Sci*, 2011, **4**, 269-284.

133 P. Butnoi, W. Senanon, N. Chanlek, Y. Poo-arporn, S. Pinitsoontorn, S. Maensiri, P. Songsiriritthigul, P. Khemthong and P. Kidkhunthod, *Progress in Natural Science: Materials International*, 2021, **31**, 420–427.

134 D. Kido, M. M. Rahman, T. Takeguchi and K. Asakura, *Chem Lett*, 2022, **51**, 538–541.

135 K. R. Tallman, G. P. Wheeler, C. J. Kern, E. Stavitski, X. Tong, K. J. Takeuchi, A. C. Marschilok, D. C. Bock and E. S. Takeuchi, *J. Phys. Chem. C*, 2021, **125**, 58–73.

136 S. Aryal, K. Kucuk, E. V. Timofeeva and C. U. Segre, *Mater Today Commun*, *Materials Today Communications, 2021, **26**, 101693.*

137 S. I. Hussain, *Thesis titled*: *Advanced characterisation of next generation battery cathode materials using X-rays*, 2023, University of Southampton, Department of Chemistry.